

University of St Andrews



Full metadata for this thesis is available in
St Andrews Research Repository
at:

<http://research-repository.st-andrews.ac.uk/>

This thesis is protected by original copyright

THE UNIVERSITY OF ST. ANDREWS

Doppler imaging of late type stars

John Robert Barnes

Submitted for the degree of Ph.D.

November 1999



THE UNIVERSITY OF ST. ANDREWS

Doppler imaging of late type stars

Submitted for the degree of Ph.D.

November 1999

John Robert Barnes

ABSTRACT

Surface images of a number of rapidly rotating cool stars are presented. Temperature inhomogeneities due to starspots are generally found to exist on the surface of rapid rotators. These features can be seen as 'emission bumps' crossing the Doppler broadened absorption profiles. Doppler imaging takes a time series of high resolution spectroscopic absorption profiles, and inverts them to form a high resolution image of the stellar surface.

The technique of least squares deconvolution is applied to each échellogram in a given time series. This technique uses most of the large number of photospheric absorption lines available in an échelle spectrum to derive a single profile with a high signal to noise ratio. This is in effect a sophisticated cross-correlation process, but removes the effects of side-lobes due to blending of the rotationally broadened profiles. An implementation of the least squares deconvolution method is tested for suitability for Doppler imaging purposes.

Using least squares deconvolution to obtain rotation profiles with signal to noise ratios of typically 1000, images of four α Persei stars are derived. These are the first high resolution images of cluster G dwarfs and reveal starspots concentrated in latitude bands. An upper limit on the lifetime for individual spots of one month is inferred, based upon two images of one of these stars (He 699), separated by a one month interval.

Images of two rapidly rotating K stars in the solar neighbourhood are also presented. These are the K0 dwarf PZ Tel (HD 174429) and the K3 dwarf Speedy Mic (HD 197890). Pairs of images of these stars are compared in order to determine latitude dependent surface differential rotation patterns.

The $H\alpha$ line is also examined for transient features. These appear in absorption and cross the profile on timescales shorter than photospheric starspot transients. All the stars with the exception of AP 193 reveal these features which are attributed to circumstellar slingshot prominences. AP 149 shows variable $H\alpha$ in emission, with two lobes which describe s-wave patterns during a rotation cycle. The $H\alpha$ time series is used to derive a Doppler tomogram of the emission region.

ACKNOWLEDGEMENTS

I would like to dedicate this thesis to my parents who have supported me throughout my education. I would never have got this far without your support.

I am most grateful to my supervisor, Andrew Collier Cameron, for his support and continued patience throughout the course of this work. Many thanks must also go to Jean-Francois Donati for help with some of the finer points of coding the least squares deconvolution routine. I would also like to thank Moira Jardine for helpful discussions which have led to additional avenues of research. A special thanks to Yvonne Unruh who had to put up with so many questions in the early stages of this thesis, and who also accompanied me on two observing trips. I forgive you for bringing the system down at the William Herschel Telescope by the way! Dave, thanks for a “marvellous” observing run at the William Herschel Telescope, and thanks for the help with the lithium analysis. Also, many thanks to Danny for producing the Doppler tomograms presented in Chapter 7. Tim and Gaitee, I wasn’t ashamed to ask stupid questions, thanks for being honest! Your help in manning the James Gregory Telescope at St Andrews while I was observing in sunnier climes is much appreciated. Graham, well done for coping with having to share an office with me, especially during the write up, where boredom frequently set in.

I would like to thank all the friends I have known over the years, many who have now left, but especially those who remain. Leisle and Ysmena, thanks for putting up with my attempts at music making, and especially for helping and putting up with my singing. Caroline, trips to the beach are not the same now you have gone. Mark, I guess it is fair to say that without your endless enthusiasm for just about everything, from philosophising until the early hours of the morning, to playing the ‘Rackett’, I would have done far less wacky things over the years. Clare, I’m not sure if I would have returned from the whiteout on Beinn Dearg without your assurances that we *were* going the right way. Many thanks to Sarah and Heather who must both have depleted food stocks by now. I’ll replace all those biscuits, honest. A special thanks must go to Robert for over seven years of friendship. Especially, many thanks for listening when I couldn’t make my mind up what to do, a not infrequent occurrence!

I look forward to future visits to the Royal Burgh of St Andrews and to Scotland. There are too many mountains to climb to keep me away!

“Never write any unnecessary notes because every note should have a life of its own.”
Jean Sibelius (1867 - 1957)

CONTENTS

1	Introduction	2
1.1	Stellar rotation	3
1.1.1	The distribution of rotation in young open clusters	4
1.2	The evolution of angular momentum	7
1.2.1	Components of the models	7
1.2.2	Angular momentum evolution models	10
1.3	Solar and stellar dynamos	13
1.3.1	Magnetic activity	13
1.3.2	The solar dynamo	14
1.4	A dynamo model and the latitude distributions of starspots	16
1.5	Starspot patterns from observations	21
1.5.1	Binaries	22
1.5.2	Single stars	23
1.6	Latitude distributions - observation vs theory	25
1.7	The solar/stellar magnetic cycle	26
1.7.1	Photospheric activity indicators	26
1.7.2	Chromospheric activity indicators - The Mount Wilson Survey	27

1.8	Aims	28
2	Least Squares Deconvolution	31
2.1	Introduction	31
2.2	The least squares technique	32
2.2.1	Spectrum normalisation and weighting scheme	36
2.2.2	Errors in the deconvolved profiles	39
2.2.3	Limb Darkening	40
2.2.4	Reliability of the deconvolved profile shape	41
2.2.5	Deconvolution reliability with increasing $v \sin i$	45
2.2.6	The line list	46
3	Doppler Imaging	50
3.1	Chapter synopsis	50
3.2	The line profile	50
3.3	Imaging	55
3.3.1	The forward problem - Image to Data transformation	55
3.4	The inverse problem	59
3.4.1	The regularising function	60
3.4.2	Image reconstruction procedure	61
3.5	Image reconstruction	62
3.5.1	Determination of stellar parameters	63
3.5.2	Inclination determination	69
3.6	Conclusion	69

4	G dwarfs in the α Persei Cluster	72
4.1	Synopsis	72
4.2	Introduction	73
4.3	Observations	74
4.3.1	Spectroscopy	74
4.3.2	Photometry	75
4.4	Data reduction	79
4.4.1	Extraction	79
4.4.2	Continuum fitting	80
4.5	Least squares deconvolution	82
4.5.1	Errors	83
4.5.2	Limb Darkening Coefficient	84
4.5.3	The local specific intensity profiles	84
4.6	Image reconstruction	92
4.6.1	Fine tuning parameters	92
4.6.2	The Images	93
4.7	Discussion	94
4.7.1	Differential rotation	99
4.8	Conclusion	100
4.9	Synopsis	101
4.10	Introduction	103
4.11	Observations and data reduction	104
4.11.1	Spectral Types	105

4.11.2	Continuum fitting	106
4.11.3	Multiplex gain from least squares deconvolution	106
4.12	System parameters	107
4.13	Results	109
4.13.1	Images	109
4.13.2	Polar spot strength/inclination dependence	113
4.14	Discussion & conclusions	113
5	Images of Southern rapid rotators I: Differential rotation on PZ Telescopium	117
5.1	Chapter synopsis	117
5.2	Introduction	117
5.3	Data reduction	121
5.3.1	Observations	121
5.3.2	Continuum fitting	122
5.3.3	Radial velocity	123
5.3.4	Lithium abundance measurements	123
5.4	Physical Parameters of PZ Tel	124
5.5	Imaging	127
5.5.1	Dual-site observations	128
5.5.2	Determination of system parameters	129
5.6	Results	134
5.6.1	Images and Differential Rotation	134
5.7	Deconvolved subsets	136
5.8	Discussion	140

5.9	Conclusion	147
5.10	Acknowledgement	149
6	Images of Southern rapid rotators II: Starspot patterns and differential rotation on HD 197890 “Speedy Mic”	150
6.1	Synopsis	150
6.2	Introduction	153
6.3	Observations	154
6.3.1	Local intensity profiles	154
6.3.2	Continuum fitting	156
6.4	Imaging	156
6.4.1	Least squares deconvolution	156
6.5	Derivation of system parameters	156
6.6	Results	161
6.6.1	Images	161
6.7	Discussion	166
6.8	Conclusion	168
7	Prominences	170
7.1	Introduction	170
7.2	Stellar prominences	171
7.2.1	Observational evidence	171
7.2.2	Measurement of prominence features	173
7.3	Results & Discussion	174
7.3.1	α Persei G dwarfs	174

7.3.2	PZ Tel	181
7.3.3	Speedy Mic	184
7.4	Summary and Discussion	187
8	Summary and Conclusions	190
8.1	Least squares deconvolution	190
8.2	Surface distribution of starspots	191
8.3	Comparison of theory and observations	192
8.4	Differential rotation	195
8.5	Future Work	197
	REFERENCES	198
A	Spdecon Guide	204
A.1	Introduction	204
A.2	Program subroutines	204
A.2.1	acc_decon	204
A.2.2	acc_decon1	205
A.2.3	acc_decon2	205
A.2.4	choldc and cholsl	205
A.2.5	acc_decon3	205
A.3	Input Parameters	205
	Appendices	204

LIST OF FIGURES

1.1	<i>v</i> sin <i>i</i> vs (B-V) ₀ for α Persei, Pleiades and Hyades.	5
1.2	Rotational evolution tracks for 0.8 M _⊙ and 1.0 M _⊙ stars (Figure 16 from Allain, 1998)	11
1.3	Undulatory stability in convection zone (From Schüssler et al. 1996)	17
1.4	Flux tube trajectories (Schussler et al. 1996)	18
1.5	Latitude emergence of flux tubes (Deluca et al. 1997)	20
1.6	AB Dor mean lightcurve over the period 1978 to 1996. From Kürster (1997). 27	27
2.1	A synthesised échelle order with synthetic line list of delta functions	33
2.2	He 520 deconvolved profile and multiplex gain	37
2.3	Plot showing approximate associative nature of the deconvolution process .	38
2.4	Correct treatment of limb darkening vs constant limb darkening	42
2.5	Continuum intensity for wavelength dependent limb-darkening divided by constant limb-darkening...	43
2.6	Synthetic deconvolved profiles	44
2.7	Deconvolved profile shape for various <i>v</i> sin <i>i</i> values	47
3.1	How starspot signatures are formed	52
3.2	Limiting spot radius detected vs S:N ratio.	54
3.3	Example Lookup tables	57

3.4	Test image and synthetic profiles.	64
3.5	Minimisation of $v \sin i$ for various EWs	65
3.6	Image reconstructions from varying pairs of $v \sin i$ and EW	66
3.7	Image reconstruction from mis-determined parameters & mean fit profiles	67
3.8	Parameter determination, $v \sin i$ vs limb-darkening coefficient and inclination, and inclination vs photospheric/spot continuum intensities	70
3.9	Inclination determination - synthetic data	71
4.1	He 520 & He 699 Finding Charts	77
4.2	He 520 & He 699 light curves	78
4.3	Normalised He 520 spectrum	82
4.4	He 520 & He 699 minimum spot area parameter determination	85
4.5	Max-Ent reconstructions of He 520	86
4.6	Max-Ent regulated fits to He 520 profiles & light curve	87
4.7	Max-Ent reconstructions of He 699 (1996 October)	88
4.8	Max-Ent regulated fits to 1996 October He 699 profiles & light curve	89
4.9	Max-Ent reconstructions of He 699 (1996 November)	90
4.10	Max-Ent regulated fits to 1996 October He 699 profiles & light curve	91
4.11	Time series spectra of He 520 and He 699. Mean profile subtracted, deconvolved spectra.	95
4.12	He 520 & He 699 spot coverage	97
4.13	He 520 & He 699 cross-correlation images	98
4.14	Inclination determinations for He 520, He 699, AP 149 and AP 193	108
4.15	Time series profiles and maximum entropy regularised fits for AP 149 and AP 193	110

4.16	Maximum entropy images of He 520 and He 699 (χ^2 minimised parameters)	111
4.17	Maximum entropy images of AP 149 and AP 193	112
4.18	Mean observed profiles and immaculate profiles.	114
4.19	The effect of a 30° polar spot on the stellar profile for a star at various axial inclinations	116
5.1	Optimisation of stellar parameters for PZ Tel	130
5.2	PZ Tel - inclination determination	131
5.3	PZ Tel - Profiles and Max-Ent fits to data	133
5.4	PZ Tel - Max-Ent image reconstructions	137
5.5	PZ Tel - cross-correlation	138
5.6	Latitude distribution of spots in Red & Blue data sets for PZ Tel	141
5.7	10/07/98: PZ Tel image reconstructions from Red & Blue data sets and cross-correlation image	142
5.8	12/07/98: PZ Tel image reconstructions from Red & Blue data sets and cross-correlation image	143
5.9	Cross correlation of blue images of PZ Tel for 10/07/98 and 12/07/98	144
5.10	Cross correlation of red images of PZ Tel for 10/07/98 and 12/07/98	145
5.11	Fractional spot filling against latitude on PZ Tel	148
6.1	Speedy Mic - Profiles and Max-Ent fits to data	155
6.2	An échelle order of HD 16160 taken using E31 and E79 gratings	157
6.3	Minimum χ^2 against inclination for various Speedy Mic data sets.	160
6.4	[Speedy Mic - Max-Ent image reconstructions of Speedy Mic from SAAO data alone	163
6.5	Max-Ent image reconstructions of Speedy Mic	164

6.6	Cross-correlation images for Speedy Mic	165
7.1	He 520 and He 699 mean H α profiles	175
7.2	He 520 & He 699 times series spectra for H α	177
7.3	AP 193, mean H α profile	178
7.4	Time series and Doppler maps of H α emission on AP 149.	179
7.5	PZ Tel mean H α profile	182
7.6	PZ Tel H α time series	183
7.7	Speedy Mic - H α average profiles demonstrating the high degree of chromospheric filling.	184
7.8	Speedy Mic mean H α profile	185
7.9	Speedy Mic - Time series spectra for H α profiles	186
8.1	Multiplex gain vs (Number of lines) ^{1/2}	191

LIST OF TABLES

2.1	Limiting S:N ratio attainable at various $v\sin i$ values for synthetic data sets with no noise	46
2.2	Table showing the effect of using synthetic line lists of different spectral type on a star of fixed spectral type	48
3.1	EW and $v\sin i$ for reconstructed images in Figure 3.6	67
4.1	Observations of He 699 in 1996 October	75
4.2	Observations of He 520 and He 699 in 1996 November	76
4.3	Least squares multiplex gain for He 520 and He 699	83
4.4	Inclination estimates	93
4.5	Observations of AP 149 & AP 193 on 1998 December 6,7,8	102
4.6	Photometric data and spectral types of the α Persei stars.	105
4.7	Least squares multiplex gain for α Persei data sets	107
4.8	Estimated stellar parameters of the α Persei stars from χ^2 minimisation . .	113
5.1	Observations of PZ Tel in 1998 July with the Sutherland 1.9m and GIRAFFE at the SAAO	118
5.2	Observations of PZ Tel in 1998 July with the AAT and UCLES at the AAO	119
5.3	Input and output S:N ratios for PZ Tel data	128
5.4	Best fit parameters for PZ Tel data sets	134

6.1	SAAO observations of Speedy Mic in 1998 July	151
6.2	AAT observations of Speedy Mic in 1998 July	152
6.3	Input and output S:N ratios for Speedy Mic	158
6.4	Best fit parameters for Speedy Mic data sets	159
6.5	Speedy Mic - differential rotation. Minimum equator-lap-pole times	166
7.1	He 520 and He 699 prominence positions and stellar parameters.	176
7.2	AP 149 Prominence details.	180
7.3	PZ Tel prominence positions	182
7.4	Speedy Mic prominence positions	185
7.5	Axial inclination and co-rotation radii for all stars	189
8.1	Spot distributions for a number of single rapid rotators.	193

CHAPTER 1

Introduction

The majority of middle aged main sequence stars like the Sun are relatively well behaved, in that they exhibit a sedate rotation speed, and moderate levels of chromospheric emission. Despite this, the Sun exhibits various phenomena demonstrating that it is by no means inactive. The large number of active solar phenomena such as sunspots, faculae, flares and prominences owe their existence to magnetic fields. The intensive study of solar activity, at and above the photospheric level, at various wavelengths, has prompted a great deal of detailed study in the form of magnetohydrodynamic modeling. Helioseismology on the other hand offers a means of probing the solar interior in search of the underlying processes at work. The proximity of the Sun and therefore relative detail in which it has been studied, when compared with stellar analogues mean that it is regarded as the prototype star. Comparisons of the Sun with late type stars of similar spectral type are often, but not always possible.

The slower rotation which distinguishes low mass stars with outer convection envelopes from rapidly rotating high mass stars with outer radiative envelopes is not present at the ages of stars observed in the Pleiades and α Persei young open clusters. Some objects in young open clusters (approx 30 Myr - 100 Myr) exhibit projected equatorial rotation velocities of several tens of km s^{-1} , up to $\sim 200 \text{ km s}^{-1}$. The resulting short periods of $\leq 1\text{d}$ lead to high degrees of activity when compared with the Sun. At the age of the 600 Myr old Hyades open cluster, the K dwarfs exhibit slow rotation velocities at typically $< 10 \text{ km s}^{-1}$ (e.g. Stauffer, Hartmann & Latham 1987). These Hyades stars nevertheless still rotate 3 to 4 times faster than the Sun, and the the majority of late-type stars in the solar neighbourhood.

Photospheric variability of $\sim 0.1 \text{ mag}$ (in the V band) on young, late type rapidly

rotating stars indicates the presence of cool surface inhomogeneities in the form of starspots rotating in and out of view. This is confirmed by the growing number of surface images using maximum entropy regulated techniques. High degrees of chromospheric emission are often revealed through the large degree of profile filling in the $H\alpha$ line and Mg II h & k and Ca II H & K resonance lines. The coronae are known to be active since $H\alpha$ absorption transients due to circumstellar prominences are seen. These clouds scatter the photons out of the line of sight when they pass in front of the stellar disc. Further evidence of active coronae comes from X-ray studies which reveal high levels of emission, saturating at moderate rotation rates.

1.1 Stellar rotation

Of importance in understanding the formation and ultimate fate of a star is the evolution of angular momentum. In late type stars, the interaction of rotation and convection in the outer layers produce a dynamo effect which generates magnetic fields. The resulting fields grip the ionised stellar wind beyond the surface of the star and are consequently responsible for depositing angular momentum (AM) into that wind. Faster rotation leads to a stronger field, quicker loss of AM and hence a convergence of rotation rates with time. The model for loss of angular momentum in solar-type stars was first put forward by Schatzman (1962). Whereas Wilson (1963) suggested that activity and rotation decline with age, it was Weber & Davis (1967) who first computed the role of the magnetic field properly. The decline of AM with age was quantified by Skumanich (1972) in the $\Omega \propto t^{-1/2}$ relation.

Pre-main-sequence (PMS) T Tauri stars (≤ 10 Myr) are known to rotate relatively slowly. The solar-type stars in the young open clusters such as α Persei (50 Myr) and the Pleiades (70 Myr) are also much younger than the Sun, and have only reached the zero age main sequence (ZAMS) relatively recently. Attridge & Herbst (1992) measured the rotation rates of Orion Nebula stars (30 Myr) and found a fraction of ultra-fast-rotator (UFR) precursors, with the implication that spin-up takes place at an age and on a timescale related closely to the absolute and relative ages of the Orion stars, α Persei and the Pleiades stars. This implies that the spin-up takes place during the PMS stage of evolution. Since these UFRs are seen in greater numbers in both the α Persei (50

Myr) and Pleiades (70 Myr) clusters, it can be concluded that these populations are an important phase in the evolution of stars like the Sun.

Traditional ages (i.e. from main-sequence fitting) place the α Persei cluster, Pleiades and Hyades at 50 Myr, 70 Myr and 600 Myr (Patenaude 1978) respectively. However work on stellar evolution models (e.g. Maeder & Meynet 1989 & Charbonnel, Vauclair & Zahn 1992) which include convective overshoot allow stars to remain on the main sequence for much longer than was originally thought. Further evidence for greater ages of the α Persei and Pleiades clusters has come from lithium abundance tests in Brown Dwarfs. Stauffer et al. (1999) and Stauffer (1999) have determined ages for the α Persei cluster and the Pleiades, of 90 Myr and 120 Myr based upon the lower lithium depletion boundary. These are in close agreement with some degree of convective overshoot in stellar evolution models. For simplicity of argument I refer to the traditional ages.

1.1.1 The distribution of rotation in young open clusters

Figure 1.1 (taken from Soderblom et al. 1993) shows the projected rotation velocities ($v \sin i$ distributions) as a function of $(B-V)_0$ colour index in the α Persei, Pleiades and Hyades clusters. The α Persei and the Pleiades clusters show similar distributions except there are more fast rotators among the G dwarfs in α Persei. In fact, approximately half the fast rotators in α Persei are G dwarfs whereas in the Pleiades, the K dwarfs are the predominant fast rotators. Fast rotators are however seen at all colours in the α Persei cluster, up to a $v \sin i$ of 200 km s^{-1} (Prosser 1992). When we consider the Hyades distribution, it can be seen that at any one colour, contrary to what we see in the younger clusters, there is very little spread in $v \sin i$ (Radick et al. 1987; for further references see Soderblom et al. 1993).

It is quite clear that not all stars undergo a UFR stage. Duncan (1993) noted that several of the Orion Nebula PMS stars are slow rotators. This is also shown in a more recent study by Stassun et al. (1999) on a larger sample of stars. Attempts to predict ZAMS rotation rates from the known rotation rates of T Tauri stars through angular momentum redistribution alone lead to a predominance of slow rotators (Duncan 1993). The predicted distribution is however in reasonable agreement with that of the α Persei cluster. Only a small number of stars appear to be the possible progenitors of UFRs. This indicates that only a small number of stars are actually born with sufficient angular momentum

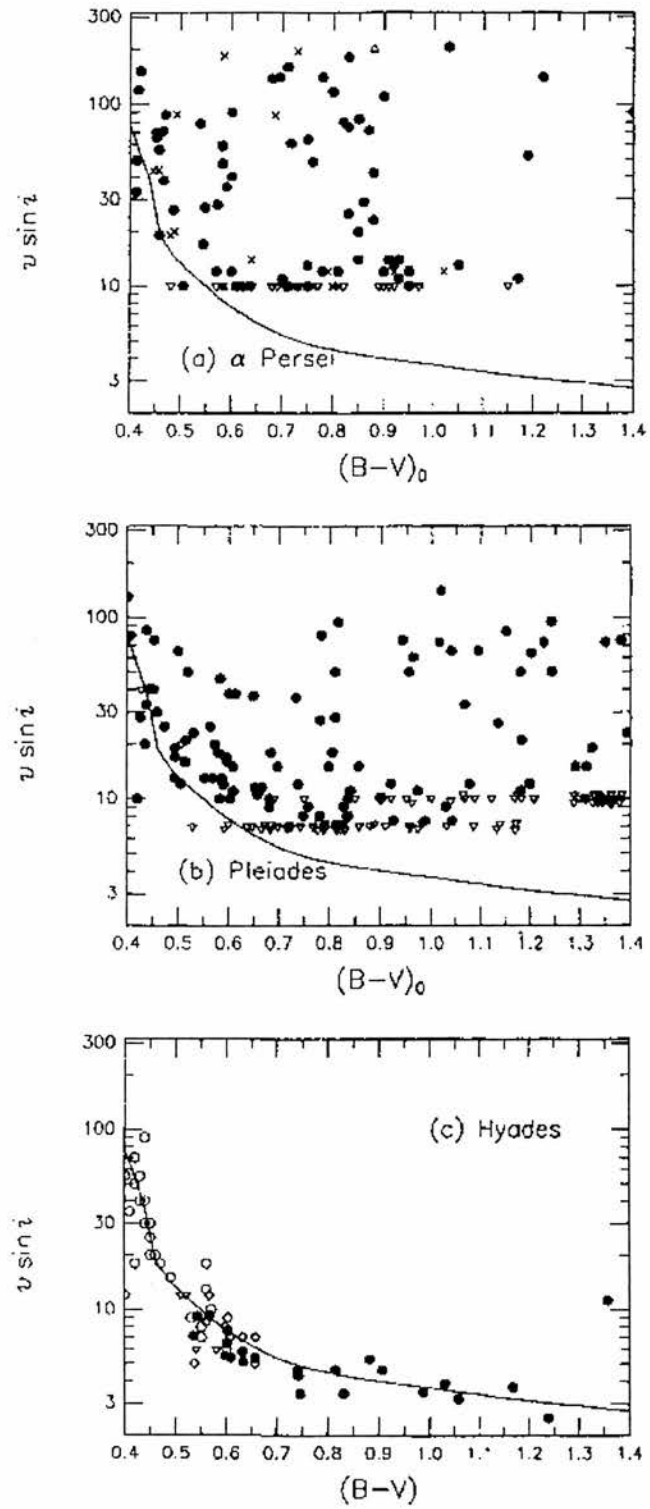


Figure 1.1: $v \sin i$ vs $(B-V)_0$ for α Persei, Pleiades and Hyades (Soderblom et al. 1993a)

to become fast rotators. There have been several attempts to explain the existence of both slow and fast rotators within a given cluster. The observations were initially thought (Stauffer et al. 1984) to imply that most UFRs could spin down in a time which was less than any age spread within the Pleiades. In this scenario, the UFRs represent the youngest stars in the cluster. An explanation put forward by Stauffer & Hartmann (1987) suggested that pre-main-sequence stars evolved into a Pleiades type distribution by making the rate of change of angular momentum a weak function of rotation.

The need for models incorporating rapid spin down within the age spread of a cluster is then removed since not all slow rotators are necessarily the descendants of rapid rotators. The presence of UFRs in both the α Persei and the Pleiades clusters means that many of these objects maintain rapid rotation for at least as long as the age difference between the two clusters if the age difference is greater than the age spread within each cluster. Core envelope decoupling was suggested by Stauffer et al. (1984). In this scenario the radiative core may rotate faster than the decoupled convective shell, or a gradient of angular velocity with radius may exist. This idea goes some way to explaining apparent inconsistencies between Pleiades stars and their Hyades counterparts. For example Soderblom et al. (1993b) noted that in evolving from the Pleiades to the Hyades, rotation rates converge by much more than they change on average. Many of the slow rotators in the Pleiades already rotate as slowly as their counterparts in the Hyades. Core envelope decoupling can then be invoked as a means of keeping slow rotators from rotating *too* slowly by the time they reach Hyades age since the stellar core acts as an angular momentum reservoir. In addition, extrapolating Hyades rotation rates back to the Pleiades age with a Skumanich type relation ($\Omega \propto t^{-1/2}$) results in values of 15 - 20 km s⁻¹, well above the Pleiades median of 10 km s⁻¹. Extrapolation of Hyades rotation rates using a Skumanich type relation have however been successful at reproducing the distribution seen in the 300 Myr Ursa Majoris Group. Any successful model of angular velocity versus time must therefore be able to describe the rotation distribution seen from the ZAMS all the way to 200 - 300 Myr where it apparently converges to a Skumanich type representation.

Further complications arise when we look at T Tauri stars, the precursors of main-sequence stars which rotate at typically an order of magnitude less than the rotational breakup speed (Vogel & Kuhl 1981; Hartmann et al. 1986; Bouvier et al. 1986). Given that these objects have recently formed from gravitational collapse of star forming clouds,

their slow rotation is contrary to expectation. Hartmann et al. (1986) found typical values of $v \sin i < 15 \text{ km s}^{-1}$ for 80 per cent of the 50 stars surveyed in the Taurus-Auriga and Orion star forming regions. Stauffer & Hartmann (1987) evolved the T Tauri $v \sin i$ distribution to the main-sequence age assuming zero angular momentum loss. On transforming the resulting velocity distribution to Pleiades age accounting for Skumanich AM loss, the resulting distribution does not match that of the Pleiades. The distribution of $v \sin i$ values becomes compressed as time proceeds because the rapid rotators spin down much faster than the slower rotators. This implies that in addition to the inappropriate use of the Skumanich relation to extrapolate AM evolution for Hyades ages to the Pleiades age this relation is also not appropriate for rapid rotators at younger ages over shorter timescales. An AM loss model which is independent of rotation for stars with equatorial rotation velocities $> 10 \text{ km s}^{-1}$ is however more successful at reproducing the Pleiades type distribution.

1.2 The evolution of angular momentum

1.2.1 Components of the models

Various other models which predict the angular momentum evolution from PMS to MS ages have been developed in recent years. These models usually rely upon two or three postulates. The models of Macgregor & Brenner (1991) and Keppens, Macgregor & Charbonneau (1995) for example assume core envelope decoupling. The models of Li & Collier Cameron (1993) however showed that for solar-type stars, only weak coupling models, where little of the AM stored in the core of a fast rotator has been transferred to the convective envelope by the age of the Hyades can provide a reasonable fit to the observed rotational distributions at the ages of the α Persei, Pleiades and Hyades clusters. Bouvier, Forestini & Allain (1997) use rigid body rotation models. Disc locking (where the T Tauri star is coupled to slowly rotating material in the circumstellar disc beyond the co-rotation radius) must be considered when modelling the PMS to MS angular momentum evolution. Cameron & Campbell (1993) examined the rotational evolution of magnetic T Tauri stars with accretion discs. Stellar magnetic field lines thread the stellar disc and are drawn out by the shear at the disc-magnetosphere boundary. This results in a disruption of the inner part of the disc, and so AM is transferred within the co-rotation radius onto the

stellar surface. The magnetic field lines also transfer AM from the star to the stellar disc, beyond the co-rotation radius. The models showed that an equilibrium is maintained on a contracting star during the few million years of the T Tauri stage. Hence, while a young star interacts with its circumstellar disc, it retains essentially constant angular velocity

$$\Omega(t \leq \tau_{disc}) \simeq \Omega_0, \quad (1.1)$$

where Ω_0 is the initial angular velocity, and τ_{disc} is the disc lifetime. Attridge & Herbst (1992) and Choi & Herbst (1996) found a bimodal distribution of rotation periods among 75 stars in the 10^6 yr - a few times 10^7 yr Orion Nebula region. There are two distinct populations divided by a significant gap at a period of 4-5 days. One third of the total population are rapid rotators with a mean period of 2.55 d (dispersion 0.7 d). The remaining stars are slow rotators with a mean period of 8.3 d (dispersion 3.8 d), and a tail of very long period stars extending up to 34.5 d (Choi & Herbst 1996). Bouvier et al. (1993) noted that among 26 stars in the Taurus-Auriga region, the classical T Tauri (CTT) stars which show evidence of accretion and circumstellar discs rotate more slowly than the weak lined T Tauri (WTT) stars. The slow rotators are those which are magnetically coupled to circumstellar discs while the rapid rotators are those which are no longer locked (due to disc depletion). This is confirmed by Edwards et al. (1993) who showed that the CTTs show excess IR emission due to reprocessing of light in the circumstellar disc. By comparison, the faster rotating WTTs are more consistent with main sequence stars. Despite the large number of rapid rotators in young open clusters they are still outnumbered by the larger proportion of slow rotators. The existence of a bimodal distribution among young T Tauri objects may provide a useful explanation for the preponderance of slow rotators in young clusters such as α Persei and the Pleiades. However Stassun et al. (1999), finds no evidence for bimodality in the period distributions for a larger sample size of 254 stars in the Orion Nebula region. A similar situation is also found for Upper Sco (Adams, Walter & Wolk 1998) and NGC 2264 (Kearns et al. 1997 & Kearns & Herbst 1998). Although disc locking undoubtedly plays an important role in stellar evolution models, the correct treatment of this phenomenon remains uncertain.

Lastly, magnetic braking of some particular form is invoked. Angular momentum is extracted from the surface of low mass stars by a magnetised stellar wind as discussed in §1.1. In order to describe this process quantitatively, models include a braking law which

relates the rate of loss of angular momentum to the evolving stellar and wind properties. For example the activity rotation relationship formulated by Kawaler (1988) assumes that the surface magnetic flux obeys a dynamo relationship of the form $R_* B \propto \Omega$, where R_* is the stellar radius, B the magnetic field strength and Ω the angular velocity. This linear dynamo relation is supported by direct measurements showing that the integrated surface magnetic field strength increases with Ω up to $\Omega \approx 10\Omega_\odot$ (Saar 1996).

For larger rotation rates however, the dynamo relationship appears to saturate. X-ray emission in late type stars arises from coronal activity such as magnetic reconnection and flaring events. The degree of X-ray activity is in other words related to the degree of magnetic activity on and above the surface of the star. So, the higher the measured X-ray luminosity, the greater the degree of magnetic activity, and hence the greater the loss of angular momentum via the magnetised stellar wind. The X-ray rotation relationship holds only up to a certain point beyond which the X-ray luminosity levels out at $L_x/L_{bol} \approx 10^{-3}$. This saturation limit appears to extend all the way along the main sequence from G dwarfs to the latest M dwarfs (Fleming et al. 1993). A rotation-independent angular momentum loss mechanism for rapid rotators in young open clusters has been demonstrated for the Pleiades (Stauffer et al. 1994) and α Persei (Randich et al. 1996) clusters. For rotation velocities of $< 15 \text{ km s}^{-1}$, L_x/L_{bol} shows a linear increase with increasing velocity. Above rotation velocities of $\sim 15 \text{ km s}^{-1}$, the L_x/L_{bol} values all cluster around a value of 10^{-3} . It has been suggested that this may demonstrate an upper limit on the available surface area of the star which can accommodate active magnetic regions and plage. However, other diagnostics of magnetic activity such as starspot coverage (O’Dell et al. 1995) and Ca II H & K emission (Vilhu 1984) (see below) do not show saturation at the same angular velocities. O’Dell et al. (1995) showed that starspot areas go on increasing, and *may* saturate for $P < 0.5 \text{ d}$ whereas the chromosphere and transition region indicators saturate for $P \sim 2 \text{ d}$ (Doyle 1996).

Further, Prosser et al. (1996) and Randich (1998) showed that the X-ray emission does not simply flatten out at high $v \sin i$ values, but in fact begins to decline slightly. Jardine & Unruh (1999) have attributed this so called “supersaturation” to centrifugal stripping of the corona. For stars rotating sufficiently rapidly, the co-rotation radius moves inside the Corona. This corresponds to rotation periods of 2-3 d, at the point where saturation of coronal X-ray emission is observed. For the most rapid rotators, the plasma which collects in the coronal loops increases the local pressure. If this pressure

exceeds the local magnetic pressure, the loop may be blown open. This would suggest that X-ray flux and therefore other indicators of magnetic activity are not reliable indicators of dynamo saturation.

Nevertheless, the angular momentum loss rate in models is generally accounted for both in the case where $\Omega < \Omega_{sat}$ and in the case where $\Omega \geq \Omega_{sat}$ (i.e. $R_*B = \text{constant}$). The exact value of Ω at which saturation occurs is a free parameter which is generally adjusted to fit the data. But, as outlined above, the models used may be incorrect if the activity indicators are not reliable indicators of dynamo saturation. The models used by Bouvier, Forestini & Allain (1997) and Allain (1998) use the Kawaler (1988) parameterised form of the Weber & Davis (1967) angular momentum loss model. The equations governing the rate of change of angular momentum are

$$\left(\frac{dJ}{dt}\right)_w = -K\Omega^3 \left(\frac{R}{R_\odot}\right)^{1/2} \left(\frac{M}{M_\odot}\right)^{-1/2} \quad (\Omega < \Omega_{sat}) \quad (1.2)$$

and

$$\left(\frac{dJ}{dt}\right)_w = -K\Omega\Omega_{sat}^2 \left(\frac{R}{R_\odot}\right)^{1/2} \left(\frac{M}{M_\odot}\right)^{-1/2} \quad (\Omega \geq \Omega_{sat}) \quad (1.3)$$

1.2.2 Angular momentum evolution models

Macgregor & Brenner (1991) presented a parameterised model for the redistribution of angular momentum between core and envelope in solar-type stars. General agreement with observation was found for models (1) which allowed for surface magnetic field strength being largely independent of surface angular velocity Ω (for rapid rotation) and approximately linearly dependent on Ω for $\Omega \approx \Omega_\odot$ and (2) with a timescale of angular momentum transfer from core to envelope which remains constant at 10^7 years.

Keppens, Macgregor & Charbonneau (1995) produced models which describe the evolution of angular momentum from the T Tauri phase to the MS. The model included the effect of angular momentum loss through a stellar wind, disc-locking, and angular momentum transport from the interior to the convective envelope using the earlier description of McGregor & Brenner. In order to explain the large spread of velocities seen in young open clusters along with the rapid spin down which takes place on the ZAMS, a

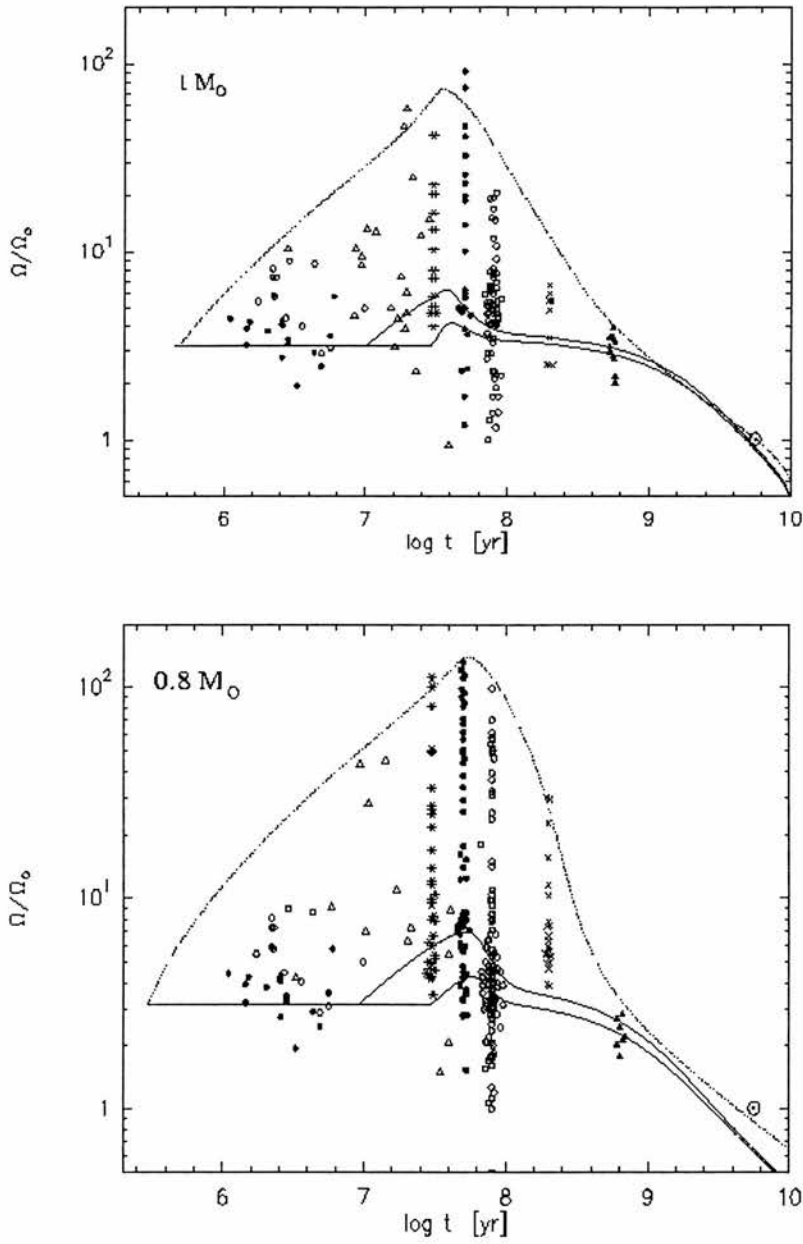


Figure 1.2: Rotational evolution tracks for $0.8 M_{\odot}$ and $1.0 M_{\odot}$ stars (Figure 16 from Allain, 1998). The dotted line represents the solid body rotation model whereas the solid lines represent the decoupled models. Each track has a different disc lifetime: 0.3, 10 and 30 Myr for the $1 M_{\odot}$ case (top), and 0.3, 10 and 30 Myr for the $0.8 M_{\odot}$ case (bottom)

disc coupling time (among the T Tauri progenitors) of 10^7 years, and a dynamo saturation law for $\Omega > 20\Omega_{\odot}$ were necessary. Also, an initial bimodal velocity distribution and a spread of masses, containing equal proportions of $0.8 M_{\odot}$ and $1 M_{\odot}$ stars, was required. The model fell into difficulties in producing the observed fraction of ZAMS slow rotators. For example in the α Persei and Pleiades clusters, the proportion of slow rotators is 30 per cent and 50 per cent respectively, while the model gives fractions of less than 5 per cent in both these clusters.

Cameron, Campbell & Quaintrell (1995) expanded on earlier work on T Tauri stars (Cameron & Campbell 1993) by evolving a solar-mass protostar with surrounding accretion disc through Henyey-track evolution onto the ZAMS. It was found that the ZAMS rotation rate is a strong function of the mass of the proto-stellar accretion disc at low masses, but nearly independent of disc mass for more massive discs. The form of the rotation distribution with peak at low rotation velocities and an extended tail was found to match observations of the α Persei cluster distributions (Stauffer et al. 1985 and Prosser 1992).

Investigations into PMS and MS angular momentum evolution have been carried out by Krishnamurthi et al. (1997), who considered models with both solid body rotation and differential rotation. They find that the behaviour of rapid rotators is highly sensitive to the saturation threshold for AM loss above which angular momentum loss scales linearly with rotation rate. Slow rotation in young clusters is achieved by having T Tauri disc lifetimes of 3 - 10 Myr for the differentially rotating models whereas disc lifetimes of greater than 10 Myr are required in the solid body models. Finally, Bouvier, Forestini & Allain (1997) investigated the evolution of a population of T Tauri stars with a gaussian period distribution. Solid rotation and a mass dependent saturation rate and a disc lifetime distribution was then able to reproduce the observed rotation velocities at different ages and masses. However whereas the model did not try to reproduce the fraction of slow rotators with velocities less than 5 km s^{-1} , the core - envelope decoupled models of Allain (1998) are successful at reproducing the existence of a large number of very slow rotators in the $0.9 M_{\odot}$ - $1.1 M_{\odot}$ mass range without requiring long disc lifetimes (e.g. up to 20 Myr in the Bouvier, Forestini & Allain (1997) model). The solid body rotation model is good at reproducing the braking of rapid rotators all over the main sequence phase for both $0.8 M_{\odot}$ and $1 M_{\odot}$ stars. This requires a core-envelope coupling time of 1 Myr. However the decoupled model with a longer coupling time of 100 Myr is able to explain the existence of slow rotators in the $0.9 M_{\odot}$ - $1.1 M_{\odot}$ mass range with disc-lifetimes of 10 Myr at the

most. The explanation for why some discs may last longer than others is not offered. This question is probably answered by Cameron, Campbell & Quaintrell (1995) who used a normal distribution of disc masses with a mean of $0.01 M_{\odot}$ and a range of $0.001 M_{\odot}$ to $0.1 M_{\odot}$ to predict the ZAMS rotation distribution. The fact that some discs are more massive than others will result in different disc lifetimes.

Figure 1.2 is taken from Allain (1998) and shows $0.8 M_{\odot}$ and $1.0 M_{\odot}$ evolutionary tracks. The tracks shown start with an initial period of 8 days, and can fit velocities as low as 6 km s^{-1} (an important fraction of the Pleiades stars) at the Pleiades age. A T Tauri distribution with periods up to 16 days is required to explain the existence of stars with rotational velocities of 6 km s^{-1} .

The above models demonstrate that the problem of angular momentum evolution is still far from being fully understood. While many trends such as X-ray activity with rotation rate are observed, the underlying fundamental evolution still requires further study. One such avenue is study of the stellar dynamo mechanism which arises primarily as a result of the differential rotation of the convective envelope of late type stars. Knowing the degree of differential rotation for various spectral types and ages will provide further constraints for AM evolution models.

1.3 Solar and stellar dynamos

1.3.1 Magnetic activity

Sunspots are probably the first phenomenon which come to mind when one thinks of active solar features. They were first reported by the Chinese, and are reported to have been seen with the naked eye in 350 BC by Theophrastus, a pupil of Aristotle. They were later re-discovered by Galileo in the 17th Century, who used them as tracers to measure the solar rotation period at close to one month. Galileo and his contemporary Scheiner noted that sunspots only ever seem to exist at low latitudes. Again by tracking sunspots, but at different latitudes, Scheiner recorded the fact that the solar rotation varies with latitude. It is now well known that sunspots appear in a latitude band within $\pm 40^{\circ}$ of the solar equator, with few or no spots appearing outside this range. Sunspots also avoid latitudes within the range $\pm 5^{\circ}$.

Doppler images of young, rapidly rotating stars however have revealed this to be the exception rather than the rule, as many stars show dark caps (as shown in the first Doppler image by Vogt & Penrod 1983) which are covered with magnetic fields (e.g. Donati et al. 1992). A crucial question which must be considered is whether rotation rate plays an important role in the action of a stellar dynamo. While Doppler imaging is a powerful tool for studying fast rotators (with angular velocities typically 10-50 times that of the Sun), it should be remembered that these stars are only one extreme of parameter space. As stated previously, magnetic activity increases with rotation rate, and so the rapid rotators which can be imaged are much more active than the Sun, as the Doppler images in the literature show. The other important difference between the Sun and stars for which Doppler images exist, is that most are either giants or sub-giants in close binary systems. Apart from being older objects when compared with young solar analogues, these stars have deeper convective zones which may affect the way the magnetic fields are generated, and subsequently evolve. The fact that they are mostly RS CVn binaries and therefore tidally locked in synchronous orbit also affects magnetic activity. The choice of these objects as Doppler imaging targets lies in their bright apparent magnitudes. There are more subgiant binaries than young single rapidly rotating dwarfs brighter than $m_v \sim 8$. With increased telescope sizes and instruments with improved efficiency, this bias to the brighter candidates eligible for Doppler imaging studies is being eliminated so larger areas of parameter space are being, and will be explored.

1.3.2 The solar dynamo

A relic magnetic field has been suggested as the origin of the solar magnetic field. The classical diffusion timescale, R_{\odot}^2/η (η is the magnetic diffusivity), for the decay of a global solar magnetic field at 10^{10} years is comparable to the 4.5×10^9 years age of the Sun (Priest 1984). Other diffusive processes are however likely to reduce the diffusion timescale, and so some means of maintaining the solar magnetic field is necessary (Priest 1984). The most likely explanation invokes a magnetohydrodynamical dynamo (Parker 1955) in the outer atmosphere of the Sun which can explain the periodic nature of the solar activity cycle and the observed magnetic structures.

In the dynamo scenario first advanced by Parker (1955), an initial poloidal field is assumed to be frozen into the solar plasma. On the Sun, the equatorial regions rotate

faster than the polar regions with the result that this *differential rotation* creates a toroidal component from the original wholly poloidal magnetic field. This is known as an Ω -effect. Poloidal field is regenerated through the action of rising plasma in the convection zone. As the blobs of plasma rise, they are twisted because of the Coriolis force. These anti-cyclonic motions are clockwise in the northern hemisphere and anti-clockwise in the southern hemisphere. If flux tubes are carried up with the plasma, the twist converts toroidal fields into poloidal fields. This regeneration of poloidal field is known as the α -effect. The combined mode at work in the Sun is known as the $\alpha\Omega$ -dynamo in which the Ω -effect is dominant (Parker 1979). Other modes of dynamo operation (Priest 1984) are an $\alpha^2\Omega$ -dynamo (which generates toroidal field with approximately equal contributions from the α -effect and Ω -effect) and the α^2 -dynamo (where both the toroidal and poloidal fields are generated by the α -effect and the Ω -effect is relatively small). In fact, Johns-Krull (1996) ruled out extreme differential rotation, and concluded that T Tauri stars rotate effectively as solid bodies. More sensitive measurements, using starspots as markers, and cross-correlation of constant latitude strips in two Doppler images allows measurement of the magnitude of differential rotation. The young (~ 30 Myr) K0 dwarf AB Doradus was shown (Donati & Collier Cameron 1997) to rotate almost as a solid body, with $d\Omega/\Omega = 0.0046$, whereas the post T Tauri star RX J1508.6-4423 yielded $d\Omega/\Omega = 0.0064$ (Donati et al. 1999b). Magnetic fields are known to exist on T Tauris, a lack of *any* differential rotation eliminates the Ω -effect. Indeed Küker & Rüdiger (1997) concluded that the stellar magnetic field on T Tauris is generated by an α^2 -dynamo. It is still unclear whether the small but significant degree of differential rotation found on PMS and young main sequence rapid rotators is also present on T Tauris. Confirmation of this would suggest that the Ω -effect *does* play a crucial role in the magnetic dynamo process.

Two major physical models through which the dynamo is produced have been proposed. In the *distributed dynamo*, the α and Ω -effects operate throughout the convection zone, whereas the *shell dynamo* model consists of a dynamo at work in the overshoot layer, between the radiative core and convective envelope (Spiegel & Weiss 1980). I give an account of the shell type dynamo model of Schüssler et al. (1996) (hereafter S96), since this model, which is based upon the solar case, is applied to solar-type stars of different rotation rates and ages.

1.4 A dynamo model and the latitude distributions of starspots

The properties of spot groups as observed on the Sun shows that they form from the emergence of magnetic structures at the surface. These *magnetic flux tubes* are generated in a source region of well ordered magnetic flux in the Solar interior. It has been suggested that this region is located at the base of the convection zone (Spiegel & Weiss 1980), in the region of *convective overshoot*; a hypothesis born out by the discovery (through helioseismological measurements) of a shear layer of strong radial differential rotation in this region. The region must be relatively stable since the magnetic flux must be given time to amplify in the course of the dynamo's 11 year (in the solar case) time scale. For this reason S96 argued that the solar dynamo is not situated in the convective region proper as any magnetic flux is quickly expelled through convective motions.

It is assumed that toroidal magnetic flux tubes are generated by the dynamo, and stored in force equilibrium in the overshoot layer until the field strength reaches a point where an *undulatory instability* sets in. S96 found this to be the case for field strengths above 10^5G . The instability sets in for non-axisymmetric perturbations as represented in Figure 1.3, causing a downflow of plasma along the field lines within the flux tube, since these flux tubes are essentially isolated from the surrounding convection zone. An upward buoyancy force then acts upon the displaced parts causing the troughs to sink and the peaks to rise, thus 'feeding' the instability. Loops then form, and emerge at the surface forming sunspots, while the sinking parts reach a new equilibrium in the overshoot region, forming an anchor for the erupted loop.

The simulations of S96 take the diameter of the flux tube to be small when compared with other length scales such as scale heights, wavelengths and radius of curvature, which greatly simplifies the treatment. The most important forces to take into consideration then are the buoyancy force, the magnetic curvature force, the drag force (ie. for motion relative to the surrounding plasma) and the Coriolis force due to rotation. The drag force is always anti-parallel to the velocity of the flux tube, the buoyancy force anti-parallel to the direction of gravity while the Coriolis and centrifugal forces are perpendicular to the rotation axis of the star.

It is the Coriolis force which deflects the buoyant flux rings, which subsequently rise to high latitudes unless their initial field strength is great enough. In the equatorial

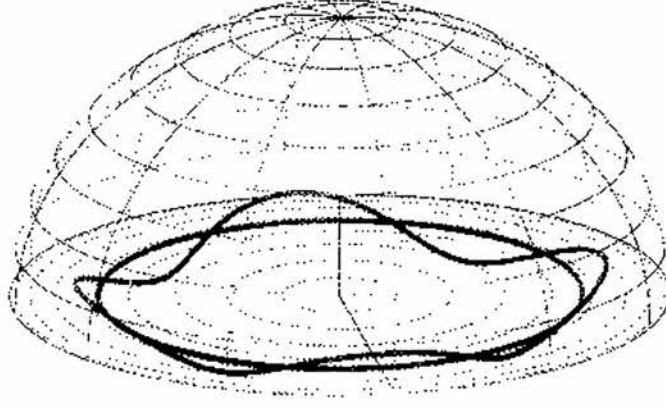


Figure 1.3: A representation of the formation of an undulatory stability, set up in a *thin* magnetic flux tube at the base of the convection zone. From Schüssler et al. (1996)

plane, a radially expanding flux ring is subject to a Coriolis force through conservation of angular momentum which drives a flow of plasma along the flux tube in the ϕ direction, against the direction of rotation, reflecting the conservation of angular momentum. The resulting internally directed Coriolis force causes an oscillation of period 2Ω to be set up, the amplitude of oscillation being dependent upon the strength of the initial buoyancy force. However when we look at the same situation outside the equatorial plane, only the component of buoyancy force perpendicular to the axis of rotation is affected by the Coriolis force. The trajectory of the flux ring is then dependent upon the inertial oscillation in the the plane perpendicular to the rotation axis, and a rise parallel to the axis. If the period of inertial oscillation is shorter than the rise time, this leads to the emergence of magnetic flux at high latitudes (ie. the Coriolis force dominates). The ratio of the Coriolis Force (F_R) to the buoyancy force (F_B) is given by:

$$\frac{|F_R|}{|F_B|} \approx \frac{2\rho v_{rise}\Omega}{B^2/8\pi H} \propto \frac{\Omega}{B} \quad (1.4)$$

where B is the magnetic field strength, H the pressure scale height, ρ the density, and Ω the stellar rotation rate (Schüssler & Solanki 1992). The rise velocity, is approximately equal to the Alfvén velocity, $v_{rise} \approx v_A = B/4\pi\rho^{\frac{1}{2}}$. The flux tubes are therefore deflected upward for a given rotation rate as long as the field strength is not too large, i.e.

$$B < B_m \equiv 8H\Omega\sqrt{\pi\rho} \quad (1.5)$$

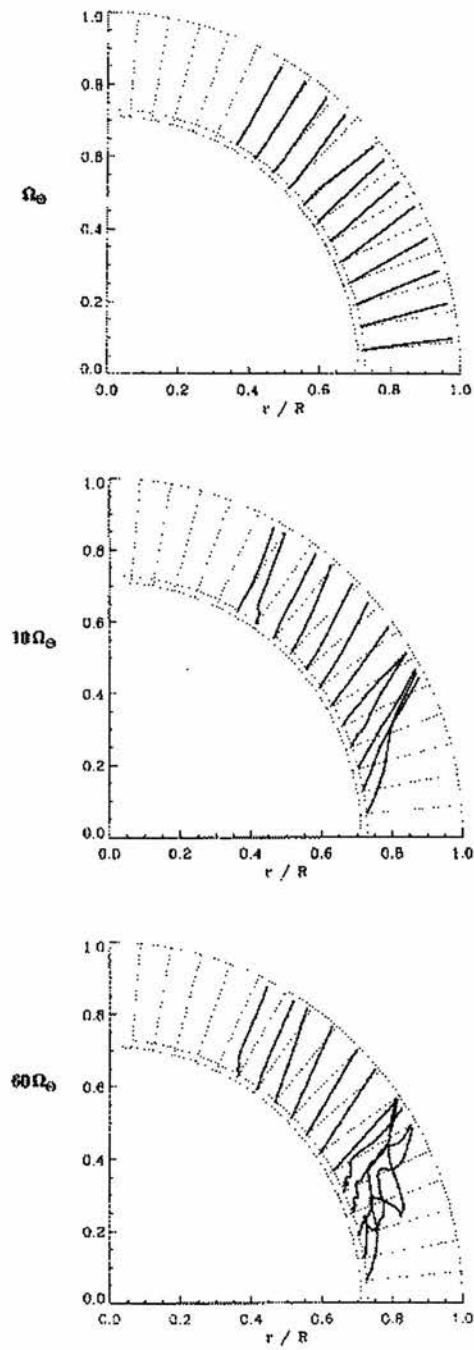


Figure 1.4: Diagram showing the meridional projection of trajectories of rising flux loops for a star at the age of the present day Sun. Rotation rates are Ω_{\odot} , $10\Omega_{\odot}$, $60\Omega_{\odot}$ (top to bottom). Schussler et al. (1996)

For field strengths greater than this value, the buoyancy force dominates, allowing flux tubes to erupt radially, and thus resulting in the formation of spot groups and active regions at low latitudes. A detailed study of the linear stability criteria to determine B and the non-linear evolution of the instability by numerical simulation was carried out in order to determine the emergent latitudes. Figure 1.4 shows the plots for the emergent latitude of flux tubes for a star at the same age as the present Sun. The plots from top to bottom are for rotation rates of Ω_{\odot} , $10 \Omega_{\odot}$, and $60 \Omega_{\odot}$, the latter being the applicable case for fast rotators (equivalent to a rotation period of 0.45d). As can be seen, no truly polar spots result from the simulation, although we know that many of the stars for which polar spots are observed are subgiants in RS CVn binaries. The results of the subgiant model also do not show flux emergence near the poles. The simulations of S96 however apply only to regions of flux emergence, and do not deal with any subsequent motion of emergent flux. Vogt (1996) however has reported the poleward motion of mid-latitude spots on HR 1099, and it has been suggested that a poleward slip of the flux tube could occur for very strong initial fields or a small stellar core. In this case, the force equilibrium in the submerged part of the magnetic flux tube which is anchored in the overshoot layer breaks down; angular momentum conservation in the rising loop then decelerates the equilibrium flow along the tube, and the tension force is no longer balanced. This results in slippage of the anchored part of the flux tube towards the pole. If the poleward movement of spots seen on HR 1099 proves to be a common feature on other stars, then this explanation, substantiated by Schüssler & Solanki (1992) provides one way around the problem. Consideration of the polar spot phenomenon is given in the next section.

Updated stellar models and a wider range of parameter space using the code of S96 have been considered by Granzer et al. (2000) in detail. The results are essentially the same, however the prediction of polar caps for T Tauri stars with $\Omega \geq 10 \Omega_{\odot}$ will be discussed in later chapters.

A further study of the emergence of magnetic flux loops in solar-like stars has been carried out by DeLuca, Fan & Saar (1997) who have also expanded on the work of S96 by exploring a wider range of relevant parameter space. Simulations are carried out for injection of flux into the convection zone for $\phi_I \leq 40^{\circ}$. This range of ϕ_I is consistent with the solar case. The results compare well with those of S96 in that they predict a narrow range of latitudes at which flux emerges, while the emergent latitude increases with increasing period. For solar rotation rates, the emergent flux is confined to $0^{\circ} \leq \phi_E \leq$

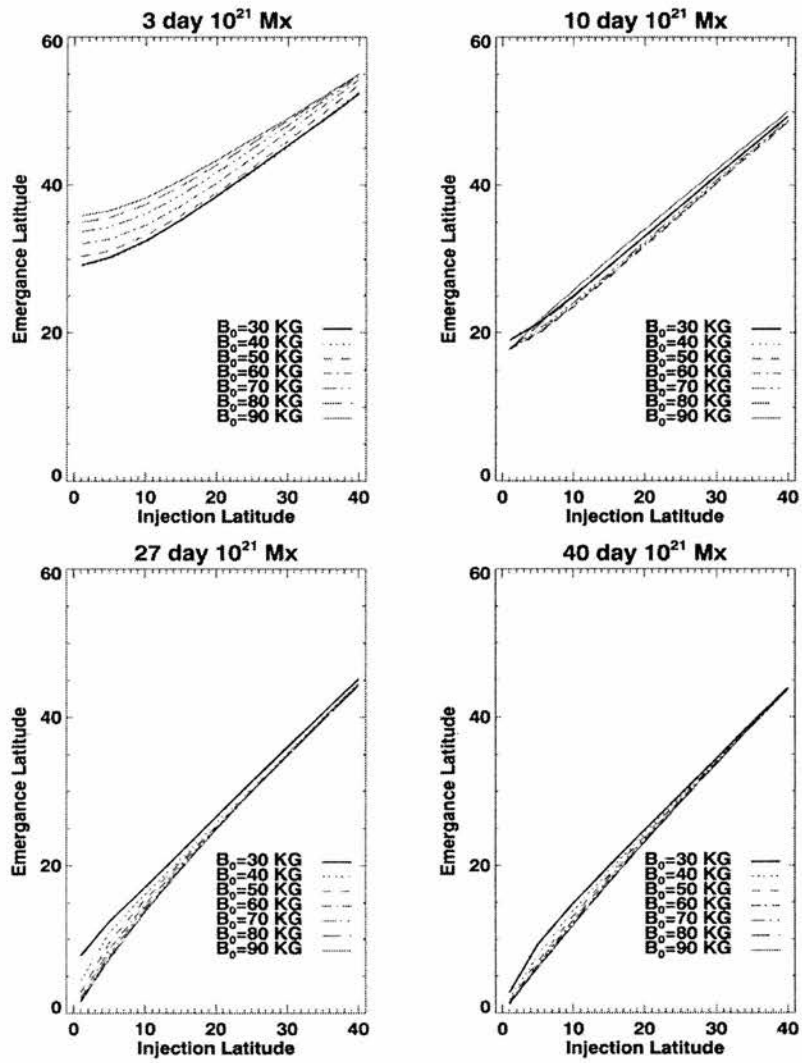


Figure 1.5: Latitude emergence ϕ_E as a function of injection latitude ϕ_I for different initial field strengths and different rotation rates. Total magnetic flux is 10^{21} Mx. Deluca et al. (1997)

45° , and for $\phi_E \geq 30^\circ$ for periods shorter than 3d (Figure 1.5). An upper limit of $\phi_E \approx 55^\circ$ is probably due to the assumption of a limiting upper injection latitude taken from the models which predict the correct range of emergent latitudes for the solar case. Also like the models of S96, polar spots are not predicted. Without going into full detail of the simulations, a discussion of the implications and comparison with observations should give some indication as to the validity of these models. Doppler imaging is currently the only realistic means of mapping the starspot distributions on late-type stars. I therefore give a brief overview of the current images to be found in the literature.

1.5 Starspot patterns from observations

Simple photometric models of rapid rotators have suggested the presence of large spots near the pole (Herbst 1989). This kind of model is sensitive to the assumed parameters of the non-spotted star such as the magnitude of the immaculate photosphere. The model attempts to fit several free parameters assuming circular spots, and care must be taken with regards interpretation. It is known that long term brightness variability exists on late type stars as is shown for AB Dor in Figure 1.6. Byrne (1996) also reports on the long term variability of II Peg which shows a different maximum in 1974 when compared with a light curve recorded in 1989. This difference may be attributable to a changing global spot coverage. A high degree of spottedness is indeed found on II Peg by O’Neal & Saar (1998) from TiO bands which act as both temperature and area indicators. One possible explanation is the presence of a large polar spot. However photometry alone cannot distinguish between a polar spot and low-latitude uniform spot coverage, both of which show no modulation of the lightcurve during a single rotation.

Doppler Imaging on the other hand is capable of producing stellar surface maps which are less dependent on assumption. There exist images for both single and binary stars (mainly of the RS CVn type) which show clear similarities and differences. A number of stars of different spectral type have now been mapped and often show spots confined to particular latitudes. One such feature is the polar spot, the reality of which has been called into question (Byrne 1996). There are a number of factors which could result in the recovery of a polar spot in Doppler images when a polar spot may not actually be present. The atmospheres of rapidly rotating active stars are different from those of slowly

rotating inactive stars, and so the line formation process is likely to be different. Active stars are highly magnetic for instance. They undergo large amounts of non-radiative heating which may include their upper atmospheres. Their photospheres are bathed in a high temperature back-heating flux from the corona. Thanks to the work of Hatzes et al. (1996), Unruh & Collier Cameron (1997) and Bruls, Solanki & Schüssler (1998) NLTE effects which could conceivably produce an apparent polar cap have been largely rejected and the existence of a true photospheric spot is now widely accepted. Other explanations such as blends, bright equatorial bands, incorrect limb-darkening and gravity darkening have been disposed of by these authors.

Not all stars show a polar cap. The doppler images of AB Dor from 1989 (Kürster, Schmitt & Cutispoto 1994) do not show a strong polar feature. It seems likely that the polar spot is not always present, and may wax and wane, if a stellar magnetic activity cycle is present for instance. Also, the technique of Doppler imaging has been used to map chemical abundances on Ap stars (Vogt, Penrod & Hatzes 1987, Hatzes 1990 and Kuschnig et al. 1999) which usually do not show abundance concentrations near the rotation poles.

1.5.1 Binaries

The polar spot appears in images of both single stars and RS CVn stars, and is often the dominant feature, especially in the latter case, as evinced by the long term study of HR 1099 (see Vogt et al. 1999 and references therein) for example. Other RS CVn maps which are dominated by polar spots include EI Eri = HD 26337 (Hatzes & Vogt 1992); HU Virginis = HD 106225 (Strassmeier 1994). UZ Librae (Strassmeier 1996b) on the other hand reveals a polar feature consisting of three appendages between 60° and 80° . The active pre-main-sequence binary, V824 Ara (HD 155555) comprising G0 and K0 stars reveals (Hatzes & Kürster 1999) surface images on both components, which are mirror images of each other. Although only observed once this would seem to suggest that tidal forces may influence the spot distribution on these stars.

RS CVn stars are generally considered to be tidally locked such that the stellar rotation period is the same as the binary orbital period. This is thought to inhibit effects such as differential rotation and is thus partly responsible for the slowly changing features found on these stars. Vogt et al. (1999) find that over the 11 year period for which 23 Doppler images of HR 1099 are present, the polar cap shows only marginal evidence of

being variable, with a 3 year period and an amplitude in area variations of 1 per cent. The dependence of rotation on latitude can be determined by comparing features persistent at two epochs, at different latitudes. For HR 1099 Vogt et al. (1999) find migration rates of 1 part in 300 to 1 part in 3600 of the rotation period, in the sense that intermediate and low latitude features rotate more slowly than the orbital angular velocity, while the highest latitudes and pole appear to be synchronised to orbital period. This is approximately a factor of 56 less than, and in the opposite sense to the latitudinal differential rotation seen on the Sun. A similar result is found for the evolved double lined binary, IL Hydrae (Weber & Strassmeier 1998) for which a differential rotation rate of $1/\Delta\Omega \approx 3500$ days (smaller than the solar value by a factor of 30) exists. In this case, the inferred rotation law is in the same sense as the Sun, so that equatorial regions rotate faster than the polar regions. Marginal solar type differential rotation is also reported on EI Eridani (Hatzes & Vogt 1992), whereas reversed differential rotation is reported on UX Ari (Vogt & Hatzes 1991) and HU Virgo (Strassmeier 1994). In many cases however, these studies are based on Doppler images derived from spectra taken over periods of weeks, or from pairs of more densely sampled data sets taken months apart. If the lifetimes of individual spots or spot groups are significantly shorter than this, the possibility must be considered that some of these differential rotation results could be spurious.

Apparent contradictions exist, however the period over which these estimates are made (excepting IL Hydrae) may be longer than the lifetimes over which the morphology of the spots remains consistent.

1.5.2 Single stars

The work of this thesis is concerned mainly with single stars which show similarities and differences when compared with binaries. There is now a growing set of images for single stars with spectral types ranging from early-G to mid-K, a range of projected rotation velocities $v\sin i$, rotation periods; and ages from T Tauri stars through to giants. Doppler images reveal that starspots on single stars tend to congregate at high and low latitudes, with intermediate latitudes showing a relative lack of cool photospheric features. This scenario is found on the K2 dwarf LQ Hydrae (Strassmeier et al. 1993; Rice & Strassmeier 1998), and the K0 dwarf AB Doradus (Collier Cameron & Unruh 1994; Unruh, Collier Cameron & Cutispoto 1995; Donati & Collier Cameron 1997; Donati et al. 1999a).

The G1.5V star, EK Draconis shows spots at all latitudes however (Strassmeier & Rice 1998), whereas the two Pleiades dwarfs HII 686 (K4V) and HII 3163 (K0V) only display reliably reconstructed spot groups above 70° latitude. The signal to noise ratio (hereafter S:N ratio) of the few spectra (seven) used to reconstruct images of these Pleiades dwarfs does not necessarily exclude the presence of low latitude features.

A few single objects other than (pre-) main sequence stars have also been Doppler imaged. One notable group are T Tauri stars. Both CTTs with a circumstellar disc and WTTs with no apparent disc have been imaged. The CTT star, DF Tau was found to exhibit hot spots (Unruh, Collier Cameron & Guenther 1997). The presence of redshifted absorption components in the Na D lines (usually tracers of mass-infall) and the hotspots in the resultant images lead the authors to infer an accretion shock close to the stellar surface. Infalling matter from the circumstellar disc, along magnetic field lines results in hotspots of around 5500 K, compared to an immaculate photosphere of 3750 K (M2V). Unlike DF Tau, the CTT, Sz 68 shows little continuum veiling (Johns-Krull & Hatzes 1997). Veiling is the UV and optical continuum excess which results from the release of energy as material accretes from the disc to the stellar surface, and is known to be variable. Indeed although Unruh, Collier Cameron & Guenther (1997) find significant veiling consistent with the positions of the hotspots, Johns-Krull & Hatzes (1997) find that the effects of veiling can be neglected. The images only show cool starspot features (including a polar cap) indicating no significant accretion from Sz 86's circumstellar disc. The suggestion that strong differential rotation may be present in T Tauri stars (Smith 1994), was contradicted by Johns-Krull (1996) who found only small amounts of anti-solar differential rotation (of modest significance) on three of the most rapidly rotating T Tauri stars. Also image reconstructions of Sz 68 which did not take account of differential rotation were marginally favoured over those which take account of substantial anti-solar differential rotation Johns-Krull & Hatzes (1997).

The well studied WTT (Strassmeier, Welty & Rice 1994; Joncour, Bertout & Menard 1994; Hatzes 1995 and Rice & Strassmeier 1996), V410 Tauri reveals a high latitude cool feature which persists over the three year period of observations. Lower latitude features are also seen which change on shorter timescales. Joncour, Bertout & Bouvier (1994) also find one large polar spot on the WTT, HDE 283572. All these T Tauri stars show considerable chromospheric activity from very variable $H\alpha$ lines

The effectively single G8 giant, CM Camelopardalis (HD 51066) shows spots at predominantly low latitudes, but no polar spot (Strassmeier et al. 1998) while the FK Comae type star V1794 Cygni has a polar spot and appendages plus low latitude features. Such a small set of data for both T Tauri stars and single giants makes it difficult to discern any trends. The models of S96 lead us to expect however that only high-latitude spots should be present in stars with such deep convection zones.

The latitude distributions of starspots on single stars may be interpreted as being dependent upon a stellar analogue of the solar magnetic cycle. In such a scenario, one may experience the waxing and waning of polar caps and the changing latitude of emergence of magnetic flux tubes throughout the activity cycle. This is one issue which will be pursued in later chapters. It is quite clear that the total set of Doppler images is small, and further studies are required before conclusions can be drawn based on patterns and general trends. With the advent of 8m telescopes and techniques such as least squares deconvolution (Chapter 2), it will be possible to address this problem.

1.6 Latitude distributions - observation vs theory

The upper limit of the emergent latitude of flux, $\phi_E \simeq 55^\circ$ in the models of DeLuca et al. is mainly due to the assumption that the injection latitude, $\phi_I \leq 40^\circ$. The short period K dwarfs such as AB Dor certainly do show (circum-) polar spots for which $\phi_E \geq 75^\circ$. It is therefore possible that dynamos on rapid rotators appear to have a larger range of ϕ_I than those with rotation periods close to the Sun. A further explanation may exist in the form of bulk flows in the convection zone, such as differential rotation and meridional circulation, which may be more effective at transporting flux to high latitudes in fast rotators. It is not possible to test the limitation of cool surface features to $\phi_E \leq 45^\circ$, since the rotation speed of stars on which we expect this type of spot distribution pattern are too slow for doppler imaging. The Sun may remain the only test of this prediction for some time as a result. The low latitude spots found on many rapid rotators are inconsistent with the overshoot layer dynamo of Schüssler and DeLuca. DeLuca, Fan & Saar (1997) note that significant flows such as meridional circulation or a distributed dynamo are required to explain the existence of significant low latitude features.

Lastly, many stars appear to have spots at all latitudes (Strassmeier 1996a). It may

be that some of the magnetic flux on rapidly rotating dwarfs is not generated by a boundary layer dynamo at all. Recent Zeeman Doppler images (Donati & Collier Cameron 1997) of AB Dor have revealed the structure of the radial and azimuthal magnetic field. The main radial field features detected at intermediate latitude are spatially associated with equally intense azimuthal field regions which from the images implies that the corresponding field lines are significantly tilted, by as much as 45° with respect to the local normal to the stellar surface. This implies that the local toroidal field structure is not confined to the overshoot layer at the base of the convection zone, since buoyancy would turn it into a purely radial structure at the photospheric level. Rather, the field appears to be distributed at least partially throughout the whole convective envelope.

1.7 The solar/stellar magnetic cycle

The 11 year solar cycle was not discovered until the 19th century by Heinrich Schwabe. During this cycle, spot groups on the stellar surface appear at successively lower latitudes. In any one cycle, a spot group pair is always orientated in an approximately East-West direction with a tilt, the leading spot always having the same polarity (Hale 1908). Over this cycle of 11 years, spots initially appear at latitudes of 40° , but then appear at successively lower latitudes down to about 5° . After eleven years, the cycle begins again, but with the polarity of spots reversed. The observations of Hale led to the conclusion that one complete cycle is therefore 22 years.

1.7.1 Photospheric activity indicators

How might one observe possible activity cycles on the Sun from a great distance, or equivalently on other solar-type stars? There are a number of ways of observing variable stellar activity. As discussed, rapid rotators generally exhibit modulation at optical wavelengths due to surface temperature inhomogeneities such as starspots. This short term modulation offers the chance to determine the stellar rotation period. However, long term monitoring often shows changes in the mean absolute level of the light curve, indicating long-term changes in spot coverage. Although complete cycles analogous to the 11 year solar cycle have not yet been detected in the optical, modulations do exist as evinced by the K0 dwarf, AB Dor (see Figure 1.6). The apparent magnitude of AB Dor rose from the start

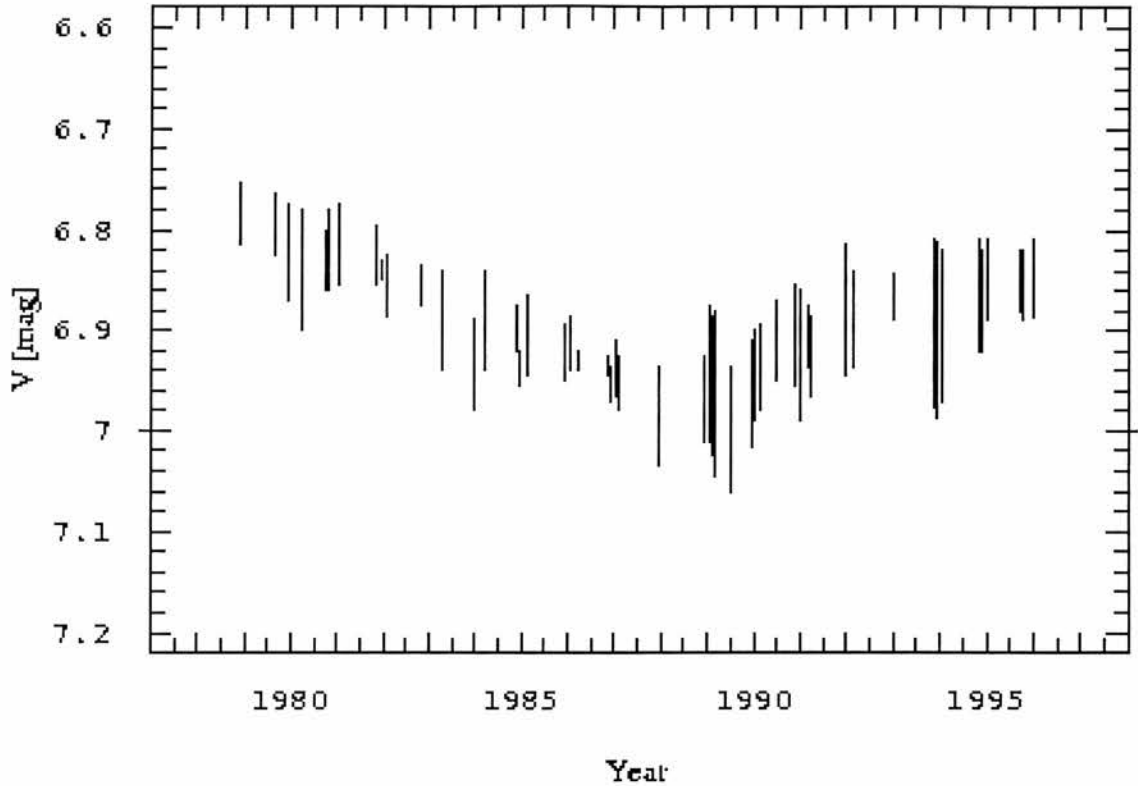


Figure 1.6: AB Dor mean lightcurve over the period 1978 to 1996. From Kürster (1997).

of observations in 1978, before reaching a maximum in 1989. After this, the apparent magnitude has been in decline until the epoch of most recent observations in 1996. The overall amplitude of the long term variation, measured so far, is approximately $\Delta V = 0.2$. A second rise in the absolute magnitude (or decline in brightness) indicating one complete cycle has not yet begun, suggesting a possible magnetic cycle of *at least* 18 years.

Interestingly data obtained at the time of minimum brightness by Kürster, Schmitt & Cutispoto (1994) reveals no polar spot on AB Dor of the type found by Collier Cameron & Unruh (1994), Unruh, Collier Cameron & Cutispoto (1995), Donati & Collier Cameron (1997) & Donati et al. (1999a).

1.7.2 Chromospheric activity indicators - The Mount Wilson Survey

Wilson (1978) reported the results of a survey begun in 1966 to study the activity of a number of slowly rotating solar-type stars. The most recent findings are reported in Baliunas et al. (1995). The study focuses on the chromospheric Ca II H & K lines which are strong indicators of magnetic activity. Areas of concentrated magnetic field on the Sun

emit Ca II H (3968 Å) & K (3934 Å) more intensely than areas where less magnetic field is present. The strength of the emission lines increases with the amount of non-thermal heating in the chromosphere. It is therefore a useful indicator of the strength of and the area covered by, magnetic fields (Leighton 1959). To date, the survey has revealed magnetic cycles from 2.5 years to the length of the survey (25 years), with none of the period determinations classified as “good” or “excellent” by Baliunas et al. (1995) being shorter than 7 years.

From existing observations, it has become apparent (Baliunas et al. 1995) that the observed stars can be split into three groups

1) Stars with very low modulated amplitudes of chromospheric emission (26 per cent of sample). It is believed that such stars may be undergoing similar episodes to the solar Maunder minimum of the seventeenth century. This lull in activity usually occurs in older stars. Stars have been seen apparently entering these quiet periods which are also seen in some younger objects, indicating that the lack of activity cannot simply be a result of old-age.

2) Stars which exhibit regular cyclic behaviour (46 per cent of sample) forming the core of the results quoted above.

3) Objects which exhibit irregular magnetic cycles (28 per cent of sample). These stars are generally the younger objects.

Correlation of photometric variability with Ca II H & K emission reveals that in the younger objects, the brightness decreases as Ca II H & K emission increases whereas in older stars (including the Sun), the brightness increases as Ca II H & K emission increases (Radick et al. 1998). A simple interpretation may mean that the long term variability in young stars is dominated by spots, whereas in older stars such as the Sun, it is dominated by faculae.

1.8 Aims

I have given a brief introduction to the rotation and angular momentum evolution of late-type stars. Details concerning rapid rotation have been considered, in the form of dynamo

processes and activity cycles. One method of probing theoretical predictions, Doppler imaging, has also been discussed. It is hoped that further studies using this technique will help us to better understand the processes at work in young solar analogues.

Chapter 2 introduces the technique of least squares deconvolution, which makes use of all the available absorption lines in an échelle spectrum. The absorption line patterns are effectively cross-correlated and co-added to give a single high S:N ratio line profile. Using fake data sets, we test our implementation of this method, and its suitability for Doppler imaging purposes. Chapter 3 introduces the technique of Doppler imaging. With the use of fake data sets with the expected high S:N ratio line profiles obtained from least squares deconvolution, various aspects of the reconstructed images are examined.

The purpose of the present work is to extend the current number of Doppler maps of late type stars with a number of primary aims. In Chapter 4 the established techniques are applied to real data, and Doppler images of G dwarfs in the Alpha Persei cluster are presented. The observed spot distributions on these stars will serve as a comparison and test of the convective overshoot dynamo models. An upper limit on starspot lifetimes is also estimated from a pair of images of one object, separated by a one month interval.

In Chapter 5, I present a differential rotation measurement of the K0V dwarf PZ Tel, whereas in Chapter 6 an upper limit on the differential rotation is determined for the K3 dwarf Speedy Mic. Other general questions relating to the preceding discussion will also be addressed. What are the spot distributions on solar neighbourhood K dwarfs with different periods and slightly different spectral type? Do the spot distributions show definite patterns, or are the patterns independent of spectral type? Can we deduce anything about possible magnetic activity cycles on these stars, as inferred from differential rotation measurements combined with starspot patterns?

Circumstellar coronal condensations have been discovered around a number of late-type stars. In Chapter 7, time series $H\alpha$ spectra of each star are presented, and examined for the absorption transient signatures of these condensations or prominences. All but one of the stars exhibit large prominence systems, which may provide an additional explanation of stellar spindown as material is ejected from the large magnetic loops.

Chapter 8 is a brief summary and conclusion drawn from the preceding work. Themes such as magnetic dynamo models which predict the emergence of magnetic flux,

are common to all chapters and are discussed here.

CHAPTER 2

Least Squares Deconvolution

2.1 Introduction

Doppler imaging (Vogt & Penrod 1983) is an extremely powerful tool allowing high resolution surface images of rapidly rotating stars to be derived. One of the main drawbacks has been the restriction of the technique to relatively bright stars due to a limitation of the available light collecting power of telescopes and efficiency of the instrumentation. Conventional Doppler imaging uses one or several absorption lines to derive a surface map. Because the stars suitable for imaging are rapid rotators, the absorption lines suffer from rotational blending, necessitating use of isolated features. Doppler imaging requires absorption lines with S:N ratios of a few hundred per pixel in order to reliably constrain a useful image. The exposure length of a given spectrum must however be minimised to reduce the effects of rotational blurring. The multitude of constraints has limited the sample of available objects to those with $m_v \sim 8$ or less, and has resulted in a bias toward images of giants (due to their higher luminosities), usually in binary systems. There are however a growing number of Doppler images of single dwarf stars, which are limited largely (though not exclusively) to a spectral type of early K. This is because M dwarfs are too faint whereas there are no known sufficiently bright, rapidly rotating G dwarfs in the solar neighbourhood.

Modern CCD detectors are now relatively large, with $2K \times 2K$ chip sizes in common use on 4m class telescopes. Least squares deconvolution is a sophisticated cross-correlation technique which can be used to compute average profiles from thousands of spectral lines simultaneously. This makes efficient use of the available information in a single échelle spectrum. By assuming a similar local profile shape for every line, the stellar spectra are

treated as the convolution of a line pattern and an average line profile. In this context, extracting the average line profile amounts to a linear deconvolution problem, which can be treated as a matrix equation in which we look for the least-squares solution. In practice, least squares deconvolution is very similar to most other cross-correlation techniques, though slightly more sophisticated in the sense that it cleans the cross-correlation profile from the auto-correlation profile of the line pattern. Effects such as side lobes due to rotational blending of close by neighbouring lines are therefore removed. Fig. 2.1 shows a typical échelle spectrum order, with the line list of delta functions plotted below. The deconvolution process yields a profile with a high S:N ratio, suitable for image reconstruction. The technique was first applied by Donati et al. (1997) primarily for use with spectropolarimetric échelle data, but as was shown is also applicable to unpolarised data.

2.2 The least squares technique

To carry out the procedure successfully, a list of lines is required, along with their relative weightings (defined as the depths of the unbroadened absorption lines) for a normalised spectrum. Line lists have been generated by Donati et al. (1997) from a full LTE spectral synthesis (assuming a 2 km s^{-1} microturbulent velocity) using the ATLAS9 model atmospheres and SYNTH routines of Kurucz (1993). In order not to overrepresent the weak-line class in the list, only central depths exceeding 0.4 (normalised units) were selected. Rotationally broadened lines (e.g. $v \sin i \ 90 = \text{km s}^{-1}$) which have depths < 0.4 tend to be very shallow, and almost indistinguishable from the continuum, especially in lower S:N spectra.

The telluric lines which are numerous in the red part of the spectrum also affect some photospheric lines. The relative location of tellurics is random with respect to the object lines, and so no line will be positioned in exactly the same place in a rotationally broadened object line. Also, stellar lines are generally weaker and much more scarce in the orders affected by tellurics, with the main body of photospheric lines occurring at the blue end of the spectrum. However due to the number of telluric lines, and their larger depth relative to the photospheric object lines, they would only serve to add noise to the deconvolved profile, hence any lines in the most badly affected regions are removed from the line list

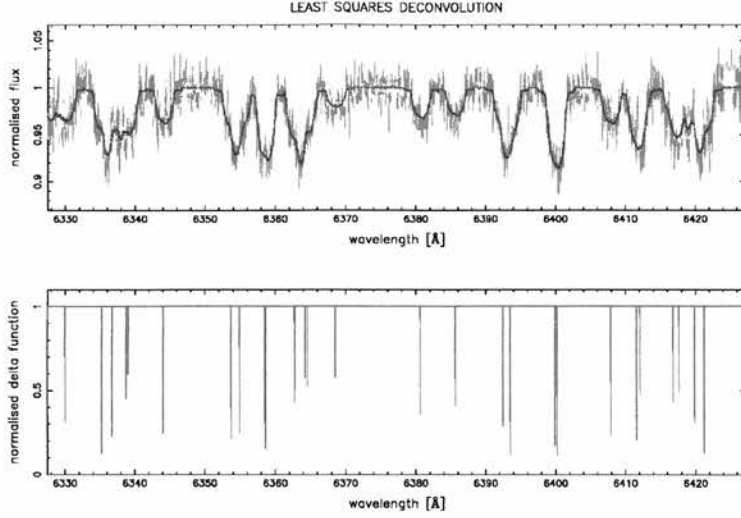


Figure 2.1: Top: A synthesised échelle order with noise, and the convolution of the ‘least squares’ line pattern with the line weighting mask. Bottom: are shown the line depths used to calculate the line mask (see text for details)

¹. Since the stellar photospheric lines in this region are themselves generally weak, their removal, and the subsequent decrease in the S:N ratio of the deconvolved profile, is less than the degradation that tellurics would produce if the affected regions were included. Strong chromospheric absorption lines such as the hydrogen Balmer series, sodium D (Na I 5889.95Å & 5895.92Å), the magnesium triplet (Mg I 5167.32Å, 5172.68Å & 5183.60Å) and lines close enough to be affected by their pressure-broadened wings (which will introduce a local tilt and depression in the continuum) are also removed.

If we denote the deconvolved profile elements by z_k , then the predicted data, p_j (i.e. the convolution of the line list and deconvolved profile), can be written as

$$p_j = \sum_k \alpha_{jk} z_k, \quad (2.1)$$

The elements of the $N_j \times N_k$ matrix, α , are defined by the line depths, d_i , and the triangular interpolation function, $\Lambda(x)$, as

¹We generally take the atmospheric cutoff at ~ 7000 Å

$$\alpha_{jk} = \sum_i d_i \Lambda(x) \quad (2.2)$$

where

$$x = \left(v_k - c \left(\frac{\lambda_j - \lambda_i}{\lambda_i} \right) \right) / \Delta v, \quad (2.3)$$

and

d_i = depth of line i

λ_i = wavelength of line i

λ_j = wavelength of spectrum pixel j

v_k = radial velocity of profile bin k

Δv = velocity increment per pixel in deconvolved profile

The triangular function $\Lambda(x)$ is such that

$$\begin{aligned} \Lambda(x) &= 1 + x & \text{for } -1 < x < 0 \\ &= 1 - x & \text{for } 0 < x < 1 \\ &= 0 & \text{elsewhere} \end{aligned} \quad (2.4)$$

In this way, the weight of each spectrum element, j is partitioned across 2 or more pixels, k . Hence a sparse matrix α is built up such that it contains minor diagonals, usually with pairs of partitioned elements in k for each element or pixel in j . In other words, the method given in Equations 2.2, 2.3 and 2.4 is defined such that the interpolated pairs of elements in k , at a given j , add to give the depth of line i in question. The design matrix, α , is effectively a weighting mask which only includes the regions of spectrum over the desired deconvolution range in wavelength/velocity space.

Simply convolving the normalised, observed spectrum (elements, r_j) with the matrix, α , i.e.

$$\mathbf{x}_k = \sum_j \alpha_{jk} \mathbf{r}_j, \quad (2.5)$$

would be equivalent to co-adding all the weighted lines in the object spectrum which occur in the synthetic line list, but would not properly account for the effects of rotationally blended lines. Rotational blending occurs when there is more than one set of non-zero

k elements per j element in the design matrix. The least squares deconvolution process means that the number of lines which can be used is independent of the degree of rotational blurring. The output least squares profile is binned at the average pixel resolution of the object spectrum and is determined by the size of the CCD pixels (usually 2-3 km s⁻¹). Generally the velocity range over which the deconvolution takes place relative to the theoretical rest wavelength of each absorption line is chosen such that the total half-width is greater than the $v \sin i$ of the object itself. This allows continuum to be included on either side of the deconvolved line. The χ^2 function is used to obtain the inverse variance weighted fit of the convolution of the line list with the deconvolved profile to the normalised and continuum-subtracted spectrum r_j ,

$$\chi^2 = \sum_j \left(\frac{r_j - \sum_k \alpha_{jk} z_k}{\sigma_j} \right)^2. \quad (2.6)$$

The equation is minimised by finding the solution to the set of equations

$$\frac{\partial \chi^2}{\partial z_k} = 0, \quad (2.7)$$

where the unknown quantity is the least squares profile, z_k . This yields

$$\sum_j \frac{1}{\sigma_j^2} \sum_k \alpha_{jk} \sum_l \alpha_{jl} z_l = \sum_j \frac{1}{\sigma_j^2} r_j \sum_k \alpha_{jk} \quad (2.8)$$

The deconvolution process can be given in the same form as Equation 4 in Donati et al. (1997). If the inverse variances, $1/\sigma_j^2$ are contained in the the vector, \mathbf{V} , and the spectrum elements r_j in the vector, \mathbf{R} , the solution can be written in matrix form as

$$\mathbf{z} = (\boldsymbol{\alpha}^T \cdot \mathbf{V} \cdot \boldsymbol{\alpha})^{-1} \boldsymbol{\alpha}^T \cdot \mathbf{V} \cdot \mathbf{R} \quad (2.9)$$

The right hand part of Equation 2.9 (i.e. $\boldsymbol{\alpha}^T \cdot \mathbf{V} \cdot \mathbf{R}$) is the cross-correlation of the observed spectrum with the line mask. This, as mentioned above, is the weighted mean of all the lines. The solution however gives flat continuum outside the least squares deconvolved profile, free of sidelobes from blends, provided that the line list used is reasonably comprehensive, and the weights correct. The solution therefore effectively cleans the cross-correlation vector from the square symmetrical auto-correlation matrix $\boldsymbol{\alpha}^T \cdot \mathbf{V} \cdot \boldsymbol{\alpha}$.

The solution to equation 2.9 requires the inverse of the auto-correlation matrix to be determined. This can be found by making use of a suitable fast inversion routine such as Cholesky Decomposition as given in ‘Numerical Recipes’ (Press et al. 1986).

2.2.1 Spectrum normalisation and weighting scheme

In addition to the weighting given to each line according to the depth of the corresponding line in the synthetic list, it is necessary to specify the uncertainty or noise, σ_j , of each object spectrum pixel due to photon statistics. Of importance is the weighting scheme to be used for the least squares deconvolution which must be chosen carefully since an incorrect choice could lead to a greater than necessary error in the final profile shape. We chose to use a standard continuum, scaled to the same mean as the continuum fit to the spectrum in question, as described below.

Spectrum normalisation effectively involves dividing the object spectrum by a master spectrum comprising all the co-added object frames. The resultant, featureless residual is then fitted with a straight line or relevant low-order polynomial to correct for a change in continuum tilt or number of counts when compared with the master spectrum. The correct continuum fit to the object frame in question is obtained by multiplying this fit by the standard continuum (i.e. the continuum fit to the co-added master frame). This removes the effects of continuum tilt changes throughout the night due to extinction (see chapter 4 & 5 for further details).

For each individual object frame, the inverse variances of the standard continuum are scaled in a weighted manner to the same mean value as those of the object continuum frame. This scaled standard continuum is then used to adjust the weights of the listed lines in the calculation of the least squares fit. Denoting the spectrum elements s_j , continuum fit elements c_j , standard continuum fit elements t_j , and α_{jk} the matrix elements representing the line mask weights (see below), this scale factor, ζ , is defined as

$$\zeta = \frac{\sum_j \sum_k \alpha_{jk} c_j}{\sum_j \sum_k \alpha_{jk} t_j}, \quad (2.10)$$

and the continuum normalisation is defined as,

$$r_j = \frac{s_j - c_j}{\zeta t_j} \quad (2.11)$$

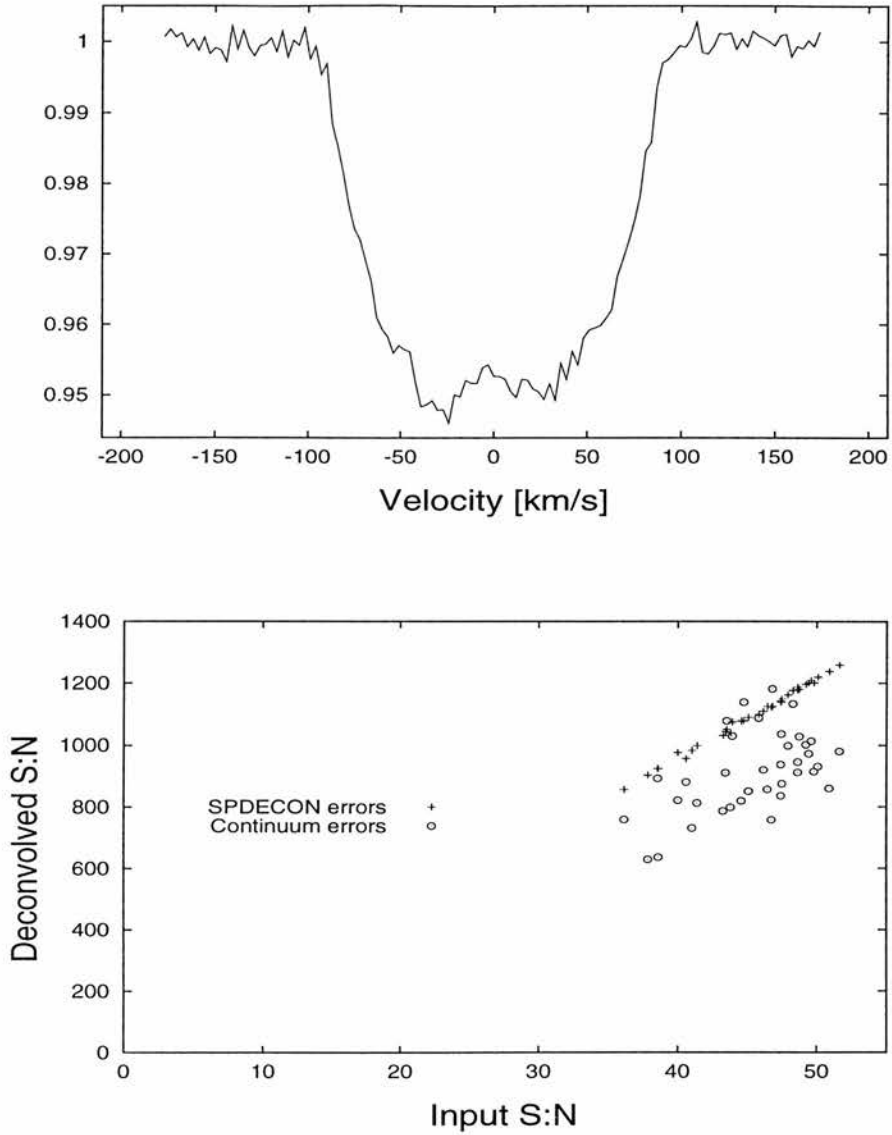


Figure 2.2: Top: He 520 - A deconvolved profile exhibiting a S:N ratio of 784 (S:N ratios are always given per pixel) measured directly from the continuum wings and an SPDECON propagated S:N ratio (mean across the whole profile) of 743. Corrected to a line of mean weighted depth, $\langle d \rangle = 0.6893$, the same respective continuum S:N ratios are 1139 and 1079. The average S:N ratio per échelle spectrum was approximately 45, which with a mean SPDECON propagated error of 1096 for all 37 spectra gives a mean multiplex gain of 24 from the deconvolution process. The equivalent SPDECON propagated S:N ratios for a line of mean weighted depth for He 699 (October 1996) and He 699 (November 1996) are 1259 and 1220 respectively (see Chapter 4). Bottom: Least squares deconvolved S:N ratio (He 520 data set shown) is approximately proportional to the range of input S:N ratio values (again S:N ratios for a mean depth line are shown).

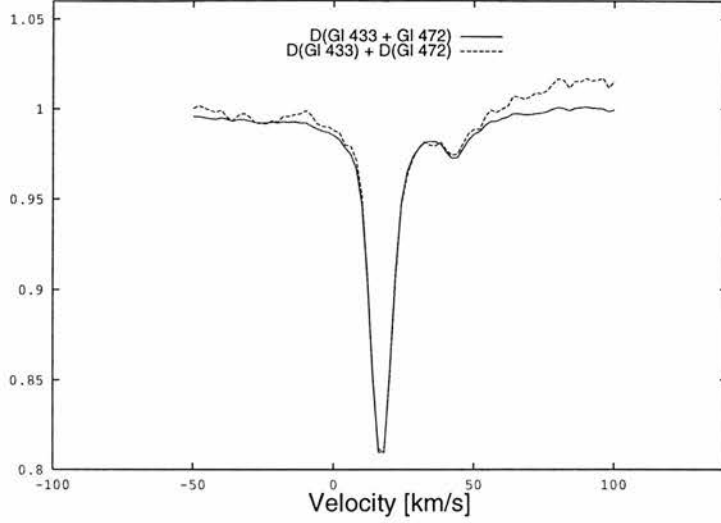


Figure 2.3: Plot showing approximate associative nature of the deconvolution process. Shown are two deconvolved profiles for Gl 433 (M1.5V) and Gl 472 (K1V) from the 1998 July/UCLES/AAT data set. The stars have different radial velocities which have not been corrected to zero, thus allowing comparisons to be made. Gl 472 is the stronger profile, centred at $v \approx 20 \text{ km s}^{-1}$, whereas Gl 433 is the weaker profile on the right, at $v \approx 45 \text{ km s}^{-1}$. This shows that the process $D(A) + D(B) \simeq D(A + B)$. Deconvolution of $0.5 \cdot \text{Gl 433} + 0.5 \cdot \text{Gl 472}$ was carried out using the continuum and standard continuum fit to Gl 472. Each object frame was deconvolved individually using the same continuum. The plots have been corrected to a continuum of 1 by adding constants. The important point is that the absolute and relative sizes of the profile flux deficits are approximately preserved.

The errors are then defined by

$$\sigma^2(r_j) = \frac{1}{\zeta t_j} \quad (2.12)$$

This imposes a consistent weighting scheme, and also results in the removal of any changes in the tilt of the continuum due to the presence of a starspot which will exhibit a spectrum of spectral type M. The definition given in Equations 2.10 and 2.11 is such that the deconvolution process is associative. That is, the process $D(A) + D(B) = D(A + B)$, where D represents the deconvolution process, and A and B are two input spectra (see Fig. 2.3).

2.2.2 Errors in the deconvolved profiles

Determination of the deconvolved profile errors is required in order to determine the correct level of maximum-entropy regulated fit for the Doppler imaging process. The diagonal elements of the auto-correlation matrix, $\boldsymbol{\alpha}^T \cdot \mathbf{V} \cdot \boldsymbol{\alpha}$ also provide errors for the deconvolved profile. i.e.

$$\sigma_k^2 = (\boldsymbol{\alpha}^T \cdot \mathbf{V} \cdot \boldsymbol{\alpha})^{-1} \quad (2.13)$$

The behaviour of the least squares process results in a profile (as shown in Figure 2.2) which is scaled according to a line depth of unity (i.e. has $EW = \Delta v$). This does not necessarily mean that the least squares profile has a depth of unity. In the case where we deconvolve a spectrum with non-broadened lines, the line list depths (measured in normalised units) *do* represent the depth of the observed line in the ideal case. When the least squares profile with actual depth unity is convolved with the line list (as given in Equation 2.2), the best match to the observed spectrum is created. In practice, the observed line depths are less than the theoretical line depths because EW is conserved in rotationally broadened profiles.

A mean deconvolved line depth, $\langle d \rangle$, in normalised units is required in order to calculate the mean multiplex gain. The factors which determine the deconvolved line depth are the inverse variance weightings ($\mathbf{s}_j \equiv 1/\sigma_j^2$) and the theoretical line depths, (\mathbf{d}_i). If \mathbf{s}_i represents the pixel closest to the rest wavelength of line i , then the weighted mean depth is given by the expression

$$\langle d \rangle = \frac{\sum_i \mathbf{s}_i \mathbf{d}_i^2}{\sum_i \mathbf{s}_i \mathbf{d}_i} \quad (2.14)$$

Throughout the remainder of this work, for image inversion and plotting purposes, the profile is always plotted scaled to a depth of unity. The deconvolved S:N ratios and multiplex gain however refer to a line of mean depth $\langle d \rangle$, in units of the local continuum level (see Figure 2.2, bottom). We use lines with theoretical, unbroadened depths of 0.4 to 1.0 in the deconvolution process, which result in a typical mean depth of ~ 0.7 from Equation 2.14.

A simple way to determine the approximate S:N ratio of the deconvolved profile is to deconvolve over a sufficiently large range in velocity space, relative to the rest wavelength

of each absorption line. In this way we obtain continuum pixels on the immediate sides of each line profile, which allow an empirical measurement of the new S:N ratio to be made. This was done by simply selecting two regions on either side of the profile, and determining the standard deviation from these regions. The result was found to vary in accordance with the quality of the input échellogram (Figure 2.2, bottom), so that final S:N ratios varying from ~ 600 per pixel to values of ~ 1200 per pixel for the highest quality spectra were recorded (the S:N ratios are always given per deconvolved spectrum bin). As is shown in Figure 2.2 (bottom), the two methods of error determination are in reasonable agreement. The direct continuum method yields a lower S:N ratio as expected, because the continuum tends not to be flat, containing fluctuations. These may be due to nearby lines during the least squares process. In any case, no attempt was made to remove these fluctuations before measuring the scatter due to noise alone, and hence they will bias the measurements to lower S:N ratios. Propagation of errors using the auto-correlation matrix provides much less scatter, and a systematically higher S:N ratio as a result.

2.2.3 Limb Darkening

Limb darkening varies with wavelength, and it is not obvious that the use of a weighted-mean value for Doppler imaging purposes (cf. Donati & Collier Cameron (1997)) is valid. The limb-darkening coefficients (LDCs) were obtained from Kurucz (1993) at the UVBRI photometric passbands. Linear interpolation was used to calculate the LDCs at all intermediate wavelength points in a spectrum. Since limb-darkening is almost linear as a function of wavelength, this procedure is valid. This was carried out for both photospheric temperature components of $T = 3750$ K and $T = 5750$ K. The centroidal wavelength

$$\langle \lambda \rangle = \frac{\sum_i s_i d_i \lambda_i}{\sum_i s_i d_i} \quad (2.15)$$

was also calculated from lines in the line-list, such that it was weighted with respect to both the line strength and the variance from the standard fit used in our implementation of the least squares process, SPDECON. This value was found to be at 5507.54 \AA for the case of the wavelength calibration file from the α Persei 1996 November data set, which is near the centre of the photometric V-band (5450 \AA). The solid lines in Figure 2.4 represent the continuum intensity at foreshortening parameter values of $\mu = \cos(\theta) = 0.1, 0.5 \text{ \& } 1.0$ (θ is the limb-angle), from bottom to top, where limb-darkening is a function of wavelength,

while the dashed lines represent the equivalent values for the constant limb-darkening case. The mean value of the continuum intensity was calculated for each limb-angle, from Equation 2.16 and was weighted according to both line-strength and local continuum intensity. (Note : the values of I_0 are taken to be unity in the plots for convenience, the vertical scale representing the limb-darkening coefficient value).

$$I(\lambda_j) = I_0 \cdot \frac{1 - u(\lambda_j) + u(\lambda_j)\mu}{1 - u(\lambda_j)/3} \quad (2.16)$$

where $u(\lambda_j)$ is the limb-darkening coefficient at wavelength λ_j . Note how the dashed and solid lines intersect close to the centroidal wavelength of 5507.54\AA ; and since the solid lines have very little curvature, any difference between the constant and wavelength dependent centroidal limb-darkening scaling values should be very small. This is indeed found to be the case, and is represented in Figure 2.5 which shows that the deviation never exceeds 0.75 per cent at the spot temperature, and 0.25 per cent at the photospheric temperature, and only near the limb. In practice, we calculate the mean weighted LDC $\langle u \rangle$ using the full treatment, i.e.

$$\langle u \rangle = \frac{\sum_i s_i d_i u(\lambda_i)}{\sum_i s_i d_i}, \quad (2.17)$$

where $u(\lambda_i)$ is the limb-darkening coefficient in the pixel closest to line i , at wavelength λ_i .

2.2.4 Reliability of the deconvolved profile shape

A semi-empirical test of the match between the deconvolved profile and the intrinsic profile is necessary to ensure that the deconvolution routine is reliable. The rotationally broadened profile $G(\lambda)$ is given by Gray (1992), such that

$$G(\lambda_j) = \frac{2(1 - u(\lambda_j))(1 - (\Delta\lambda/\Delta\lambda_L)^2)^{0.5} + 0.5\pi u(\lambda_j)(1 - (\Delta\lambda/\Delta\lambda_L)^2)}{\pi\Delta\lambda_L(1 - u(\lambda_j)/3)}, \quad (2.18)$$

where $\Delta\lambda_L$ is the broadened profile width in wavelength units.

The rotationally broadened profile was convolved with a synthetic line list of delta functions representing unbroadened profile depths in order to obtain a synthetic échellogram.

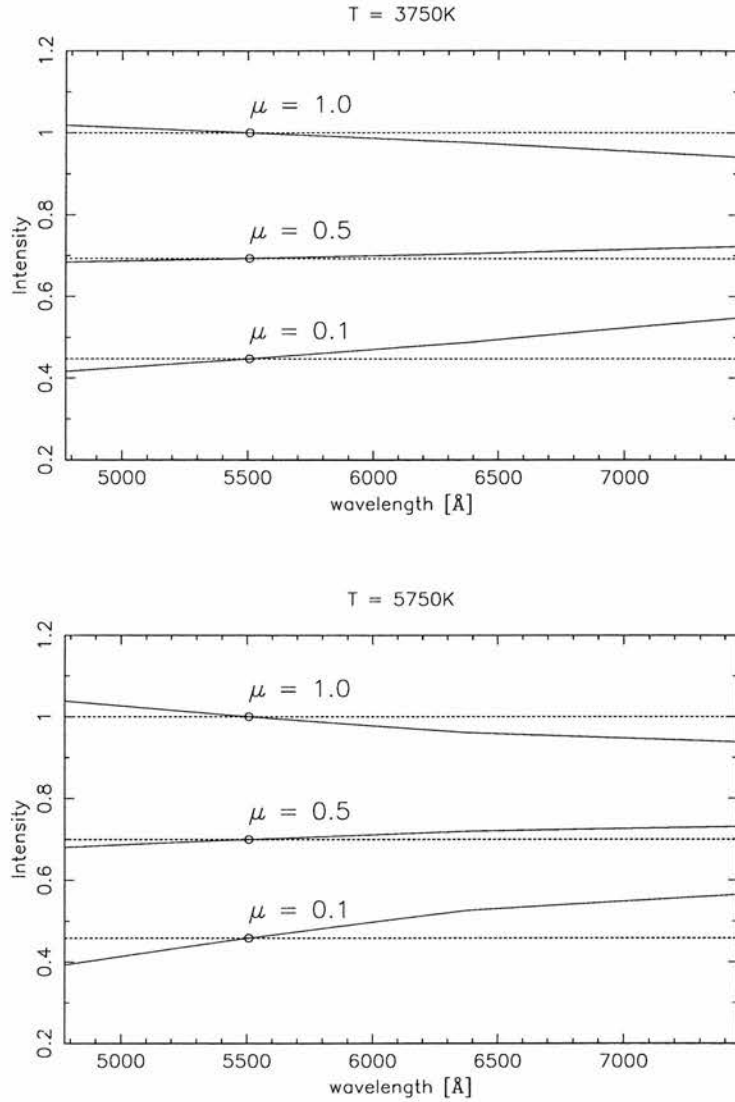


Figure 2.4: Diagram showing the effect of limb-darkening as a function of wavelength for two different temperatures, $T=3750\text{K}$ (above) and $T=5750\text{K}$ (below). Solid lines show the continuum intensity (see text) as a function of wavelength at limb angles ($\mu = \cos\theta$) of 0.1, 0.5 & 1.0 (bottom to top) whereas dashed lines show the case where limb-darkening is constant. Note that the dashed and solid lines cross at approximately the centroid of the limb darkening coefficient. The central continuum intensity values I_0 are chosen to be unity for the purposes of the illustration.

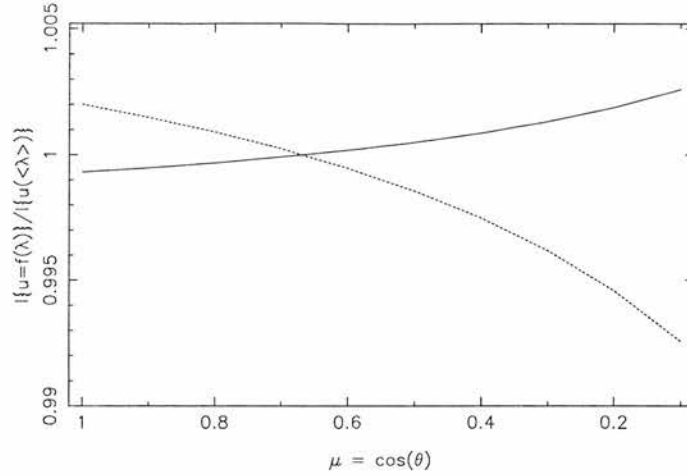


Figure 2.5: Continuum intensity for wavelength dependent limb-darkening divided by continuum intensity for constant limb-darkening for $T = 3750$ K (solid lined) and $T = 5750$ K (dashed line). The ratio is not constant, but only becomes pronounced toward the limb, even though it remains small.

Note that Eqn. 2.18 does not take account of thermal, macroturbulent and microturbulent Doppler broadening which give smooth profile wings, and as such exhibits sharp “corners”. Linear interpolation was used to calculate the correct limb-darkening coefficient at the wavelength of each absorption profile. We used the wavelength calibration file from the AAT data (see Chapter 5) for these tests since the $2K \times 2K$ MITLL CCD at the AAT offers the highest pixel resolution at $\approx 2 \text{ km s}^{-1}$. The synthetic échellograms have infinite S:N ratios, and the intrinsic profile width is $v \sin i$ of 90 km s^{-1} .

The synthetic échellogram was deconvolved in order to determine how well the broadened profile shape is retained. The option to reject profiles near the edges of orders has also been included in SPDECON. The results are shown in Figure 2.6 (see caption for details). A comparison of the deconvolved profile with edge rejection with the intrinsic profile yields a standard deviation across the deconvolved profile (expressed as the difference as a percentage of the mean depth of the two profiles) of 0.7 per cent or in absolute terms 0.04 per cent of the continuum level. Similarly for the case of no rejection of profiles at order edges, the corresponding values are 0.4 per cent and 0.02 per cent respectively. These deviations are small and usually below the level of the S:N ratio of the deconvolved profiles, but they do represent a systematic deviation from the intrinsic profile shape.

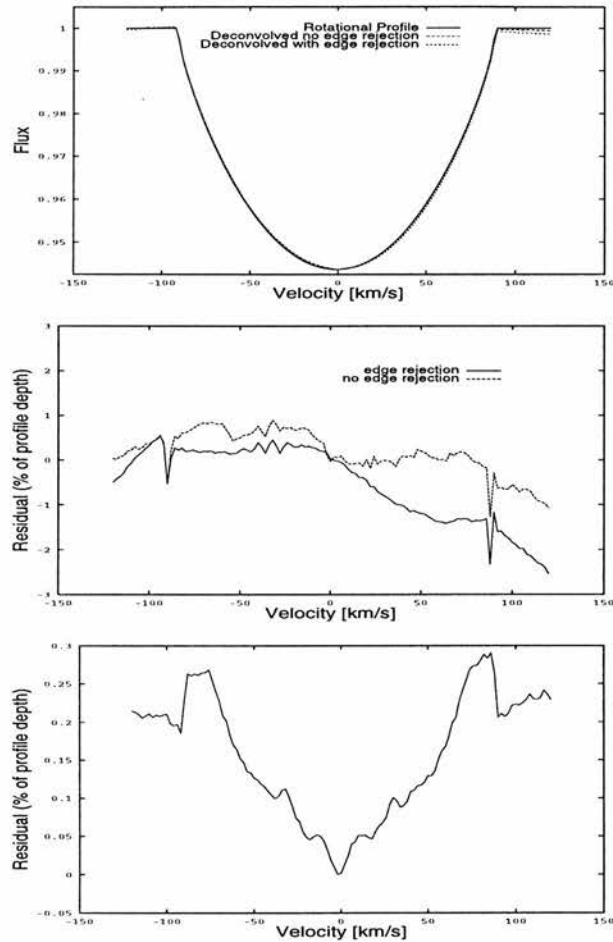


Figure 2.6: Synthetic Spectrum - Top: are shown the deconvolved profiles for deconvolution using edge rejection (solid line) and no edge rejection. The actual rotation profile is also shown. Middle: are shown the residuals as a percentage of the profile depth for deconvolved rotation profile with edge rejection minus the actual profile, and deconvolved rotation profile with no edge rejection minus the actual profile. Bottom: is shown the residual as a percentage of the mean profile depth for the deconvolution profile of the synthetic spectrum taking account of limb-darkening minus the synthetic spectrum with a constant profile

The plots in Fig 2.6 show a tilt in the deconvolved profile continuum for the case where edge rejection is used. The effect is less pronounced in the case of no edge rejection. The degree of this tilt is not constant for different data sets and so we include the option of order edge rejection to enable minimisation of these deviations. The tilt is due mostly to asymmetry in the covered region of the blaze profile and hence larger chips which cover a larger part of the of the envelope at the camera focus tend to produce less tilt in the deconvolved profile. The tilt is produced by strong absorption lines. The free spectral range of an échelle spectrograph is such that wavelengths and therefore absorption profiles which appear at the end of one order also appear at the beginning of the next order. The effect is most prominent in the bluer orders where adjacent orders may contain nearly the same wavelength ranges. 1K×1K chips can only cover half of the blaze profile in a given order. If the continuum tilt at the wavelength of a strong line suffers from a considerable slope (for example at the end of an order), the deconvolved profile shape may suffer from a slope if the line is not repeated near the start of the next order, where it would have a balancing continuum tilt of opposite sign. Rejection of order edges is by no means an ideal solution since wherever one cuts the order edges, there may still be strong lines contributing to the pixels at the limits of the desired range. Choice of lines from the synthetic line list with which to deconvolve is therefore not a trivial matter, and may require careful selection to remove groups of strong lines at order edges. A compromise between obtaining sufficient gain in signal to noise must be struck with obtaining a deconvolved profile with minimum tilt. The least squares process is not ideal, but this major departure can be minimised with a little care.

2.2.5 Deconvolution reliability with increasing $v\sin i$

It was considered pertinent to test the reliability of the deconvolved profile with increasing projected equatorial rotation velocity, $v\sin i$. As $v\sin i$ increases, the degree of rotational blending of lines becomes more extreme. Intuitively, one might expect this effect to have consequences on the shape of the deconvolved profile. To this end, synthetic échellograms with rotation velocities of 15 km s⁻¹, 30 km s⁻¹, 60 km s⁻¹, 90 km s⁻¹, 120 km s⁻¹ and 150 km s⁻¹ were created in the manner described above. The synthetic échellograms were created using the 1996 α Persei wavelength calibrated file and a G dwarf (He 520) mean

Table 2.1: Limiting S:N ratio attainable at various $v\sin i$ values for synthetic data sets with no noise

$v\sin i$ (km s^{-1})	% error of mean profile depth	error at continuum level $\times 10^{-4}$	Limiting continuum S:N ratio
15	0.429	2.188	4569
30	0.439	2.243	4458
60	0.620	3.138	3186
90	0.811	3.990	2506
120	1.003	4.725	2116
150	1.269	5.800	1724

continuum. An intrinsic profile *with infinite S:N ratio* was created for each $v\sin i$ value from the Doppler imaging code. This correct treatment of the rotationally broadened absorption line gives an intrinsic profile with rounded edges, however the limb-darkening is constant as a function of wavelength. The deconvolved profiles are shown (Figure 2.7 compared with the intrinsic rotation profile. Plotted below each profile is the residual as a percentage of the intrinsic profile depth. There are no serious systematic deviations within the $v\sin i$ range of each individual deconvolved profile when compared with the intrinsic profile. It is unclear why the continuum slopes away outside the deconvolved profile. This may due to some kind of aliasing effect in the least squares process. Further testing is however required to understand this phenomenon. As expected, the limiting S:N ratio decreases with increasing $v\sin i$ (Table 2.1). These values are intended for demonstration purposes, and are expected to vary with each data set. The larger chip sizes offer more lines and as such are expected to yield a greater limiting continuum S:N ratio.

2.2.6 The line list

We currently use line lists generated by J.-F. Donati from Kurucz (1993). The deconvolution process is fairly robust with respect to choice of line list spectral type. Obviously, the later the spectral type of the spectrum to be deconvolved, the more photospheric absorption lines are available. For this reason we do not wish to use a line list of significantly later spectral type than the object, as there may only exist continuum in the actual spectrum where a synthetic line exists. Table 2.2 shows the effect of deconvolving a spectrum

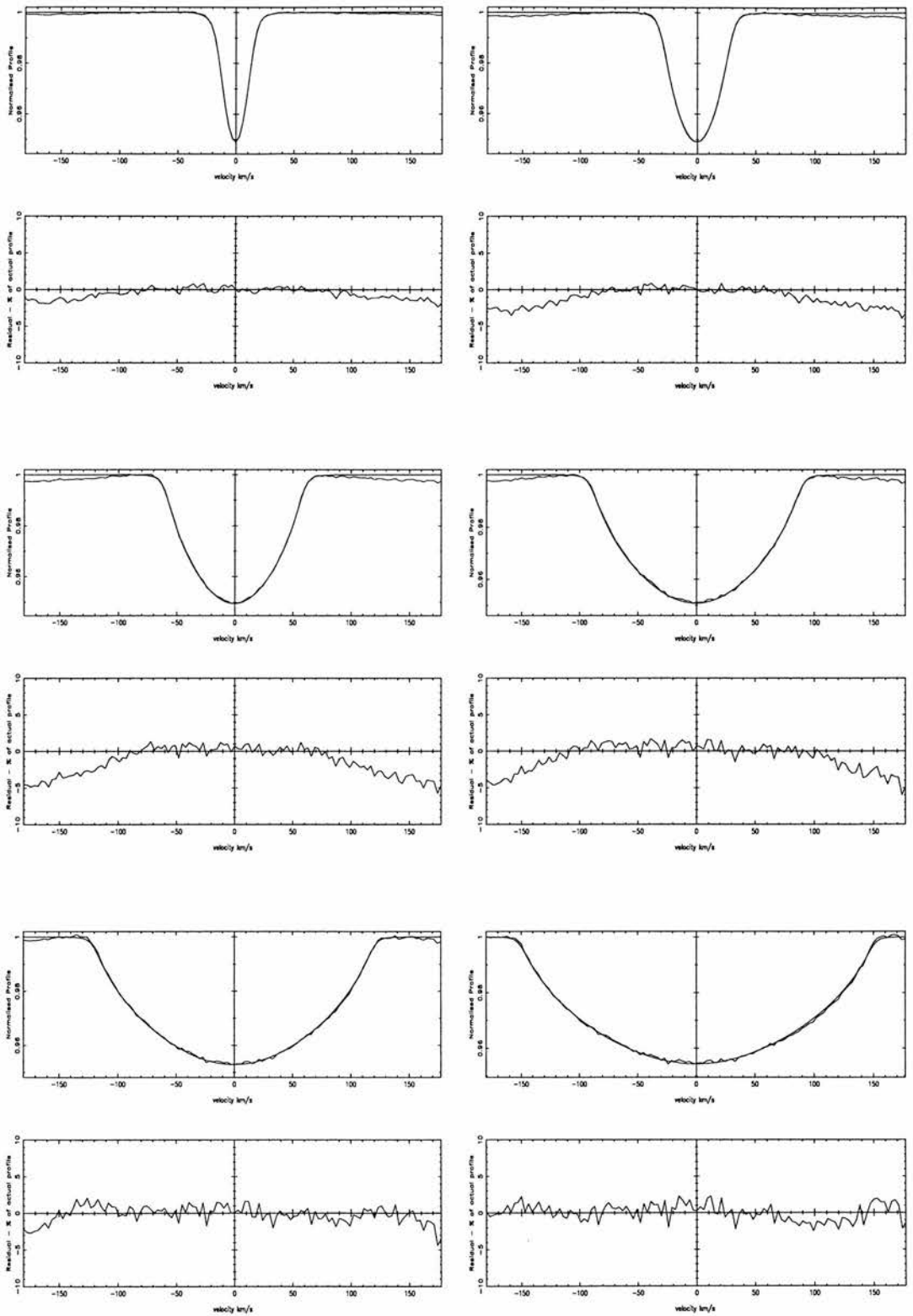


Figure 2.7: Deconvolved profile shape for $v \sin i = 15, 30, 60, 90, 120, 150 \text{ km s}^{-1}$

Table 2.2: Table showing the effect of using synthetic line lists of different spectral type on a star of fixed spectral type. Note that the multiplex gain (calculated from the diagonals of the correlation matrix) in each case is small since the input spectrum already has a S:N of 633. See text for details. The depth of the deconvolved line changes with each line list, necessitating a correction factor so the gains can be compared. The mean error relative to the deconvolved line depth is calculated before calculating the percentage of the K1 gain in column 5

Spectral type of line list	No of synthetic lines	Multiplex gain	Output S:N ratio	% of K1 gain
G2	1766	4.5	2841	83.7
G7	2360	5.1	3255	90.0
K1	2832	5.6	3521	100.0
K5	3137	5.8	3643	107.8

with synthetic line lists of different spectral type. The spectrum used was the co-added (67 frames) PZ Tel master spectrum from the 1998 July 10 data set using UCLES at the AAT. As can be seen, the overall range in S:N is reasonably constant, with late spectral types yielding the highest S:N ratios, and earlier spectral types yielding lower S:N ratios. Since the spectral type of PZ Tel is K0V, using a K5V line list with more lines would be expected to give a greater S:N ratio but is dangerous because line patterns which do not exist are included in the least squares calculation. Continuum may also be included where a line occurs in the list but not in the observed spectrum. Similarly, using a line list of earlier spectral type, with too few lines, will result in incorrect treatment of the line pattern. Also, the effects of metallicity are not taken into account, as these line lists are for solar type abundances. Although PZ Tel is metal poor relative to the Sun, with $[\text{Fe}/\text{H}] = -0.25$ (Soderblom, King & Henry 1998), the effects on multiplex gain are expected to be small given the lack of sensitivity when using a line list of incorrect spectral type.

We deconvolve spectra which are essentially a combination of an immaculate photosphere and a cooler spectrum due to spots. In a given exposure, the degree of cool, M dwarf like spectrum will depend upon the presence of spots visible at that time. Although the spot signature is therefore not treated with the correct line list, it is treated consistently with the same list as an imagined photospheric standard. The spot signatures which

are clearly present after deconvolution further demonstrate the robust nature of the process with respect to mismatch of synthetic line list spectral type and target (immaculate photosphere) spectral type.

CHAPTER 3

Doppler Imaging

3.1 Chapter synopsis

In this chapter I give a brief introduction to the theory of Doppler imaging, and describe the process of inverting a time series of absorption spectra to form an image. Synthetic line profiles are created with the S:N ratios one might expect as a result of applying least squares deconvolution to each échelle spectrum. The best method for determination of the empirical parameters, radial velocity, projected equatorial rotation velocity, equivalent width and stellar inclination is presented. These assumed parameters are varied in order to test the sensitivity of the reconstructed image to incorrectly determined values. The results show that Doppler imaging is a robust process.

3.2 The line profile

In a slowly rotating star, the line formation physics results in narrow photospheric absorption-line profiles. The widths of these profiles are generally of order 10 km s^{-1} or less. However a rapidly rotating star is subject to Doppler effects, such that the narrow, local intensity profile arising from a small region on the stellar surface may be displaced from the rest wavelength of the line in question. The degree of displacement depends on the position of the surface element from which the flux arises, relative to the rotation axis of the star. As shown in the simplified diagram in Figure 3.1 ¹, local intensity profiles arising from constant longitude regions suffer the same shift in wavelength or velocity space. Convolution of local intensity profiles from all regions on the stellar disc results in the observed,

¹Taken from Vogt & Penrod (1983)

broadened profile. This resulting Doppler broadened absorption profile can be represented as given in Equation 2.18 (Gray 1992). The rotation profile must be convolved with both the intrinsic stellar profile and the instrumental profile for complete treatment.

A large number of rapidly rotating stars with outer convective envelopes are now known to possess spotted surfaces. The technique of Doppler imaging was first applied to the RS Canum Venaticorum type star HR 1099 by Vogt & Penrod (1983) in an attempt to map the stellar surface. Figure 3.1 is a cartoon representation of a star with a spotted region of area equal to half that of region A. On the left is a representation of how the local intensity profiles of an unspotted star sum to produce a rotationally broadened profile. The right of the diagram shows the case of the spotted star where half of region III is covered by a completely dark ($T = 0$ K) spot. As a result the summed profile has a lower continuum level with an apparent emission bump in the part of the profile corresponding to the longitude of the spot feature. When normalised, the equivalent width of the line is reduced slightly. In reality the spots are not at zero temperature, resulting in a reduced contribution from the spotted region rather than none at all.

The size of the smallest resolvable feature (Collier Cameron 1992) is governed by:

- 1) the ratio of the widths (FWHM) of the intrinsic non-rotating profile (i.e. the line used for mapping) and the stellar rotation profile.

- 2) the drift in wavelength of the spot bump as the star rotates during an exposure.

- 3) the ratio of the starspot bump amplitude to the noise in the measured spectral fluxes.

When a starspot crosses the observer's meridian, the ratio of its Doppler broadened profile width to that of the star is approximately r , the ratio of the spot radius to the stellar radius. The drift rate of a spot at the stellar equator as it crosses the observer's meridian is, from the Doppler formula given by

$$\dot{\lambda} = \frac{2\pi\lambda_0 v \sin i}{cP_{rot}}. \quad (3.1)$$

The effective width (i.e. the EW divided by the central depth) of the stellar absorption profile is approximately

$$\Delta\lambda_{rot} = \frac{\pi\lambda_0 v \sin i}{2c}. \quad (3.2)$$

The blurring, τ , of the spot feature caused by rotation during an exposure of duration Δt

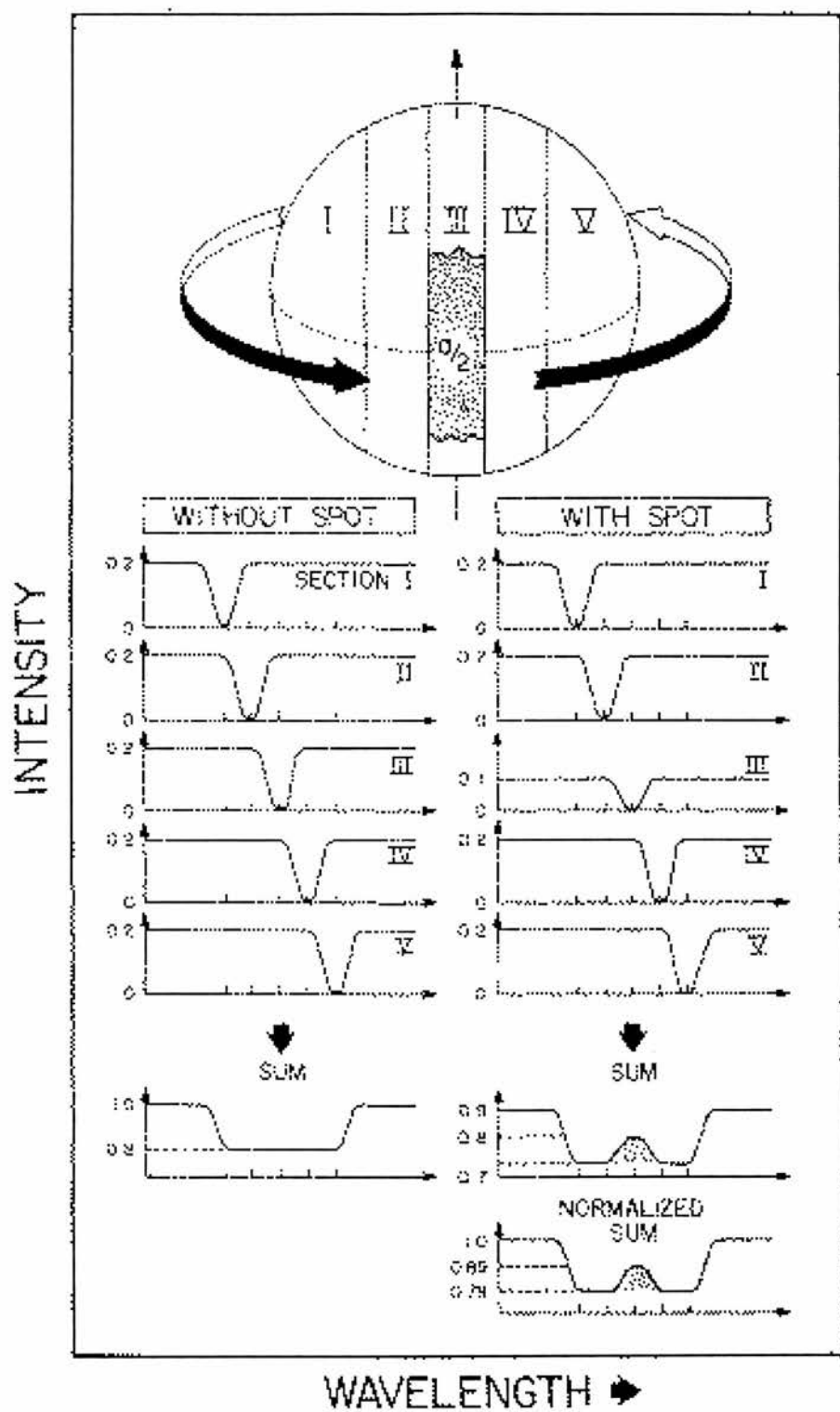


Figure 3.1: How starspot signatures are formed (taken from Vogt & Penrod 1983)

is

$$\tau \equiv \frac{\dot{\lambda}\Delta t}{\Delta\lambda_{rot}} = \frac{4\Delta t}{P_{rot}} \quad (3.3)$$

This blurring can be minimised through use of the least squares deconvolution technique because the raw spectra need not necessarily have such a high S:N ratio as would be necessary if only a single line were being used for Doppler imaging. For example Stout-Batalha & Vogt (1999) used HIRES on the 10m Keck telescope to obtain 30 minute exposures of two rapidly rotating Pleiades dwarfs. The degree of blurring, τ is approximately 5 per cent. Using 4m telescopes, we have still achieved blurring of less than 3.3 per cent in the fastest rotator in the α Persei cluster, AP 149. Assuming the photospheric mapping line to have a constant residual flux relative to the continuum (i.e. continuum flux minus flux at line centre), R_{res} , over the stellar disc, the EW of the mapping line can be written (Collier Cameron 1992) as

$$W_{obs} \simeq [1 - R_{res}(\lambda_0)]\Delta\lambda_{rot}x \quad (3.4)$$

where x is the ratio of the mapping line FWHM to the stellar doppler profile. That is to say that the EW does not change with $v\sin i$ as stated above. The central residual intensity can therefore be written as the convolution of Doppler and local intensity profiles as

$$[1 - R_{obs}(\lambda_0)] \simeq \frac{W_{obs}}{\Delta\lambda_{rot}(1 + x^2)^{1/2}}, \quad (3.5)$$

and hence,

$$[1 - R_{obs}(\lambda_0)] \simeq [1 - R_{res}(\lambda_0)]\frac{x}{(1 + x^2)^{1/2}}. \quad (3.6)$$

The equivalent width and amplitude of a completely dark spot located near the centre of the stellar disc are approximately $W_{spot} \simeq [r^2/(1 - r^2)]W_{obs}$ (provided that the spot is small) and $R_{spot} \simeq W_{spot}/\Delta\lambda_{spot}$. The FWHM of the spot bump is then given by the convolution of the rotation profile of the spot with the intrinsic profile of the mapping line and the blurring effects during a finite exposure, so $\Delta\lambda_{bump} \simeq \Delta\lambda_{rot}(r^2 + x^2 + y^2 + \tau^2)^{1/2}$. Hence

$$R_{spot} \simeq [1 - R_{res}(\lambda_0)]\frac{x}{(r^2 + x^2 + y^2 + \tau^2)^{1/2}}\frac{r^2}{1 - r^2} \quad (3.7)$$

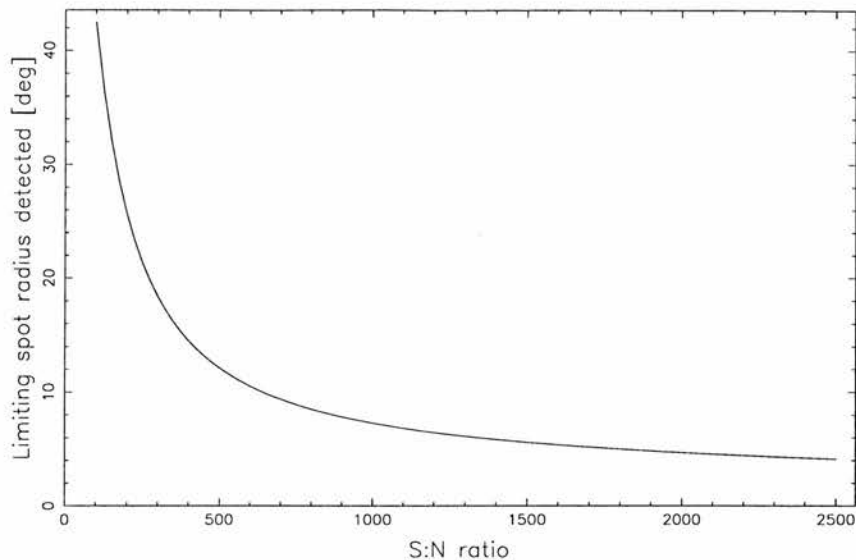


Figure 3.2: Limiting spot radius detected vs S:N ratio. The plot is shown for the situation where $v \sin i = 90 \text{ km s}^{-1}$, $x = 3 \text{ km s}^{-1}$, $y = 6 \text{ km s}^{-1}$, and $R_{line} = 0.5$.

where y is the ratio of the instrumental profile width to the stellar rotation profile width. In reality there are further limitations on the resolution of the mapping line. For a successful spot detection, the bump amplitude must exceed the required threshold level times the RMS error in the profile due for example to readout noise and photon statistics. Figure 3.2 shows the limiting spot radius detected for various S:N ratio profiles. The plot is for a star with $v \sin i = 90 \text{ km s}^{-1}$, $x = 3 \text{ km s}^{-1}$, $y = 6 \text{ km s}^{-1}$, and $R_{res} = 0.5$. Clearly once a S:N ratio of ~ 400 is achieved, further increasing the S:N ratio has less effect on the limiting spot radius detected. Comparing single line Doppler imaging techniques with least squares techniques means that higher time resolution can also be obtained. It is therefore the combination of higher S:N and time resolution which will result in higher resolution images. Microturbulence imposes a lower FWHM limit on the profile width of $\sim 0.15 \text{ \AA}$ or $\sim 8.25 \text{ km s}^{-1}$ at the centre of the photometric V-band (i.e. 5450 \AA). Because of the higher S:N ratio available while keeping the exposure times low through use of least squares deconvolution, a wider range of parameter space can be explored.

3.3 Imaging

3.3.1 The forward problem - Image to Data transformation

The forward problem involves computing a synthetic spectrum from a given surface image. The surface can effectively be treated as a grid of pixels i such that the total surface area, w of the image is given by the sum of the individual pixel areas, w_i

$$w = \sum_i^n w_i \quad (3.8)$$

A 3D representation of the star is calculated for each phase. This allows the pixels on the stellar surface which contribute to the stellar absorption profile at the phase in question to be identified. The foreshortening cosine factor, $\mu_{ik} = \cos\theta_{ik}$, gives the area by which each pixel is reduced at the k^{th} phase, where θ_{ik} is the angle between the outward normal of the centre of the i^{th} pixel, and the direction of the observer at the k^{th} phase. The velocity shift u_{ik} is calculated at the same time.

The geometric kernel, which contains the local intensity profile for each element on the stellar surface, is calculated. This is a time consuming business which renders a full line synthesis infeasible. We therefore use a lookup table (LUT) containing pre-computed specific intensity profiles of photospheric lines in slowly-rotating stars of the same spectral types as the photosphere and spot regions. The photospheric local intensity profile is generally represented by a slowly rotating “template” star of the same spectral type as the star for which we wish to derive a surface image. A “template” M dwarf is used to represent the local intensity profile at the assumed temperature of starspots. This two-temperature (Figure 3.3) LUT consists of each profile scaled at 10 limb-angles calculated for a given linear limb darkening coefficient (as given by equation 2.16). Linear interpolation of the LUT is then used to determine the intermediate local spectroscopic and photometric (if required) intensities for each pixel.

A function f_i represents the fraction of the i^{th} image pixel occupied by spots, with a fraction $1 - f_i$ containing clean photosphere. The resulting image is described by

$$\mathbf{f} = (f_1, f_2, \dots, f_n) \quad (3.9)$$

which represents a single point in the n-dimensional image space. The choice of image parameter will be discussed later.

The data can be represented as a set of line profiles observed at m_s rotation phases, with each profile consisting of l_s logarithmic wavelength increments. Similarly l_p photometric broadband fluxes may be given at m_p different rotation phases. The data vector \mathbf{F} therefore consists of $m_s l_s + m_p l_p$ elements. Each data element, f_i , has a corresponding error estimate, σ_i , computed from the observed fluxes. Synthetic fluxes computed from a model image are stored in the data vector \mathbf{D} .

By altering the value of a single image pixel, f_i , a given pixel in the synthetic vector \mathbf{D} can be made to match the corresponding data pixel. The image-data transformation resulting in the predicted data D'_{jk} in the spectral bin, j , of the line profile at the k^{th} phase, can be written (Collier Cameron, Jeffery & Unruh 1992) as

$$D'_{jk} = \sum_i w_i \mu_{ik} [(1 - f_i) I_{phot}(\Delta\lambda_{ijk}, \mu_{ik}) + f_i I_{spot}(\Delta\lambda_{ijk}, \mu_{ik})]. \quad (3.10)$$

The pixel area w_i and the foreshortening cosine, μ_{ik} have already been defined. The convolution of local intensity profiles with the rotation profile is defined at each temperature by $I_{phot}(\Delta\lambda_{ijk}, \mu_{ik})$ and $I_{spot}(\Delta\lambda_{ijk}, \mu_{ik})$ which are continuous functions of both wavelength and limb angle. $\Delta\lambda_{ijk}$ is the difference between the wavelength shift $\Delta\lambda_j$ of bin j from line centre and the wavelength shift $\Delta\lambda_{ik} = \lambda_0 \mu_{ik} / c$, of pixel i from line centre at phase, k .

In general, the transformation of an image into a series of profiles is a non-linear process, since the relationship between the value of an image pixel and its contribution to the data is a non-linear function of both *temperature* and *limb-angle*. Due to the broad nature of the absorption lines and finite S:N ratio, it is not possible to exactly determine the observed continuum flux in each spectrum, or the zero point for each lightcurve. As a result, we must renormalise the individual synthetic line profiles at each phase so their mean values (which are weighted according to the inverse variances of the observed fluxes) match those of the observed profiles at each iteration. Similarly the synthetic light curve in each photometric band must be renormalised so that its inverse variance weighted mean value matches that of the observations. This type of data renormalisation introduces a factor that is itself dependent on the computed fluxes.

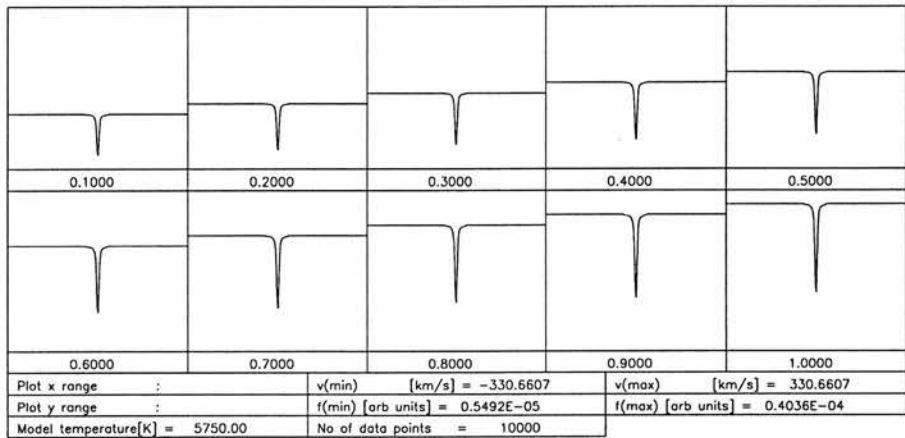
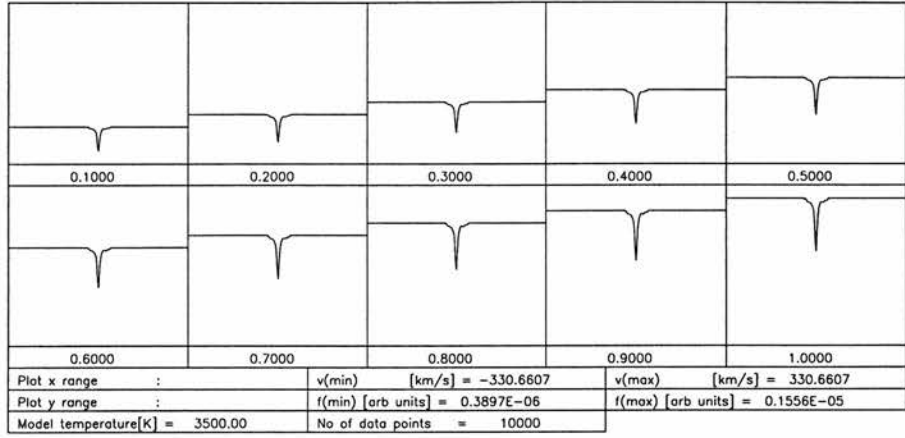


Figure 3.3: Lookup tables plotted of the local intensity profile used to represent the spot (top), and the the photosphere (bottom). The slowly rotating template star used to represent the spot local intensity profile is the least squares deconvolved profile of the spectrum of the M2V dwarf, HD 1326. Similarly, the photospheric local intensity profile is represented by the G2 dwarf, HD 42807. For each of the two temperatures, the local intensity profile is given at 10 foreshortening cosine factors, μ_{ik} , and scaled relative to the central disc intensity using a linear limb-darkening law

I give a description of the image renormalisation procedure taken from Collier Cameron, Jeffery & Unruh (1992). The weighted mean fluxes in the observed and computed line profiles at phase k are

$$C_{o,k} = \sum_j \frac{F_{jk}}{\sigma_{jk}^2} \text{ and } C_{c,k} = \sum_j \frac{D'_{jk}}{\sigma_{jk}^2}, \quad (3.11)$$

where F_{jk} is the observed flux in spectral bin j at phase k , and σ_{jk}^2 is the variance in the corresponding flux. The renormalised computed spectral data elements are therefore given by

$$D_{jk} = \frac{C_{o,k}}{C_{c,k}} D'_{jk}. \quad (3.12)$$

Similarly, the unscaled flux of the k^{th} photometric observation in the j^{th} wavelength band is given by

$$D'_{jk} = \sum_i w_i \mu_{ik} [(1 - f_i) I_{phot}(\lambda_j, \mu_{ik}) + f_i I_{spot}(\lambda_j, \mu_{ik})]. \quad (3.13)$$

Here, λ_j labels the effective wavelength band, j , with the photometric intensities, $I_{phot}(\lambda_j, \mu_{ik})$ and $I_{spot}(\lambda_j, \mu_{ik})$ being continuous functions of limb angle. Following equations 3.11, the mean weighted flux in the j^{th} observed lightcurve is given by

$$C_{o,j} = \sum_k \frac{F_{jk}}{\sigma_{jk}^2} \text{ and } C_{c,j} = \sum_k \frac{D'_{jk}}{\sigma_{jk}^2}, \quad (3.14)$$

where F_{jk} is the observed flux in band j at phase k , and σ_{jk}^2 is the variance in the corresponding flux. The renormalised computed photometric data elements are given by

$$D_{jk} = \frac{C_{o,k}}{C_{c,k}} D'_{jk}. \quad (3.15)$$

The visibility, V_{ijk} , representing the matrix marginal responses of the data elements D_{jk} to all the image values f_i are required in order to calculate the gradients of the regularising function and the discrepancy function in the multi-dimensional search algorithm used for the reconstruction. The response matrix elements are given by $V_{ijk} = (\partial D_{jk} / \partial f_i)$, and for the spectroscopic data are given by

$$V_{ijk} = \frac{1}{C_{c,k}} \left(C_{o,k} w_i \mu_{ik} [I_{spot}(\Delta \lambda_{ijk}, \mu_{ik}) - I_{phot}(\Delta \lambda_{ijk}, \mu_{ik})] - D_{jk} \frac{\partial C_{c,k}}{\partial f_i} \right), \quad (3.16)$$

with

$$\frac{\partial C_{c,k}}{\partial f_i} = w_i \sum_m \frac{\mu_{ik}}{\sigma_{mk}^2} [I_{spot}(\Delta\lambda_{imk}, \mu_{ik}) - I_{phot}(\Delta\lambda_{imk}, \mu_{ik})] \quad (3.17)$$

For the photometric data, the marginal responses are

$$V_{ijk} = \frac{1}{C_{c,j}} \left(C_{o,j} w_i \mu_{ik} [I_{spot}(\lambda_j, \mu_{ik}) - I_{phot}(\lambda_j, \mu_{ik})] - D_{jk} \frac{\partial C_{c,j}}{\partial f_i} \right), \quad (3.18)$$

with

$$\frac{\partial C_{c,j}}{\partial f_i} = w_i \sum_l \frac{\mu_{il}}{\sigma_{jl}^2} [I_{spot}(\lambda_j, \mu_{il}) - I_{phot}(\lambda_j, \mu_{il})]. \quad (3.19)$$

The synthetic data must be renormalised to match the data after each iteration, which means that the marginal dependencies are themselves functions of the current image. The visibility matrix must therefore be recalculated after each iteration.

3.4 The inverse problem

In the inverse problem, we wish to determine an image from one or more time series of spectra and a simultaneous broadband photometric lightcurve. A possible image is represented by a single point, \mathbf{f} , in a vector space, with one dimension for each pixel in the image. For the spectroscopic data, \mathbf{F} , and synthetic data \mathbf{D} the goodness of fit is measured by the statistic

$$\chi_s^2(\mathbf{f}) = \sum_{k=1}^{l_s m_s} \left(\frac{F_k - D_k}{\sigma_k} \right)^2 \quad (3.20)$$

and for photometric data by

$$\chi_p^2(\mathbf{f}) = \sum_{k=l_s m_s + 1}^{l_s m_s + l_p m_p} \left(\frac{F_k - D_k}{\sigma_k} \right)^2 \quad (3.21)$$

The possible images which then produce ‘adequate’ fits (as described in Eqns. 3.20 & 3.21 above) to the spectroscopic and photometric observations at a given level of χ_s^2 or χ_p^2 , occupy closed surfaces in image space.

For each data set, a satisfactory fit to the data requires $\chi_s^2 \leq l_s m_s$ and $\chi_p^2 \leq l_p m_p$. This then represents the closed region of possible solutions for each data set. To satisfy both fitting constraints simultaneously, the reconstructed image must lie inside the intersection of these two regions. The number of possible solutions are infinite nevertheless, so an additional constraint or regularising function is required.

3.4.1 The regularising function

Given the constraints of incomplete data, finite S:N ratio of absorption profiles and finite exposure length, we wish to determine a solution which retains all the useful information without introducing spurious noise. This is done by choosing a *regularising function* which gives the *smoothest* possible solution. The choice of regularising function however affects the final solution. A form developed by Tikhonov (1963) can be generalised as

$$r_T(f) = \int \int_{surface} |\nabla f(M)|^2 dS(M). \quad (3.22)$$

Here, $f(M)$ is the image parameter value in the stellar surface element M , of area $dS(M)$. The other regularising function commonly used is the image entropy, which can be generalised as

$$r_E(f) = \int \int_{surface} f(M) \ln(f(M)) dS(M). \quad (3.23)$$

The Tikhonov solution introduces strong correlations between the values of f at neighbouring points in the image resulting in a smoother image in the absence of strong data constraints. In contrast, the image entropy eliminates any correlations between different parts of the image which are not demanded by the data.

For a regularising function to have a unique solution on the boundary of the feasible region of image space, it must have a unique maximum value. We use the image entropy regularising function for images restricted to take on values in the range $0 < f_i < 1$. The specific form of the entropy is

$$S(\mathbf{f}) = - \sum_{i=1}^n w_i \left[f_i \ln \frac{f_i}{m} + (1 - f_i) \ln \frac{1 - f_i}{1 - m} \right] \quad (3.24)$$

where m is the default spotted fraction, and is set to a very small value. This maximises the entropy ($\mathbf{f} \ln \mathbf{f}$) of both the image \mathbf{f} of the spots and the image $1 - \mathbf{f}$ of the clean photosphere, when all the pixels in the image are set to the default level, with the implicit constraint that the spotted and unspotted area within each pixel must sum to give the pixel area.

The image entropy can only be defined for images which have the property of being additive. For example two neighbouring, non-overlapping pixels a and b contribute fluxes F_a and F_b which can simply be added to give the combined flux F_{a+b} . The bolometric

flux times the area gives the bolometric power and is also additive such that $P_{a+b} = P_a + P_b$, while the pixel temperature is an example of a non-additive image parameter (i.e. $T_{a+b} \neq T_a + T_b$).

The choice of image parameter is discussed in Collier Cameron (1992). When bolometric flux is used (instead of spot filling factor, f_i), the assumption that each image pixel can be assigned a unique temperature based upon the surface bolometric flux is made. This implies that all temperature variations on the stellar surface are fully resolved. However in practice, the data have finite S:N ratios with mapping lines of finite width, and exposure times which are limited by rotational blurring. The combined spectrum of two neighbouring pixels with different temperatures will be different from the spectrum of the same two pixels at an effective temperature corresponding to the averaged bolometric flux. Due to the large areas of blurred spot features, the model spectrum then contains specific intensity contributions from temperature components which do not have physical reality on the stellar surface (Collier Cameron 1992).

3.4.2 Image reconstruction procedure

We maximise the entropy, S , along the intersection of the constraint surfaces for the spectral and photospheric data sets by finding the extremum of the function

$$Q(\mathbf{f}) = S(\mathbf{f}) - \mu\chi_s^2(\mathbf{f}) + \nu\chi_p^2(\mathbf{f}), \quad (3.25)$$

subject to the constraints, $\chi_s^2(\mathbf{f}) = l_s m_s$ and $\chi_p^2(\mathbf{f}) = l_p m_p$. A user defined weighting factor β is supplied in order to enable a simultaneous fit to both data sets, and is given by

$$\chi_t^2 = \beta\chi_s^2 + (1 - \beta)\chi_p^2 \quad (3.26)$$

i.e.

$$Q(\mathbf{f}) = S(\mathbf{f}) - \lambda\chi_t^2(\mathbf{f}) \quad (3.27)$$

In this case, $\mu = \lambda\beta$ and $\nu = \lambda(1 - \beta)$. The value of λ , the Lagrangian multiplier is chosen so that

$$\chi_t^2(\mathbf{f}) = \beta l_s m_s + (1 - \beta) l_p m_p \quad (3.28)$$

defines the feasible subset of image space according to the two independent fitting constraints. Suggested modifications (Y.C. Unruh, private communication) were made to

DoTS in order to allow dual-site spectroscopic input (see Chapter 5). A further modification to allow for simultaneous solutions for two data sets is also defined in the same way as use of the β factor above. In this instance, the additional parameter, γ is required such that χ_s^2 is replaced by $\gamma\chi_{sa}^2 + (1 - \gamma)\chi_{sb}^2$, and hence χ_t^2 is now defined by the equation

$$\chi_t^2 = \beta(\gamma\chi_{sa}^2 + (1 - \gamma)\chi_{sb}^2) + (1 - \beta)\chi_p^2, \quad (3.29)$$

where sa and sb are the two spectroscopic data sets. Similarly, μ is replaced by $\mu a = \lambda\beta\gamma$ and $\mu b = \lambda\beta(1 - \gamma)$. Hence f_i is found by solving $\partial Q(\mathbf{f})/\partial f_i = 0$, i.e.

$$\sum_{i=1}^n w_i \left[\ln \frac{m}{1 - m} - \ln \frac{f_i}{1 - f_i} \right] = \lambda \frac{\partial^2 \chi_t}{\partial f_i^2}. \quad (3.30)$$

Our Doppler imaging code, DoTS (*Doppler Tomography of Stars*) uses MEMSYS, the routine developed by Skilling & Bryan (1984) for iterative calculation of maximum image entropy.

A number of iterations are required to converge to a solution. After each iteration, the current χ_t^2 and value χ^2 for each individual data set is given. Trial and error is required in order to choose the correct values of β and γ at which both spectroscopic and photometric data (if used) are fitted simultaneously at the desired value of χ_t^2 . Incorrect determination of β and γ , while still allowing the desired level of χ_t^2 to be reached, will result in overfitting of one data set when compared with the other(s).

3.5 Image reconstruction

Given the increased S:N ratio we can attain with least squares deconvolution, it seems appropriate to examine the robustness of the reconstructed image with respect to the stellar parameters used. Extensive tests have already been carried out by Collier Cameron & Unruh (1994) and Unruh, Collier Cameron & Cutispoto (1995) on determination and fine tuning of stellar parameters for single line data. Unruh (1996) also dealt with the effects of incorrectly determined stellar parameters. Since we now work with input profiles with enhanced temporal and wavelength resolution and higher S:N ratios, and therefore higher surface resolution, a re-examination of these procedures and analyses is presented.

3.5.1 Determination of stellar parameters

Accurate stellar parameters such as v_{rad} (stellar radial velocity), $v\sin i$ & EW can be difficult to obtain. Doppler imaging provides a means of determination to within $\sim 2\%$ of the intrinsic parameter in question. Determination of the best-fitting values for the physical parameters such as radial velocity, v_{rad} , $v\sin i$ and EW have been outlined in detail in Collier Cameron & Unruh (1994). The pseudo-entropy parameter, spot area (the degree of spot filling in the reconstructed image), is a good method for empirical determination of these parameters when the S:N ratio of data are of the order of a few hundred, minimising spurious features due to noise. We will show through tests on synthetic data that spot area minimisation tends to overestimate the known $v\sin i$. This gives a more ‘V’ shaped fit to the data, under-fitting low-latitude features, and overestimating polar features. In practice the effects on Max-Ent reconstructions are small (demonstrating the robust nature of the Max-Ent process for small variations in the stellar parameters), provided the image is relatively well constrained by the data. After obtaining initial estimates of v_{rad} , $v\sin i$ and EW, we hold two parameters constant and vary the third over a range of values. A large number of Max-Ent iterations are performed in order to force χ^2 to the lowest attainable value.

Using the synthetic data generated from the image shown in Figure 3.4 with $v_{rad} = 0$ km s⁻¹, $v\sin i = 90$ km s⁻¹, $i = 60^\circ$, and S:N ratio = 2000, parameter determination using spot area minimisation and χ^2 minimisation (numerical χ^2 values are for reduced χ^2 unless otherwise stated) are compared. Figure 3.5 reveals that in this case, $v\sin i$ is overestimated by ~ 0.75 km s⁻¹, while the correct EW appears to be recovered, when using the spot area minimisation method. In fact the EW is also overestimated by some amount less than the test grid increment, since the parabola for an EW overestimated by 2.5 per cent has a similar minimum to the parabola with the correct EW. The degree of systematic mis-determination varies from one data set to the next, and as Figure 3.5 shows, there is little difference in the global minimum and the minimum spot area for an EW overestimated by 2.5 per cent for which $v\sin i$ is overestimated by 1.5 km s⁻¹. In both cases (i.e. spot area minimisation and χ^2 minimisation), EW and $v\sin i$ are clearly correlated, since a minimum $v\sin i$ can be found for any EW value provided the parameters are not too discrepant from the actual values. The reconstructed images are shown in Figure 3.6, for the pairs of EW and $v\sin i$ shown in Table 3.1.

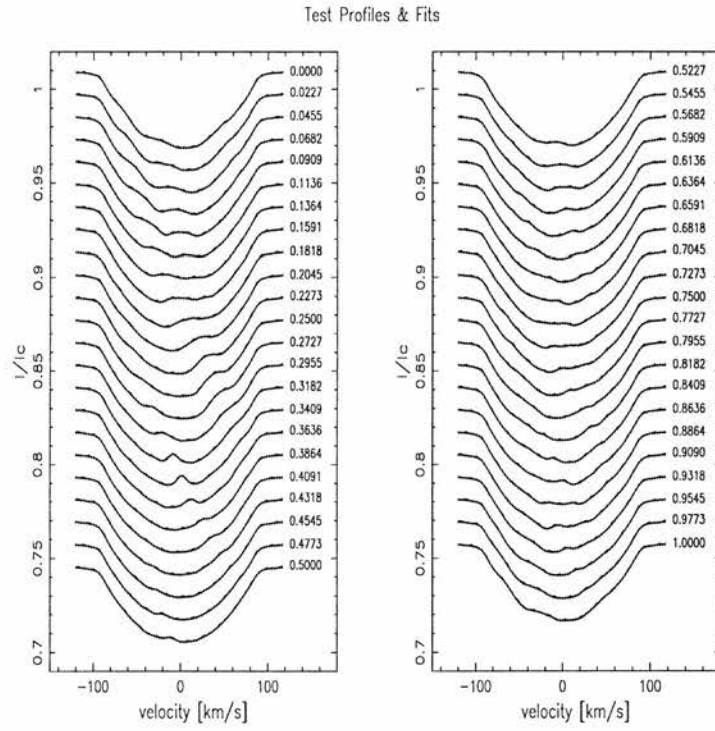
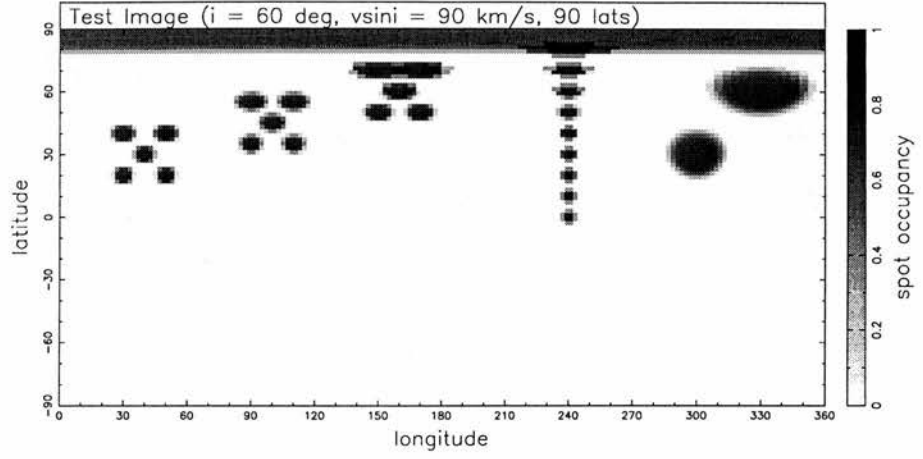


Figure 3.4: Test image and synthetic profiles. $v_{rad} = 0 \text{ km s}^{-1}$, $vsini = 90 \text{ km s}^{-1}$, $i = 60^\circ$, photospheric limb-darkening coefficient = 0.7. The S:N ratio in the profiles is 2000.

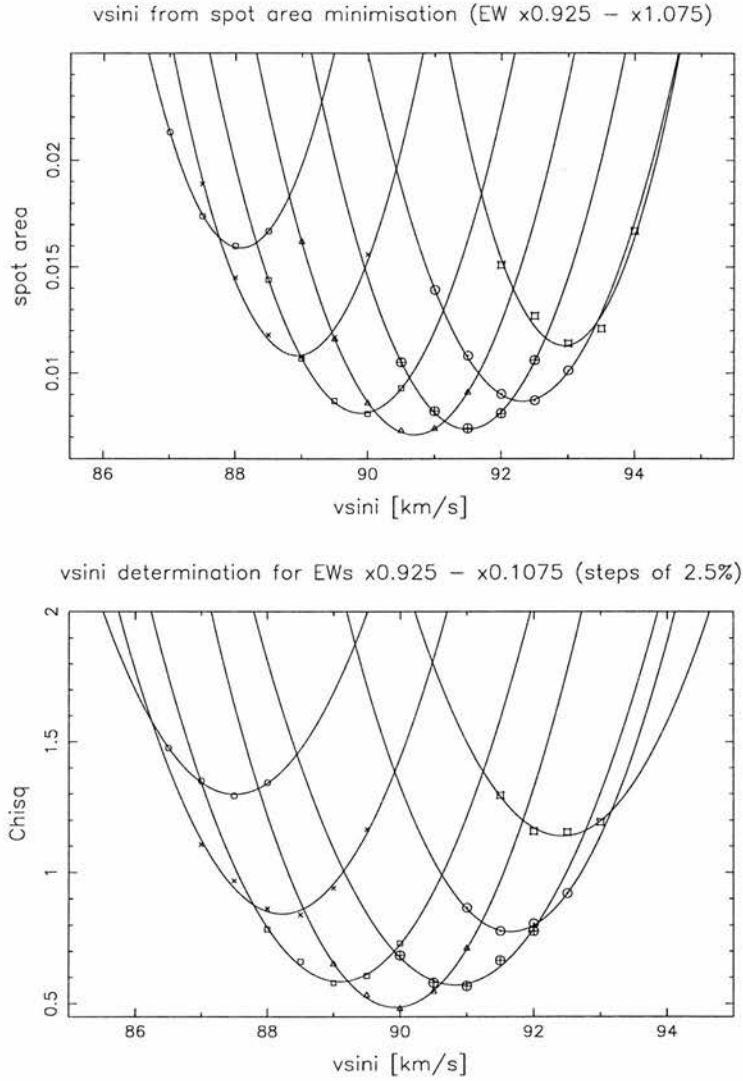


Figure 3.5: Minimisation for EWs varying from 0.925 times the correct EW to 1.075 times the correct EW in steps of 0.025. Top: Spot area minimisation, Bottom: χ^2 minimisation (Note: Reduced χ^2 is plotted). For each EW, a least squares parabolic fit through the tested $v\sin i$ values is made. The global minimum is given by the lowest attainable spot area for the correct EW (EW x 1.025 also shows a similar minimum, indicating EW is probably overestimated at a greater sampling resolution than the 2.5 per cent steps used here) and a $v\sin i$ of 90.5 km s⁻¹. The global minimum is given by the lowest attainable χ^2 for the *correct* model EW and $v\sin i$.

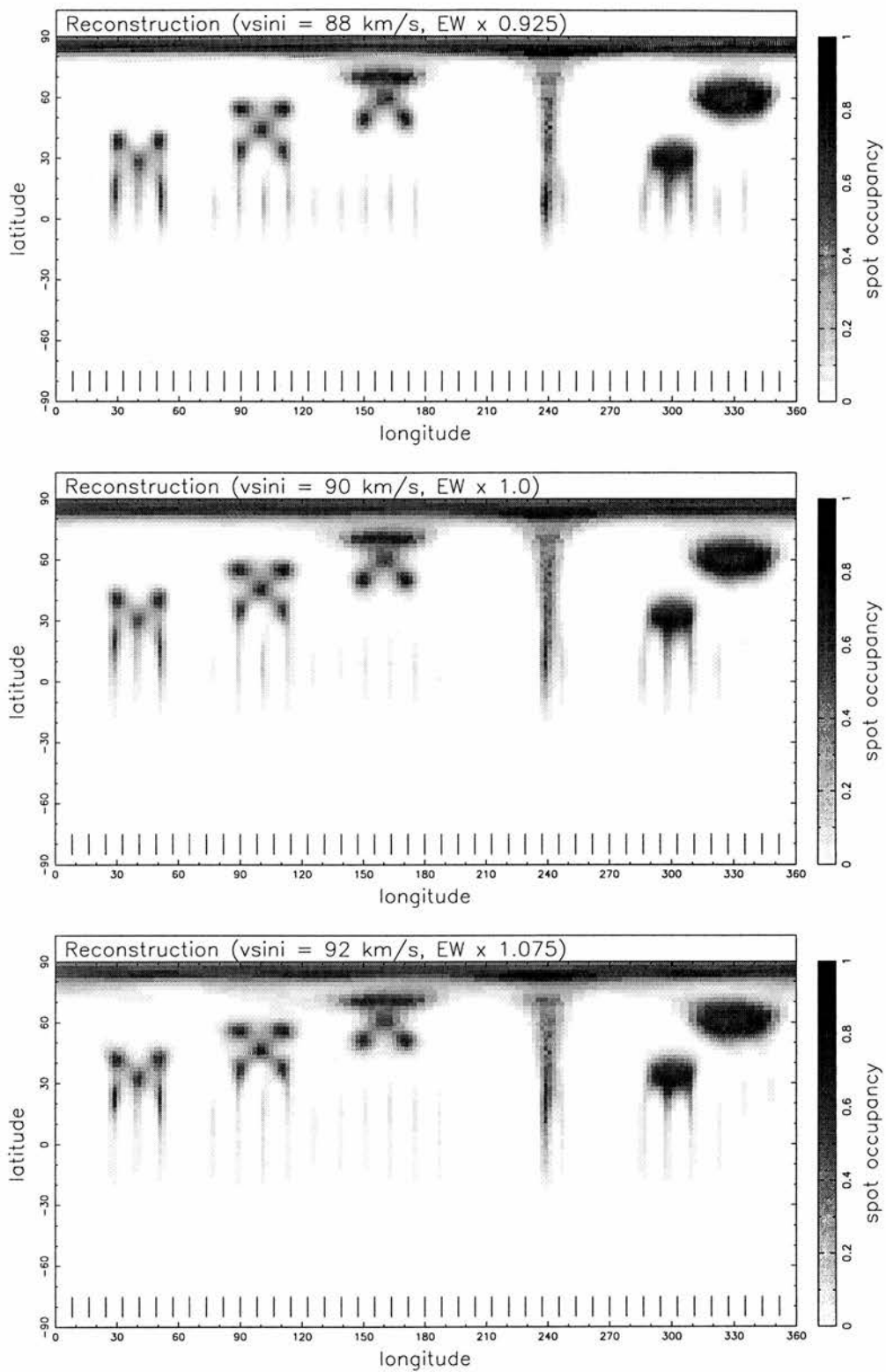


Figure 3.6: Image Reconstructions. Top: $v \sin i = 88 \text{ km s}^{-1}$, EW x 0.925 (Fit $\chi^2 = 1.23$); Middle: $v \sin i = 90 \text{ km s}^{-1}$, EW x 1.0 (Fit $\chi^2 = 0.48$); Bottom: $v \sin i = 92 \text{ km s}^{-1}$, EW x 1.075 (Fit $\chi^2 = 1.16$)

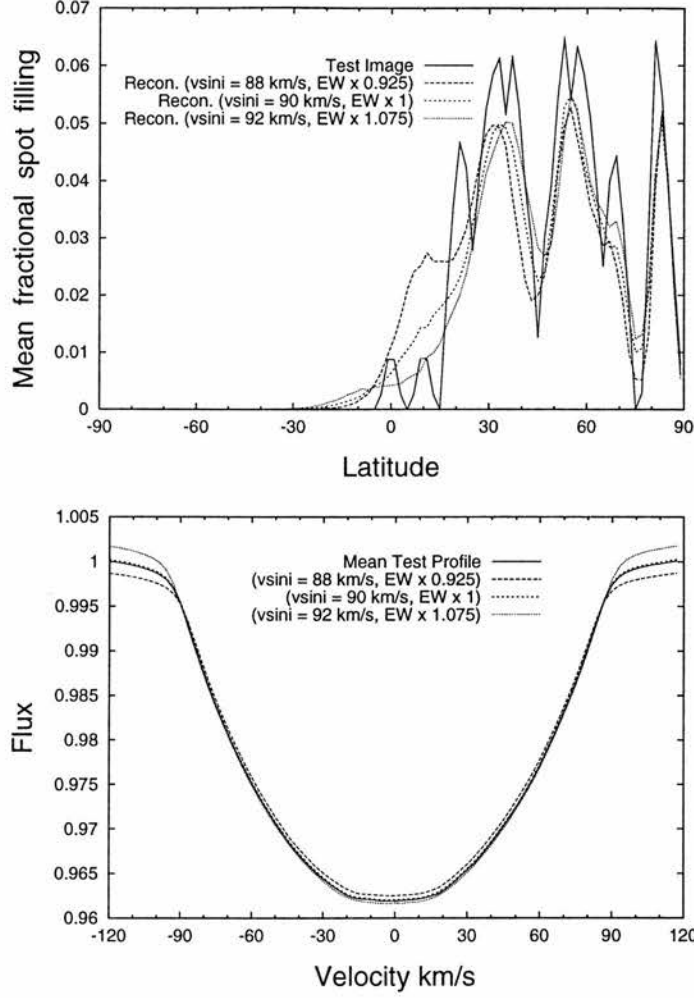


Figure 3.7: Top: Collapsed longitude plot showing mean latitude position of features. Bottom: Mean profile shape (Test image) and mean fits in reconstructions. As can be seen underestimation of $v\sin i$ and EW means that the line centre region can be reasonably well fitted. The same goes for overestimation of $v\sin i$ and EW. Since we apply a mask to the line which excludes the wings of the profile, the relative difference in the fits (which are re-normalised to the data after each iteration) has only a small effect on the final image.

Table 3.1: EW and $v\sin i$ for reconstructed images in Figure 3.5.

$v\sin i$	EW
km s ⁻¹	
88	0.925
90	1.000
92	1.075

To the eye, the images in Figure 3.6 are almost indistinguishable, and in all cases show significant latitudinal blurring of the low latitude features. Low latitude features in all reconstructed data sets are blurred in latitude due to uncertainties in their correct position because they travel through the line profile at a quicker rate when compared with spot features situated at higher latitudes. A spot feature at latitudes above the inclination angle will always be visible, allowing better determination of its latitudinal position. The effect is also worsened by the fact that a larger entropy penalty is introduced when placing features near the equator, as the pixel area weighting values w_i (equation 3.24) are larger in this region.

What is striking about the three image reconstructions in Figure 3.6 is not so much their differences as their similarities. Underestimation of $v\sin i$ by 2 km s^{-1} results in lower latitude features appearing closer to the equator through the effect of rotational blurring, with this effect increasing with decreasing latitude (Figure 3.7). The instantaneous gradient, $\Omega^2 \varpi \sin i$, of a spot passing through a profile determines the distance of the spot from the rotation axis, irrespective of $v\sin i$. If $v\sin i$ is underestimated, then $\Omega \varpi \sin i / v\sin i$ will be overestimated and the spot in question will be placed at too low a latitude. Overestimation of $v\sin i$ by 2 km s^{-1} results in the opposite effect, tending to push low latitude features to higher latitude in the image reconstruction. The effect is not large, although may be crucial if for example longitudinal cross-correlation of constant latitude strips is being carried out in an attempt to measure differential rotation. A systematic error would be introduced as a result.

Incorrect limb-darkening will also introduce a systematic shift of features in image reconstructions. Figure 3.8 shows however that a mis-determination of ± 10 per cent of the limb-darkening at the correct EW gives only a 0.5 km s^{-1} mis-determination of the $v\sin i$. Underestimation of limb-darkening produces a more V-shaped profile which will result in under-representation of features in the profile wings. This leads to fewer features near the equator. The opposite applies for over-estimation of limb-darkening coefficient.

Figure 3.8 (middle) shows that determination of $v\sin i$ is not significantly affected by incorrect inclination determination. The plot in Figure 3.8 (bottom) shows that inclination can be correctly determined using the χ^2 minimisation technique, even if the continuum intensity ratio of the photospheric local intensity profile to that of the spot local intensity profile is incorrectly estimated. Overestimation by a factor of two leads to a slightly

higher inclination determination however. Care must be taken that the intensity ratios of the photospheric and spot mapping lines are not underestimated. Underestimation of this ratio (determined from ATLAS9, Kurucz 1993) can result in insufficient EW difference between a fully spotted star and a star with no spots at all. This means that the correct contrast of spots and photosphere appearing in the time series cannot be accounted for by the image reconstruction process, resulting in underfitted profiles, and reconstructed spot features which are too weak.

3.5.2 Inclination determination

The χ^2 minimisation used to determine stellar parameters can also be applied to inclination. For the synthetic image shown in Figure 3.4, synthetic data sets were computed for inclination values of $i = 30^\circ, 45^\circ, 60^\circ, 75^\circ$ & 90° . The same values of $v_{rad} = 0 \text{ km s}^{-1}$, $v \sin i = 90 \text{ km s}^{-1}$, were used (as in previous tests) to create the synthetic data sets. These values were held fixed while the minimum attainable χ^2 was determined for a range of axial inclinations, i . The results of χ^2 minimisation performed on each data set, are presented in Figure 3.9. While the data recovers the correct model inclination at low to intermediate axial inclinations, there exists a bias towards low inclination values for $i \geq 60^\circ$. For higher inclinations, it is found that the correct inclination is given by the point where the gradient increases most rapidly above the minimum point in the χ^2 vs axial inclination plot. In the case where $i = 90^\circ$, the curve remains relatively flat, and it is difficult to determine the correct inclination, since the maximum gradient change occurs at $i \sim 75^\circ$. Different spot patterns give slightly different shaped curves, which are often better defined than the examples given here. The trend shown in Figure 3.9 however, is always repeated, in that the uncertainty in inclination value increases toward higher axial inclinations. Consideration of both the overall morphology of the minimised χ^2 vs axial inclination plot, and the location of maximum gradient change should be considered simultaneously.

3.6 Conclusion

Broadly speaking, Doppler imaging is a robust procedure, even at the higher S:N ratios which result in greater detail in the reconstructed images. Systematic mis-determination

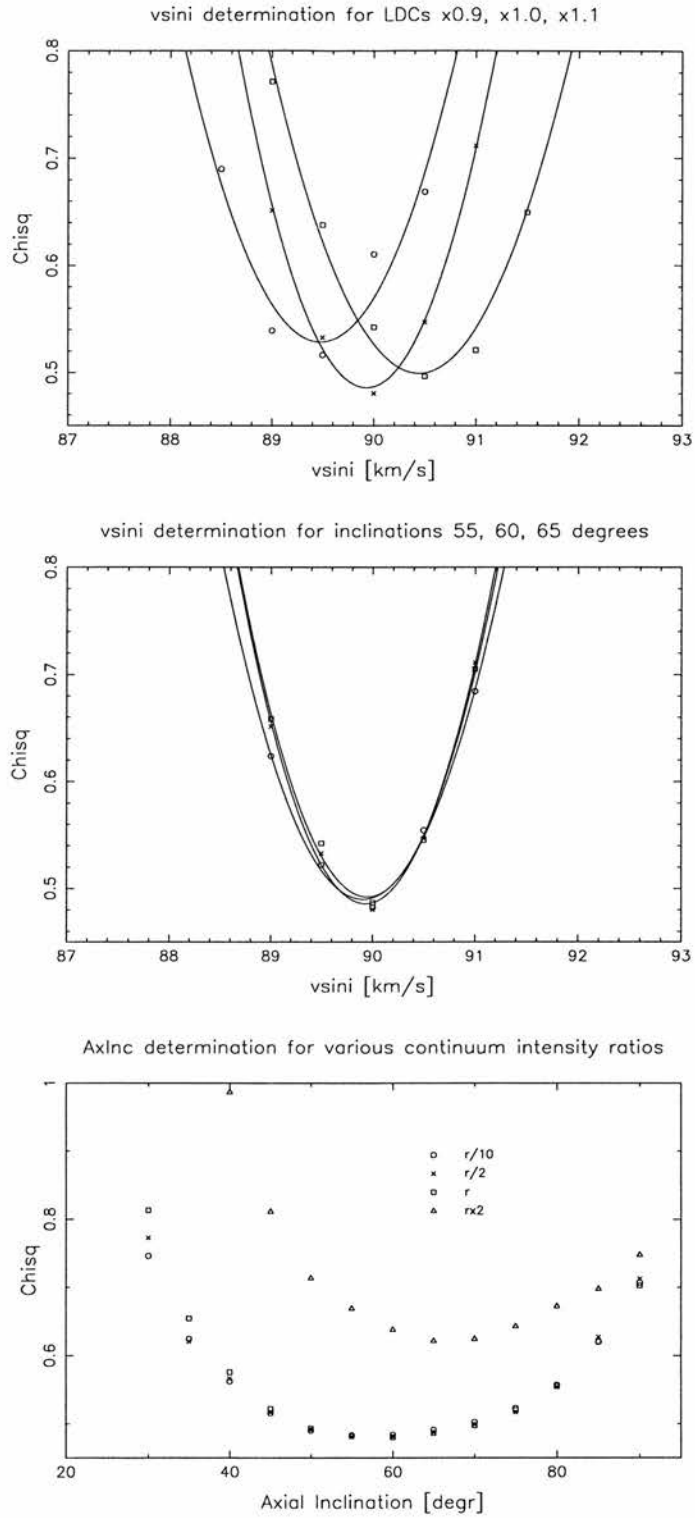


Figure 3.8: Top: The effect of incorrect limb-darkening coefficient. Middle: $v \sin i$ determined at the correct inclination of $60^\circ \pm 5^\circ$. Bottom: Determination of stellar inclination for different continuum intensity scaling values of the mapping lines (see text for details). Reduced χ^2 is plotted in all cases.

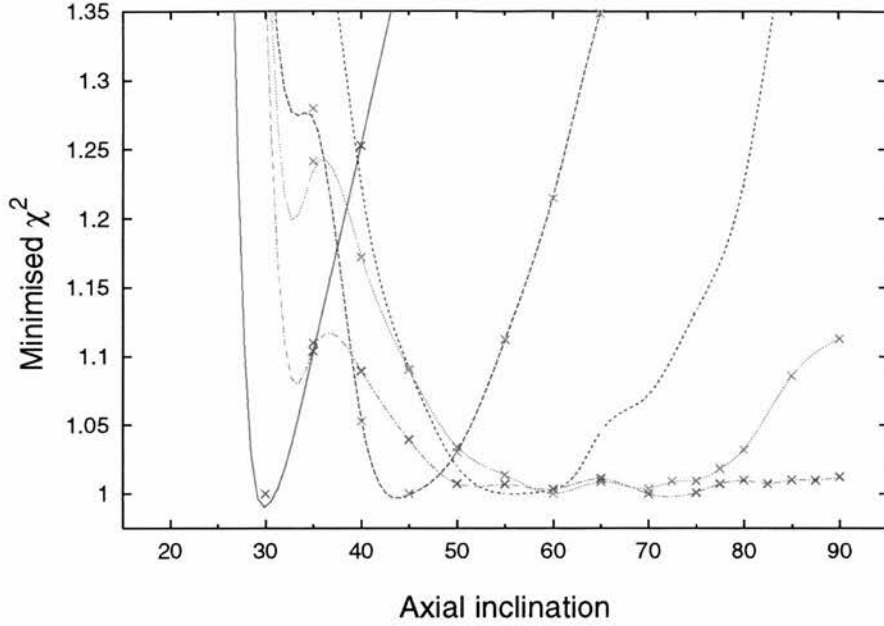


Figure 3.9: Determination of inclination for synthetic data sets (see text for details). The correct inclination is given by the point of maximum change (i.e. $\max(\partial\chi^2/\partial i)$). The spline fits are added as an aid to the eye.

of parameters (~ 2 per cent in $v\sin i$ and EW and ± 10 per cent in LDC value) is not usually crucial, and may result in an adjustment of other parameters in order to fit the data. Tests with synthetic data show that the resulting images are consistent with images reconstructed using the correct parameters. Obtaining the correct parameters may however be more crucial if a differential rotation measurement from cross-correlation of constant latitude strips between two images is required.

The reliability of images reconstructed using the high S:N ratios expected from least squares deconvolution has been demonstrated. The methods presented and tested in Chapter 2 and Chapter 3 can now confidently be applied to ‘real data’ sets.

CHAPTER 4

G dwarfs in the α Persei Cluster

Part I: Latitude distributions and lifetimes of starspots

The work in Part I of this chapter is published in Monthly Notices of the Royal Astronomical Society, “Latitude distributions and spot lifetimes on G dwarfs in the α Persei Cluster” *MNRAS* (1998) 299, 904.

4.1 Synopsis

We present a set of maximum entropy reconstructions of the starspot distribution on two rapidly rotating G dwarfs in the Alpha Persei Cluster, from spectra taken at the William Herschel Telescope on three nights in 1996 October & November. Since these stars are too faint for conventional Doppler Imaging, which makes use of only one or a few lines, we take the large number of photospheric metal lines available in an echelle spectrum, and deconvolve into a single, high S:N profile. We show that this technique results in a typical multiplex gain of 20 for a given spectrum, the equivalent of using a single line obtained on an 84 m telescope. The image reconstructions demonstrate that both these stars have cool high latitude regions or polar crowns, and low latitude features, in contradiction to the suggestion that only high latitude spots should be present. We also discuss the effects of limb-darkening after deconvolution, which should be considered before image reconstruction.

4.2 Introduction

The large number of rapidly rotating late-type stars in the α Persei cluster is discussed in detail in Chapter 1. The young open cluster of which α Persei is the brightest member lies at a distance of 180-187 pc (O'Dell, Hendry & Collier Cameron 1994). The distance given by the Hipparcos survey is 181.5 ± 22.1 pc (VizieR-service 1997). From main sequence fitting, the Pleiades cluster is found to have an age of 70 Myr (Patenaude 1978), with the α Persei having an age of 50 My, on the same scale. Being a young cluster, it exhibits many late type stars with high rotation rates, typically of the order of 0.5 d (Prosser 1991). The rotation rates can be measured since a large number of the stars show periodic photometric variations, due to the presence of surface temperature inhomogeneities, such as starspots. The colour index is known for many of these stars, and so it is possible to make an estimate of the spectral type. Collier Cameron & Woods (1992) have carried out spectroscopic observations of selected stars, finding variations in the $H\alpha$ profile attributable to prominence features, similar to those seen on AB Doradus (Collier Cameron & Robinson (1989a), Collier Cameron & Robinson (1989b), Unruh, Collier Cameron & Cutispoto (1995)).

Conventional Doppler imaging of the α Persei stars has not been possible since the stars are too faint ($m_v \sim 11.5$) to yield spectra with a high S:N ratio while at the same time keeping the exposure time low enough to reduce the effects of rotational blurring of spot features. Recently, Donati & Collier Cameron (1997) have used the method of *least squares deconvolution* (Donati et al. 1997) on polarimetric échelle spectra to produce magnetic and surface brightness reconstructions of the K0 dwarf AB Doradus. We apply our implementation of the technique, SPDECOR to make use of the large number (~ 1100 in this instance) of metal lines available in the échelle spectrum. By combining all these lines with appropriate weighting schemes using line lists generated from a full LTE spectral synthesis for a given spectral type, it is possible to find a *least squares profile*, thereby significantly increasing the effective S:N ratio of the spectrum in question. The aim of this paper is to apply this technique to two early G dwarfs (He 520 and He 699), which have already been studied (Collier Cameron & Woods 1992), and are known to exhibit fast rotation, and prominence activity.

The α Persei cluster is the *nearest* association of stars containing fast rotators (with $v \sin i \sim 90$ km s $^{-1}$) among the G dwarfs. Surface reconstructions will therefore allow

us to test theoretical predictions of spot distributions on these objects. As discussed in Chapter 1, Schüssler et al. (1996) and DeLuca, Fan & Saar (1997) have recently carried out simulations on solar type stars in an effort to predict the emergent latitude of magnetic flux tubes, after evolution from a toroidal magnetic field located at the base of the convection zone. They carried out simulations for stars of different age and equatorial rotation velocities. The results predict high latitude spots, the result of Coriolis forces in a fast rotator, acting on a rising magnetic flux tube, causing movement parallel to the rotation axis. From this it is predicted that stars such as He 699 and He 520 should exhibit flux tube emergence, and hence starspot formation only at latitudes above 30° , with a strong concentration in that region.

4.3 Observations

4.3.1 Spectroscopy

The data were obtained in two observing runs, on the nights of 1996 October 23 to 24, and 1996 November 24 to 25, with the *Utrecht Échelle Spectrograph* on the 4.2 m *William Herschel Telescope*. Of the two nights of observing in October, the first was lost due to cloud cover. The star with the shorter period, He 699, was observed on the second night in observing conditions of photometric quality, the seeing being typically $1''$. A total of 31 spectra of duration 900 s were obtained, with breaks to observe spectral standard stars. Both nights in November were clear, although the first suffered from some degradation in transparency due to light cloud throughout the night. A total of 30 spectra of He 699 were obtained on the first night, as well as two spectra of He 520. Similarly on the second night, two spectra of He 699 were taken to fill in the missing phase from the previous night in addition to 35 spectra of He 520. The seeing was generally good at typically $1.1''$ but deteriorated as the zenith distance increased toward the end of each night. Again, breaks were taken on the first night to observe standard and template stars. Tables 4.1 and 4.2 show the journal of observations for the three nights. The 1124×1124 pixel TEK2 CCD detector was centered at a wavelength of 5800 \AA , in order 98 of the $31.6 \text{ grooves mm}^{-1}$ UES grating. This allowed 43 orders to be extracted in October, and 44 orders in November (the difference is due to a slightly different setup of the spectrograph at each time of observation), giving a wavelength coverage of $4778 \text{ \AA} - 7450 \text{ \AA}$ and $4738 \text{ \AA} -$

Table 4.1: Observations of He 699 in 1996 October

Object	UT Start (Oct 24)	UT End	Exp time [s]	No. of frames	comments
HD 1326	20:14:11	20:21:41	450	1	M2V template
HD 217014	20:24:53	20:27:53	180	1	G2.5IVa template
BS 179	20:31:42	20:33:42	120	1	B3V tell H ₂ O
HD 1326	20:41:11	20:48:41	450	1	M2V template
He 699	20:52:11	21:57:30	900	4	
He 622	22:00:01	22:15:01	900	1	Phot. template
He 699	22:19:51	23:25:11	900	4	
He 699	23:44:39	00:49:23	900	4	
BS 179	00:51:00	00:53:00	120	2	B3V tell H ₂ O
He 699	01:02:24	02:40:18	900	6	
Gl 172	02:42:11	02:52:11	600	1	M0V template
He 699	02:55:42	04:00:30	900	4	
HD 42807	04:05:40	04:10:40	300	1	G2V template
He 699	04:15:32	06:43:13	900	9	

7450 Å respectively. The velocity increment per pixel at the detector is 3 km s⁻¹, with the resolution of the spectrograph being 6 km s⁻¹. The count rate was found to be a maximum in order 31 (6314 Å - 6376 Å).

4.3.2 Photometry

Light curves were secured in the V band with the 93 cm *James Gregory Telescope*¹, at St Andrews, using a Wright Instruments CCD camera mounted at the Cassagrain focus. Figure 4.1 shows the field of view, with the object and comparison stars. Observations were made between 1996 October 18 and October 31, and between 1996 November 17 and November 25. The axial rotation periods of the stars are 0.49 d and 0.61 d making it impossible to obtain full phase coverage in one cycle, and requiring prolonged monitoring close to the date of spectroscopic observations. Observations alternated between the two fields, with several 60s exposures being taken at each phase.

¹Observations made by G.A.J.H. Hussain

Table 4.2: Observations of He 520 and He 699 in 1996 November

Object	UT Start (Nov 24)	UT End	Exp time [s]	No. of frames	comments
BS 179	18:56:38	19:02:13	120	2	B3V tell H ₂ O
He 699	19:17:49	20:57:03	900	6	
BS 179	21:05:20	21:10:55	120	2	B3V tell H ₂ O
He 699	21:17:14	00:34:37	900	12	
BS 179	00:38:35	00:44:11	120	2	B3V tell H ₂ O
He 699	00:50:25	02:28:51	900	6	
He 520	02:37:55	03:10:01	900	2	
He 699	03:13:05	04:50:59	900	6	
HD 100030	06:04:57	06:09:57	300	1	G8IV template
HD 110501	06:20:34	06:25:34	300	1	K2V template
HD 42807	06:31:27	06:37:27	360	1	G2V template
Object	UT Start (Nov 25)	UT End	Exp time [s]	No. of frames frames	comments
BS 179	18:48:52	18:55:43	120	2	B3V tell H ₂ O
He 520	19:02:54	23:45:25	900	17	
Moon	23:49:25	23:49:26	1	1	
Moon	23:51:55	23:54:05	5	2	
He 520	00:00:24	04:58:37	900	18	
He 699	05:02:48	05:34:23	900	6	
HD 103095	06:44:53	06:56:58	300	2	G5V template

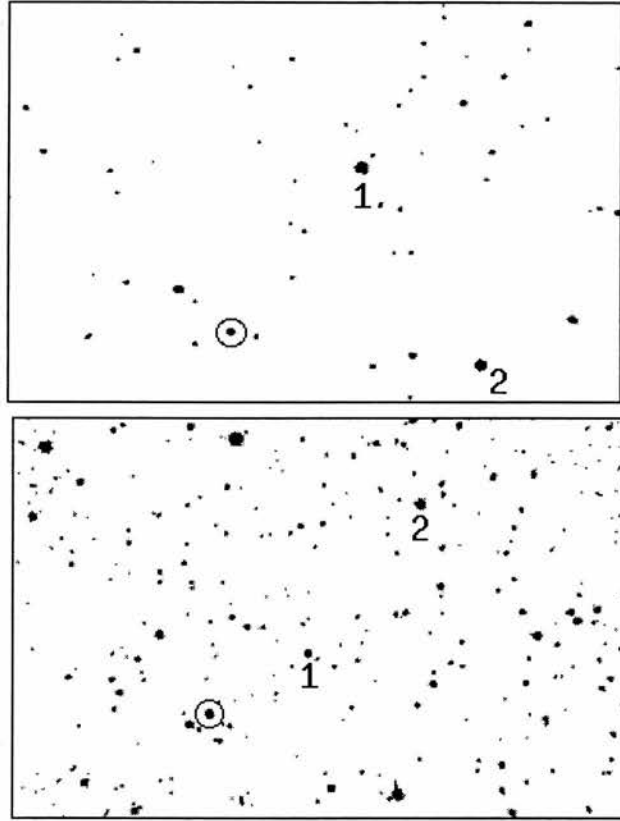


Figure 4.1: Finding charts, showing object and comparison positions for He 520 and He 699. Differential photometry with respect to the first comparison was carried out, while the second comparison acted as a check. The field size is approximately 17'x 11'.

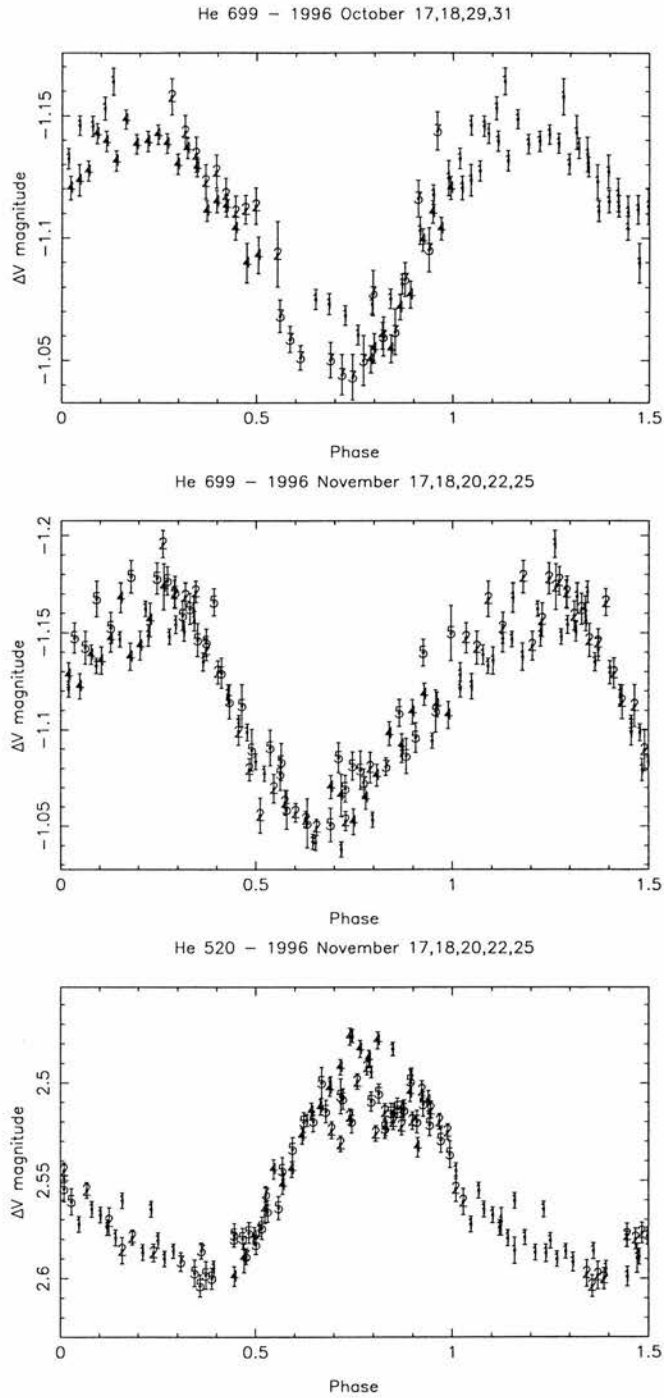


Figure 4.2: Light curves. The night of observation is numbered, and corresponds to the date given in the respective title. Note how quickly the morphology of He 520 changes, at phase 0.75.

4.4 Data reduction

4.4.1 Extraction

Photometric data reduction was carried out using JGTPHOT, a suite of dedicated software developed for use in conjunction with the James Gregory Telescope at St Andrews (Bell, Hilditch & Edwin 1993). The resulting light curves are plotted as differential magnitude values with respect to the stars marked (Figure 4.2). A re-binning of points helped reduce the scatter, thus producing light curves of sufficient quality for use as a further constraint in Doppler imaging. The monitoring allowed several incomplete light curves to be obtained over baselines of several days. This resulted in more accurate determinations of the rotation periods. The re-determined period of 0.490798 ± 0.000120 d for He 699 is approximately 1.5 times the 0.328 d period found by O’Dell & Collier Cameron (1993); and indeed a strong peak is revealed in the Lomb-Scargle periodogram at the corresponding frequency. The re-determined period of He 520 yields a value of 0.607903 ± 0.000185 d (cf. 0.603 d, Stauffer et al. 1985). Not all the data points seen in Figure 4.2 were used in reconstruction of the image; only those obtained on nights closest to those of spectroscopic observation were used. In the case of the He 699 October observations, fewer photometric data were secured simultaneously, hence observations from 18, 29 and 31 October were used with a lower weighting. For the observations in November we used photometry from 22 and 25 for He 699 and He 520 (see section 5.2).

The spectra were extracted using ECHOMOP, the échelle reduction package developed by Mills (1994). Pixel to pixel variations were removed using flat-field exposures taken with an internal tungsten reference lamp. Since the average spectrum has an average S:N ratio of $\simeq 45$, certain orders are rather faint, especially in the blue part of the spectrum. ECHOMOP had difficulty setting the object and sky limits to be extracted in batch mode, because the widths varied with the seeing, and the positions of the orders were found to shift slightly throughout the night, (by $\sim \frac{1}{3}$ of a pixel) due to small changes in the pointing. Each spectrum was therefore checked individually, and the object/sky pixels were set manually for groups of spectra which exhibited no significant change. The raw spectra being 900 s integrations contain many cosmic ray events, the worst of which were removed using the iterative rejection routine in ECHOMOP, with a threshold of 3.5σ . The rejection threshold was set at a relatively high value of 3.5σ , because the routine had

difficulty removing cosmic rays at a lower threshold. This was found to be the best method for removal of inter-order cosmic rays, but those crossing orders were often unsuccessfully removed. Since the presence of a cosmic ray in a spectral line is a random event, it was decided not to remove the remaining events, since they are dealt with by virtue of the deconvolution process (section 4). The Thorium-Argon arc-frames used for wavelength calibration were also extracted in a similar manner, calibrations being carried out using FIGARO. The scattered light was modeled using the “model sky” option in ECHOMOP, by calculating the mean sky value at each x-position across each order. The orders were extracted using ECHOMOP’s implementation of the extraction algorithm developed by Horne (1986). ECHOMOP propagates error information based on photon statistics and readout noise throughout the extraction process.

4.4.2 Continuum fitting

There are several methods by which a continuum fit can be made to an échelle spectrum. The shape of the continuum in the échelle orders is dominated by the blaze function. For CCDs of sizes up to 1K pixels², the continuum is generally well approximated by a carefully chosen n^{th} degree polynomial. A polynomial of low order may not follow the continuum adequately, whereas over-fitting is a problem with higher degree polynomials. Collier Cameron & Unruh (1994) found that for the K0 dwarf, AB Doradus, the best method was to take a spectrum of a slowly rotating star of similar spectral type, and make a continuum fit to it. This has the advantage that the lines, unlike those of the rotationally broadened object spectrum, have narrow profiles, so there are numerous well defined continuum windows to which the fit can be made. For least squares deconvolution, the best possible fit to all orders is required, so polynomial fits of order 7 were made to template G2V and G5V spectra following the example of Collier Cameron & Unruh (1994). The object spectra were then divided by these fits. He 520 was fitted best with a G5V continuum while He 699 gave a positive slope with the G2V template, and a negative slope with the G5V template, although the gradients in the latter case were not large. The $(B - V)_0$ colour indices of 0.69 and 0.61 for He 520 and He 699 respectively (Stauffer et al. 1985), indicate that He 520 may be of later spectral type, however with variable reddening, $E(B - V)$ across the cluster, we can only estimate the stars to be early to mid-G dwarfs. The continuum in both cases does not entirely remove tilt, and so to correct this

and any remaining small scale deviations, a further 9th order global polynomial fit to the continuum was made to the whole divided object spectrum across the entire wavelength range used (Figure 4.3).

This method was used in our original analysis of the data, and appears in Barnes et al. (1998) and the current presentation. A number of aspects of data reduction and analysis have changed during the course of further work (namely continuum normalisation, error determination and empirical parameter determination), and I present re-calculated images of He 520 and He 699 in Chapter 7. In subsequent work (presented in the following chapters), a different means of continuum fitting was adopted. The size of CCDs has increased in recent years, with most 4m class telescopes being equipped with arrays of at least 2K pixels². Current spectrograph cameras are now the limiting factor (in terms of wavelength coverage) when observing faint stars, as the size of the blaze function are such the area of a CCD more than covers the useful range. The size of the CCD chip means that significant vignetting occurs at the edges of the bluest orders. For some of the relatively faint objects studied in this work, the 2K pixels² spectra have had to be trimmed because not enough counts are obtained at the edges of chip. This problem is not made easier by the requirements of least squares deconvolution and Doppler imaging. Since we require a template (see chapter 2) of spectral type M to represent the spot local intensity profile, the number of counts may be lacking, especially in the bluer orders. To be consistent, all deconvolved spectra must be treated in the same way, which means the same wavelength range must be used for every object required in the Doppler imaging process.

For the increased wavelength coverage available in 2K pixels² CCD échellograms, the blaze dominated *sinc*-function shape of the continuum is not well approximated by a polynomial. As described in Chapter 2, a standard continuum fit is required in our implementation of the least squares process. A frame consisting of all the co-added object spectra is normalised by first fitting cubic splines to a slow rotating, narrow lined standard star of the same spectral type. This process is similar to that detailed above. The co-added object spectrum was divided by the narrow lined standard star fit, and then fitted by a quartic polynomial to remove residual mis-fits, and to normalise the spectrum, resulting in a master or standard continuum fit suitable for least squares deconvolution.

Normalisation of the object to be imaged was carried out by dividing each object spectrum by the co-added, and therefore high S:N, object master spectrum to obtain an

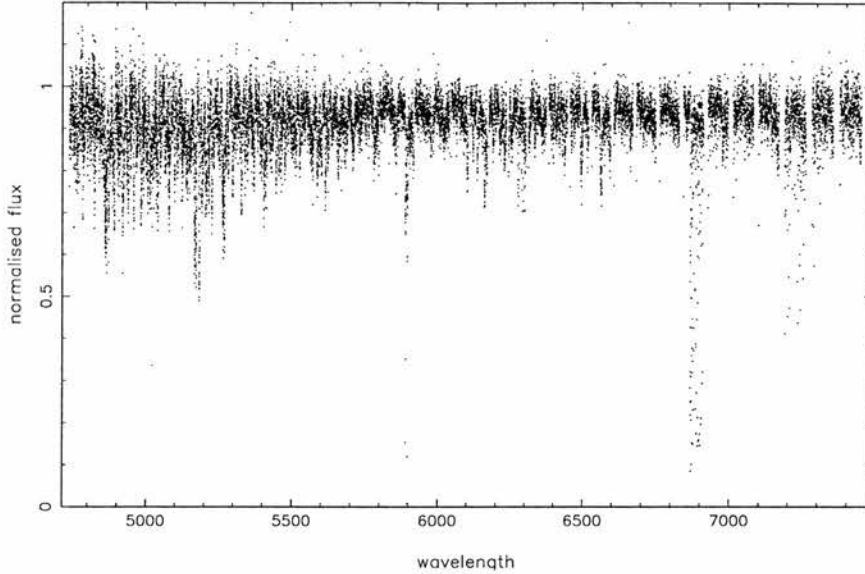


Figure 4.3: He 520: Normalised spectrum, showing the telluric H_2O lines in the red part of the spectrum.

essentially flat residual. This residual was then fitted with a quartic polynomial to remove residual mis-fits and any remaining tilt, mainly due to extinction effects throughout the night's observing as the star rises and sets. Slight changes in continuum tilt due to starspot contribution are also removed. This fit was then multiplied by the standard continuum fit to the co-added standard continuum.

The slowly rotating standards used as the local intensity profiles for Doppler imaging can generally be fitted with a spline function. The number of knots required in the spline fit varies from one data set to the next, and is best determined from trial and error.

4.5 Least squares deconvolution

Since the individual spectra have a low S:N ratio, normal image construction would be difficult given the relatively small number of spectra (between 31 and 37) per rotation cycle. Latitude resolution of features would be poor, as any profile distortions due to photospheric features are lost in noise. Given the large size of our CCD spectra; in our case the 1124×1124 chip size covers a wavelength range of $\simeq 2700 \text{ \AA}$, which means that $\simeq 1150$ lines with line depths (before the effects of non thermal broadening) > 0.4 are recorded on any one G2V spectrum. Least Squares Deconvolution is applied to the

Table 4.3: Least squares multiplex gain for each data set. The gain for each spectrum is calculated by dividing the output S:N ratio by the input S:N ratio. The scatter in the gain is small and of the order of 1 per cent. The gain given here and subsequently for other data sets is the mean of the gains calculated for each spectrum. The output S:N ratios and gains are for mean depth scaled profiles (see §2.2.1). The number of lines used in each spectrum is 995, however due to overlap of wavelength coverage between orders, 66 lines occurred twice resulting in an effective number of lines equal to 1061. This places an upper limit of $1061^{\frac{1}{2}} = 32.5$ on the gain.

Object	Input S:N	Output S:N	Gain
He 520	45.4	912	20.0
He 699 (Oct)	52.4	1032	19.7
He 520 (Nov)	50.3	983	19.5

data set. As discussed in §2.2, lines with wavelengths $> 7000 \text{ \AA}$ are not included in the deconvolution due to the large numbers of telluric lines also present.

4.5.1 Errors

At the time of publication in *MNRAS*, our implementation of the deconvolution process, *SPDECON* did not yet propagate the errors which are required by a Doppler imaging routine. The simplest way around this problem was to deconvolve the continuum on the immediate sides of each line profile, so that there is ample continuum in the least squares profile to allow an empirical measurement of the new S:N ratio. A description of this process and the results are presented as an example in Chapter 2. Table 4.3 shows the multiplex gain of the average line, for each of the three data sets presented here. A comparison of the results can be made with those of chapter 7 which show the multiplex gain determined from the least squares propagated errors.

Figure 1 of Donati et al. (1997) reveals the theoretical gain and empirical results for data sets with different numbers of lines confirming that the current data sets are photon noise limited.

4.5.2 Limb Darkening Coefficient

The centroidal wavelength (5507.54 \AA) was calculated from lines in the line-list, such that it was weighted with respect to both the line strength and the variance from the standard fit used in SPDECON. Since the limb-darkening coefficient is a fairly linear function of wavelength, we used linear interpolation to obtain a value from Kurucz (1993) LTE models. The limb-darkening coefficients are 0.6142 and 0.6015 for the spot and photospheric temperatures of $T = 3750 \text{ K}$ and $T = 5750 \text{ K}$ respectively.

4.5.3 The local specific intensity profiles

For the purposes of Doppler imaging, a spotted star is taken to consist of two temperature components (i.e. photospheric temperature, and spot temperature), and hence it is necessary to use two template spectra. These are calculated from the least squares deconvolved spectra of two template stars, an M0 dwarf (photospheric temperature, $T = 3750 \text{ K}$) for the spots, and a G2 dwarf (photospheric temperature, $T = 5750 \text{ K}$) for the photosphere. These were deconvolved in the same way as the object spectrum, using the same scaled standard continuum frame as was used on each given night, thus ensuring the correct corresponding line equivalent width. Since the deconvolved equivalent width varies slightly through the use of a different standard continuum star in the deconvolution, care must be taken to ensure that the equivalent width of the local specific intensity profiles is kept invariant. This problem arises because we do not have G2V and M0V template spectra for each night and so they must be deconvolved using the wavelength calibration file and standard continuum star from a different night. These lines were then scaled at ten different limb angles (i.e. 0.1, 0.2, ..., 1.0) for each temperature, according to the mean continuum scaled intensity value, and the relative central intensity I_0 (See chapter 2). The resulting data is stored as a lookup table for use within DOTS.

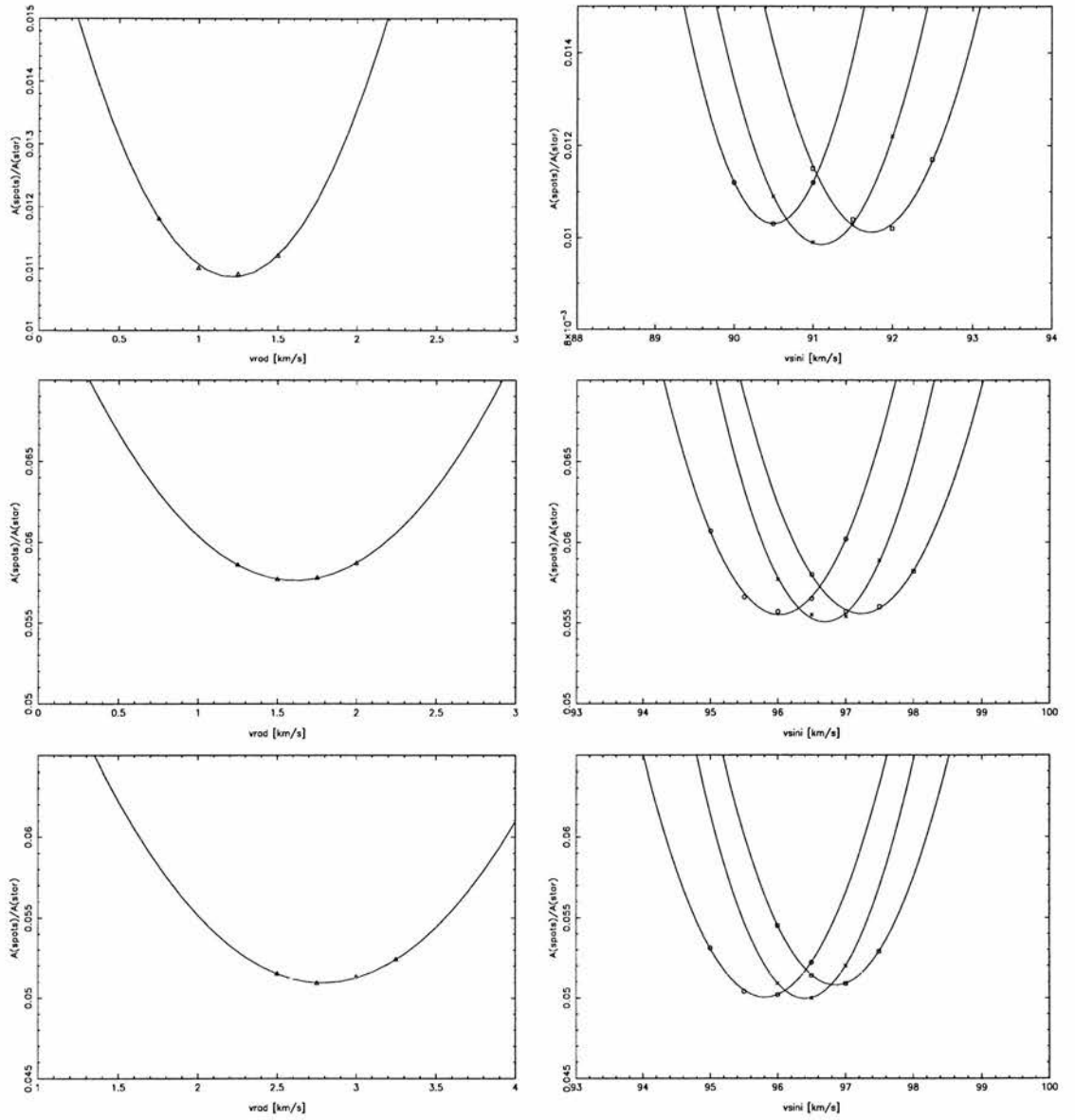


Figure 4.4: The plots on the left show the spot coverage as a function of heliocentric radial velocity; the plots on the right show the spot coverage as a function of $v \sin i$ for different equivalent widths. Top: He 520, Middle: He 699 (Oct), Bottom: He 699 (Nov). The equivalent widths plotted are $0.1280 \pm 0.0030 \text{ \AA}$ (He 520), $0.1220 \pm 0.0028 \text{ \AA}$ (He 699 Oct) and $0.1240 \pm 0.0028 \text{ \AA}$ (He 699 Nov).

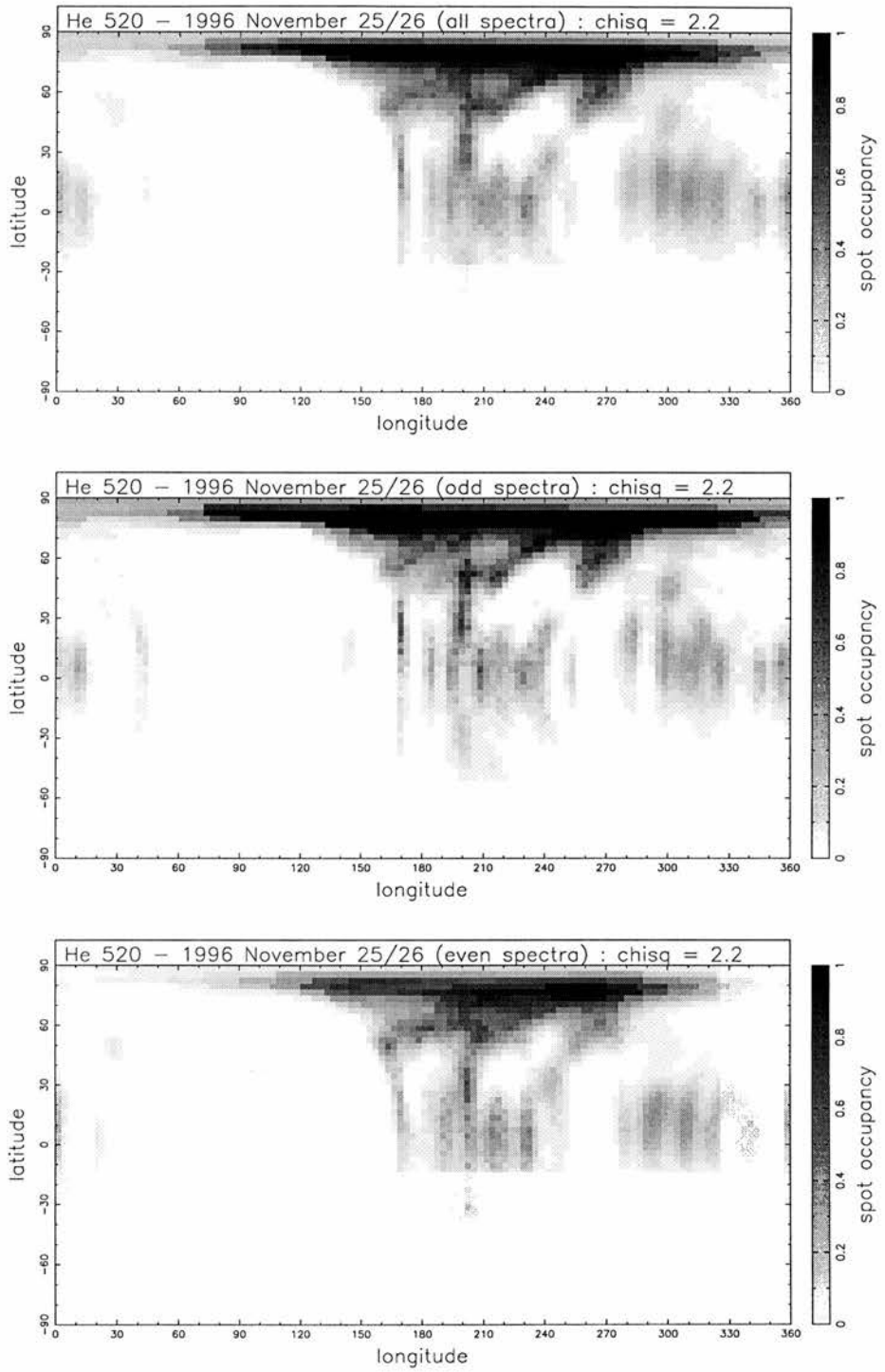


Figure 4.5: Reconstructed Images of He 520. Top: All 37 spectra, Middle: Odd numbered spectra, Bottom: Even numbered spectra

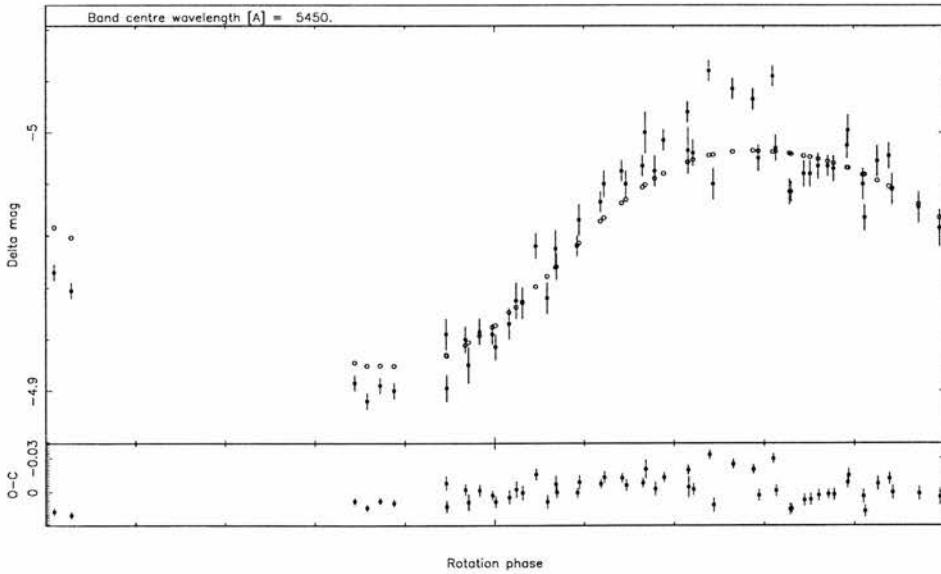
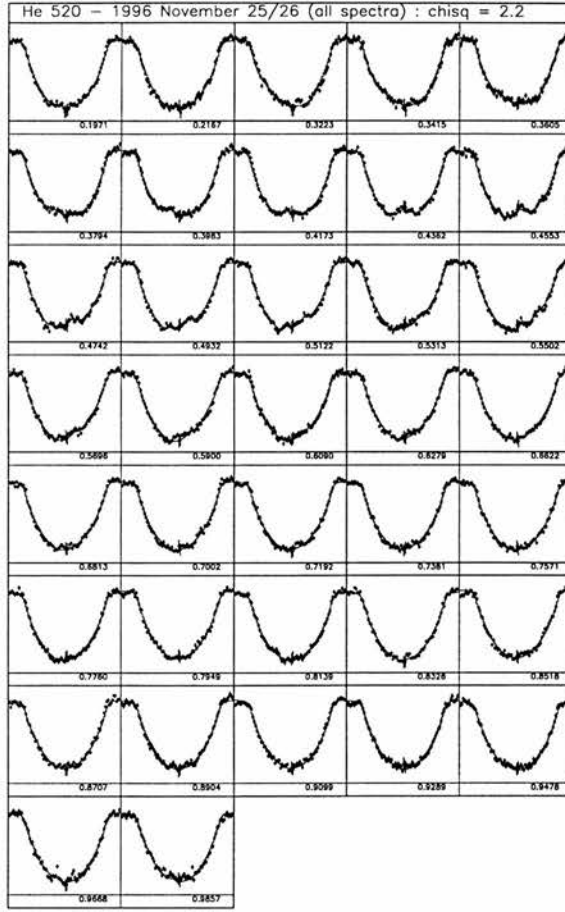


Figure 4.6: He 520 Top: Profile fits, Bottom: lightcurve fit.

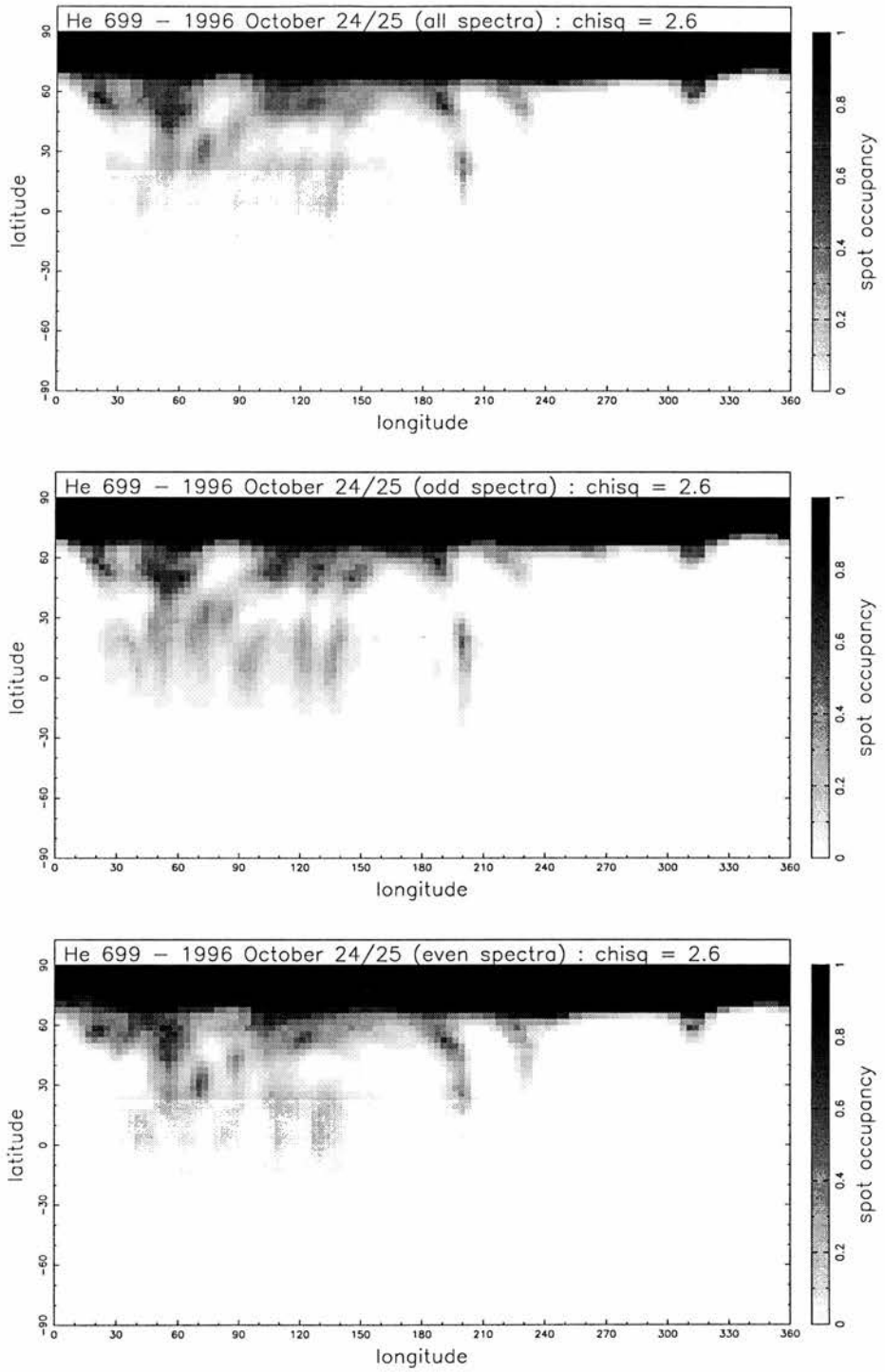


Figure 4.7: Reconstructed Images of He 699 (October). Top: All 32 spectra, Middle: Odd numbered spectra, Bottom: Even numbered spectra

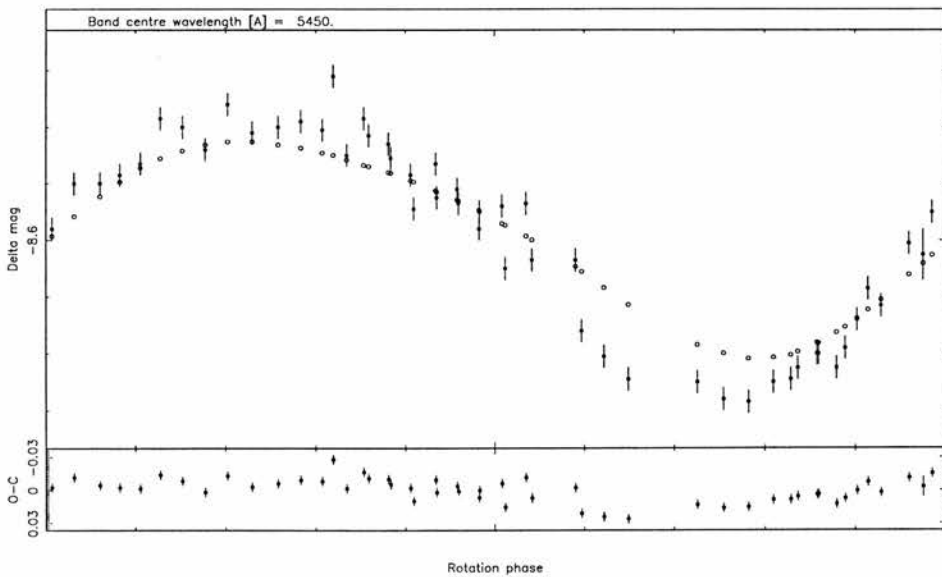
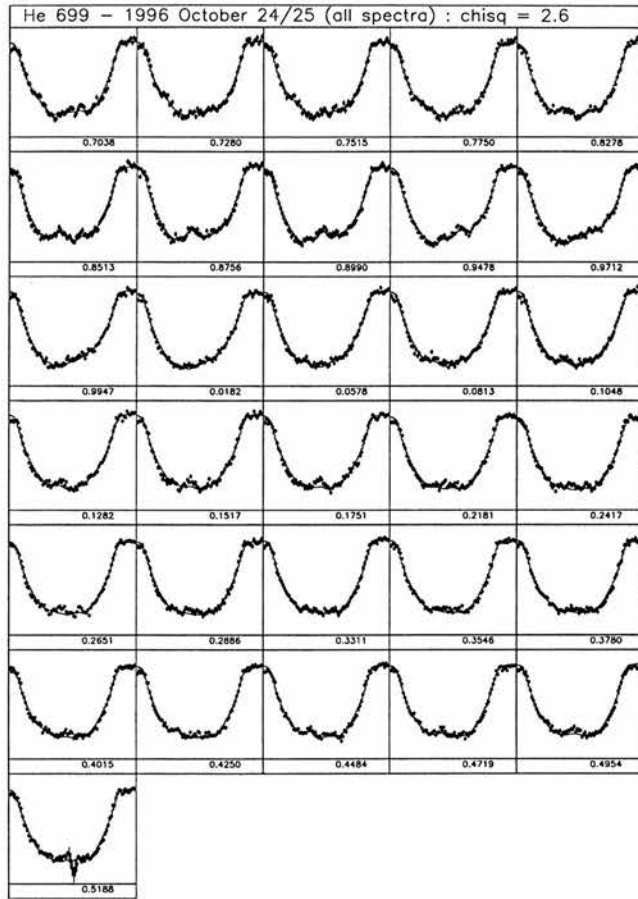


Figure 4.8: He 699 (October) Top: Profile fits, Bottom: lightcurve fit.

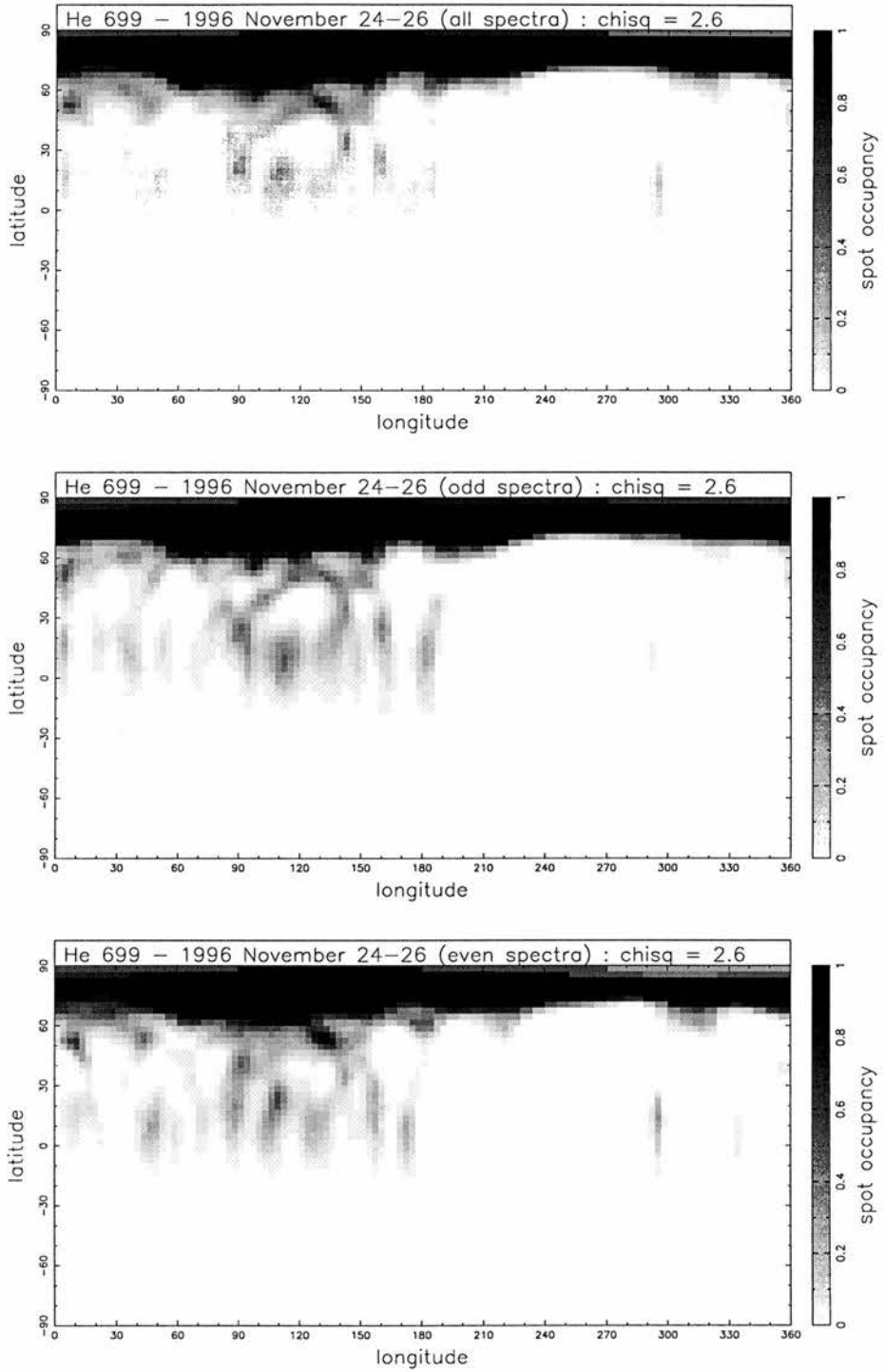


Figure 4.9: Reconstructed Images of He 699 (November), at the same phase as the October images. Top: All 31 spectra, Middle: Odd numbered spectra, Bottom: Even numbered spectra

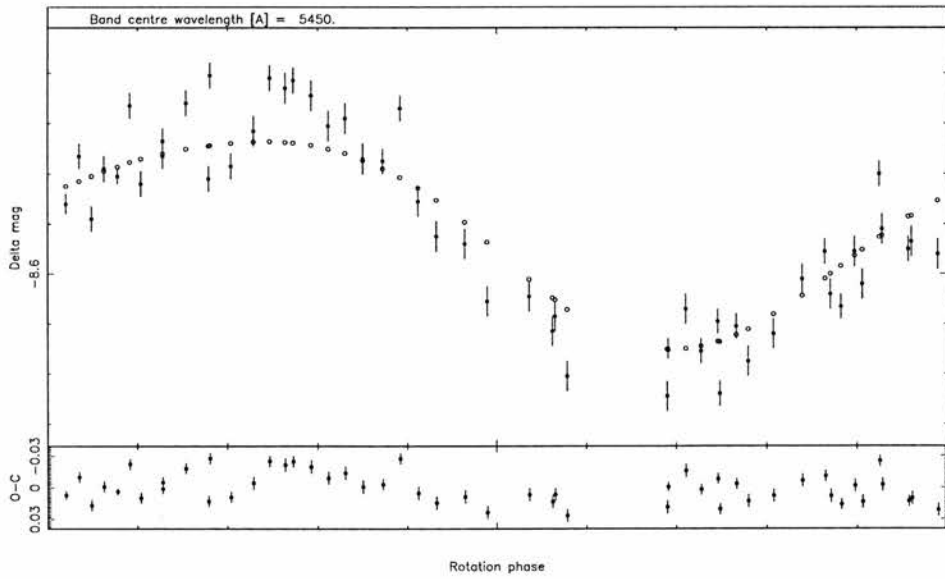
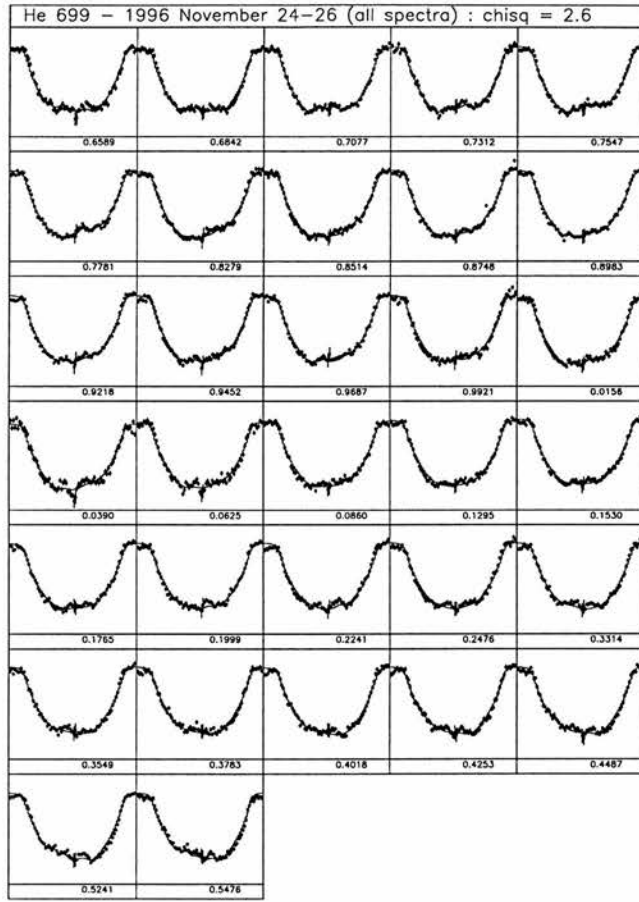


Figure 4.10: He 699 (November) Top : Profile fits, Bottom : lightcurve fit.

4.6 Image reconstruction

4.6.1 Fine tuning parameters

It is important to choose the correct stellar parameters for the final image, since spurious features are produced as a result of badly chosen values (Collier Cameron & Unruh 1994). Reconstructions were carried out for different values of equivalent width, radial velocity and $v\sin i$ for a given inclination value; in order to minimise the total spot area of the image. Using the spot area as a proxy for entropy, the image with the maximum entropy then corresponds to the one with the smallest spot area (Collier Cameron & Unruh 1994). Figure 4.4 shows plots of spot coverage as a function of geocentric radial velocity and $v\sin i$, with parabolic fits to each set of points. A solution is only possible within a narrow range of radial velocities, and is dependent upon a number of factors including the positioning of the deconvolved template spectrum about zero shift. Since this is the case, the minimum value of radial velocity corresponds to an instrumental value rather than a truly corrected value. The $v\sin i$ plots show parabolic fits for different values of equivalent width (see caption), and show He 520 to give the best fit when $v\sin i = 91 \text{ km s}^{-1}$ whereas He 699 gives a best fit with $v\sin i = 96.5 \text{ km s}^{-1}$ (October and November). These are slightly greater than values measured by Stauffer et al. (1985) as 87 km s^{-1} and 90 km s^{-1} respectively. Using χ^2 minimisation may be a more valid method of obtaining the best parameters. For He 520, identical parameters were found using this method, while He 699 resulted in $v\sin i = 95.5 \text{ km s}^{-1}$ and an equivalent width of 0.1198 \AA and 0.1112 \AA for October and November data sets respectively. The resultant image reconstructions were found not to be significantly different from those obtained using parameters determined by spot area minimisation, demonstrating that small variations in the parameter values when close to the correct values do not significantly effect the image reconstructions.

The axial inclination is the most difficult parameter to constrain since it is not possible to minimise the spot area in the same way as for $v\sin i$. Hendry, O'Dell & Collier Cameron (1993) and O'Dell, Hendry & Collier Cameron (1994) used a statistical technique for measuring the distance of the α Persei cluster through use of the Barnes-Evans relationship (Barnes, Evans & Moffett 1978), and the shape of the distribution of axial inclinations among rapid rotators. They estimated a distance of $187 \pm 11 \text{ pc}$, based upon Bayesian statistical methods, and 180 pc through main-sequence fitting of Vanden-

Table 4.4: Inclination estimates

	He 520	He 699
Period/diameter	$78^\circ \leq i \leq 90^\circ$	$57^\circ \leq i=69^\circ \leq 90^\circ$
Barnes-Evans	$70^\circ \leq i \leq 90^\circ$	$52^\circ \leq i=61^\circ \leq 75^\circ$

berg isochrones. It is possible to calculate the value of $D\sin i$ for each star since the angular diameter is known from the Barnes-Evans relation.

Table 4.4 below shows inclination values from the Barnes-Evans relation, and an estimate from

$$\sin i = \frac{P \cdot v \sin i}{2\pi R} \quad (4.1)$$

As can be seen, there is a large uncertainty in the value of $\sin i$ in each case. The range of values of $\sin i$ for He 520 extend above unity, when the uncertainties of 10% in radius and angular diameter are included. From these values, we adopted $i=65^\circ$ for He 699. He 520 gave poor images for i greater than 75° (i.e. reflection and banding of structure), and hence this value was chosen ².

4.6.2 The Images

Figures 4.5- 4.10 show maximum entropy data fits and plots of the reconstructed images. Because of the high S:N ratio and number of spectra, we tried reconstructing images using all spectra, odd-numbered spectra alone, and even-numbered spectra alone, in an attempt to test the reliability of the reconstructed features. The final images are the results of fits to both the light curve and the spectroscopic data which are also shown as a stacked greyscale phased time-series in Figure 4.11. Fits are made to a pre-defined level of reduced χ^2 . In combining the two data sets, a weighting scheme is used, and is controlled by the factor β , such that $\beta = 0$ when all weight is attributed to the photometric data, and $\beta = 1$ for a solution based solely on the spectroscopic observations, and is also dependent upon the uncertainties in the data (Unruh, Collier Cameron & Cutispoto 1995). For He 520, data are used from 1996 November 18, 20 and 25. As can be seen, from Figures 2 and 10, there is considerable change in the morphology of the lightcurve over just a few days. A solution which converged to a χ^2 simultaneously for both sets of data was

²Important: The technique of minimisation of χ^2 was not yet adopted. Inclination determination using minimised spot area is not possible. See Chapter 4, Part II, for subsequent inclination determinations and comparisons.

then found to occur when $\beta = 0.965$ for $\chi^2 = 1.3$. The spectroscopic data contribute the strongest constraints on latitude features, whereas the photometric data yield information only about features at relatively low latitudes (Unruh, Collier Cameron & Cutispoto 1995). It is found that the inclusion of photometric data in the case of He 520 indeed serves to emphasize those spot areas at low latitude when compared to the spectroscopic solution ($\beta = 1$). In the case of He 699, the spectroscopic data were given weights of $\beta = 0.975$ and $\beta = 0.98$, for the October and November data sets respectively, and solutions found for $\chi^2 = 1.6$ in both cases. Solutions with $\chi^2 = 1.1$ for He 520, and $\chi^2 = 1.5$ for He 699 (October and November) were obtained by using the spectroscopic data alone. (Note: The errors given in Barnes et al. (1998) were not corrected to those for a line of unit depth, and hence the higher χ^2 values given. Given that convergence to a solution was obtained using the TEST statistic, the level of fit at an apparent high value of χ^2 is correct). The higher χ^2 statistic for the He 699 data sets when compared with the He 520 data set is probably due to the lower weighting and subsequent fit of the photometric data.

4.7 Discussion

Figure 4.12 shows the total spot occupation of a given latitude as a function of latitude, demonstrating the main regions of spot coverage. The low latitude band on He 520 is centred at $+10^\circ \pm 20^\circ$ with a decrease in spot coverage at mid-latitudes. On He 699, there is a definite low latitude region centred at $+15^\circ \pm 20^\circ$, the structure also appears to extend to higher latitudes, the spot coverage decreasing at mid-latitudes to a lesser extent than on He 520. Both stars appear to exhibit either a polar crown or high latitude spot. It will be noted that only in the October image of He 699 does the high latitude region truly stretch over the pole. The second set of images of He 699 however has a lower spot filling factor along part of the highest latitude band, near the pole. A probable reason for this is that in November, the high cirrus cloud reflected light from the bright moon, and the spectra suffered from contamination of a solar spectrum (apparent absorption) in the line core as a result. In an attempt to minimise this effect, the two central pixels of all profiles in November were given larger error bars, and hence a lower weighting in the subsequent imaging fits. Since the two central pixels are crucial in the immediate polar region of the reconstructed image, it would seem that this effect has not been completely removed by the inclusion of large error bars. Looking carefully at the profiles for the November He 699

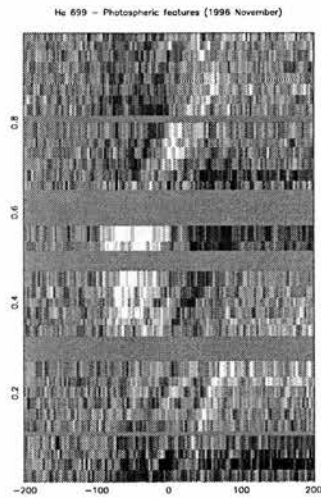
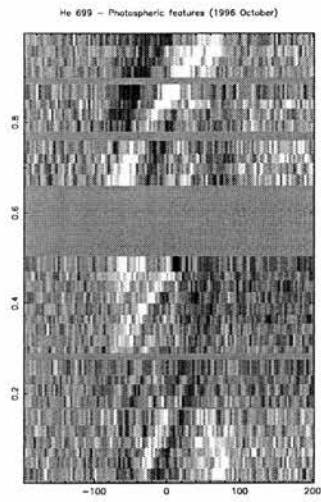
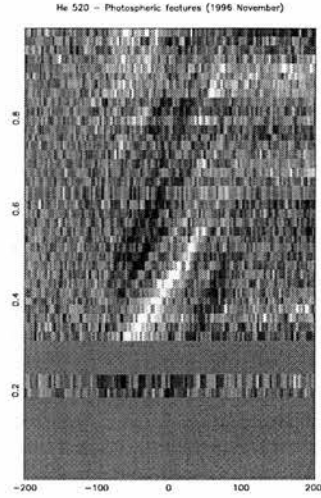


Figure 4.11: Time series spectra of He 520 and He 699 (phase vs velocity). Mean profile subtracted, deconvolved spectra (i.e. spot features appear white).

data reveals a slight distortion in some of the fits. He 520 poses a slightly different case, in that the main feature is located at high latitude rather than at the pole. This is confirmed by looking at the profiles for this star. The distortions corresponding to this feature take $\sim \frac{1}{3}$ of a rotation to cross the profile, and are centred at approximately phase 0.4173 where the profile can be seen to be relatively more flat-bottomed. Once again, distortions can be seen in some of the fits (e.g. phase 0.3794) due to moonlight, so that while the spot filling factor may be reduced at some longitudes in the highest latitude band, the spot feature itself is almost certainly not a polar cap.

The high S:N ratio available in these spectra affords the opportunity to test the reality of the reconstructed image. We carried out image reconstructions on odd numbered spectra and even numbered spectra individually from each set of spectra, the equivalent of having two sets of independent but simultaneous data. As can be seen in the middle and lower images for each star, the spot structure is accurately reproduced. The images are not exactly identical, but taking into consideration the reduced number of spectra in each reconstruction (between 15 and 18), and the different S:N ratios in each individual spectrum, the similarities of the images give an independent check on the reality of features.

It is quite clear from the reconstructed images of both stars that the spotted regions are *not* confined to high latitudes only. It is immediately apparent that the present Doppler maps tell a different story, and both stars appear to have equatorial or near equatorial bands, with a slight depletion of spot coverage at latitude ~ 40 .

Hatzes et al. (1996) have recently carried out an investigation into the manifestations of polar spots, as seen in many RS CVn stars, at different axial inclinations. They carried out a number of simulations in an attempt to reproduce the flat bottomed profile shape seen in such stars. The spectral line plots (Figures 4.6, 4.8 and 4.10) clearly demonstrate the flat-bottomed profile on the lower inclination He 699. Hatzes et al. attempted to reproduce this shape through the effects of gravity darkening, which is corrected for by our code, differential rotation and temperature dependence on the spectral line. They found that the flattening of line cores in spotted stars cannot be entirely attributed to these effects. The effect of a bright equatorial facular band does produce flattened line cores, but its effect with respect to inclination was found not to be as great as for a polar spot. Of these four effects, it is hardest to make a comparison with the effect of temperature on line strength since the deconvolved profile is a combination of ~ 1000 lines

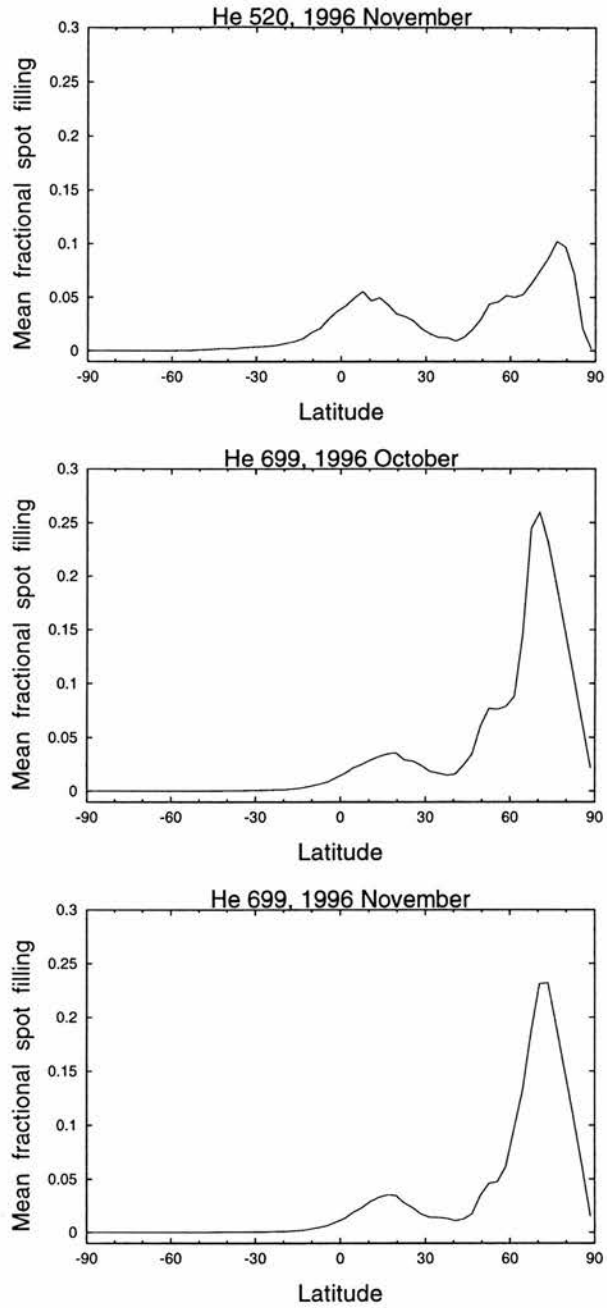


Figure 4.12: Spot coverage (as a percentage of immaculate surface at the given latitude) as a function of latitude. The plots have been corrected for the mercator projection by multiplying the average spot filling at a given latitude by the *cosine* of the latitude. There is slight bias to underfilling at the poles due to the large error bars places on the central pixels of the He 699 profiles. Top: He 520, Middle: He 699 October, Bottom: He 699 November.

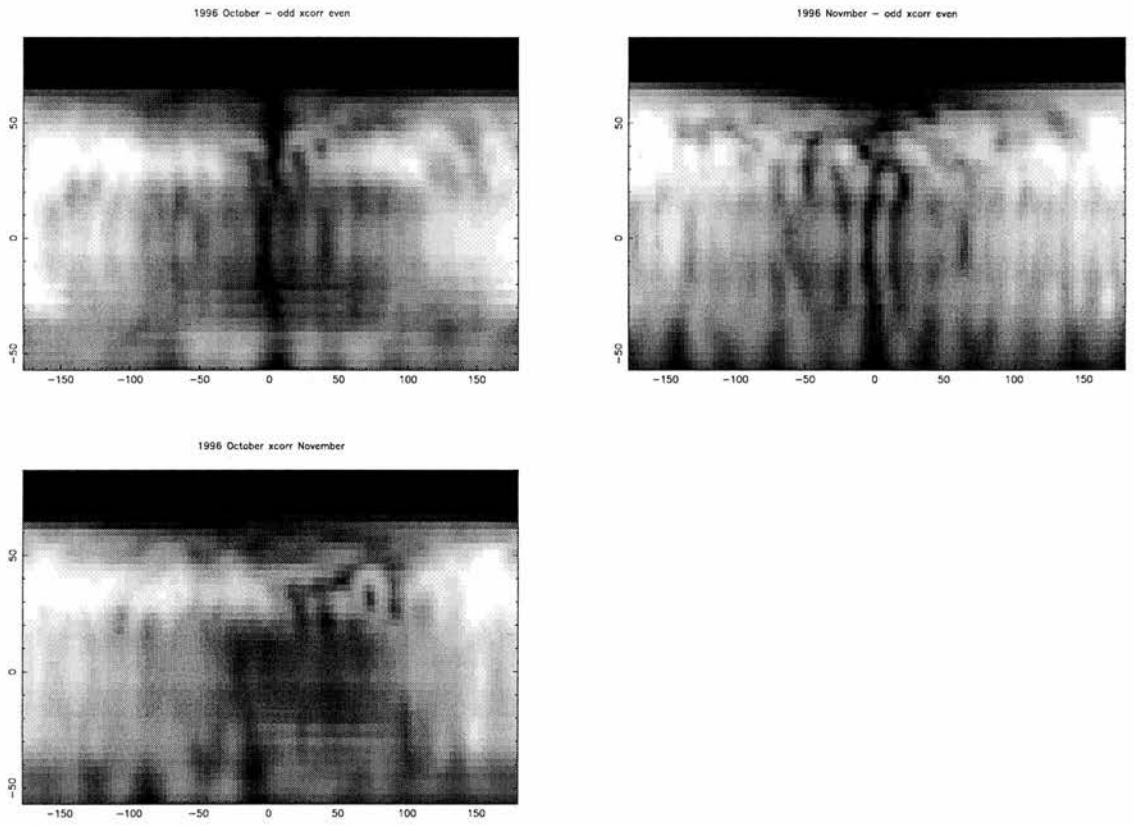


Figure 4.13: Images (latitude vs longitude shift) obtained by cross-correlating each latitude band between odd and even spectra image reconstructions in October (top) and November (middle). Cross-correlation images of reconstructions from full sets of spectra in October and November (bottom). The maximum value of the auto-correlation function (at each latitude band) from the six individual images was used to obtain an appropriate grey-scale for each of the above maps.

with different excitation potentials over a wavelength range of $\sim 2000 \text{ \AA}$. As a result, any distortion due to a surface temperature variation will not be present at the same relative amplitude in every line considered. Future investigations into this effect with respect to the lines used will be limited for stars of this magnitude, due to the large number of lines needed to obtain a sufficient S:N ratio for Doppler imaging. It will therefore be useful to carry out such tests on brighter stars where the S:N ratio is greater. Collier Cameron & Unruh (1994) for example noted the different strength of profile features in lines of different excitation potential. They found that the higher excitation potential Fe I 6663 line has a more flat-bottomed shape than the Ca I 6439 line. In this respect modelling individual lines may have some advantages over using Least Squares Deconvolution, although the combined S:N ratio may not be as great. In Chapter 5, subsets of data covering different wavelength ranges are deconvolved. The resulting, independent data sets are used to create effectively independent images which are compared. Based on the premise that the Polar spot is a real photospheric feature, the mean profile shapes of HE 520, He 699 and two further α Persei G dwarfs will be considered.

4.7.1 Differential rotation

There exists only one ‘single’ star apart from the Sun on which a definite differential rotation rate is well determined. Donati & Collier Cameron (1997) have measured the differential rotation rate of the K0 dwarf AB Doradus, from observations made in 1995 December 7 to 1995 December 13. By cross-correlating slices taken at each latitude, for both photospheric and magnetic reconstructions, it was found that in the case of AB Doradus, the pole rotates slower than the equator by approximately one part in 220. This yields a beat period of 110 d for the equator to pull one full rotation ahead of the polar regions. This value is surprisingly similar to the 120 d lap time over the same range of latitudes on the Sun. Unfortunately, we do not have the luxury of several maps derived from observations over several days. A glance at the two images of He 699 shows the low-latitude features to have evolved on a small scale as one would expect, although the active region as a whole seems to have retained the same basic shape. Since the period is determined from photometric data, this low-latitude active region must be responsible for most of the modulation in the light curve, since there is no significant shift in its longitudinal position between the two image reconstructions.

Cross-correlation was carried out firstly between images reconstructed from odd and even numbered spectra for each data set, in an attempt to check the reality of reconstructed spot features, and then between images reconstructed from the full set of spectra for October and November (Figure 4.13). It is interesting to see from the correlation function between the odd and even spectra image reconstructions for both months that cross-correlation seems to be valid from -50° to $+70^\circ$. Above 70° the area of each latitude band quickly diminishes, and cross-correlation gives spurious shifts, due to equal spot filling of pixels in the longitudinal direction. The structure seen from 0° to -50° is in part due to reflection of features about the equator, whereas below -50° little to no structure is seen. The measured shift for October and November is $0.4^\circ \pm 3.6^\circ$ and $1.4^\circ \pm 18.4^\circ$ respectively. The greater deviation in the latter (November data) is a reflection of the reality of reconstructed features, and may in part be due to the higher average S:N ratio of the October data set (see Figure 2.2 caption and Tables 4.3 & 4.7).

The difficulty in obtaining a measure of the differential rotation rate between the October and November (full) data sets, is probably attributable to evolution of individual spots on much shorter timescales. The degree of differential rotation we would expect to see on the Sun over this period is equivalent to the equator pulling 90° ahead of the polar region. Only the low latitude region has maintained its *overall* morphology over the 60 rotation cycles, an observation in agreement with the lifetime of spot groups on the Sun where most individual spot features disappear within a few days of forming. This implies that a reliable measure of differential rotation may only be obtained from sets of data which are separated by timescales of the order of one week. Previous claims of differential rotation determinations over intervals of 3 months on EI Eri (Hatzes & Vogt 1992) to a year on HU Vir (Strassmeier 1994) should therefore be treated with caution. It may however be that the factors governing spot lifetimes on RS CVn binaries as compared to lifetimes on single G dwarfs warrant further investigation.

4.8 Conclusion

We have shown that by use of least squares deconvolution of the large number of lines available in an échelle spectrum, it is possible to obtain Doppler images of faint stars from the resultant high S:N ratio spectra; thereby enormously increasing the number of stars

available for imaging.

Both of the G dwarfs studied here appear to have had low latitude active regions at the times of observation. Similarly both stars exhibit polar spots. Unfortunately from the two sets of data obtained for He 699, it has not been possible to measure differential rotation. This is not unreasonable since the two maps are 60 rotations apart, which may be greater than the evolution timescale of surface features. The light curves in Figure 4.2 for example contain points from several nights around the time of spectroscopic observation and show evolution on timescales of a few days. Further observations with full phase coverage, and an interval between observations of only several rotation cycles should allow us to view the evolution of surface and coronal features, thus allowing a determination of differential rotation in these objects.

Part II: Further Images - Latitude distributions and the polar spot controversy

4.9 Synopsis

Two further images of intermediate and low inclination G dwarfs (AP 149 & AP 193) in the young open cluster, α Persei are presented. In light of revised data reduction techniques, the data from Part I are re-analysed in a consistent manner with the new data. The main difference is due to the χ^2 minimisation of stellar parameters. The re-analysis offers a convenient comparison with the spot area minimisation for a real data set. Detailed comparisons of parameter optimisation methods using spot area and χ^2 minimisation are given in Chapter 3 for a synthetic data set. In chapter 5, both techniques are applied to the PZ Tel data set.

The new images of He 520 and He 699 are compared with those presented in Part I of this chapter, and the new observations of AP 149 & AP 193. All stars show starspots at high latitudes, with one star having a strong polar spot. Polar spots are reconstructed in many Doppler images of rapidly rotating cool stars. Their existence has been called into question (Byrne 1996), and it has been suggested that they are the manifestations of NLTE effects rather than real photospheric features as discussed in Chapter 1. We

Table 4.5: Observations of AP 149 & AP 193 on 1998 December 6,7,8

Object	UT Start	UT End	Exp time	No. of frames	comments
	1998 Dec 6		[s]		
BS 179	19:05:56	19:07:56	120	1	B2V tell H ₂ O
HD 1326	19:20:15	19:26:15	360	1	M2V template
AP 193	19:44:22	21:31:09	900	6	seeing 2-2.5 ''
HD 32963	21:55:02	22:03:22	500	1	G2V RV standard
HD 101501	05:04:47	05:08:57	250	1	G8V standard
Object	UT Start	UT End	Exp time	No. of frames	comments
	1998 Dec 7		[s]		
BS 179	19:37:55	19:39:15	80	1	B2V tell H ₂ O
HD 222368	19:48:20	19:49:20	60	1	F7V RV standard
HD 10780	19:54:11	19:57:31	200	1	K0V standard
AP 193	20:02:07	23:48:19	900	13	seeing 2-2.5 ''
AP 193	23:50:51	04:13:51	1200	10	seeing 2-2.5 ''
HD 126053	07:06:26	07:16:26	600	1	G1V RV standard
HD 115167	07:19:53	07:25:17	324	1	G5V RV standard
Object	UT Start	UT End	Exp time	No. of frames	comments
	1998 Dec 8		[s]		
BS 179	18:57:58	19:59:18	80	1	B2V tell H ₂ O
AP 149	20:18:49	22:00:45	900	6	
AP 149	22:31:12	04:25:27	900	18	seeing 2 ''

examine the mean absorption profile shapes of each star as functions of axial inclination testing the conclusions of Hatzes et al. (1996). We assume the polar spots to be real photospheric features, and conclude that the flat bottomed shape of the profile can be attributed to photospheric polar spots. The amount of distortion in the mean profile of a star for a polar spot of given size depends on the axial inclination of the star.

4.10 Introduction

In Part I, we successfully applied least squares deconvolution in order to obtain sufficiently high S:N ratio profiles for maximum entropy Doppler imaging of the two G dwarfs, He 520 and He 699. These G dwarfs were shown to exhibit large polar or near-polar spots and low latitude features, contradicting predictions by Schüssler et al. (1996) that only high latitude features should be present. We present two further images of a low inclination G dwarf, AP 149 ($m_v = 11.71$) and a G dwarf of intermediate axial inclination, AP 193 ($m_v = 12.28$). These stars are known to exhibit modulation in the photometric V-band, a phenomenon which can be attributed to asymmetric starspot coverage. Periodic modulations allowed determination of the rotation periods (Prosser et al. 1993, O'Dell & Collier Cameron 1993 and O'Dell et al. 1997) while multi-colour photometry enables spectral type determinations. The projected equatorial rotation velocities of AP 149 and AP 193 were determined by Prosser et al. (1993), as $v \sin i = 117 \text{ km s}^{-1}$ and $v \sin i = 64 \text{ km s}^{-1}$ respectively.

The growing number of images for single and double stars of different spectral types and classes is beginning to reveal common patterns, but is also leaving many questions unanswered. It is becoming apparent that while global trends are discernible each star is individual in some sense. One common feature of particular interest is the polar spot which exists in many Doppler images. It is well known that the Sun for example does not possess such a feature, and hence the reality of the polar spot has been called into question. It has been suggested that polar spots are an artefact due to incorrect treatment of the atmospheric physics of rapid rotators. Errors in the calculation of the local line profile cannot however account for the mean shape of the observed spectral profile in spotted rapid rotators. The shape of the rotationally Doppler broadened profile is effectively the convolution of narrow local intensity profiles with the Doppler broadened profile. As such it is the Doppler broadening which dominates the shape of the line. The polar spot appears because part of the line profile corresponding to parts of the star which are always visible (circumpolar) appears in relative emission. That is to say the line core appears flat-bottomed.

Mechanisms which could produce a flat-bottomed mean profile have been suggested by Byrne (1996), Hatzes et al. (1996) and Bruls, Solanki & Schüssler (1998), and were discussed in Chapter 1. It is normally assumed that an inactive slowly rotating star

can be used to derive the immaculate broadened profile used for Doppler imaging. This assumption may not hold if the magnetic activity levels of the template and target star result in differences in the vertical temperature structure in the layers where the mapping lines are formed. A case in point is the Na D doublet (Andretta, Doyle & Byrne 1997), where the cores form above the chromospheric temperature minimum due to sufficiently low opacities. Unruh & Collier Cameron (1997) used time series spectra of the sodium doublet at 5890 Å and 5896 Å from spectra of the K0 dwarf, AB Doradus, to investigate chromospheric effects on resulting Doppler images. In fact it was shown that less high latitude structure was present in images formed from these lines when compared with other commonly used photospheric mapping lines. Bruls, Solanki & Schüssler (1998) presented NLTE radiative transfer analysis of 14 of the most commonly used Doppler imaging lines and found that chromospheric filling of the line cores was present for only a few of the lines considered. Filling in of the central parts of the rotationally-broadened profiles alone was only possible by restricting the chromospheric activity to the poles.

Further evidence for the reality of the polar spot was presented by Hatzes et al. (1996) who considered the shape of the profile as a function of inclination for four RS CVn binaries. Differential rotation, a real polar spot, a bright facular band and gravity darkening were considered as mechanisms for producing the mean profile shapes seen in these stars. It was found that only a polar spot could produce the observed variation in profile shape, as a function of inclination. A similar investigation has not been made for single stars of a given spectral type. In an attempt to apply this idea to a homogeneous set of stars for which Doppler images exist, we examine the four α Persei G dwarfs for which Doppler images currently exist.

4.11 Observations and data reduction

Observations were made with the Utrecht Échelle Spectrograph (UES) at the William Herschel Telescope on 1998 December 6, 7 & 8. The seeing was generally moderate to poor at between 1.5'' - 2.5''. The 2K x 2K SITE CCD was used in conjunction with the 31 gmm⁻¹ UES grating giving a wavelength coverage of 4013Å - 7269Å. A total of 63 orders were recorded. We rejected the 10th order (4286Å - 4356Å) due to a bad column. The observations are recorded in Table 4.5.

Table 4.6: Photometric data and spectral types of the target stars. $(V-I)_k$ colours only exist for AP 149 and AP 193. The B-V colours are estimated from other stars in the cluster for which both $(V-I)_k$ and B-V are known. Given that the reddening is variable across the cluster, temperatures and spectral types estimated from colours should be treated with caution.

Object	V	B-V	$(V-I)_k$	T_{eff} /K	SpT
AP 149	11.71	0.76*	0.81	5387	G8V
AP 193	12.28	0.68*	0.76	5621	G5-6V
He 520	11.69	0.69	0.69	5589	G6V
He 699	11.27	0.61	0.61	5855	G2-3V

Data reduction was carried out in the same manner as described in Part I, using the STARLINK package ECHOMOP. The thorium-argon arc-frames used for wavelength calibration were extracted in conjunction with a target spectrum, and calibrated using this package.

4.11.1 Spectral Types

Multi-colour photometry is still lacking for many of the α Persei cluster stars, which can make spectral type estimation difficult. Table 4.6 presents known parameters for these stars along with determined colours in B-V if none exist. Estimates of B-V from $(V-I)_k$ were made from Bessell (1990) for AP 149 and AP 193. It is immediately clear that this transformation is unsatisfactory since although AP 149 is 0.57 magnitudes brighter than AP 193 in V, it appears to have a larger $(V-I)_k$ and hence a larger estimated B-V, suggesting a later spectral type. There are two factors which may affect this result. Firstly, the reddening across the α Persei cluster is known to be variable, although a fixed value of $0.1 E(B-V) \approx 0.1$ is generally used (and was adopted here for He 520 and He 699). Also, a difference in spot coverage will affect the determination of B-V from $(V-I)_k$ which is more sensitive to temperature changes. It may be that AP 149 is more active than AP 193 and has a higher degree of spot coverage.

The photospheric and spot temperatures necessary for Doppler imaging were determined from the B-V vs T_{eff} calibration of Flower (1996). In Part I no appreciable differences between the continuum slopes of He 520 and He 699 was found. For the above quoted reasons $T_{eff} = 5750\text{K}$ was adopted as the photospheric temperature (the G2 dwarf, HD42807 was used to represent the local intensity profile). Similarly we adopt $T_{eff} = 5500\text{K}$ as the photospheric temperature for both AP 149 and AP 193, using the G8V dwarf, HD 101501 to represent the local intensity profile. The main factor affected by choice of photospheric temperature in Doppler imaging is the limb-darkening coefficient. At $T_{eff} = 5500\text{K}$, an error of $\pm 250\text{K}$ leads to an error of 6 per cent in the limb-darkening coefficient in the V band. We have already shown that limb-darkening coefficients which are incorrect by as much as 10 per cent should not significantly affect the resulting maximum entropy reconstructions. Residuals in the maximum entropy regulated fits to the data do not show any strong mis-matches in the wings of the profiles indicating a reasonable estimate of the limb-darkening coefficients.

4.11.2 Continuum fitting

The continua of the standard stars were found to be well approximated by splines with 8 knots (see Part I for full details). As can be seen from Tables 4.5 and 4.6, the atmospheric seeing was poor during observations of AP 193 which is also 0.57 magnitudes (in the V band) fainter than AP 149. As a result, fewer counts were recorded at the order edges, and away from the blaze maximum. For this reason we trimmed off the last 50 pixels in all orders of the AP 193 spectra, giving 1600 pixels in the wavelength direction.

4.11.3 Multiplex gain from least squares deconvolution

The advantage of using the (2K pixels)² SITe chip is immediately apparent. The CCD image is wider than the free spectral range of the spectrograph, yielding approximately 5500 images of the 3175 lines (for AP 149) present in the wavelength range recorded. The trimming of 50 pixels at the end of each order in the AP 193 spectra (see above) resulted in fewer effective lines when compared with the AP 149 spectra.

Table 4.7 presents the statistics for the four α Persei stars. The output S:N ratios are calculated by SPDECON. The output S:N ratios for He 520 and He 699 can be compared

Table 4.7: Least squares multiplex gain for each data set. The mean output S:N ratios and gains are for mean depth scaled profiles (see §2.2.1). The uncertainties on the input S:N ratios are calculated from the input S:N ratio of each spectrum.

Object	Input S:N	Output S:N	Gain	Effective no. of lines	Gain limit
He 520	45.4± 4.0	1096 ± 102	24.1	1061	32.6
He 699 (Oct)	52.4± 3.8	1259 ± 89	24.0	1061	32.6
He 699 (Nov)	50.3± 4.2	1220 ± 104	24.2	1061	32.6
AP 149	26.7± 3.5	1443 ± 192	54.0	5837	76.4
AP 193	20.7± 3.6	1097 ± 182	53.0	5302	72.8

with those in Table 4.3 which were calculated by measuring the continuum noise.

The theoretical upper limit to the gain is equal to the square root of the total number of lines. Comparing these limits for the 1996 October/November and the 1998 December data yields a theoretical gain ratio of approximately $(5569/1061)^{\frac{1}{2}} = 2.29$. The empirically determined gain ratio is approximately $(53.5/24.1) = 2.22$. Although the upper gain limit is never reached in all cases, the actual gain ratio between the 1996 and 1998 data sets is in good agreement with that which we expect.

4.12 System parameters

We have re-determined, using χ^2 minimisation, the system parameters of the two α Persei G dwarfs He 520 and He 699, presented in Part I and published in Barnes et al. (1998). Figure 4.14 shows the trial values of inclination against χ^2 after 40 iterations of our maximum entropy Doppler imaging program, DoTS, for all four stars. This number of iterations is sufficient as the value of χ^2 changes by only small amounts with further iterations at this stage. The derived system parameters are given in Table 4.8. Prosser et al. (1993) found that the mean radial velocity of the α Persei cluster is $\sim -2 \text{ km s}^{-1}$. A mean dispersion of 2 km s^{-1} was used as the criterion to identify slow rotating member, whereas the rapid rotators were allowed deviations of up to several km s^{-1} from the mean. The combined effects of a time series of profiles and the least squares process to obtain

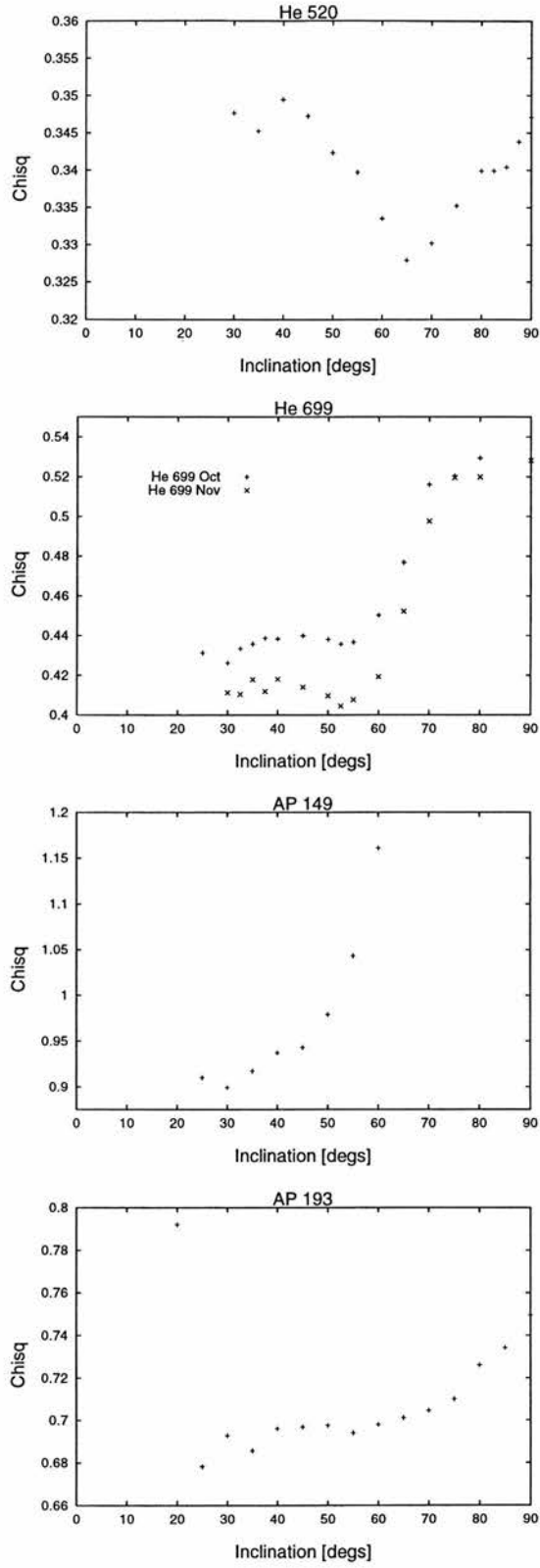


Figure 4.14: Inclination determinations for He 520, He 699, AP 149 and AP 193

high S:N ratio profiles shows that the radial velocities of all the stars considered here agree to within 1.5 km s^{-1} . Perhaps the most alarming result is the apparent discrepancy of the radial velocity measurement for the two He 699 data sets. A probable explanation lies in the combination of a slightly different phase coverage, which is incomplete in both cases, and a change in the starspot distributions between the two epochs.

Like both PZ Tel and Speedy Mic (Chapters 5 & 6), all the stars imaged are oversized for their spectral types, having typical radii of $\sim 1.2 R_{\odot}$. For example Gray (1992) gives radii of $0.88 M_{\odot}$ to $1.02 M_{\odot}$ for stars of spectral type G8 to G2. These typical values may not be appropriate however given the relative youth, degree of spot coverage (see Chapter 5) and high equatorial rotation velocities, which may all contribute to this apparent systematically large radius.

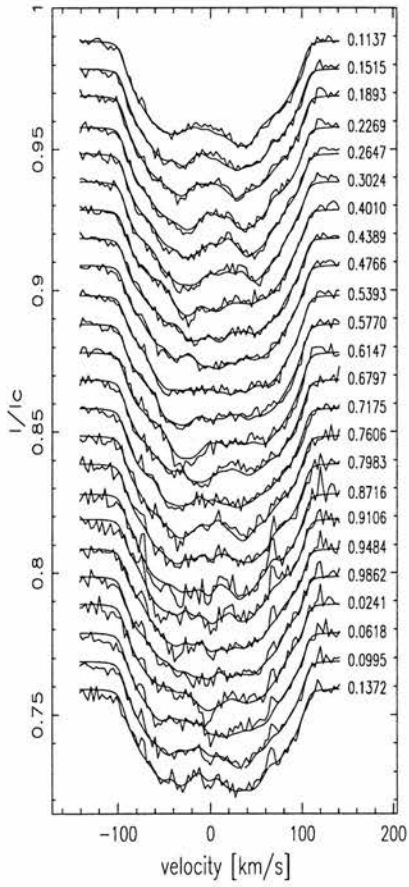
4.13 Results

4.13.1 Images

Maximum entropy images derived from the redetermined system parameters for He 699 & He 520 are shown in Figure 4.16. Comparison with the earlier images (Figures 4.5, 4.7 and 4.9) shows that the low latitude features have a slightly different morphology. The polar/asymmetric-polar spots on each star appear less strong in the new images. The high latitude regions show much more detail than the reconstructions presented in Barnes et al. (1998). This may be due partly to pushing the value of χ^2 slightly lower, but is probably mainly due to the lower inclinations used in the image reconstruction. Incorrectly overestimating the axial inclination has the primary effect of producing polar features which are too strong while under-representing low latitude features. The opposite is true for underestimation of the axial inclination.

Figures 4.15 and 4.17 show the maximum entropy fits to the least squares deconvolved time series and the entropy regularised image reconstructions respectively. It is immediately apparent that both high and low latitude features are also present on both these stars. The phase coverage is not complete on AP 193 because of its longer rotation period so the latitudinal mean fractional spot filling is calculated only over phases where the observations were made (see plot for details).

AP 149 – Data & Fits – 1998 Dec 8



AP 193 – Data & Fits – 1998 Dec 6 & 7

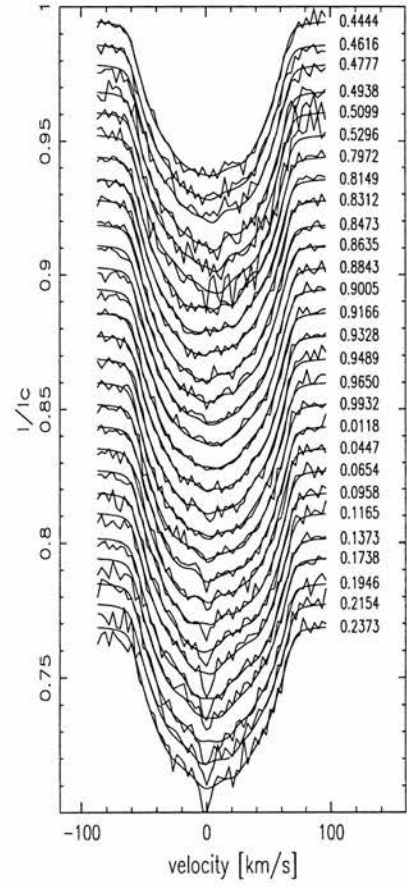


Figure 4.15: Time series profiles and maximum entropy regularised fits for AP 149 (reduced $\chi^2 = 1.02$) and AP 193 (reduced $\chi^2 = 0.85$)

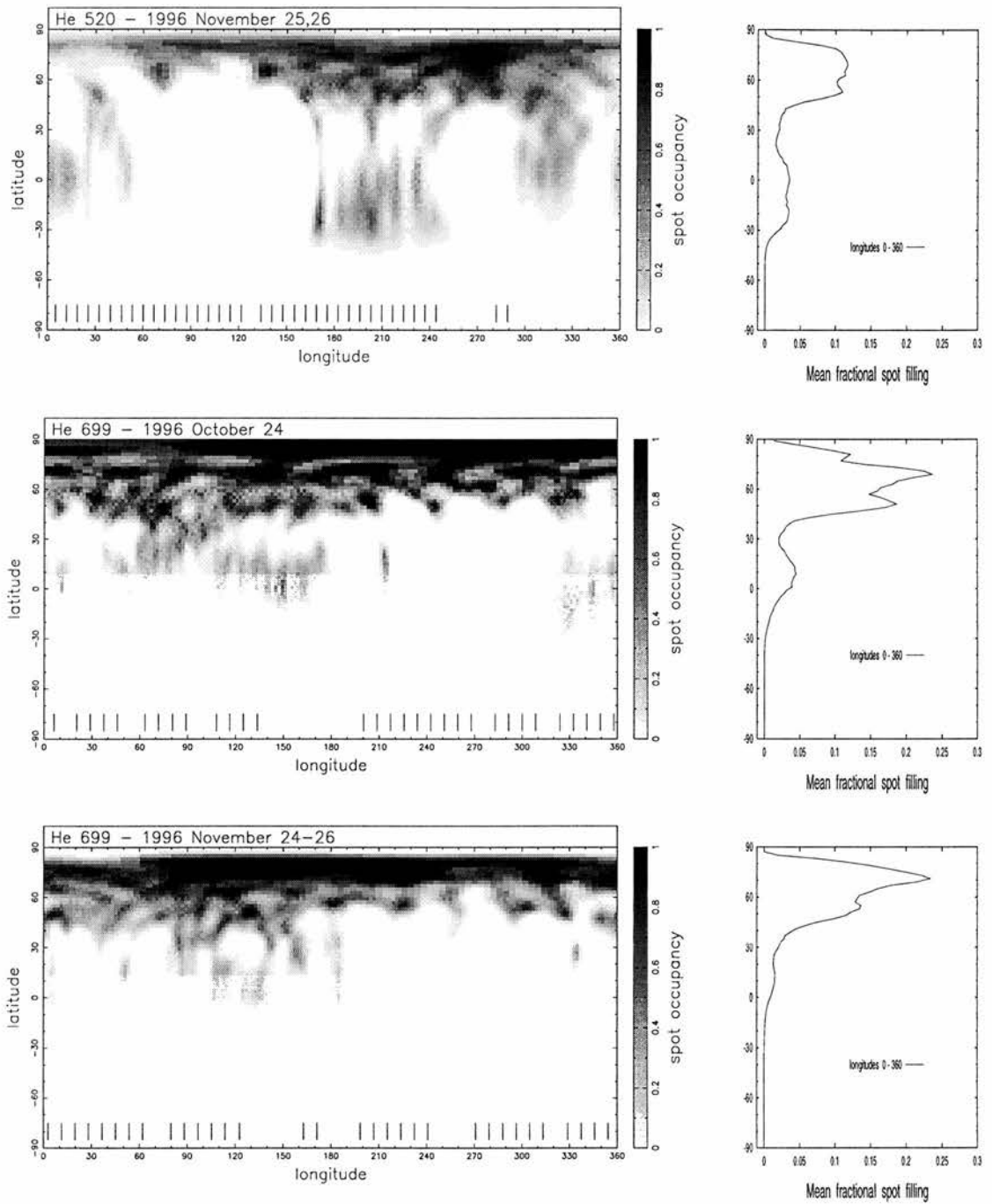


Figure 4.16: Maximum entropy image reconstructions. Tick marks indicate phases of observations. Top: He 520, Middle: He 699 (October), Bottom: He 699 (November). Compare with the spot area minimised images in Chapter 4 (Figures 4.7, 4.9 and 4.11).

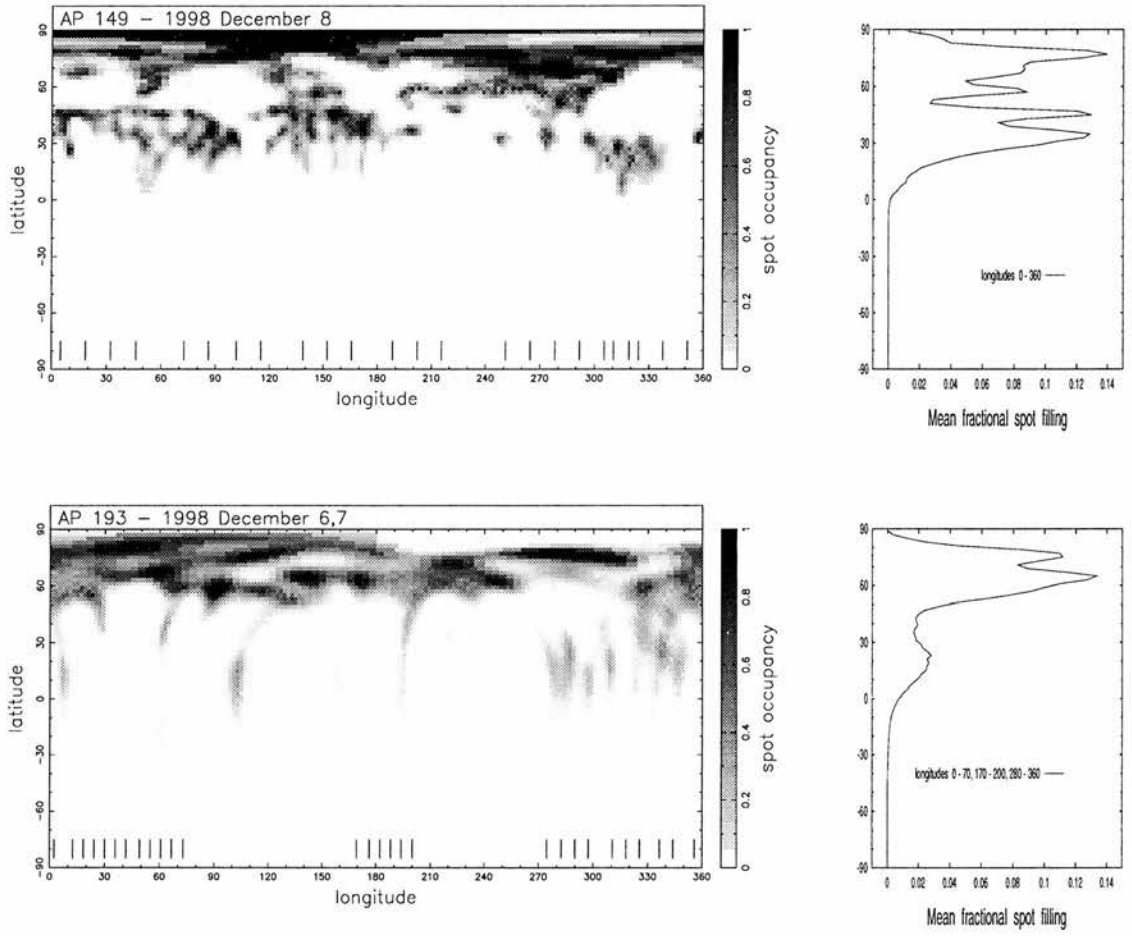


Figure 4.17: Maximum entropy image reconstructions. Top: AP 149, Bottom: AP 193. Both stars exhibit high latitude structure and a low latitude band at the phases of observation.

Table 4.8: Estimated stellar parameters from the χ^2 minimisation of maximum entropy fits to the data. The average radial velocity of -2.5 km s^{-1} is in good agreement with Prosser's (1993) mean cluster velocity of -2 km s^{-1} . The same EW (not shown), $v \sin i$ & inclination were recovered on the two He 699 data sets. However the radial velocity differs by 1.1 km s^{-1} . This radial velocity variation is likely due to a combination of incomplete phase coverage (different phase ranges in each data set) and asymmetries introduced by different spot patterns.

Object	v_{rad} km s ⁻¹	$v \sin i$ km s ⁻¹	Period days	$R \sin i$ R _⊙	i deg	R M _⊙
AP 149	-3.1	102	0.3200	0.645	30	1.29
AP 193	-1.8	64	0.7483	0.946	55	1.16
He 520	-3.5	89	0.6038	1.069	65	1.18
He 699a	-1.4	93	0.4908	0.902	52.5	1.10
He 699b	-2.5	93			52.5	

4.13.2 Polar spot strength/inclination dependence

In Fig 4.19 we show the mean profile of each of the four stars compared with the profile one would expect from an immaculate star. The comparison is less straightforward than that presented in Hatzes et al. (1996) since each of the stars appears to exhibit a different size of polar/circum-polar spot. This in itself demonstrates that not all Doppler images of single stars exhibit a polar spot. Perhaps the best comparison can be made between AP 149 and AP 193 which have similar degrees of spot filling at high latitudes. It is quite clear that the star with the lower axial inclination, AP 149, shows a mean profile with apparently greater core filling. He 520 shows an off-centre polar spot (as noted and discussed in Barnes et al. 1998) which is reasonably large whereas He 699 shows a very strong and extensive polar spot.

4.14 Discussion & conclusions

All the images presented here reveal the presence of a low latitude band of spots as evinced by the right-hand plot in Figures 4.16 and 4.17. Given that this low latitude band appears

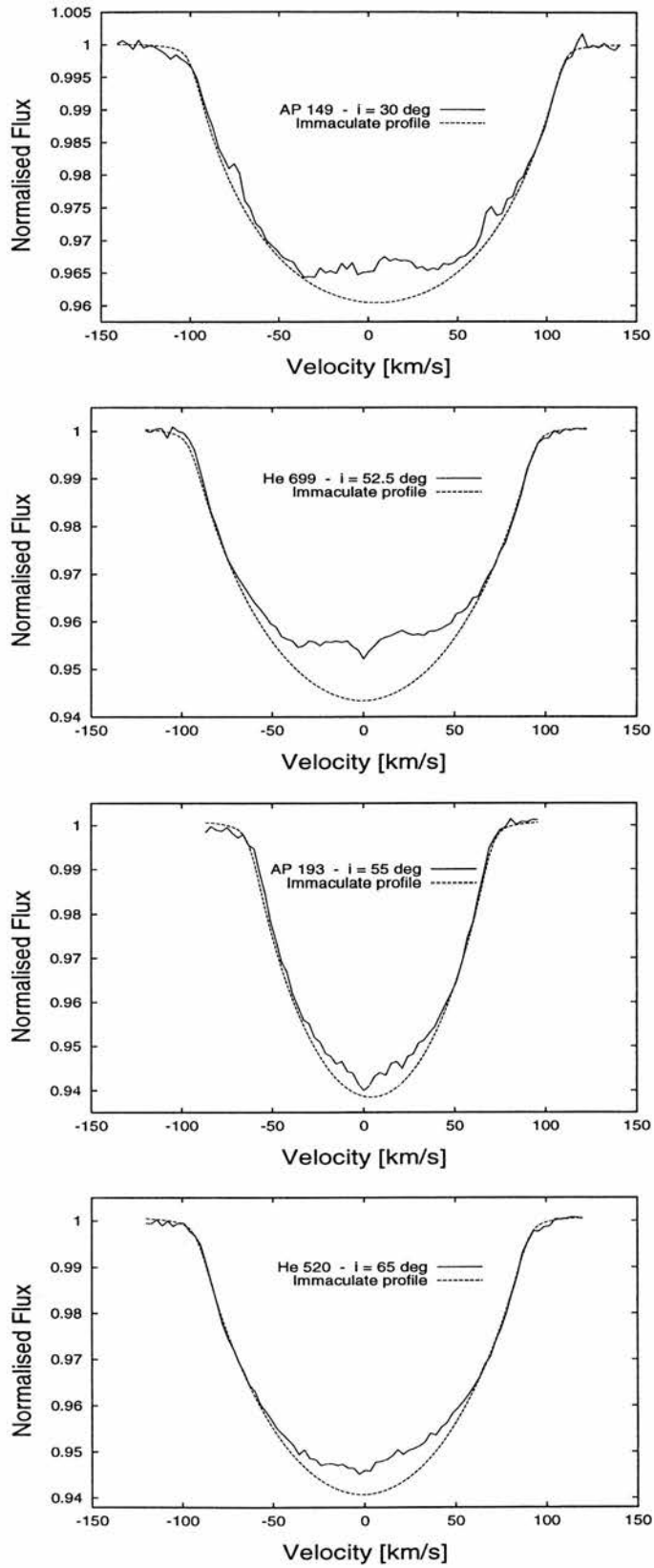


Figure 4.18: Mean observed profiles and immaculate profiles.

at different latitudes in all the stars, it is tempting to speculate that we are seeing each star at a different stage in a stellar analogue to the solar cycle. If this is the case we are effectively observing slices through a stellar butterfly diagram.

Other effects such as meridional flows may cause magnetic flux loops (and hence starspots) emerging at intermediate latitudes to drift towards the equator, as suggested by Schüssler et al. (1996). If these α Persei dwarfs exhibit stellar cycles clustering around 11 years (i.e. Wilson 1978 & Baliunas et al. 1995) one would not expect significant drift of low latitude starspot groups over a one month period, in agreement with the observations presented for He 699.

AP 149 in particular shows a strong low latitude band centred at latitude $\sim 35^\circ$. Given the low inclination of this star, it is this band which must be responsible for photometric modulations. More specifically, since only latitudes below 30° are not always visible during a rotation cycle, it is likely to be these features which cause the modulation. If this band drifts in latitude over a magnetic cycle, a low amplitude of photometric modulation may indicate that a band of spots appears below 30° or becomes nearly uniform as a function of latitude, rather than being the result of fewer spots. If little modulation of the V band lightcurve throughout a rotation cycle coincides with a drop in Ca II H & K chromospheric emission, this may indicate that the low latitude band has moved to latitudes below 30° . Care should be exercised in such an interpretation, as the spot band may simply have disappeared. Only long term monitoring of one object in this manner can ascertain whether a true stellar butterfly pattern exists.

While both AP 149 and AP 193 show relatively weak circum-polar features, neither star shows a true polar spot. Measurement of the spot filling between latitudes 50° - 90° (i.e. the area under the curve in the right hand plots in Figures 4.16 and 4.17) yields mean filling factors of 0.148 (He 699 Oct), 0.142 (He 699 Nov), 0.088 (He 520), 0.074 (AP 149) and 0.068 (AP 193). For the purposes of comparison, these factors can be given relative to the lowest inclination object (AP 149) the factors are 2.0, 1.9, 1.2, 1.0 & 0.9 respectively. If we make the simple assumption that the missing area (i.e. Immaculate profile EW - mean profile EW) is directly proportional to the above factors when compared with the lowest inclination object, comparisons become easier. With all the profiles corrected to the same degree of spottedness it is quite clear that the profile shape as a function of inclination roughly agrees with that shown in Figure 4.19. That is,

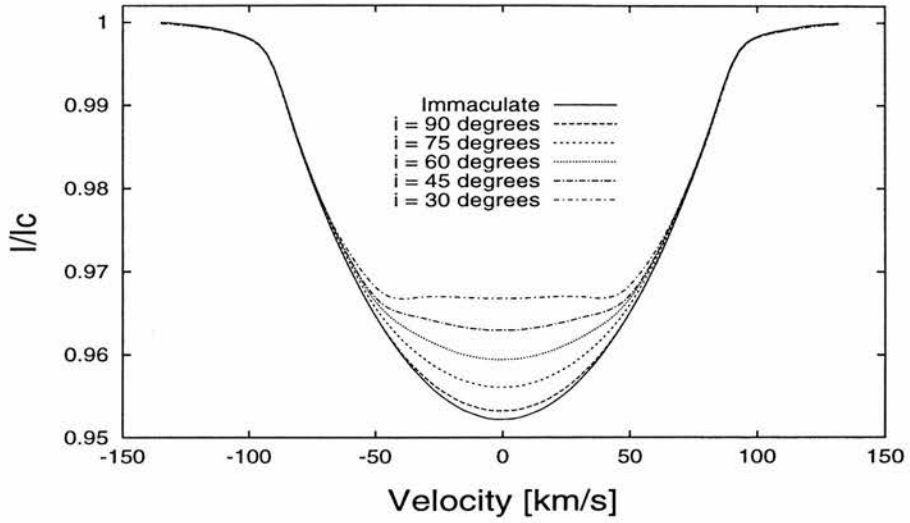


Figure 4.19: Profiles for a star with immaculate photosphere and $v \sin i = 90 \text{ km s}^{-1}$, and for a star at various inclinations with a polar spot of radius 30° .

the missing flux in He 699 is reduced by a factor of 2, and in He 520 by a factor 1.2 for the mean profile. The missing area in the AP 193 profiles is increased by a factor 1.11. The comparisons are more difficult to make than for the RS CVn binaries (Hatzes et al. 1996) which showed similar polar spot sizes.

CHAPTER 5

Images of Southern rapid rotators I: Differential rotation on PZ Telescopium

Work contained in this chapter can be found in “Doppler images from dual-site observations of southern rapidly rotating stars I: Differential rotation on PZ Tel”, *MNRAS*, 2000, *In Press*, J.R. Barnes, A. Collier Cameron, D.J. James, J.-F. Donati

5.1 Chapter synopsis

Doppler images of the young, late-type star, PZ Tel are presented from spectroscopic observations at two epochs. The 0.95d period necessitated dual-site observations in order to obtain full phase coverage. The resulting maximum entropy reconstructions based on least-squares deconvolved profiles derived from ~ 2800 photospheric absorption lines reveal the presence of starspots at all latitudes. By cross-correlation of constant-latitude strips from the images, we derive a measure of rotation as a function of latitude. Rate of surface shear is found to be in close agreement with the solar value. We also examine further evidence for the young evolutionary status of PZ Tel through radial velocity, and lithium abundance.

5.2 Introduction

The late-type single star, PZ Tel (HD 174429) has been the subject of numerous photometric studies over the past two decades. Several sets of V-band light curves have been derived from observations between 1979 and 1984 (Innis et al. 1990 and references therein). The

Table 5.1: Observations of PZ Tel in 1998 July with the Sutherland 1.9m and GIRAFFE at the SAAO

Sutherland 1.9m				
Object	UT Start	Exp time	No. of frames	comments
	1998 Jul 09	[s]		
HR 4390	18:13:55	100, 250	2	B5Vn telluric stand.
Gl 472	18:26:14	900	1	K1V template
HD 125072	18:44:46	500	1	K3V template
HD 118972	18:56:01	450	1	K2V template
HD 131156	19:08:09	250	1	G8V RV stand.
PZ Tel	19:20:35	600	32	
Object	UT Start	Exp time	No. of frames	comments
	1998 Jul 12	[s]		
HD 119850	17:08:46	900	1	M3V template
HR 4390	17:28:14	100, 250	2	B5Vn telluric stand.
HD 131156	17:38:01	250	1	G8V RV stand.
PZ Tel	17:49:12	600	18	
Gl 615	21:26:34	700	1	K0V template
PZ Tel	21:53:47	600	23	
HD 202917	02:37:43	900	2	
HD 224618	03:20:59	900	2	
HD 693	03:56:43	500	1	
HR 472	04:11:58	50	1	B3Vpe telluric stand.

Table 5.2: Observations of PZ Tel in 1998 July with the AAT and UCLES at the AAO

AAT				
Object	UT Start	Exp time	No. of frames	comments
	1998 Jul 10	[s]		
PZ Tel	07:54:41	300	7	seeing 3''
HR 4390	08:41:26	180	2	B5Vn telluric stand.
PZ Tel	08:54:00	300	14	
Gl 433	10:23:41	600	1	M1.5V template
PZ Tel	10:38:30	300	2	
HD 119850	10:53:34	300	2	M3V template
PZ Tel	11:08:05	300	6	
Gl 472	11:47:25	300	1	K1V template
PZ Tel	11:55:25	300	6	
Gl 673	12:34:10	300	2	K5V template
PZ Tel	12:56:31	300	6	
HD 19007	13:36:55	300	1	K4V template
PZ Tel	13:44:54	300	6	
HR 7121	14:22:58	40	2	B8V telluric stand.
PZ Tel	14:27:34	300	12	
HR 1835	15:43:11	200	1	G3V RV standard
PZ Tel	15:50:15	300	6	
Object	UT Start	Exp time	No. of frames	comments
	1998 Jul 12	[s]		
PZ Tel	07:55:54	300	40	
PZ Tel	12:48:48	300	8	
PZ Tel	14:03:26	300	10	

V-band modulation of up to 0.12, due to cool photospheric starspots rotating in and out of view, enabled the same authors to derive a period of 0.94486 d. A $v \sin i$ measurement of 70 km s^{-1} was made by Randich, Gratton & Pallavicini (1993). As part of a long term study of active stars, V-band light curves and $UBV(RI)_c$ colours have been derived by Cutispoto (Cutispoto 1997 & 1998)) and the G9/K0 dwarf or G9 IV/V classification is in good agreement with the K0Vp spectral type of Houk (1978). A three spot model of the V-band light curves enabled Innis et al. (1990) to infer a differential rotation shear consistent with the solar value.

Balona (1987) and Innis et al. (1988) found heliocentric radial velocities of $+4.4 \pm 6.2 \text{ km s}^{-1}$ and $-3.2 \pm 3.7 \text{ km s}^{-1}$. These measurements suggest that PZ Tel is a member of the Eggen (1975) local association or Pleiades group. Soderblom, King & Henry (1998) however find a heliocentric radial velocity of -13.5 km s^{-1} , suggesting that PZ Tel is not an association member. The HIPPARCOS parallax of $20.14 \pm 1.18''$ yields a distance of $49.7 \pm 2.9 \text{ pc}$, which is lower than the Innis et al. (1988) value of $\sim 68 \text{ pc}$. Favata et al. (1998) used the HIPPARCOS distance and photometric data in conjunction with the pre-main-sequence evolution tracks of D'Antona (1994) and found that PZ Tel lies above the main sequence, on the evolutionary track of a $1.1 M_{\odot}$ star, corresponding to an age of 20 Myr.

The study by Innis et al. (1988) revealed a strong emission core in the Ca II K line and thus indicated that PZ Tel is chromospherically active. This was confirmed by Soderblom, King & Henry (1998). Innis et al. (1988) also found that $H\alpha$ is seen as a shallow absorption feature, being at times completely filled in. A highly active corona is confirmed from a ROSAT all sky survey detection, but the derived $\log(L_x/L_{bol})$ of -3.68 ¹ is unusually low for such a young active object, and may be in error. PZ Tel has also been detected as a radio source with the photoelectric Astrolabe Mark II (Manrique et al. 1999).

Long term observations of chromospheric activity in a number of stars of intermediate rotation rate have been carried out at Mount Wilson (Wilson 1978 and Baliunas et al. 1995). Results suggest that a large number of stars show activity modulation on timescales similar to the 11 year solar cycle. Recent theoretical work by Kitchatinov &

¹HEASARC ROSAT data archive: http://legacy.gsfc.nasa.gov/docs/rosat/rhp_archive.html

Rüdiger (1999) predicts that late-type stars with a range of rotation periods from 1 d to the solar period should all have the same degree of absolute differential rotation. This means that the rate of latitudinal shear should be independent of rotation rate. It seems reasonable that a dynamo process dependent upon this differential rotation would go some way to explaining the similarity of activity cycle lengths seen in the Mount Wilson Survey.

Cross-correlation of constant latitude strips (using starspots as tracers) from Doppler images taken at epochs separated by several days offers a means of measuring the magnitude and sense of differential rotation of fast rotators. This technique already suggests (Donati & Collier Cameron 1997) that the absolute differential rotation of the K1 dwarf AB Doradus is the same as is found on the Sun.

5.3 Data reduction

5.3.1 Observations

One set of observations was secured using the Grating Instrument for Radiation Analysis with a Fibre Fed Échelle (GIRAFFE), at the Sutherland 1.9m Telescope (South African Astronomical Observatory - SAAO) on 1998 July 9 - 13. The second set of data was obtained on 1998 July 9-14 using the University College of London échelle spectrograph (UCLES) on the Anglo Australian Telescope (AAT). Since the period of close to one day makes complete phase coverage at one site impossible, we observed PZ Tel at the SAAO on 1998 July 09 & 12, and at the AAT 1998 July 10 & 12 allowing two complete cycles to be observed with a gap of two days. Conditions were of variable quality at both sites, with the intermittent cloud on July 12th at the AAT. Observations (see journal of observations, Table 5.1 and Table 5.2) of the target were separated by observations of standard and template stars. The 1K x 1K TEK6 CCD was used at the Sutherland 1.9m Telescope. With the grating set in the red position (July 9th), this resulted in a central wavelength, in the extracted data, of 6520Å (range: 5027Å - 9215Å). On July 12th, the grating was used at the intermediate setting resulting in a central wavelength of 5454Å (range: 4504 Å - 6967Å). The 2K x 4K MITLL CCD chip was used in conjunction with UCLES, was windowed to 2088 x 2496 pixels, and centred on a wavelength of 5307.6 Å (range: 4304 Å - 6921Å). Slowly rotating “template” stars with effective temperatures similar to the photosphere and spots

of PZ Tel were also observed for use as local intensity profile templates for Doppler imaging.

For both data sets, pixel to pixel variations were removed using flat-field exposures taken with an internal tungsten reference lamp. The worst cosmic ray events were removed at the pre-extraction stage using the FIGARO routine BCLEAN. The spectra were extracted using ECHOMOP, the échelle reduction package developed by Mills (1994). The Thorium-Argon arc-frames used for wavelength calibration were extracted in conjunction with a target spectrum, and calibrated using this package. The scattered light was modeled by fitting polynomials of degree 7 at each x-position to the inter-order pixels, using option 22 in ECHOMOP. The orders were extracted using ECHOMOP implementation of the extraction algorithm developed by Horne (1986). ECHOMOP propagates error information based on photon statistics and readout noise throughout the extraction process.

5.3.2 Continuum fitting

For a 1K x 1K chip, the shape of the continuum in the échelle orders is generally well approximated by a carefully chosen n^{th} degree polynomial, as approximately only half an order can be recorded across the chip. However, with increasing chip sizes, complete orders can be recorded, and the *sinc*-function shape of the continuum is not well approximated by a polynomial.

The continua of the slowly rotating photospheric and spot temperature standards can generally be fitted with a spline function. The number of knots required in the spline fit varies from one data set to the next, and in this case 8 knots were used on the SAAO data, and 11 knots were used on the AAT data. An object master frame consisting of all the co-added PZ Tel spectra was divided by the continuum fit to the slow rotating photospheric standard. This process is similar to that first detailed by Collier Cameron & Unruh (1994). Since the continuum level and shape of PZ Tel differ slightly from those of the photospheric standard, a quartic polynomial was fitted to this divided spectrum to remove residual mis-fits, and to normalise the spectrum, resulting in a standard or master continuum fit.

Normalisation of the PZ Tel spectra was carried out by dividing each target spectrum by the co-added high S:N ratio master frame, in order to obtain an essentially flat residual.

This residual was then fitted with a quartic polynomial to remove residual mis-fits and any remaining tilt, mainly due to extinction effects throughout the night’s observing as the star rises and sets. Slight changes in continuum tilt due to the starspot contribution are also removed in the process. This fit, when multiplied by the master continuum fit results in the correct continuum for the individual target spectrum in question.

5.3.3 Radial velocity

The heliocentric radial velocity of PZ Tel has been derived using a cross-correlation technique, with the IAU radial velocity standard star HD 693. Two SAAO échelle orders ranging from 5360-5440 Å and 5465-5545 Å were used because they both contained deep photospheric lines and negligible telluric contamination. The slightly lower resolution SAAO data were used instead of the AAT data because of the lack of suitable radial velocity standards taken during the AAT run. A radial velocity of $-0.1 \pm 1.0 \text{ km s}^{-1}$ is calculated from the SAAO spectra. The mean internal error on the radial velocities is estimated to be of order 1 km s^{-1} . The external zero-point error, based on the radial velocity standards, is about 0.5 km s^{-1} , and systematic shifts of the spectrograph during the night are of typically 1.5 km s^{-1} for the GIRAFFE system (see §5.2.2). The projected equatorial velocity of PZ Tel is calculated from a Doppler imaging analysis of this system, and is presented in §5.2.2.

5.3.4 Lithium abundance measurements

The AAT échellograms also contain an order ranging from 6628-6725 Å, which includes the lithium 6708 Å feature. This is a two-line neutral resonance doublet, one pair from the ^6Li isotope (6707.933 & 6708.121 Å), and one from the ^7Li (6707.833 & 6707.932 Å) isotope (Soderblom et al. 1990). In the Sun, and meteorites, the isotope ratio $^6\text{Li}/^7\text{Li}$ is ≈ 8 per cent (Grevesse & Anders 1989), and it is assumed that the Li abundance in the Sun, and field stars, is dominated by the ^7Li isotope. The equivalent widths (EWs) of the Li I 6708 Å doublet were calculated by integrating under the normalized Li feature over $\pm (v \sin i \text{ plus the FWHM of an unresolved line})$. Our K0V standard, Gl 615, is a metal poor old disc star (see §5.5) which precludes use of the spectral subtraction technique to measure the Li EW. Using this latter technique however, with Gl 472, a K1V standard gave

an EW of $246 \pm 8 \text{ m}\text{\AA}$. This is consistent with the result using the integration method (§4), but probably suffers from a systematic error due to the inappropriate EW of the K1 standard. Unlike the spectral-standard subtraction technique, the integration method does not account for the small contribution from the nearby Fe+CN 6707.441 \AA feature. We estimated the strength of this line from the empirical relation

$$\text{EW}(\text{Fe} + \text{CN}) = 20(\text{B} - \text{V}) - 3\text{m}\text{\AA} \quad (5.1)$$

presented in Soderblom et al. (1993a), and subtracted it from our Li + (Fe+CN) equivalent width. LTE Li abundances were calculated by interpolating the curves of growth given in Soderblom et al. (1993a), and non-LTE effects were accounted for using the corrections given by Carlsson et al. (1994). The effective temperature of PZ Tel was estimated from its B-V photometry, using Equation (3) in Soderblom et al. (1993b). The V, B-V photometry has been taken from Cutispoto (1998).

5.4 Physical Parameters of PZ Tel

We choose to discuss the physical parameters of PZ Tel because our high-resolution spectra, and data available in the literature, provide the ideal opportunity to link some observable properties to the physical properties in a meaningful way. We present analysis and discussion which indicates that PZ Tel is probably a single, rapidly rotating, magnetically-active, pre-main sequence, solar-type star.

BVI_c photometry of PZ Tel has been reported by Cutispoto (1998) with values of V=8.44, B-V=0.78, V-I_c=0.87 being derived, and a reported spectral-type of G9 IV/V. Using these photometric data and a HIPPARCOS distance of 49.65 pc, Favata et al. (1998) found the position of PZ Tel on a colour-magnitude diagram (CMD) indicates that the star lies above the zero age main sequence. Compared with theoretical pre-main sequence (PMS) isochrones, its distance and colours are consistent with its position in the CMD for an age of 15-20 Myr (Favata et al. 1998 and Soderblom, King & Henry 1998). Furthermore, the analysis presented in §5.5.2 yields a rotation velocity of 68 km s^{-1} , and Innis et al. (1990) present a photometric period for PZ Tel of 0.9447 days. Therefore, the projected or *minimum* stellar radius, relative to the solar radius is $R\sin i = 1.27 R_{\odot}$. Such a radius is too large for a K0/G9 dwarf by over 50 per cent (Gray 1992), further indicative of the

PMS status of PZ Tel. Indeed, the empirically determined inclination (§5.5.2) suggests a radius of $1.47 R_{\odot}$.

The Galactic U, V, W space motions of PZ Tel can also be calculated using the measured radial velocity and using the HIPPARCOS proper motions and distance. We calculated a radial velocity of -0.1 ± 1.0 (see § 5.3.3). There are now several radial velocity measurements for this star, however, there is some debate as to whether it is a single or binary system. Our velocity is consistent with the values of Balona (1987) and Innis et al. (1988) who report radial velocities of $+4.4 \pm 6.2 \text{ km s}^{-1}$ & $-3.2 \pm 3.7 \text{ km s}^{-1}$, respectively. However, Soderblom, King & Henry (1998) report an RV of $-13.5 \pm 2.5 \text{ km s}^{-1}$, which is inconsistent with both our value and the other two values. Clearly, either PZ Tel is a spectroscopic binary system or the Soderblom et al. value maybe in error. If PZ Tel is a binary, the three other self-consistent values, determined independently, have unfortunately come from observations at or near-close to the system's centre-of-mass. One further possibility for radial velocity variations is due to the profile distortion as a result of starspots rotating in and out of view. Although this may affect individual measurements, the above value is derived from all co-added SAAO spectra on 12/07/98 (phases 0.0000 to 0.3754 & 0.9992 to 1.0000). We also derive radial velocity measurements in order to find best maximum entropy regulated fits to our data (see §5.5.2). These results are not inconsistent with the currently derived measurement. Assuming PZ Tel is a single star, and using HIPPARCOS data and the procedures outlined in Johnson & Soderblom (1987), we derive U, V, W space velocities of $U = -7.6 \pm 1.9 \text{ km s}^{-1}$, $V = -16.2 \pm 1.1 \text{ km s}^{-1}$ and $W = -9.0 \pm 0.9 \text{ km s}^{-1}$ (using an assumed RV error of 2.0 km s^{-1}).

Investigations of the kinematics of some of the nearest early and late-type stars have shown that many of them are possible members of the Pleiades kinematic group, and lie within a tightly defined kinematic domain which has been termed the *Local Association* (Eggen 1983a, Eggen 1983b and Jeffries 1995). The emerging scenario is that the Local Association consists of a reasonably coherent kinematic stream of young stars with embedded open clusters and star formation associations such as the Pleiades, α Per, IC 2602, NGC 2516 clusters and the Scorpio-Centaurus moving cluster (Eggen 1983a). Ages of Local Association stars are reflected in the ages of the component clusters, and appear to cover an age range from about 20 to 150 Myr. While the Galactic space motions we determine for PZ Tel are not formally consistent with those of the Local Association, they are consistent with PZ Tel being a kinematic member of the young disc population (Eggen

1989), albeit on the edge of the young disc domain in (U,V) space.

Further indications of the evolutionary status of PZ Tel can be gained from the physical parameters which, at the present time, are commonly used to infer age estimates. From the AAT spectra we have measured the Li I 6708 Å EW (using the technique described in § 2) to be $255 \pm 13 \text{ m}\text{\AA}$, after the removal of the contribution from the small Fe+CN line at 6707.441 Å. Using a B–V of 0.78, and Equation 3 (Soderblom et al. 1993b), this translates to an effective temperature of 5238 K. From the EW and effective temperature, we calculate (D. J. James, private communication) a lithium abundance, $N(\text{Li}) = 2.97 \pm 0.06 \text{ dex}$. This abundance is consistent with that derived by Soderblom, King & Henry (1998), allowing for small differences in $v\sin i$ and effective temperature). Our $N(\text{Li})$ abundance determination is 0.14 dex lower than their abundance value, however their method relies upon measuring metal line breadths. Stuik, Bruls & Rutten (1997) showed that even large amounts of spot coverage will have little effect on the measured lithium abundance. A study of the lithium equivalent width variation on the K0 dwarf AB Dor (Hussain, Unruh & Collier Cameron 1997) showed that a spot of exaggerated size (25°) could produce a variation of $30 \text{ m}\text{\AA}$. Such an error would account for the difference in measurement compared with the Soderblom, King & Henry (1998) value given changing starspot patterns, however spot groups are generally not localised, so this estimate represents an upper limit.

The rotational velocity and lithium abundance of PZ Tel lie at or near the peak of the distributions for similar-mass stars in the 50 Myr old Alpha Persei, 50-90 Myr old Blanco 1 and 100 Myr old Pleiades open clusters (Soderblom et al. 1993a, Jeffries & James 1999 and Soderblom et al 1993b). Moreover, for the mass of PZ Tel, its $v\sin i$ and Li abundance values lie considerably above any similar-mass star in the 250 Myr NGC 1039 cluster (Jones et al. 1997). Given the current rotational spin-down and lithium depletion paradigms, it is fair to infer that PZ Tel is most probably younger than 250 Myr and at least as young as the three younger clusters mentioned above.

In conclusion, we can find no physical evidence to suggest that PZ Tel is older than about 50 Myr or so, and indeed, is far more likely to be a pre-main sequence object of order 20 Myr.

5.5 Imaging

We use the technique of least squares deconvolution, first implemented by Donati et al. (1997), to derive an average line profile from the large number of photospheric metal lines available in each echellogram. This technique was successfully applied to $m_v = 11-12$ G dwarfs in the α Persei cluster (Barnes et al. 1998). Our implementation of this method, SPDECON, now propagates errors to give an estimate of the output S:N and hence multiplex gain. The S:N ratios of the input files and output deconvolved profiles are summarised in Table 5.3. The free spectral range of the spectrographs meant that 4990 images of 2832 lines were available for the AAT data. For the SAAO, (09/07/98) data with the spectrograph at the red setting, 1587 images of 1066 lines were available, while on 12/07/98 in the intermediate setting, 3012 images of 2057 lines were available.

The Doppler imaging code, DoTS, uses a two temperature model, with a completely spotted photosphere, and an immaculate photosphere. Each pixel can take a spot occupancy value ranging from unity to zero corresponding to the two cases respectively. The photospheric standard is chosen to be of the same spectral type as PZ Tel (Gl 615) whereas the spot template is an M3 (HD 119850) dwarf. Unfortunately the deconvolved profile of Gl 615 has an anomalously small EW. This arises because Gl 615 is in fact a metal poor old disc star with $[\text{Fe}/\text{H}] = -1.27$ (Eggen 1998). The deconvolved profile of Gl 472 (K1V) is almost identical to that of Gl 615 in all but EW. Since Gl 615 is the only star observed with all data sets, it was scaled to have the same EW as Gl 472 for consistency. This procedure is justified because even moderate changes in the local intensity profile shape have little effect on the profile shape of PZ Tel which is dominated by rotational broadening (see below). The spectra of both the spot and photospheric template stars are deconvolved using the same line list as for the target, and scaled according to the continuum intensity at the same mean weighted wavelength as the target. The central wavelength defined by Equation 2.15 is different for the template stars when compared with that of the target spectrum (d_i is the central depth of the synthetic unbroadened line in question, s_i is the S:N ratio of the line taken from the variances in the input spectrum or a scaled standard continuum, and w_i is the wavelength of the pixel in the spectrum). This is because of the slightly different continuum shapes, especially in the case of the M dwarf template. The PZ Tel spectra give $\langle w \rangle = 5272.6 \text{ \AA}$, with the difference being small for the G dwarf template ($\simeq +33 \text{ \AA}$, AAT), but larger for the M dwarf template ($\simeq +220 \text{ \AA}$, AAT). The

Table 5.3: Table showing input and output S:N ratios for least squares deconvolution. Note the gain for the SAAO 12/07/98 is greatest. Input data with a significantly lower S:N, sustains a higher gain from the LSD process.

Data set	Input S:N ratio	Least squares S:N ratio	Multiplex gain	Effective no. of lines
SAAO 9th	46.5 ± 5.9	1209 ± 153	26.0	4990
AAT 10th	75.9 ± 17.3	3502 ± 844	45.9	1587
SAAO 12th	36.6 ± 8.3	1375 ± 302	37.6	4990
AAT 12th	72.5 ± 21.5	3305 ± 998	45.6	3012

equivalent widths (EW) of the profiles are corrected for and scaled using continuum intensities computed from ATLAS9 (Kurucz 1993) model atmospheres. As the template spectra are narrow compared with the Doppler broadened profile of PZ Tel, the effect of slightly different mean centroidal wavelengths and hence limb-darkening-coefficients is negligible. For example, in order to test the sensitivity of the details of the model atmosphere used to generate the local intensity profiles, Ramseyer, Hatzes & Jablonski (1995) used a square shaped local intensity profile. They found no substantial difference in the $v \sin i$ parameter for the star in question (V471 Tau) determined using a line of such extreme shape.

5.5.1 Dual-site observations

Multi-site observations pose a problem to Doppler imaging in that the profiles from individual sites are of different resolution and cover different wavelength ranges. The CCDs have different pixel sizes, and the resolutions of the two spectrographs also differ. We use the deconvolved profile of a slowly rotating standard star to derive the local intensity profiles for each pixel element on the stellar surface, at each observation phase.

The dual-site nature of the observations requires slight modification of DoTS to allow for independent look-up-tables (LUTs) from which local intensity profiles are calculated, for each data set. The maximum entropy and χ^2 fitting routines within DoTS give the profiles a weighting according to the S:N ratio of the line in question. It is therefore necessary to artificially change the ratio of the weights in one data set relative to those of the other. Failure to take this into account will result in underfitting of the lower

resolution, lower S:N ratio data set.

A factor, γ may be introduced such that the combined variances of the two data sets is given by $\sigma^2 = \gamma\sigma_a^2 + (1-\gamma)\sigma_b^2$. The constants, σ_a and σ_b represent the mean errors of the SAAO and AAT data sets respectively. For data set 1, $\gamma = 0.69$ and for data set 2, $\gamma = 0.56$. These values were determined arbitrarily by decreasing the size of the errors on the SAAO data set. Pushing the entropy regulated fits to a $\chi^2 \simeq 1$ then ensures that the SAAO data is given a greater weighting in the final images. This procedure must be carried out carefully to ensure that the SAAO data is not over-fitted, thereby introducing spurious noise features into the final images.

5.5.2 Determination of system parameters

System parameters can be determined empirically by minimisation of either spot area (i.e. in the reconstructed images) or minimisation of the χ^2 fit to the data. Determination of the best-fitting values for the physical parameters such as radial velocity, v_{rad} , $v\sin i$ and EW using the spot area minimisation method have been outlined in detail in Collier Cameron & Unruh (1994). The pseudo-entropy parameter, spot area, is a good method for empirical determination of these parameters when the S:N ratio of data is of order a few hundred, thereby minimising spurious features due to noise. Tests on synthetic data reveal that spot area minimisation tends to overestimate the known $v\sin i$ by $\simeq 2 \text{ km s}^{-1}$ (see Chapter 3), resulting in a more ‘V’ shaped fit to the data, theoretically resulting in underestimation of low-latitude features, and overestimation of polar features. In practice the effects on Max-Ent reconstructions are small (demonstrating the robust nature of the Max-Ent process for small variations in the stellar parameters), provided the image is relatively well constrained by the data.

The χ^2 minimisation method is similar to the spot area minimisation method. After obtaining initial estimates of v_{rad} , $v\sin i$ and EW, we hold two parameters constant and vary the third over a range of values. A large number of Max-Ent iterations are performed in an attempt to converge to a deliberately unattainable χ^2 . The results are shown in Figure 5.1, and compare the two methods for the first set of data (10/07/98) at the AAT. We conclude that the spot area method introduces systematic errors, and that minimisation of χ^2 is a more satisfactory method for spectra of higher S:N. Listed in

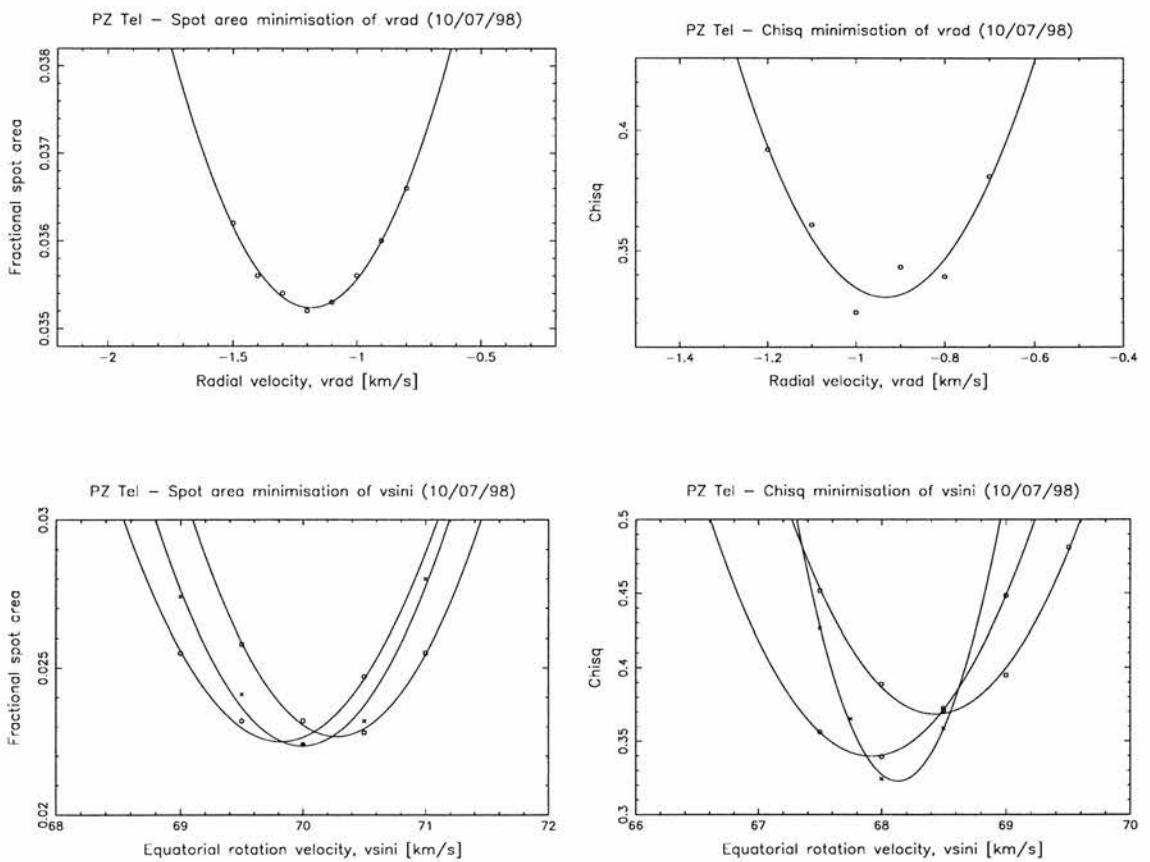


Figure 5.1: PZ Tel parameter optimisation examples for AAT data (10/07/98). Left: Spot area minimisation of radial velocity (top) and projected equatorial rotation velocity (bottom). Right: Similarly for χ^2 minimisation. The minimised equivalent width of the combined photospheric and spot local intensity profiles is 0.1233\AA .

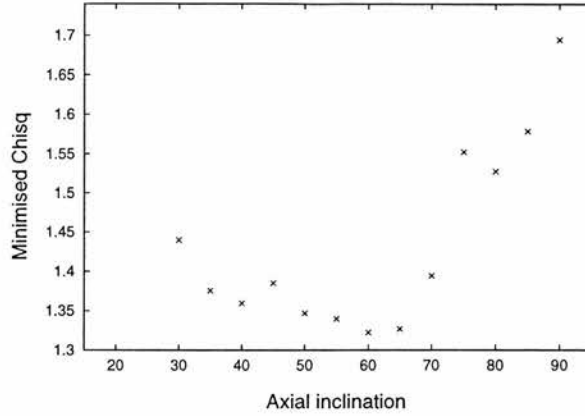


Figure 5.2: Inclination determination for PZ Tel using the combined data set for 09,10/07/98. A minimum value for χ^2 is found at $i = 60^\circ$, however the maximum curvature above this point indicates an inclination of $\sim 65^\circ$.

Table 5.4 are the best fit parameters for each data set. We adopted $v \sin i = 68 \text{ km s}^{-1}$ for PZ Tel. The minimum χ^2 for the SAAO 12/07/98 data set at the adopted $v \sin i$ occurs at a slightly higher EW than that at the empirical $v \sin i$.

DoTS makes heliocentric radial velocity corrections, and further small corrections due to shifts of the CCD and spectrograph were made by deconvolving each target spectrum with telluric line positions included in the mask. Subtraction from the least squares profiles obtained from the photospheric lines mask alone gives a narrow lined telluric feature. Cross-correlation against a reference spectrum (the first spectrum of the series) then allows the small shifts of the spectrograph to be removed. The absolute value of the internal velocity corrections was zero point corrected by fitting a gaussian to the first telluric feature. These relative shifts are small for UCLES with a standard deviation of $\simeq 0.1 \text{ km s}^{-1}$ but are larger for GIRAFFE, at typically $\simeq 1.5 \text{ km s}^{-1}$. For the AAT data sets we find radial velocities of -0.9 km s^{-1} and -1.2 km s^{-1} for 10/07/98 and 12/07/98 respectively. For the SAAO data sets we find radial velocities of -2.8 km s^{-1} and -3.2 km s^{-1} for 09/07/98 and 12/07/98 respectively. The data from each site covers approximately the same phase range at each epoch, although a slight discrepancy clearly exists between the two sites. Differences between the two nights at a given site may be attributable to the slight differences in phase coverage, and/or evolving starspot features.

The slight discrepancy which exists between the radial velocities measured at the

two sites may be due to starspot asymmetries in the profile, as the phase coverage is both incomplete and different at each site. Our local intensity profiles determined from spectral standards are also zero point shifted by fitting a gaussian. Errors between these corrections for each site are also one source of systematic error, as the deconvolved template spectra are not perfectly symmetrical. These values are slightly different to the radial velocity measurement made by standard procedures as given in §5.3.3 & §5.4. However we are using high S:N deconvolved profiles over a different spectral range.

Axial inclination is a notoriously difficult parameter to determine for single stars. Using the HIPPARCOS distance, the apparent magnitude and temperature T_{eff} yields an inclination of $71^\circ < i < 90^\circ$. The Barnes-Evans relation (Barnes, Evans & Moffett 1978) offers a further means of determining the stellar inclination. Using the O’Dell & Collier Cameron (1993) re-calibration of the Barnes-Evans relation for B-V colours, taking $B-V = 0.78$, and the brightest recorded value (Innis et al. 1990) of $m_v = 8.36$ yields $\sin i$ of 1.03 ± 0.08 . This is in good agreement with the temperature-luminosity value. A high degree of global spot coverage on the surfaces of active stars, as found by O’Neal & Saar (1998) from TiO bandhead strengths for a number of stars, could have serious implications for inclination determination. Although B-V is fairly insensitive to small temperature changes, the absolute magnitude will decrease when significant spot filling factors are considered. This has the effect of underestimating the stellar radius as discussed by Cameron & Foing (1997), which would result in overestimates of the axial inclination. Given that we see prominence systems in absorption at high axial distances, it is nevertheless likely that the inclination is relatively high.

A further possibility for axial inclination determination exists. We have used a fake image to create a time-series of profiles for the same star at different inclinations. We find that minimisation of χ^2 as described above reproduces the correct inclination at each latitude below 60° . Above this inclination, an increasing bias to lower inclinations is found. The correct inclination is given in all cases by the effective maximum curvature just above the minimum in the χ^2 vs inclination relation, and can satisfactorily be determined by eye. We found a best-fit to the data for $i = 60^\circ$, whereas for higher axial inclinations, surface structure became banded. For physically higher inclinations, attempting to fit the data results in a stronger polar cap and weaker low-mid latitude features. The region where the gradient in the χ^2 as a function of latitude plot (see Figure 5.2) changes most rapidly near the true χ^2 minimum is in the region close to 65° . When considering sys-

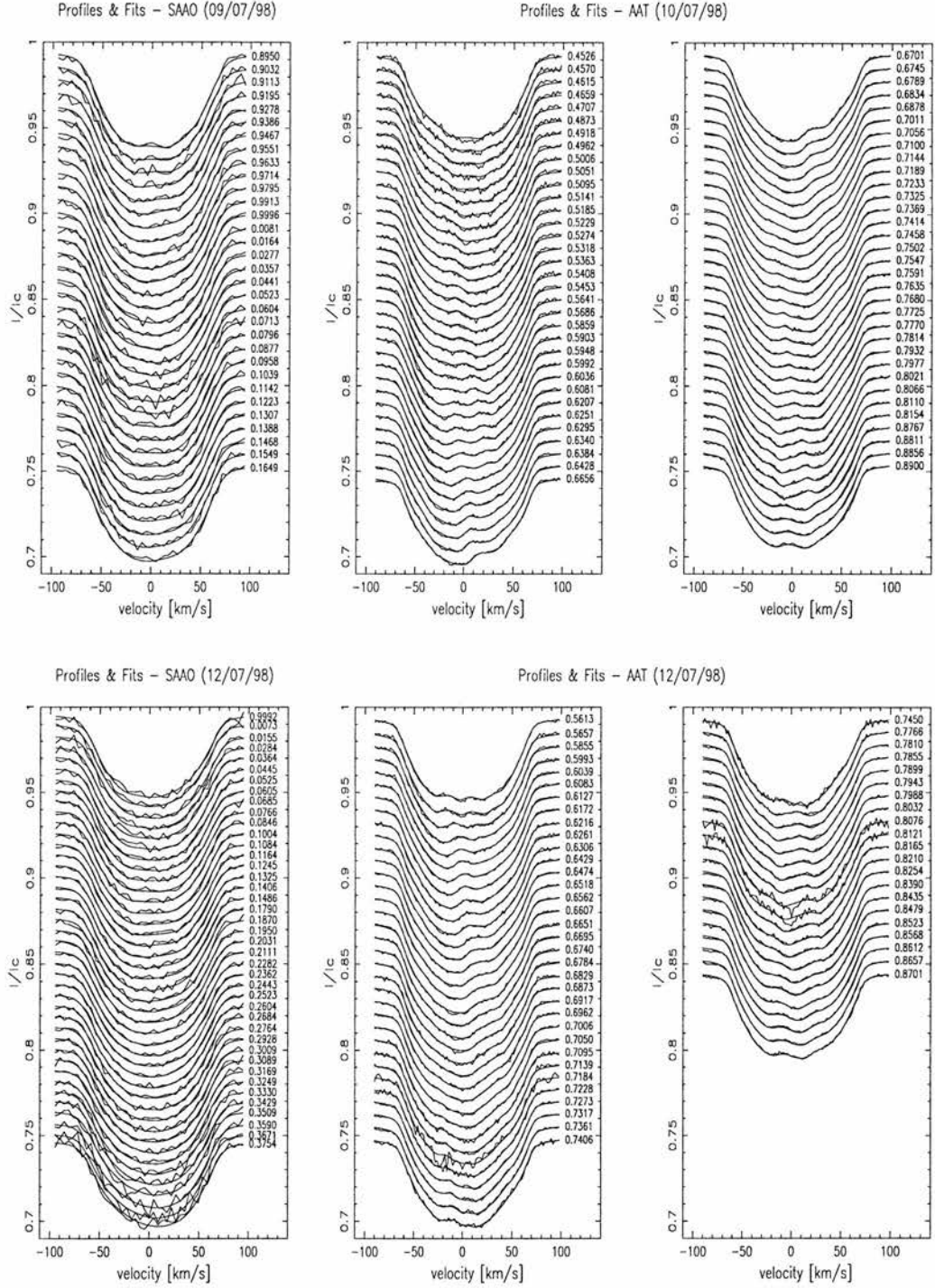


Figure 5.3: Profiles and Max-Ent fits to data for PZ Tel. The velocity increments are determined by the size of the CCD pixels in each case. Top: Sutherland 1.9m (4.5 km s^{-1}), Bottom: AAT (2.0 km s^{-1}). Note that the first few spectra have a lower S:N ratio, and so have a lower weighting in the image reconstructions. This accounts for the under-fitting of these profiles.

Table 5.4: Best fit parameters. The values for the AAT are consistent from night to night. The difference in EW for the two SAAO data sets are due to different settings of the spectrograph on each night, and hence different wavelength coverage. The $v\sin i$ values are remarkably stable, hence a fixed value of 68 km s^{-1} was adopted

Empirical parameters				
Observatory	Date	EW [Å]	$v\sin i$ [km/s]	v_{rad}
SAAO	09/07/98	0.1045	67.5	-2.8
AAT	10/07/98	0.0810	68.0	-0.9
SAAO	12/07/98	0.0782	67.0	-3.2
AAT	12/07/98	0.0826	68.0	-1.2
Adopted values				
SAAO	09/07/98	0.1045	68.0	-2.8
AAT	10/07/98	0.0810	68.0	-0.9
SAAO	12/07/98	0.0789	68.0	-3.2
AAT	12/07/98	0.0818	68.0	-1.2

tematic errors in the inclination determination as mentioned above, the Barnes-Evans and Max-Ent inclination determinations are brought into closer agreement. There are clearly also local minima in Figure 5.2 at 40° and 80° . These minima may be due to incomplete phase coverage and finite S:N ratios in the data sets, and it is unclear whether the χ^2 may be biased at other inclinations. Since errors of $\pm 10^\circ$ mainly only have an effect on the spot filling factor as a function of latitude we adopted $i = 60^\circ$ for the purposes of image reconstruction.

5.6 Results

5.6.1 Images and Differential Rotation

The least squares deconvolved profiles are shown in Figure 5.3. Figure 5.4 shows the maximum entropy reconstructions for the two epochs. Features are clearly reproduced

in both data sets. The weak feature at longitude 325° in both images is real, and is due to the weak features seen crossing disc centre at phase ~ 0.1 in the SAAO data. An increase in the value of γ increases the contribution from the SAAO data set slightly, thereby enhancing the feature at 325° . No other features appear in the images at the phases of SAAO observations indicating that the lack of features at these longitudes is real and not a result of under-fitting the SAAO data. Although the two sets of observations are only separated by two days, we attempted a latitude by latitude cross-correlation of the surface features in an attempt to derive possible differential rotation patterns. The cross-correlation (Simkin 1974 and Tonry & Davis 1979) was performed in such a way as to account for the continuous nature of a constant latitude strip. We fitted a quadratic polynomial to the cross-correlation function peak in order to obtain sub-pixel resolution in our shift measurements. We cross-correlated in the longitudinal range 48° to 150° (phase range (0.583 to 0.867) which includes common phase coverage from the AAT. The grey-scale plot of Figure 5.5 (left) shows the cross-correlation and reveals that the equatorial latitudes have pulled ahead of the mid-latitude-polar regions. The line-plot represents the peak of the correlation at each visible latitude. The solar differential rotation as a function of latitude can be described as

$$\Omega(l) = \Omega_0 + \alpha \sin^2(l) \quad (5.2)$$

to first order. For the synodic solar rotation period, the appropriate constants are $\Omega_0 = 0.235 \text{ d}^{-1}$ and $\alpha = 0.052 \text{ d}^{-1}$ (Lang 1992). The solid line in Figure 5.5 (right) is a least squares fit of this function to the computed longitudinal shifts. The FWHM of the cross-correlation peak at each latitude was used to weight the χ^2 fit to the data, the average value being 2 pixels, or 4° of longitude. Latitudinal smearing of features, an effect which increases toward the equatorial regions reflects the greater uncertainty in the position of features which cross the absorption profile quickly. Strictly speaking, this means that the use of a χ^2 fit is not valid because the data points have correlated errors due to this smearing. In an attempt to reduce this problem, we estimated (from synthetic data sets) a correction to the FWHM of the cross-correlation peak due to latitudinal smearing. The degree of blurring (FWHM in latitude) amounted to (~ 2 pixels at the equator, ~ 1.2 pixels at 70°). The existing uncertainties on each point used in the cross-correlation were hence multiplied by these relative correction factors. A $\cos(l)$ correction is also required for the Mercator projection, since cross-correlation of high latitude strips represents a smaller

surface area. The equation representing the latitude dependent rotation for PZ Tel is given by:

$$\Omega(l) = 6.650 + (0.0749 \pm 0.0123) \cdot \sin^2(l) \quad (5.3)$$

Since latitudes below -30° are relatively featureless (see Figure 5.11, they are not included in the plot and the subsequent fit. Latitudes above 60° are also excluded as the polar regions are densely spotted and cross-correlation shifts can be spurious. The range of values given in Equation 5.3 represent the uncertainty in the fit. The larger value of $d\Omega$ represents a fit to all latitude shifts between -30° and 60° . The lower limit is the same fit but excluding latitudes -10° and 10° , as these are the regions of greatest latitudinal uncertainty in our Doppler images. This is due to the pixel area weighting scheme in the entropy fits. Since the pixel areas are largest near the equator, there exists a maximum penalty for putting spots near the equator, and so features may appear at slightly higher latitude. Equation 5.3 yields a value for the difference in rotation rate between the equator and polar latitudes. For PZ Tel, we find that the equator laps the poles once every $2\pi/d\Omega = 86 \pm 14$ d. The value of the differential rotation ($d\Omega/\Omega$) is (0.0094 ± 0.0131) , and indicates that PZ Tel rotates almost as a solid body.

5.7 Deconvolved subsets

At this juncture it seems pertinent to investigate the consequences of deconvolving only subsets of data. This provides a means of determining the reliability and changes in images constructed from least squares deconvolved data sets. There are three obvious ways of subsetting the data:

- 1) Select lines only with a range of given excitation potentials.
- 2) Deconvolve using the maximum number of suitable/available lines, but splitting the number of profiles used in half and creating two independent data sets by taking alternate spectra
- 3) Deconvolve over given wavelength ranges.

The former of these methods has not been tested because of a fundamental problem with fast rotators. Since many of the lines are blended, the use of excitation potential as

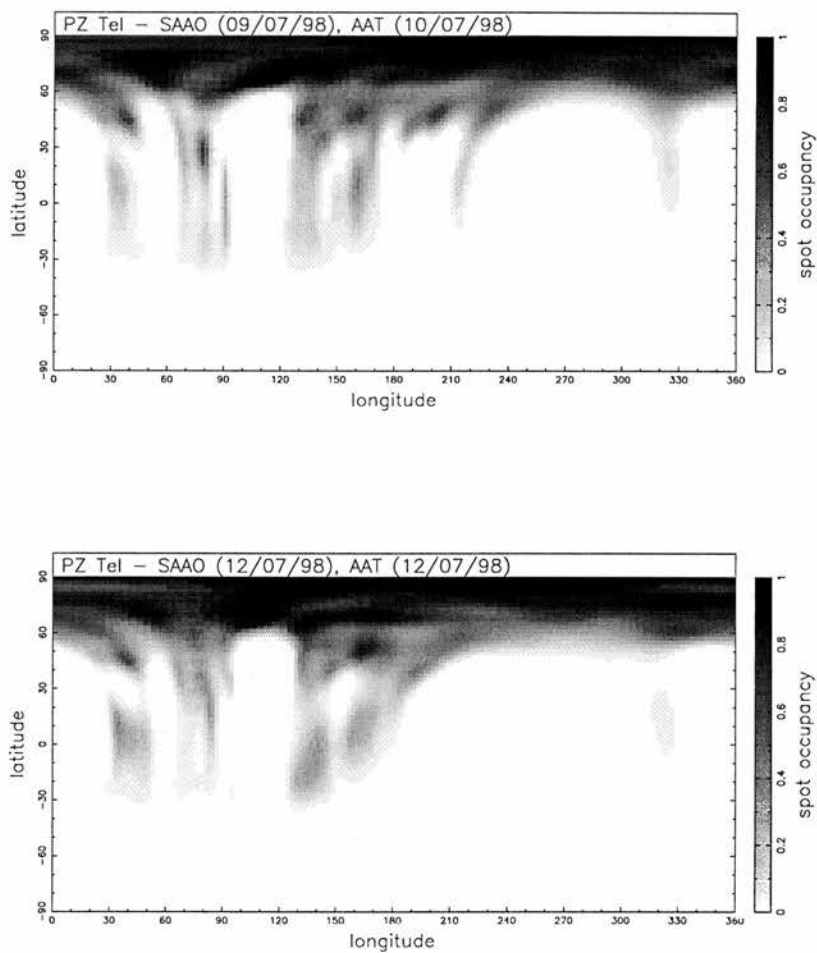


Figure 5.4: Max-Ent image reconstructions of PZ Tel from 09,10/07/98 (top) and 12/07/98 (bottom). Note the similarity of the two images which are effectively two rotation cycles apart. The weak feature at longitude 325° is real, and is associated with the first weak feature seen in the dynamic spectra for the SAAO data set on both 9th July and 12th July.

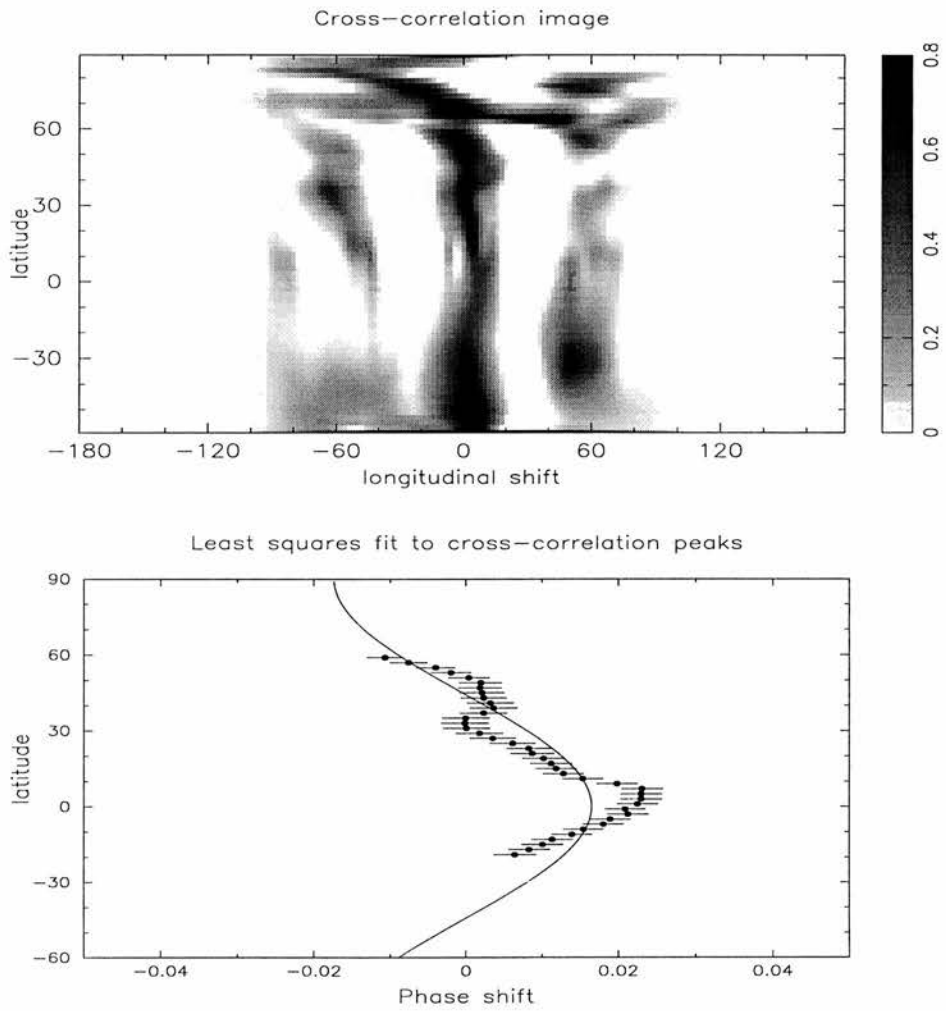


Figure 5.5: Top: Cross-correlation image of the two Max-Ent reconstructions of PZ Tel. Bottom: Least squares fit to cross-correlation peak (see text).

a line-selection criterion may result in contamination from neighbouring lines which have the incorrect excitation potential. Although the least squares process should be relatively immune to the effects of missing lines in a given range, the contamination of pixels due to rotational blending means that a comparison is not plausible.

In Chapter 4, I have already demonstrated that subsetting the data according to 2) results in essentially the same image. Any differences which were shown to be small will then be the result of relatively noisy profiles combined with a bigger phase sampling interval (i.e. less information is available). Since the rotation period of PZ Tel is approximately half that of He 699 for example, and is much brighter, differences between independent data sets in this manner are expected to be smaller.

Here we attempt to split the PZ Tel data taken at the AAT into two wavelength ranges. This will allow independent determination of the spot filling factor as a function of wavelength. Also further reliability of the differential rotation measure can be determined by cross-correlating the sub-setted maps. The red orders of a given échellogram have a greater signal and therefore weighting in the least squares process which out-balances the greater number of lines found in the bluer orders. Each échellogram was therefore split in two with the first 22 orders being deconvolved to form a ‘blue’ dataset and the subsequent 29 orders to form a ‘red’ data set. The blue data set has a mean weighted wavelength of 4768.03 Å from 3527 images of 1944 lines while the red data set has a mean weighted wavelength of 5676.10 Å from 1463 images of 942 lines. After correction of the depth of the average profile from each time series, the relative S:N is still 1.3 times greater for the red data set. This allows the effect of slightly different S:N ratios to be examined with respect to the apparent image quality.

The images are remarkably similar with little apparent difference in the surface structure between the red and blue reconstructions. Figure 5.6 shows collapsed longitude plots for the maps which in general show the same results except for the low latitude features in the 12/07/98 reconstructions. It is noteworthy that in all reconstructions of PZ Tel on 12/07/98, compared with the features corresponding to those seen on 10/07/98 appear more blurred. It may be that the individual spots which are seen on the 10th have evolved and become larger. It is more likely is the fact that the data from the 12th is noisier with some profiles having a significantly lower S:N ratio due to patchy cloud cover during observing. The feature at longitude $\approx 135^\circ$ is responsible for the apparent discrepancy

of the mean latitudinal features at low latitudes on 12/07/98. Since this feature appears more evenly distributed about the equator in other maps it is likely that the solution in this case was better constrained by placing the spot further away from the equator where the entropy penalty is lower (see earlier in this chapter).

Determination of the degree of differential rotation was carried out in the same manner as for the full data set. The blue data set yields equator-pole lap times of 95 d to 156 d (125.5 ± 30.5 d), whereas the red data set shows a greater degree of uncertainty with lap times of 81 d to 197 d (132.5 ± 44.5 d). Combining these independent results yields an equator-pole lap time of 129 ± 38 d. This is in reasonable agreement when compared with the result from the single data set of 86 ± 14 d. As mentioned above 100 d is not necessarily a true upper limit, and as such neither is the ‘combined’ 167 d (i.e. $129 + 38$ d) upper limit. A better idea of the measurement error is however obtained, and the conclusion of near solar differential rotation still holds, albeit with greater uncertainties given the lower S:N ratio of the input data.

5.8 Discussion

The location of PZ Tel in the CM diagram appears to be in conflict with the spectral classification of Houk (1978). There are however a number of factors which may affect the location of a late-type star in the CM diagram. Rotational modulation due to starspots will cause a star to change its apparent temperature and luminosity. Since we do not know the colour and brightness of the immaculate stellar surface, the exact location remains uncertain. Spruit (1982) showed that for a star with a changing spot filling factor, the location in a CM diagram will change on two timescales, the turbulent diffusion timescale (several days up to a year), and the Kelvin-Helmholtz timescale ($\sim 2 \times 10^5$ yr for the Sun). Changes in the total spot area cause a star to move to higher temperatures at constant luminosity on the Kelvin-Helmholtz timescale whereas a luminosity change at constant temperature results on short timescales. Given that PZ Tel has such a high lithium abundance, a factor which is independent (Stuik, Bruls & Rutten 1997) of even exaggerated global spot filling, it seems unlikely that it should be located significantly closer to the main sequence. Correcting for a mis-determined, mean apparent magnitude due to spots which change on short timescales would move PZ Tel to higher luminosities.

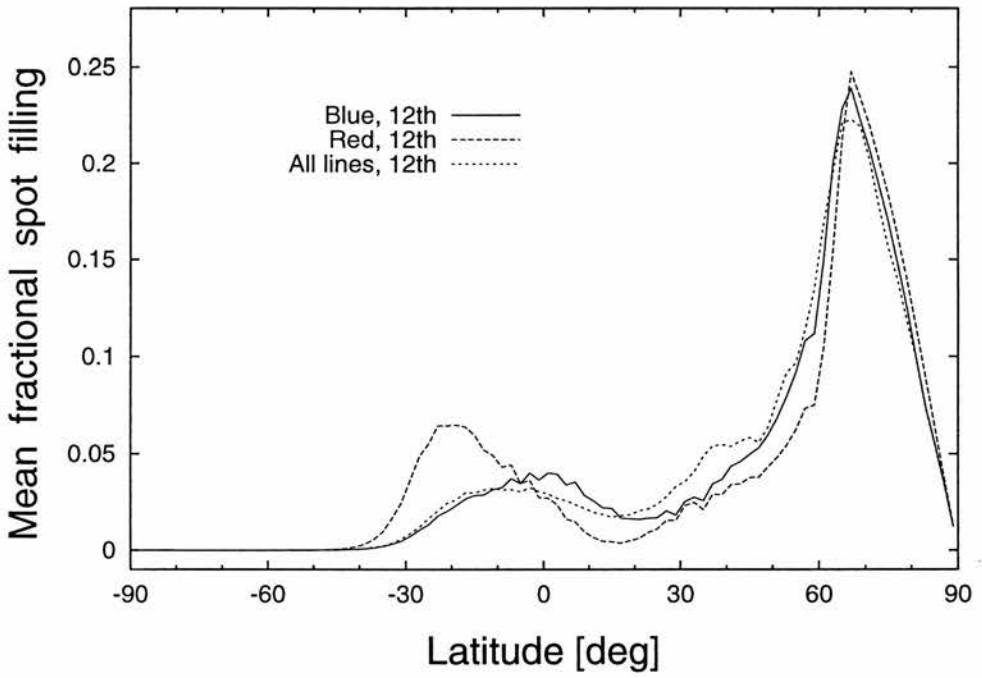
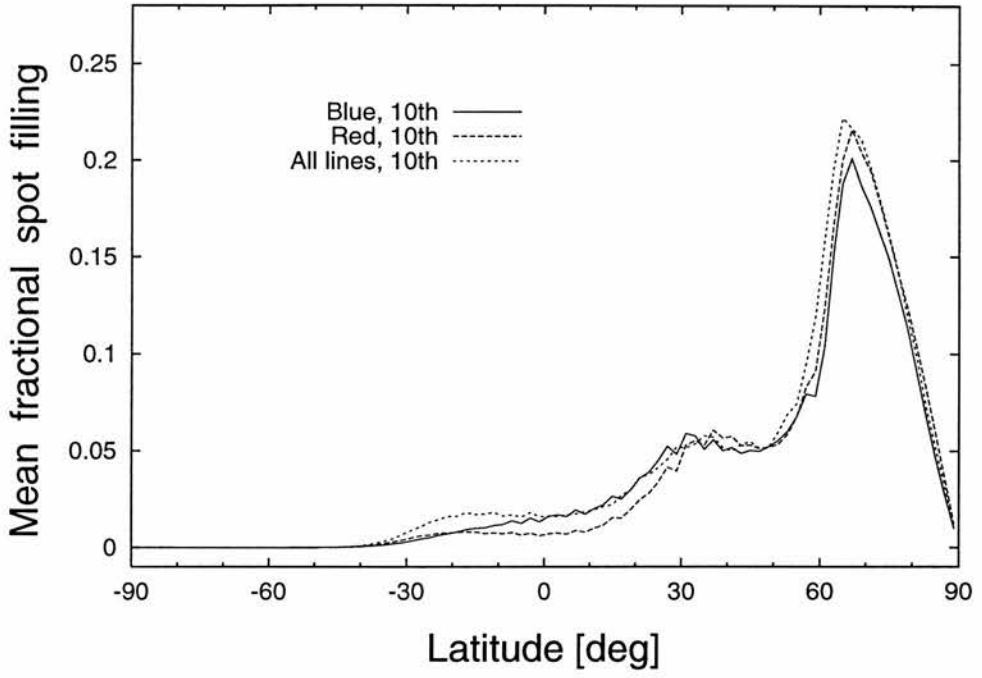


Figure 5.6: Latitude distribution of spots in Red & Blue data sets for PZ Tel

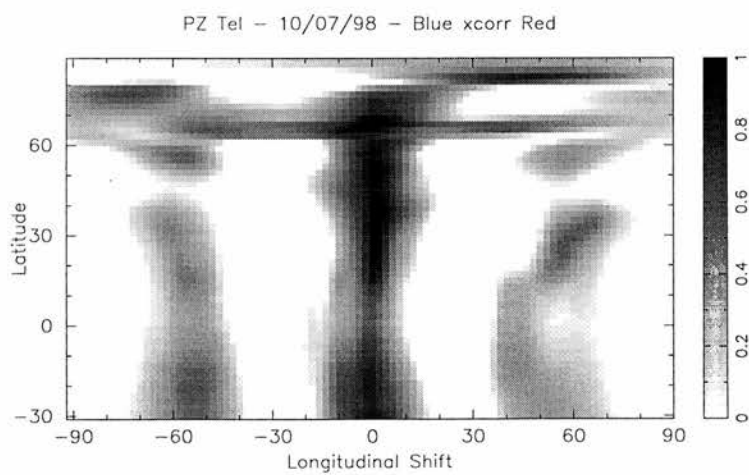
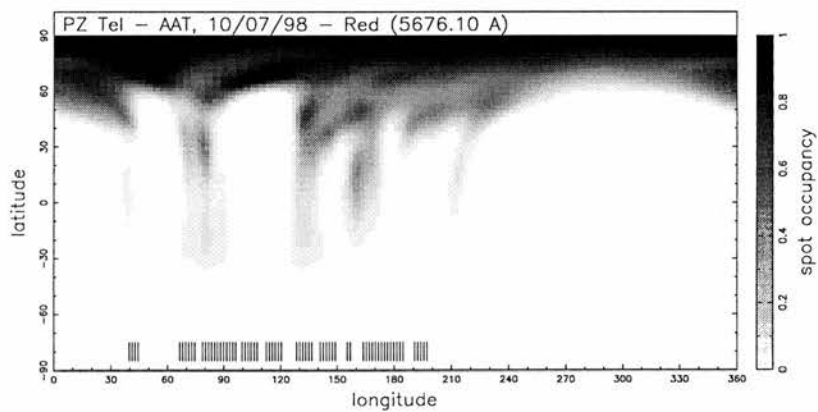
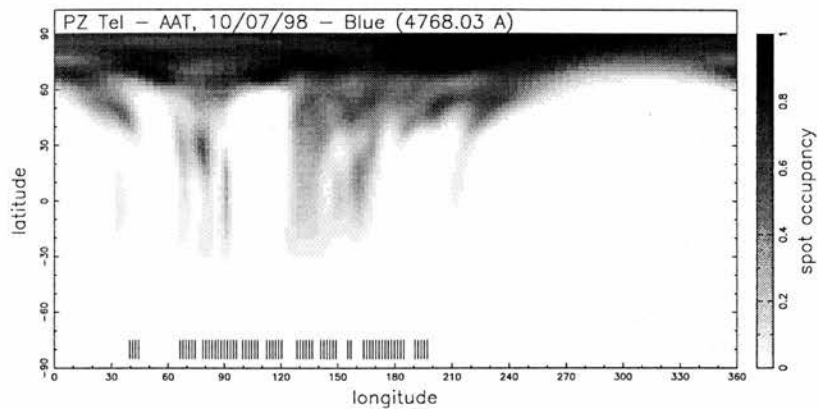


Figure 5.7: 10/07/98: PZ Tel image reconstructions from Red & Blue data sets and cross-correlation image

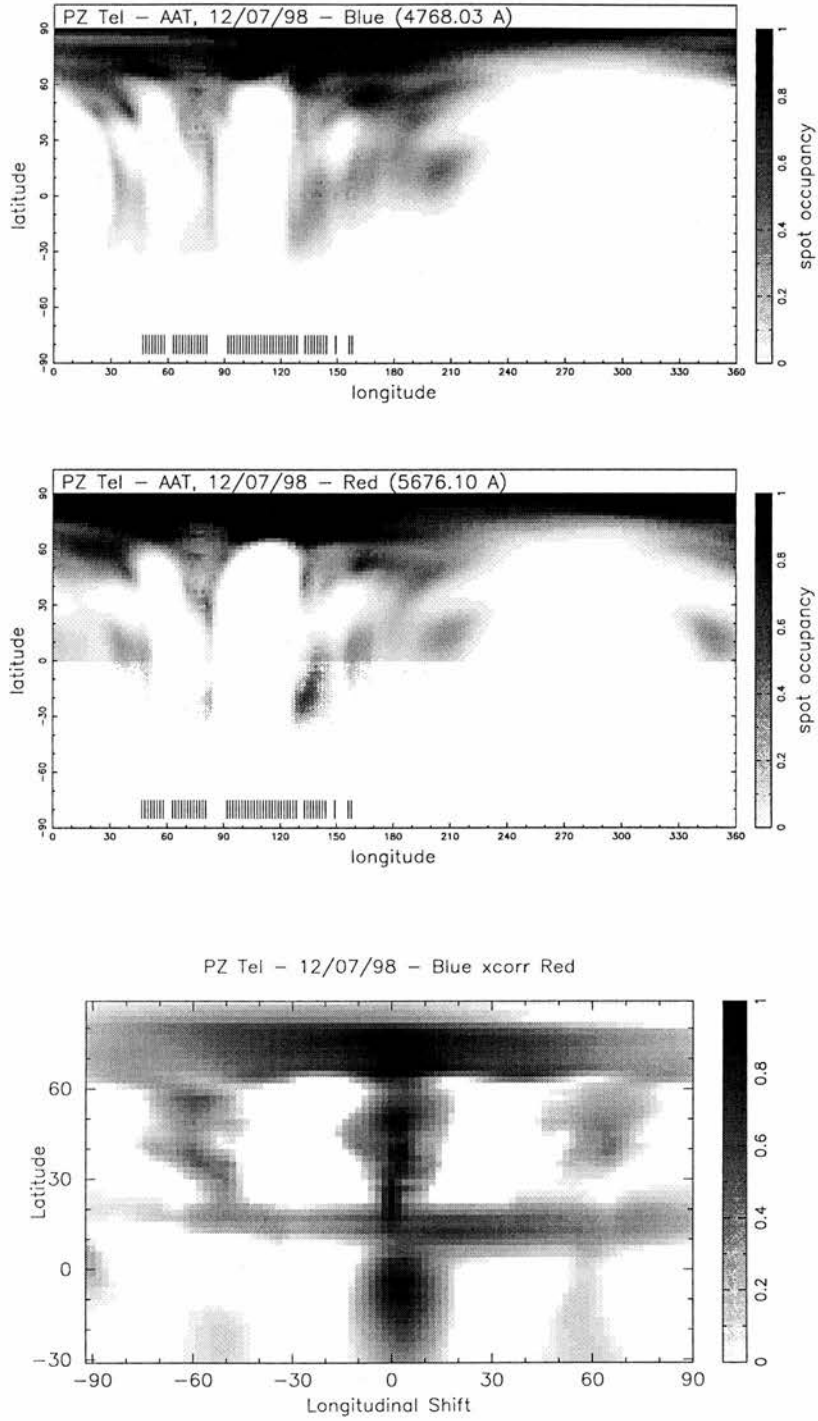


Figure 5.8: 12/07/98: PZ Tel image reconstructions from Red & Blue data sets and cross-correlation image

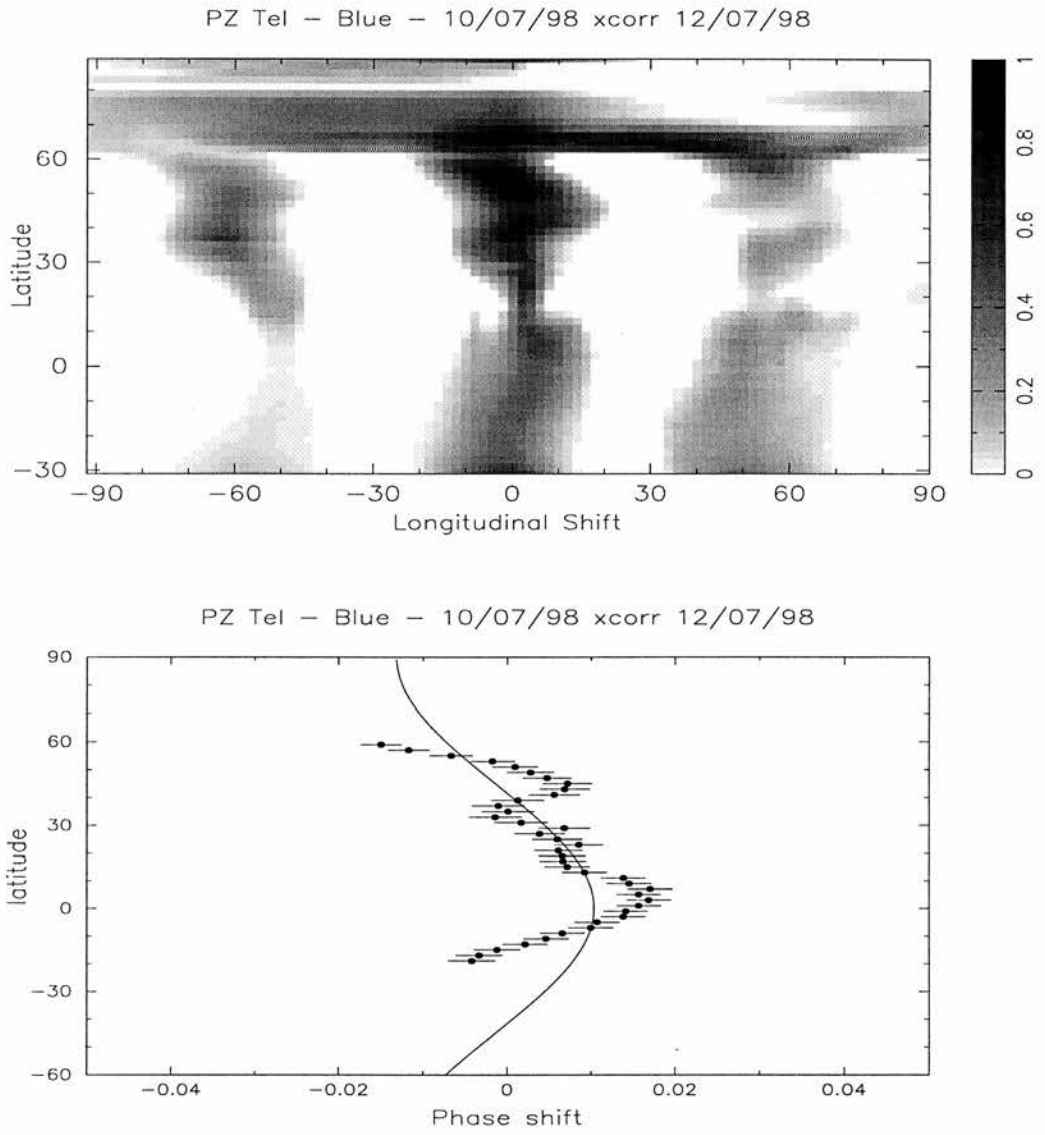


Figure 5.9: Cross correlation of blue images of PZ Tel for 10/07/98 and 12/07/98

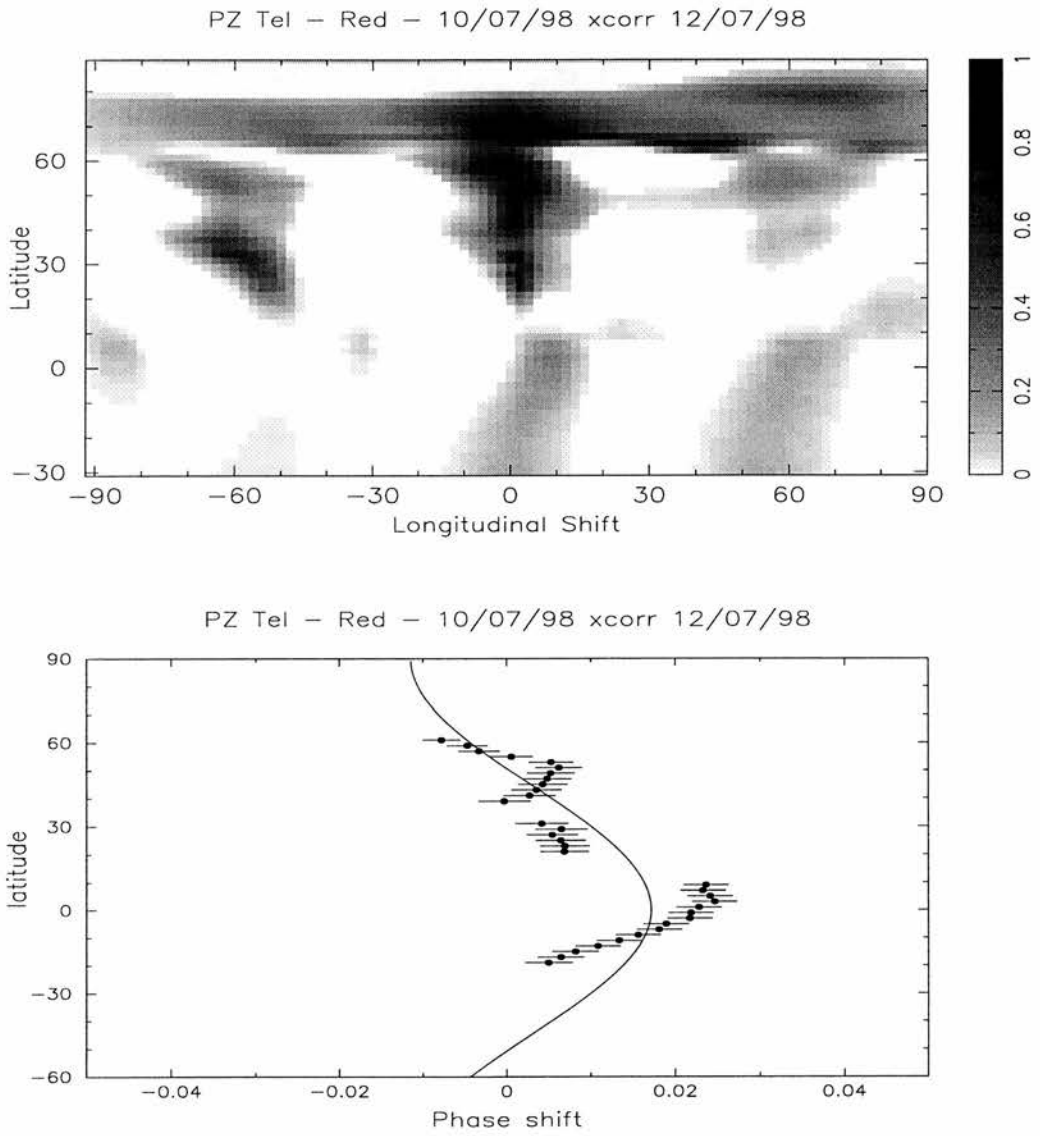


Figure 5.10: Cross correlation of red images of PZ Tel for 10/07/98 and 12/07/98

This would result in a lower age determination and greater mass. Again, given that we do not know the immaculate photospheric level, we cannot determine the significance of this discrepancy, if it exists at all.

The differential rotation timescale, $2\pi/d\Omega = 86 \pm 14$ d, is slightly shorter than that of the Sun and AB Dor (Donati & Collier Cameron 1997), which have corresponding values of 120 d and 110 d respectively. There appears to be a large degree of uncertainty in the cross-correlation, which may indicate a deviation from the simple solar-type rotation as a function of latitude. Perhaps more likely is that errors in the maximum entropy reconstructions have introduced the apparent noise. In any case, we can not obtain a true lower limit on the differential rotation, which given the present range may indicate an equator-lap-pole time of as much as 140 days. Within the large uncertainty, this result adds further support to the idea that differential rotation is at most only weakly dependent on the rotation rate. Recent models by Kitchatinov & Rüdiger (1999) suggest that $d\Omega/\Omega = 0.004 - 0.006$ in the range K5V to G2V for a star with a ~ 1 d rotation period. Although the upper value is not included within our estimated range, there exists a remarkable agreement between the theoretical trend and current observations for PZ Tel, AB Dor and the Sun. What is most important is that Kitchatinov & Rüdiger find $d\Omega$ is almost constant for the range of rotation rates considered, and is only weakly dependent upon spectral type.

These findings are supported by the Mount Wilson survey of chromospheric variations in main-sequence stars, begun by Wilson (Wilson 1978) in 1966. Areas of concentrated magnetic field on the surface of the Sun emit Ca II H & K more intensely than areas where less magnetic field is present, so these lines are good indicators of a global change of magnetic activity. Emission components centred in the Ca II H & K lines vary in magnitude for some of the stars over a cycle similar in length to the Solar cycle. Baliunas et al. (1995) published a review of this long term survey and found that that the majority of stars sampled over the 25 yr survey period showed apparent magnetic cycles of 5-11 yrs. Although periods of 2.5 yr up to at least the length of the survey were discovered, none of the stars with ‘good’ or ‘excellent’ periods were found to exhibit a cycle of less than 7 yrs. The cyclical variations tend to be of irregular period for younger stars, whereas older main-sequence stars such as the sun exhibit smooth variations. This does not necessarily rule out that the same dynamo mechanism may be at work in a large number of stars. Indeed, our results along with the AB Dor and solar results may be additional evidence

that the magnetic field is responsible for keeping $d\Omega$ constant. A constant $d\Omega$ may be important for understanding why the length of the magnetic activity cycle as evinced by the Mount Wilson data and most dynamo theories is independent of the rotation rate.

Further, the value of the shift parameter used to fit the $\sin^2 l$ differential rotation function, indicates the latitude at which the surface rotation matches the photometric period. In terms of phase shift, this function can be written as

$$\phi(l) = (0.0061 \pm 0.0010) + (0.0120 \pm 0.0020) \cdot \sin^2(l) \quad (5.4)$$

Solving equation 5.4 for $\Omega(l) = 0$ yields $l \approx 45^\circ$. Since the parts of PZ Tel above 60° are always in view, and the degree of spot filling is fairly constant at all longitudes, we would expect little if any contribution to photometric variation from these latitudes. This is in approximate agreement with the images, and Figure 5.11 as the greatest concentration of features, which are not always seen by the observer, are located at 50° (i.e. very close to the centre of the projected stellar disc, as $i = 60^\circ$). Caution should be exercised however, as the image reconstructions themselves depend upon the photometric rotation period. The photometric variations may be formed by spots at different latitudes, and this distribution may change with time. Unfortunately, we do not have simultaneous photometric data to further constrain a solution, and compare with an independent spectroscopic solution. The averaged distribution of surface features as a function of co-latitude is shown in Figure 5.11. This clearly shows the greatest spot filling at higher latitudes, especially around 70° .

5.9 Conclusion

PZ Tel poses a difficult case to the observer as its near 1d orbital period makes complete phase coverage at a single site impossible. We have demonstrated that it is possible to use multi-site observations to combat this problem successfully. Although conditions were not ideal, forcing sets of observations at a less than ideal separation of two days with intermittent cloud cover on the second night at the AAT, a successful determination of differential rotation has been possible.

We have presented further evidence confirming the young evolutionary status of

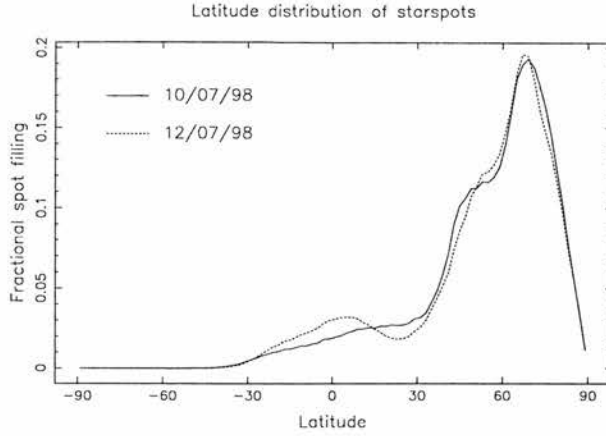


Figure 5.11: Plots of the fractional spot filling against latitude on PZ Tel, for longitudes of 20° to 240° . The spots are concentrated in a wide band of latitudes from 30° to 90° , with a small peak at 50° and a larger peak at 70° . Spots are clearly visible at lower latitudes, but the combination of lower spot-occupancy of each pixel, and greater latitudinal uncertainty results in a smeared out and lower average spot filling below 30°

PZ Tel, in agreement with the findings of other authors. At 15-20 Myr PZ Tel shows many similarities to the well studied 30 Myr old (Cameron & Foing 1997) K0V dwarf, AB Dor. The Max-Ent reconstructions are very similar to those of Donati & Collier Cameron (1997) and Donati et al. (1999a). While these images show that AB Dor has a low latitude band of features centred around 25° , PZ Tel has a similar band at 50° , although it does exhibit features at equatorial latitudes also. Both the magnitude and sense of differential rotation at the photospheric level are known only for these two single stars other than the Sun. Doppler imaging is a powerful tool which has allowed such an undertaking for AB Dor and PZ Tel. Although photometric methods do not allow the sign of the differential rotation to be determined, it has been shown (e.g. Hall 1991 and Henry et al. 1995) that the magnitude of $d\Omega/\Omega$ decreases with increasing rotation rate. Although the exact value of $d\Omega/\Omega$ at a given rotation rate does not agree with the theoretical results of Kitchatinov & Rüdiger (1999), the approach towards solid body rotation increases with rotation rate in the same way. The results for AB Dor and PZ Tel are consistent with the empirical results of Hall (1991). A greater sample of objects at different rotation periods and spectral types is needed before theory and observation can thoroughly be compared, although Doppler imaging by its very nature restricts comparisons to relatively short-period objects.

5.10 Acknowledgement

I would like to thank Dr. D. J. James for help with the lithium line analysis, and corresponding write up, and also for carrying out the observations at the Sutherland 1.9m telescope.

CHAPTER 6

Images of Southern rapid rotators II: Starspot patterns and differential rotation on HD 197890 “Speedy Mic”

6.1 Synopsis

We have secured high spectral and temporal resolution spectra of the rapidly rotating K dwarf, Speedy Mic (HD 197890) at two sites and a common epoch of observations. The 0.38 d axial rotation period and the V band magnitude of 9.33 make it a difficult target for Doppler imaging. To obtain high S:N ratio profiles from 300 s exposures, we apply the technique of least squares deconvolution to the large number of photospheric absorption lines available in each of our spectra. This allows us to derive high resolution maximum entropy regulated Doppler images of the stellar surface. Using these techniques, we also derive radial velocities and accurate projected equatorial rotation velocities which are consistent to within $\sim 1 \text{ km s}^{-1}$.

Our maps reveal one of the most heavily spotted photospheres seen on a rapid rotator, with starspots occurring at all latitudes. At the time of observations, Speedy Mic had no strong polar spot, but shows spots concentrated in low and intermediate latitude bands. We attempt a differential rotation measurement, but lack of sufficient phase coverage only allows determination of an lower limit of 56 days for the time it takes the equatorial regions to lap the polar regions.

Table 6.1: SAAO observations of Speedy Mic in 1998 July

Sutherland 1.9m				
Object	UT Start	Exp time	No. of frames	comments
	1998 Jul 10	[s]		
HR 4390	17:40:20	250	1	B5Vn telluric stand.
HD 119850	18:30:08	1000	1	M3V template
Gl 673	18:53:56	750	1	K5V template
Gl 615	19:11:00	750	1	K0V template
HR 7172	18:28:03	100	1	B2V telluric stand.
HD 171488	19:40:35	750	1	G0V RV STD
Speedy Mic	20:00:00	300	72	Target Star
1998 Jul 11				
HR 7172	21:08:20	80	1	B2V telluric stand.
Speedy Mic	21:15:30	300	43	Target Star
HD 213014	02:15:39	750	1	dG8 RV STD
Speedy Mic	02:33:37	300	15	Target Star
HD 223537	04:18:19	1000	1	G3V
HD 16160	04:40:13	750	1	K3V template

Table 6.2: AAT observations of Speedy Mic in 1998 July

AAT				
Object	UT Start	Exp time	No. of frames	comments
	1998 Jul 9	[s]		
HR 82858	18:56:21	100	2	B5V telluric stand.
HR 4628	19:10:32	300	1	K2V template
HD 16160	19:24:30	300	1	K3V template
HR 472	19:58:00	20 & 30	2	B3V pe telluric stand.
1998 Jul 10				
HD 119850	10:53:34	300	2	M3V template
HR 472	20:10:45	300	2	B3V pe telluric stand.
Speedy Mic	20:16:27	300	3	Target Star / UCLES E31
1998 Jul 11				
Speedy Mic	17:40:31	300	4	Target Star / UCLES E79
Gl 849	18:08:51	600	1	M3.5V template
Speedy Mic	18:21:03	300	8	Target Star / UCLES E79
HR 4628	19:18:36	300	1	K2V template
Speedy Mic	19:27:24	300	2	Target Star / UCLES E79
HD 16160	19:42:52	300	1	K3V template
Speedy Mic	19:51:09	300	4	Target Star / UCLES E79
1998 Jul 12				
Speedy Mic	19:15:05	300	12	Target Star / UCLES E31
1998 Jul 13				
Speedy Mic	19:12:48	300	12	Target Star / UCLES E31
HD 16160	20:30:01	300	1	K3V template
1998 Jul 14				
Speedy Mic	11:31:45	300	12	Target Star / UCLES E79
Speedy Mic	15:48:12	300	16	Target Star / UCLES E31 and focal modifier

6.2 Introduction

Evidence for the young evolutionary status of the late-type star HD 197890, nicknamed Speedy Mic, is well documented. The ROSAT/WFC all-sky survey detected strong EUV emission from a large flare event in October 1990 (Bromage et al. 1992 and Matthews et al. 1994). Previous to this observation, Speedy Mic was not known to be chromospherically active. Subsequent measurements by Bromage et al. (1992) revealed it to be an ultra-fast rapid-rotator with a measured projected equatorial rotation velocity $v \sin i = 120 \pm 20$ km s⁻¹. Further determinations have resulted in $v \sin i$ estimates of 170 ± 20 km s⁻¹ (Anders et al. 1993) and 240 ± 40 km s⁻¹ (Matthews et al. 1994). Cutispoto et al. (1997) found a V_{max} magnitude of 9.33 and a $B - V$ colour of 0.93, which is consistent with a K3V spectral classification. It was however noted that the corresponding $U - B$ and $V - I_c$ colours were too blue and too red respectively. The differences may be due to Speedy Mic being highly active and/or a pre-main-sequence (PMS) object. Favata et al. (1998) find that Speedy Mic is in fact very close to the main sequence indicating late-PMS or zero-age-main-sequence status.

Anders et al. (1993) measured the equivalent width of the Li I 6708 Å line, which is blended with the nearby Ca I 6717 Å line. They used a spectral synthesis method and found an equivalent width of the blended Li 6708 Å of 640 ± 20 mÅ. The corresponding lithium abundance for a K3V - K5V star is $N(\text{Li}) = 3.75 - 3.16$ respectively. Based upon this measurement a spectral type in this range was favoured. Studies by Jeffries (1993a) revealed the presence of H α absorption transients similar to those first seen on the K1 dwarf AB Dor (Robinson & Collier Cameron 1986). The results of our analysis of the H α absorption profile are presented in Chapter 7.

The short rotation period of 0.380 d (Cutispoto et al. 1997) and high $v \sin i$ combined with close proximity (HIPPARCOS distance, 44.5 ± 3.2 pc) have elicited much interest. Even as a rapid rotator Speedy Mic is an extreme case. Despite being well studied, accurate stellar parameters such as $v \sin i$ are still not known with great certainty. Having obtained several sets of time series, we use least squares deconvolution to derive a single high S:N profile from the many photospheric absorption lines available in a single échelle spectrum. We have studied the K0 dwarf PZ Tel in the previous chapter and attempted a measure of the differential rotation pattern from sets of maximum entropy Doppler images of the

stellar surface. A similar analysis is presented for Speedy Mic.

6.3 Observations

Observations were secured at the Sutherland 1.9 m Telescope at the South African Astronomical Observatory, and the GIRAFFE spectrograph on 1998 July 10 & 11. In addition, observations were made on 1998 July 10 - 14 using UCLES at the Anglo Australian Telescope. Observations of the target were separated by observations of standard and template stars, and are recorded in Tables 6.1 and Table 6.2. The 1K x 1K TEK6 CCD was used at the Sutherland 1.9 m Telescope, which with the grating in the red position resulted in a central wavelength in the extracted data of 6520 Å (range: 5027 Å - 9215 Å), on July 10th. On July 11th, the instrument control software had to be reset and it was subsequently found that the spectrograph had shifted resulting in a central wavelength of 6167 Å (range: 5261 Å - 7420 Å). Fewer orders were also extracted since we did not require the reddest orders which contain relatively few absorption features and are contaminated by telluric absorption features. The 2K x 4K MITLL CCD chip was used in conjunction with UCLES, was windowed to 2088 x 2496 pixels, and centred on a wavelength of 5307 Å (range: 4304 Å - 6921 Å).

Weather conditions permitted only a small number of observations at the end of each night only at the AAT. We also carried out observations for another programme which required the E79 grating. Because it was easier and less time consuming to continue using the E79 grating observations on 11/07/98 & 14/07/98 were made using this setup. The centroidal wavelength in this setup is at 5967 Å (range: 4663 Å - 8193 Å). On 12, 13 & 14/07/98, the E31 grating was used at a centroidal wavelength of 5308 Å (range: 4270 Å - 6974 Å).

The same extraction procedure as described in Chapter 5, using ECHOMOP was carried out.

6.3.1 Local intensity profiles

For Speedy Mic, the large number of grating settings used precluded use of the same spectral templates. The shape of the stellar profile is dominated by the broadening, so

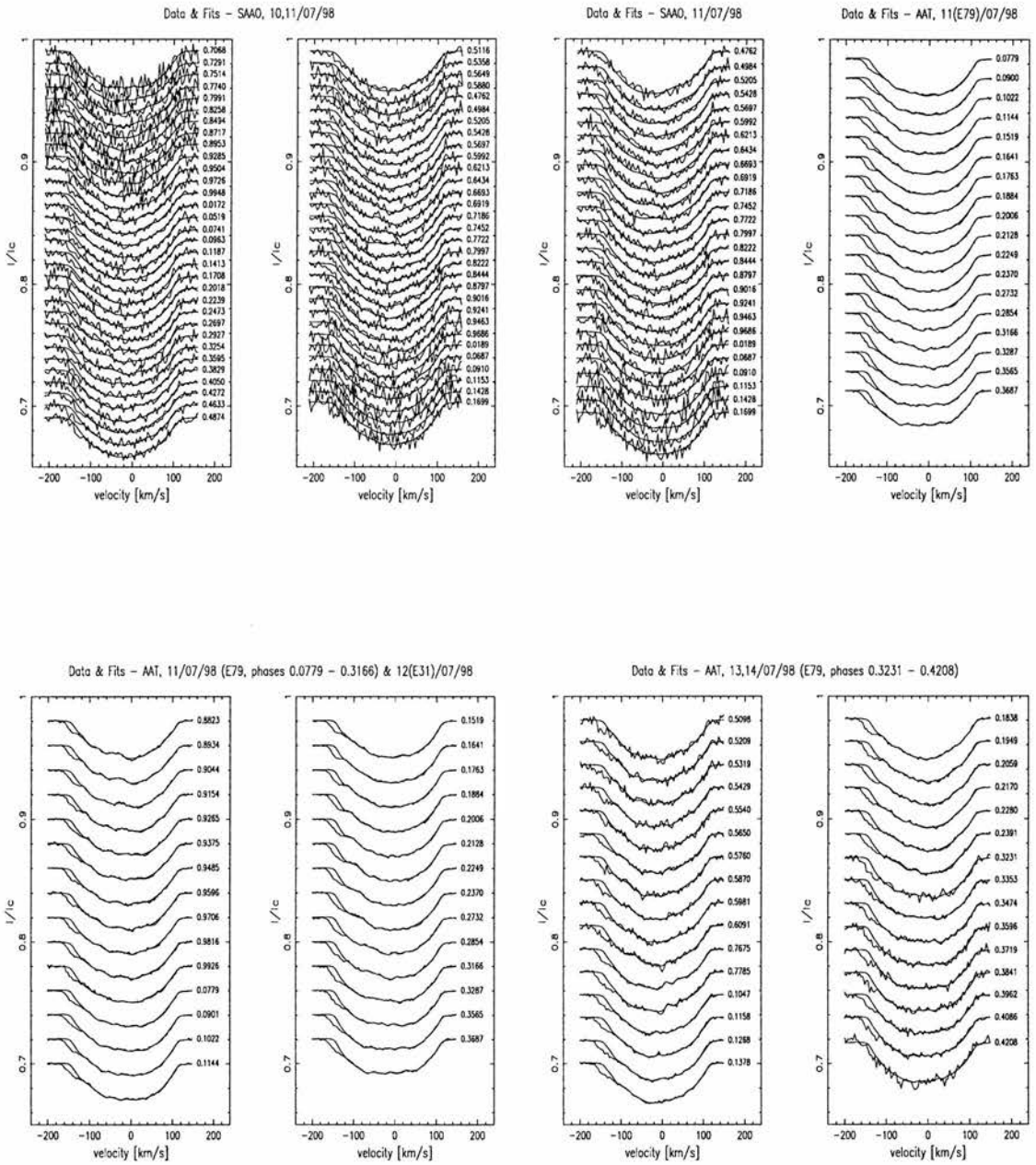


Figure 6.1: Profiles and Max-Ent fits to Speedy Mic data. The profiles pixels are equal to the size of the CCD pixels in each case. Top to Bottom, Left to Right: 10,11/07/98 SAAO data; 11/07/98 SAAO & AAT data, UCLES with E79 grating; 11,12/07/98 AAT data, UCLES with E31 (12th) grating and 13,14/07/98 using AAT, UCLES with E31 (13th & 14th) and E79 (14th) data.

that use of a different local intensity profile of the same spectral type will have negligible effect, as discussed in Chapter 5. The EW of two stars of the same spectral type may also differ slightly due to metallicity differences.

For all grating settings at both sites, we used the K3V standard HD 16160 as the photospheric intensity profile, except for the SAAO 10/07/98 data set where we used HD 125072. All grating settings used the M3V template HD 119850 to represent the spot local intensity profile except for the AAT/E79 data sets where we used Gl 849 (M3.5V).

6.3.2 Continuum fitting

The continuum fitting process is described in detail in Chapter 4. Spline fits to the co-added target frame and narrow lined standards were made with 8 knots for the SAAO data. The AAT data required 11 knots for both the E31 and E79 gratings which exhibit significantly different diffraction envelopes as shown in Figure 6.2.

6.4 Imaging

6.4.1 Least squares deconvolution

The spectra are again subjected to the least squares deconvolution code `SPDECON`. There are between ~ 1000 and ~ 3000 photospheric absorption lines available in our SAAO and AAT data sets. We assume that an échelle spectrum contains the same starspot signatures in all the photospheric Doppler broadened profiles. While the amplitude of the signature may vary from profile to profile, the morphology should remain unchanged. Table 6.3 details the statistics of each data set and the multiplex gain of the deconvolution process.

6.5 Derivation of system parameters

Accurate system parameters, v_{rad} , $v \sin i$ and equivalent width (EW) are required for the purposes of Doppler imaging. As mentioned above, there have been several attempts to measure the $v \sin i$ of Speedy Mic, ranging from $\sim 100 \text{ km s}^{-1}$ to $\sim 280 \text{ km s}^{-1}$ (including errors). Co-addition of all deconvolved profiles for a given data set reveals a profile asym-

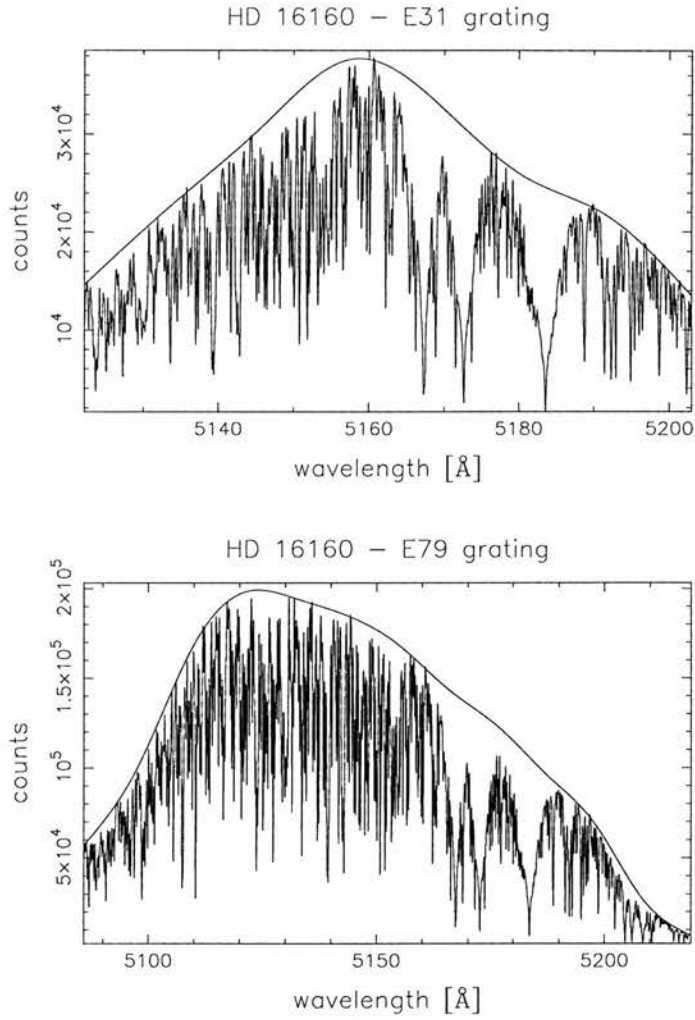


Figure 6.2: Plots of HD 16160 (K3V) spectrum around the same wavelength region taken with the E31 and E79 UCLES gratings. Note the difference in the shape of the continuum, which is dominated by the blaze function of the spectrograph

Table 6.3: Table showing input S:N ratio, output S:N ratio and multiplex gain for least squares deconvolved profiles of Speedy Mic. The associated errors are estimated from the total number of spectra taken in each data set.

Data set	Input S:N ratio	Least squares S:N ratio	Multiplex gain	Effective no. of lines
SAAO 10th	29 ± 6	778 ± 157	26	1575
SAAO 11th	22 ± 4	536 ± 87	24	1230
AAT 11th (E79)	78 ± 3	2441 ± 116	31	1738
AAT 12th (E31)	45 ± 3	2156 ± 160	48	4420
AAT 13th (E31)	24 ± 2	1139 ± 108	47	4420
AAT 14th (E31)	38 ± 4	1884 ± 184	49	4420
AAT 14th (E79)	31 ± 7	874 ± 194	28	1738

metry (even in the SAAO data sets, which afford the greatest degree of phase coverage). This asymmetry is visible in the blue wing of the profiles and fits presented in Figure 6.1. There may be some variation in the shape of the asymmetry in the 1998 July 10 data set from the SAAO. This may only be a noise effect, given the poor S:N of the profiles. However the data sets seem to show little variation in this absorption feature which always appears at $\sim -140 \text{ km s}^{-1}$.

It would appear that a background star is contaminating the spectrum. CDS-Catalogue (1999) lists no object within a $4''$ radius (the decker limit, set at the AAT) of Speedy Mic. The galactic coordinates ($l = 6.25^\circ$, $b = -38.25^\circ$) (CDS-Catalogue 1999) and HIPPARCOS distance of $44.4 \pm 3.2 \text{ pc}$ indicates that Speedy Mic is located 27.4 pc below the centre of the galactic plane. The apparently small EW and estimated FWHM of $\sim 20 \text{ km s}^{-1}$ of the alien absorption feature suggests that it is a star, probably an M dwarf.

Radial velocity corrections for internal shifts of the instruments are made using telluric features (see Collier Cameron 1998 and Chapter 5/Barnes et al. 2000). This ensures reasonably accurate radial velocity determinations. There is a slight systematic increase in radial velocity from one data set to the next. Given that different phase ranges are sampled by different data sets taken with different instruments, one would expect some spurious scatter in the radial velocity.

Table 6.4: Best fitting parameters for each Speedy Mic data set. Note that equivalent widths are the least squares deconvolved EWs of a mean-depth line. A direct comparison can therefore only be made between data sets using either the E79 or the E31 grating (the GIRAFFE setup is different on both nights). The values are reasonably consistent given that many of the data sets are incomplete. The main variation in these values is probably a result of distortions of the profiles due to starspots.

Data set	v_{rad} km s ⁻¹	$v\sin i$ km s ⁻¹	EW
SAAO 10th	-10.5	127	0.1063
SAAO 11th	-10.0	126	0.1197
AAT 11th (E79)	-10.0	128	0.0940
AAT 12th (E31)	-9.5	129	0.0885
AAT 13/14th (E31)	-8.0	129	0.0927
AAT 14th (E79)	-9.5	128	0.1019

We cannot include the alien absorption feature in the Doppler imaging process, as it will lead to significant overestimation of the $v\sin i$ value. A non variable feature in the wing of the absorption profile does not make physical sense on a single star, and would result in spurious features in the maximum entropy reconstructions. As a result, we inflated the size of the error bars in the range -176 km s⁻¹ to -116 km s⁻¹ on all data sets. This leaves a small amount of continuum blue-ward of the absorption feature, enabling reliable re-normalisation after each maximum entropy iteration. Since we include a mask which blocks the contribution from the extreme wings of the stellar profile close to the continuum level, nothing blue-ward of -116 km s⁻¹ contributes to the final image. The rest of the profile appears uncontaminated, however we expect that the resulting images may suffer from slight degradation in latitude discrimination. This will mostly affect features traversing the whole profile (i.e. low latitude features). However given the broad nature of the profiles, the spatial resolution and therefore latitude discrimination should not suffer badly from this process.

System parameters which best fit the data are found by minimisation of χ^2 for a range of input test parameters in our Doppler imaging code DOTS (see Chapter 5 / Barnes et al. 2000) for full details. Table 6.4 details the derived system parameters,

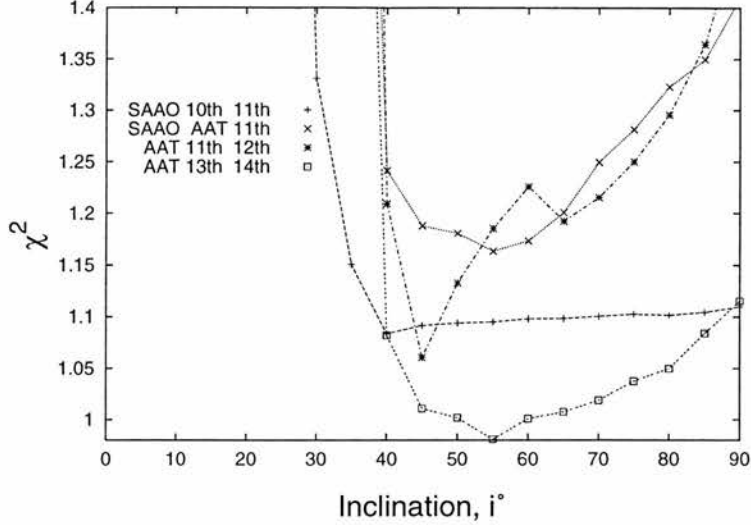


Figure 6.3: Minimum χ^2 against inclination for various Speedy Mic data sets.

showing a high degree of consistency between data sets. Given the large spot amplitudes passing through the profiles and the low degree of phase coverage for some data sets, the radial velocity measurements are remarkably consistent. Since we do not always use the same template stars to represent the local intensity profiles, slight variations in the zero-velocity-correction process (see section 2.1) may also introduce systematic radial velocity differences. Obviously we wish to choose a consistent set of parameters. Given that the imaging process is fairly robust in terms of incorrect parameter determination (e.g. overestimation of $v \sin i$ can partially be countered by a different EW) (Unruh 1996) we choose $v \sin i = 128 \text{ km s}^{-1}$. The radial velocity and EW giving the minimum χ^2 for this $v \sin i$ for each data set is then chosen as the Doppler imaging value.

Finally for a $v \sin i = 128 \text{ km s}^{-1}$ and the appropriate equivalent width for which χ^2 is minimised we applied the minimisation technique to the axial inclination parameter. This was applied to the combined data sets as shown in Figure 6.3. The SAAO July 10 & 11 data gave $i = 40^\circ$, although the plot of χ^2 against inclination shown in Figure 6.3 is rather unusual if the inclination is actually 40° . The AAT July 11 & 12 data set give a minimum χ^2 against inclination curve which is not smooth, making an inclination determination difficult. The SAAO/AAT July 11 and AAT July 13 & 14 data both gave $i = 55^\circ$, and the approximate trend one might expect (see Figure 3.9) for a star with a true inclination of $\sim 55^\circ$. Whereas the SAAO data sets are more complete, the S:N ratio of individual profiles is relatively low. The AAT data on the other hand suffers from

poor phase coverage but has high S:N ratio profiles. The inclination determination from combined dual-site observations is likely dominated by the high S:N data of the AAT.

We choose $i = 55^\circ$ since the minimised curves are closest to those seen in synthetic data sets (see Chapter 3) and also because the axial rotation period and adopted $v \sin i$ values yield an $R \sin i = 0.961 R_\odot$. This already indicates a bloated object as Gray (1992) gives a typical main-sequence K3V radius as $0.73 R_\odot$. Axial inclinations of $i = 45^\circ$ and 55° lead to radii of $1.17 R_\odot$ and $1.36 R_\odot$ respectively. In favour of minimising this exaggerated size, we choose $i = 55^\circ$. Speedy Mic is an extremely rapid rotator, and we caution that a lower inclination is not strictly ruled out. Further, use of the Barnes-Evans relationship in the form given for B-V observations by O’Dell, Hendry & Collier Cameron (1994) yields $D \sin i = 47.618 \pm 2.194$ pc. This in turn yields $R = 0.90 \pm 0.08 R_\odot$ and $i \geq 78^\circ$. If however Speedy Mic is oversized for its age and spectral type, as appears to be the case for PZ Tel and the α Persei dwarfs, the inclination estimate would decrease. An increase in the radius of order 10 per cent would bring the axial inclination determination into reasonable agreement with the adopted inclination of 55° . Incorrect determination of this parameter by ± 10 degrees is not generally expected to have serious effects on the positions and morphology of intermediate to low latitude features. Underestimation of axial inclination leads to exaggeration of low latitude spot occupancies while overestimation of leads to underestimation of the same features. The reverse is true for high latitude features and polar spots.

6.6 Results

6.6.1 Images

Figures 6.4 and 6.5 show images of Speedy Mic, formed from the maximum-entropy regularised fits to data sets from the SAAO and AAT. We combined data sets in order to obtain greater phase coverage, which given the 0.380 d period of Speedy Mic is often still not complete. There is global similarity between all the images presented here in that starspots are seen at all latitudes. The surface appears heavily spotted in all maps over the phase ranges of observations. With the possible exception of the AAT 13th & 14th image, no strong polar spot is seen on Speedy Mic at the time of observations.

There are however differences between the maps, attributable to poor S:N of the spectra and lack of phase coverage. Figure 6.4 shows reconstructions based upon SAAO data alone which when compared with the AAT (higher resolution and higher S:N ratio spectra) images in Figure 6.5 reveals less detail as may be expected. There are differences in the higher latitude structure when comparing the SAAO data set with the AAT data set, although the lower latitude structure is more consistent between data sets. The data from AAT, July 11 offers the greatest S:N and it is perhaps the corresponding phase coverage in the resulting images (Figure 6.5, upper & middle) which offer the best representation of the surface structure.

We attempted to measure the differential rotation rate on Speedy Mic by cross-correlation of constant latitude strips over common phases of observation between two maps. In common with previous attempts to measure differential rotation on AB Dor (Donati & Collier Cameron 1997) and PZ Tel (Chapter 5 / Barnes et al. 2000), we assume solar differential rotation to follow the functional form given in equation 5.2. We find however that due to lack of phase coverage and poor S:N ratios, the images are not consistent enough to measure reliably the magnitude of the differential rotation. We therefore resorted to measuring the rms scatter between a number of images. The results are summarised in Table 6.5 and can be taken as upper limits of the differential rotation. The cross-correlation images are shown in Figure 6.6, and demonstrate the lack of a well defined, continuous cross-correlation peak, over large latitude ranges. Given that we measured the scatter between latitudes -10° and 60° alone, the assumption is made that this scatter is representative of the ‘true’ scatter at all latitudes.

The resulting mean upper limit on the differential rotation of Speedy Mic yields a minimum, mean “equator lap pole” time of 39 days. Since small longitude ranges were used for cross-correlation in some instances, there may exist a slight bias to high values of equator-lap-pole times (i.e. rows 1 and 3 in Table 6.5). The best cross-correlation appears to be given by row 4 in Table 6.5, as one might expect from analysis of Figure 6.6, by eye alone. The resulting scatter in this image can therefore be taken as an upper limit to the differential rotation, which yields a minimum equator-lap-pole time of 56 days for Speedy Mic.

It should be noted that simply measuring the scatter does not in fact tell us about the form, or sense of the differential rotation. Indeed, anti-solar differential rotation, where

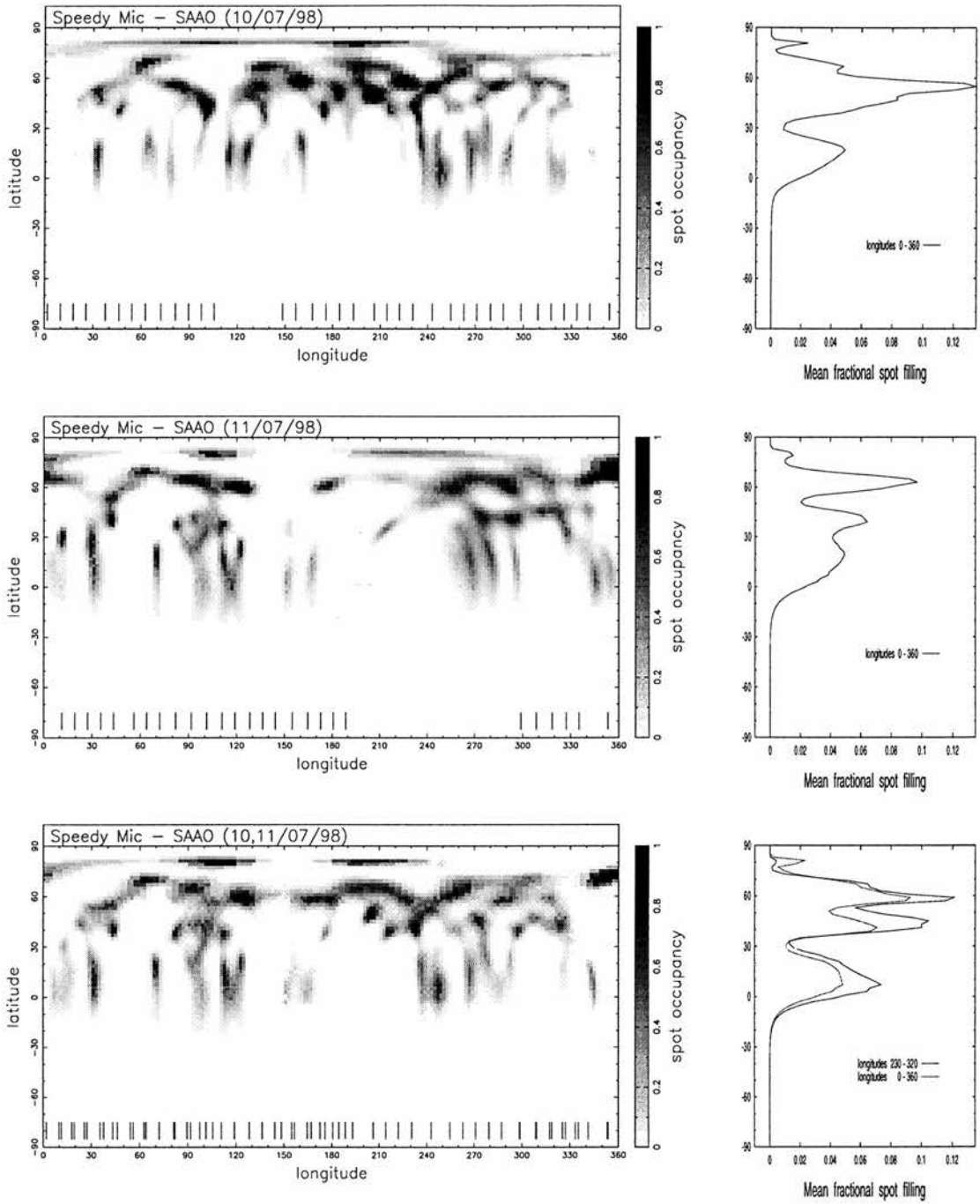


Figure 6.4: Max-Ent image reconstructions of Speedy Mic from SAAO data. From top to bottom: 10/07/98, 11/07/98, 10,11/07/98.

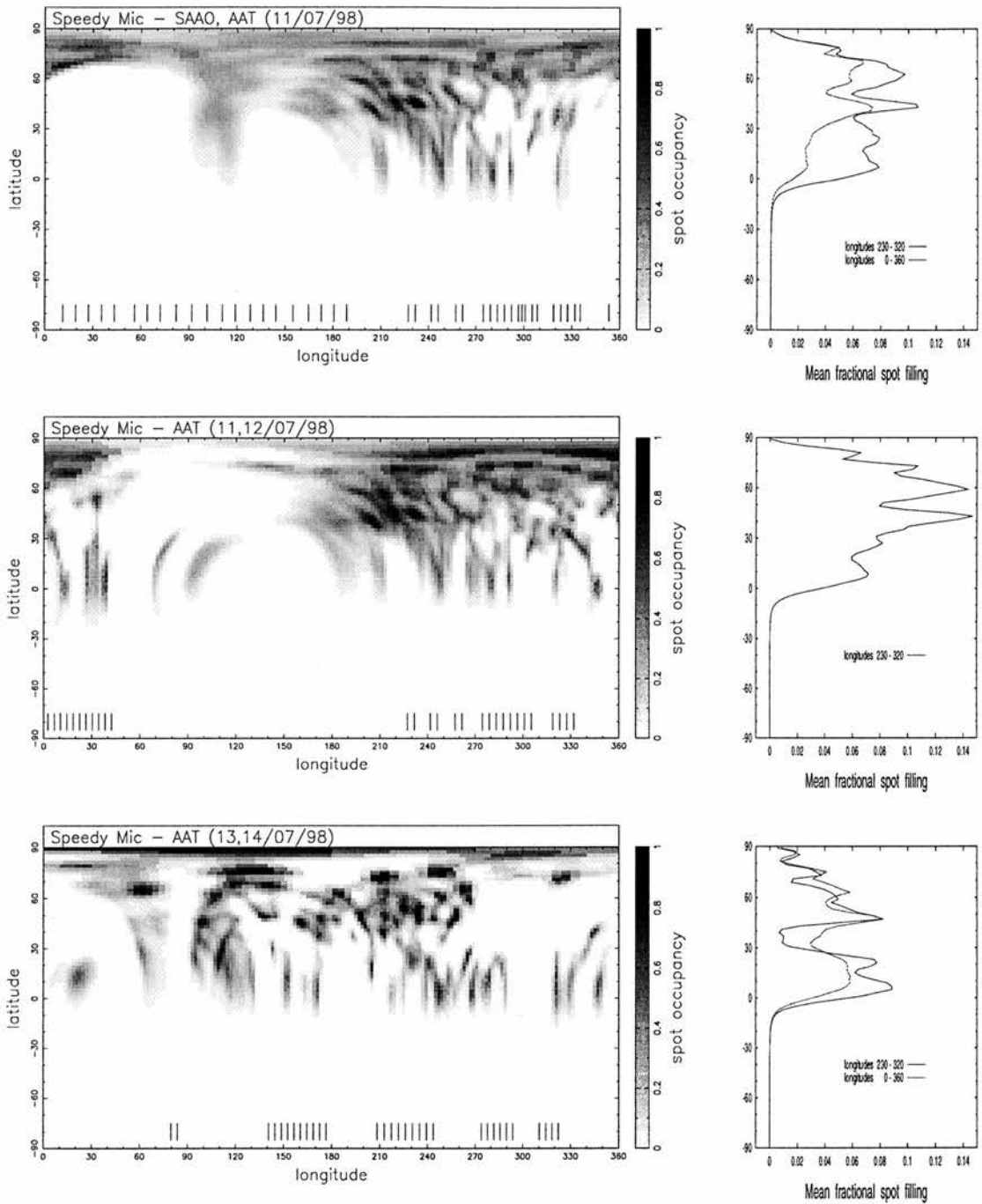


Figure 6.5: Max-Ent image reconstructions of Speedy Mic. From top to bottom: 10,11/07/98 using SAAO data, 11/07/98 using SAAO & AAT data, UCLES with E79 grating, 11,12/07/98 using AAT data, UCLES with E31 (12th) grating and 13,14/07/98 using AAT, UCLES with E31 (13th & 14th) and E79 (14th) data. The features cover the same global region on the stellar surface in all images. The same features can be compared in all images, including the reconstruction from the SAAO data alone (tick marks represent the phases of observations).

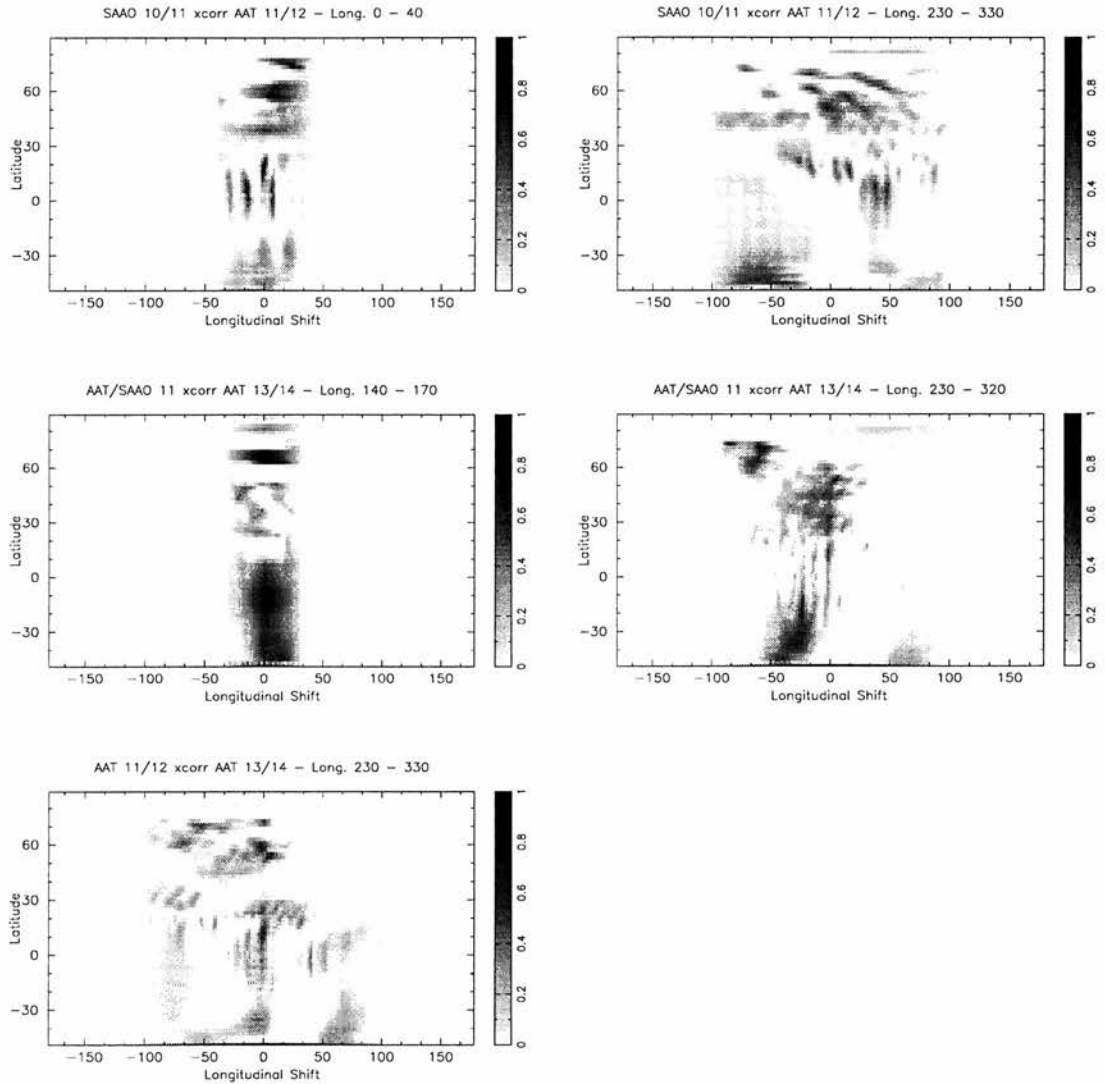


Figure 6.6: Cross-correlation images for Speedy Mic. The images correspond to those listed in Table 6.5. Although there appear to be correlations between features, they only extend over small latitude ranges. On larger scales, the cross-correlations show large degrees of scatter.

Table 6.5: Differential rotation upper limits expressed as minimum shear in days for Speedy Mic, measured from cross-correlation over a given region, between pairs of images. The scatter (standard deviation) is measured between -10° and 60° in each case.

Images used	longitudes	Minimum equator lap pole time [d]
SAAO 10/11 & AAT 11/12	0 - 40	45
SAAO 10/11 & AAT 11/12	230 - 330	14
AAT/SAAO 11 & AAT 13/14	140 - 170	48
AAT/SAAO 11 & AAT 13/14	230 - 320	56
AAT 11/12 & AAT 13/14	230 - 330	32

the polar regions rotates faster than the equatorial regions, cannot be ruled out. There are well defined narrow peaks at low latitudes, close to zero shift in some cross-correlation images. The pairs of features responsible are clearly identifiable in the original images, and would tend to suggest that extreme differential rotation can at least be ruled out near the equator.

6.7 Discussion

The distribution of spots on Speedy Mic is quite different from that seen on other stars. It appears to be much more heavily spotted at intermediate and low latitudes. There is still evidence of depletion of spots at intermediate latitudes, although the exact location varies from image to image. This is probably due to poor phase coverage and S:N ratio of the absorption profiles which are inverted to form the image. The maximum entropy solution is not as well constrained by the SAAO data for the given goodness of fit as in the case of the AAT data. There may be additional contamination in the image due to the absorption feature in the blue wing of the profiles. This should however be negligible as steps to remove any contribution from this region have been taken.

The very fast rotation and moderately late spectral type at K3V may mean that comparisons of surface distribution even with other rapid rotators is difficult. Doppler images for single stars of later spectral type than K0V are rare. To date there are only images for the K2 dwarf, LQ Hya (Rice & Strassmeier 1998 and Donati 1999) and the K5

dwarf BD +22^o 4409 (LO Peg) (Lister, Collier Cameron & Bartus 1999), which fit this criterion. Both these stars are similar to many other earlier type stars in that they exhibit low latitude/equatorial features and a polar cap, but a relative paucity of spots at some intermediate latitude. Only further images will reveal whether a more distinct and lower latitude band is ever present. If not, the high degree of spottedness may simply be due to the extreme rotation period.

The upper limit placed on the differential rotation shear is not entirely inconsistent with other differential rotation measurements found for rapidly rotating (pre-) main-sequence dwarfs. Without a more precise measurement of the magnitude of the differential rotation rate, it is difficult to say whether it is consistent with the Sun, AB Dor (Donati & Collier Cameron 1997), PZ Tel (Chapter 5/Barnes et al. 2000) and the theoretical predictions by Kitchatinov & Rüdiger (1999).

It is perhaps worthwhile to examine whether agreement between the determined stellar inclination and hence radius, when compared with the χ^2 minimisation technique, can be achieved. The $B - V$ and hence effective stellar temperature ($T = 4984$ K, from calibrations made by Flower 1996) are well determined. Starspots may result in an underestimation of stellar temperature, but presumably do not produce a significant contribution. Our derived value of $R\sin i = 0.961$ is also a well determined parameter. The stellar evolution models of Forestini (1994) reveal that Speedy Mic is a pre-main-sequence object, lying in the region between a $1 M_{\odot}$ and $1.1 M_{\odot}$ star. The effective temperature of Speedy Mic indicates that it lies between evolution models, with parameters, (a) $M = 1.0 M_{\odot}, R = 1.03 R_{\odot}, L = 0.59 L_{\odot}, age \sim 20 Myr, i \sim 69^{\circ}, M_{bol} = 5.39$ and (b) $M = 1.1 M_{\odot}, R = 1.15 R_{\odot}, L = 0.74 L_{\odot}, age \sim 15 Myr, i \sim 55^{\circ}, M_{bol} = 5.12$. Finally, a bolometric magnitude of 5.77 ± 0.15 is obtained from the HIPPARCOS parallax, $V = 9.3$ and assuming a bolometric correction of -0.295 (Flower 1996). There is apparently a large discrepancy between the observed and theoretical bolometric magnitudes. It is this discrepancy which leads to overestimates of the stellar axial inclination by methods such as the Barnes-Evans relation. The situation may be resolved if we take the model M_{bol} values as lower limits. The difference can then be explained by the unspotted V magnitude being for example 9.0 rather than 9.3. This implies a 30 per cent spottedness for the $1.0 M_{\odot}$ model or a 50 per cent spottedness for the $1.1 M_{\odot}$ model. It is worth noting however that 50 per cent spot coverage has been determined for II Peg from TiO bandhead strengths (O’Neal & Saar 1998). Given the extremely rapid rotation of Speedy Mic and

therefore presumed high dynamo efficiency, the radius may indeed be as high as $1.17 R_{\odot}$. This leaves one further discrepancy in that the recovered spot occupancy in the images (§6.6.1) is approximately 4.5 per cent. If spot occupancies of an order of magnitude greater are to be achieved, it can only be assumed that a global uniform distribution of starspots exists, above the resolution of Doppler imaging techniques.

6.8 Conclusion

Speedy Mic has attracted much attention because it is a relatively nearby dwarf with a high projected rotation velocity and short axial rotation period. Since equivalent width is approximately conserved as $v \sin i$ varies, the mean profile depth is small. Even with such extreme stellar parameters, our spectral deconvolution code SPDECON performs well. Despite the low S:N ratio of the co-added pairs of spectra from 300 s exposures at the Sutherland 1.9 m telescope/GIRAFFE (SAAO) the multiplex gains of ~ 25 produced by least squares deconvolution, allow detection of starspot signatures in the relatively shallow, rotationally broadened profiles. Least squares deconvolution has allowed us to determine a $v \sin i$ measurement to within a precision of $\sim 1 \text{ km s}^{-1}$, whereas previous measurements of $v \sin i$ varied (including errors) from 100 km s^{-1} to 280 km s^{-1} . This error is derived from the spread of values found in Table 6.4 (i.e. $127.8 \pm 1.2 \text{ km s}^{-1}$). The $\Delta\chi^2 = 1$ level in each parabolic fit yields an error of $\sim 0.3 \text{ km s}^{-1}$. This further demonstrates the invaluable nature of least squares deconvolution when applied to low S:N data. The surface maps at once show similarities, and uniqueness, when compared with other Doppler images.

It is clear from the results presented here that a successful differential rotation measurement requires several important constraints to be met. Firstly, a S:N ratio of the order of 500 is not sufficient when the surface spot features are $\leq 10^{\circ}$ in diameter. S:N ratios of 1000 are desirable for this purpose. Secondly, even with high S:N ratios, poor phase coverage makes cross-correlation difficult. One or two features which may be present in a pair of images, spanning 100° of the stellar surface were not found to yield reliable cross-correlation images which could be used to measure differential rotation. This may in part be due to different spectrograph setups however. Finally, the interval between the times of observations of each data set should be large enough that significant shifts of features have taken place. This of course depends upon the differential rotation rate and

the starspot lifetimes, which are largely unknown. It would appear that timescales of 3-5 days (Donati & Collier Cameron 1997) are ideal for the K0 dwarf AB Dor for example. The results for PZ Tel would also imply this to be a reasonable estimate, however, for the faster rotation rate of Speedy Mic, we can only assume the latitudinal dependent differential rotation, and starspot lifetimes will be of the same magnitude. Unfortunately, this kind of work is largely dependent upon good weather conditions over several nights.

CHAPTER 7

Prominences

Note: Results for He 520, He 699 & PZ Tel have appeared in:

“Latitude distributions and spot lifetimes on G dwarfs in the α Persei Cluster”, *MNRAS*, 299, 904-920, J.R. Barnes, A. Collier Cameron, Y.C. Unruh, J.-F. Donati, G.A.J. Hussain

“Doppler images from dual-site observations of southern rapidly rotating stars I: Differential rotation on PZ Tel”, *MNRAS*, *In Press*, J.R. Barnes, A. Collier Cameron, D.J. James, J.-F. Donati

7.1 Introduction

Solar prominences are a well known and well studied phenomenon which can be formed from material thrown up by a flare, coronal condensations or from support in magnetic fields. They are seen in strong neutral Hydrogen emission lines, especially $H\alpha$. Prominences appearing in front of the solar disc are seen as dark filaments with approximately 10 per cent of the disc brightness in the centre of $H\alpha$ (this is 2 per cent of the continuum level as $H\alpha$ has a normalised central depth of 0.2) (Zirin 1988). However prominences appear bright against a dark sky (i.e. off the solar limb). This is because the clouds are good examples of a pure photon scattering medium. Little collisional excitation occurs in prominences as they are relatively cool, low density regions. The emission we see is due to excitation of levels by the photospheric radiation field.

There are two classes of solar prominence:

1) Active, flare-associated or transient prominences. These are short lived dramatic events (minutes to hours).

2) Quiescent or long-lived prominences which are associated with active and quiet regions. They are among the longest lived solar features lasting for up to several rotations.

7.2 Stellar prominences

7.2.1 Observational evidence

Flares on active stars have been observed in X rays, UV and at optical wavelengths simultaneously, although they are rarely seen in the latter. Montes et al. (1999) have recently reported the detection of a flare on the K2 single dwarf LQ Hya from increased continuum intensity and blue shifted absorption lines. Flaring activity, seen as transient emission in $H\alpha$ is also reported on AB Dor by Donati & Collier Cameron (1997) with a long lived event (up to four rotation cycles) seen by Donati et al. (1999a). There is indirect evidence for cool material associated with stellar flares however. Haisch et al. (1983) associated an increase in the hydrogen column density during an X-ray detected flare on the the flare star Prox Cen as being due to a prominence passing over the site of the flare. The hydrogen column density had increased by a factor of 10 to 100 times during the flare event as compared to during its rise and decay. Doyle, Byrne & van den Oord (1989) noticed the lack of soft X-ray emission associated with a flare seen in the U-photometric band and hydrogen Balmer lines on II Peg. Again one interpretation is absorption by overlying material. Transient red-shifted $H\alpha$ absorptions seen on the RS CVn star II Peg were interpreted as post flare loops with a 50 km s^{-1} downflow.

There is however also evidence for prominences which are not necessarily associated with flaring events. The signatures of these structures may be stable over longer periods of observation, and as such may be regarded as stellar analogues of solar quiescent prominences (although they are often very large and supported in a different manner). For example, a study (Jensen et al. 1986) of the binary system V471 Tau (K0V and white dwarf) with the EXOSAT spacecraft showed dips in the X-ray emission from the white dwarf component. This coincided with the Lagrangian L4 and L5 points of the binary orbit suggesting that ejected material may be collecting at these potential minima. Alter-

natively, it was suggested that the material may be in large coronal loops anchored to the K dwarf component of the system.

Transients crossing the $H\alpha$ profile on AB Dor were noted by Collier Cameron & Robinson (1989a) to possess various characteristics. For example, the individual features are narrow compared with the rotationally broadened $H\alpha$ profile of the star itself. The RV of a given feature changes almost linearly with time, though the drift rate varies from one event to the next, and occasionally departs from linearity in the wings of the profile. The EW of the transient varies with time and reaches a maximum at the mid point over the interval at which it is observed (i.e. at or close to the centre of the $H\alpha$ profile). The radial velocity of the feature does not necessarily vary symmetrically about zero velocity, and can be displaced either to the red or to the blue.

Collier Cameron & Robinson (1989a) suggest the most likely explanation of these observations to be cool circumstellar condensations. As a cloud passes in front of the stellar disc, the EW of the feature will increase until the whole cloud is covering the disc, at which point the EW remains constant. As the cloud moves off the stellar disc, the EW begins to decrease again. These clouds are similar to stellar prominences but are seen at a large range of distances from the rotation axis. It is believed that they are trapped at the top of magnetic field loops in the corona, in co-rotation with the stellar surface, and are hence referred to as “slingshot prominences”. For example, on AB Dor, prominences are seen from below to well above the co-rotation radius, at several stellar radii (Collier Cameron & Robinson 1989a; Collier Cameron & Robinson 1989b; Donati & Collier Cameron 1997; Donati et al. 1999a). Collier Cameron & Robinson (1989b) tracked the evolution of absorption features which occurred at the same orbital phase over several nights. Features which were visible on more than one night tended to drift to larger radii, and change in density. The observed increase in density at the cloud summit, is due to radiative losses, and occurs on timescales of hours to days. This timescale is comparable to the radiative cooling time of the hot loop plasma. Upward flows from the loop footpoints may result as the loop material attempts to restore hydrostatic equilibrium as a result of the pressure loss accompanying the temperature decrease at the summit. Cloud densities on AB Dor were found to increase on timescales of 2-4 days. As such they are shorter lived than the solar quiescent prominences which exist on timescales of months, but longer lived than the prominences associated with active regions and flares which last for the order of several hours.

Collier Cameron et al. (1990) studied transients in Mg II h & k, Ca II H & K and H α and inferred cloud masses of $2\text{--}6 \times 10^{17}$ g, 2 to 3 orders of magnitude greater than a typical solar prominence. Cloud temperatures of order 8000 K to 9000 K were inferred. Hydrogen column densities of $\sim 10^{20}$ cm $^{-2}$ were found in a typical prominence transient, in agreement with the active prominence model proposed by Haisch et al. (1983).

Prominences have since been seen on a number of other late type G dwarfs in the α Persei cluster, He 373, He 520, He 622 and He 699 (Collier Cameron & Woods 1992); Speedy Mic (Jeffries 1993b); HK Aqr (Eibe 1998). However no prominences are seen on the the active K dwarf BD +22 $^{\circ}$ 4409 (Jeffries et al. 1994). The apparent lack of cool condensations may be due to a geometrical effect. If prominences are centrifugally flattened towards the equatorial plane they may only be seen in high inclination stars. The inclination of BD +22 $^{\circ}$ 4409 at $50^{\circ} \pm 10^{\circ}$ is probably too low, rendering H α transients unobservable. Large-scale global mass inflow of neutral hydrogen is inferred from asymmetries in the H α line on this star which appears shifted toward the blue compared with other absorption lines. Speedy Mic at only a slightly higher inclination of $i = 55^{\circ}$ *does* exhibit H α transients (see §7.3.3). The co-rotation radius is closer to the surface on Speedy Mic which may improve the chances of seeing a prominence projected against the stellar disc in the line of sight of the observer.

7.2.2 Measurement of prominence features

A cloud co-rotating with the star at a distance R_c from the stellar rotation axis first appears in the blue wing with the same RV as the underlying portion of the photosphere. Since the system rotates as a solid body, the RV of a given point and its projected distance from the rotation axis have the same functional dependence on R_c , i , θ (stellar latitude) and stellar longitude. The radial velocity, being the same for all points along a given line of sight, varies linearly with projected distance from the rotation axis.

The drift rate of the absorption feature can be given as

$$v(t) = v_{max} \sin\left(\frac{2\pi(t - t_0)}{P}\right), \quad (7.1)$$

where v_{max} is the amplitude of the sinusoid that is described by the prominence and t_0 is

the time at which the cloud passes the observers meridian on the star. v_{max} is given by

$$v_{max} = \frac{R_c}{R_*} v \sin i \cos \theta. \quad (7.2)$$

Combining these equations then allows the drift rate to be measured from v_{max} and t . The equation representing the radial velocity centroid of a circumstellar cloud (Collier Cameron & Robinson 1989a) is given by

$$v_c(R_c, t) = \frac{R_c}{R_*} v \sin i \cos \theta \sin \omega(t - t_0), \quad (7.3)$$

where $\omega(t - t_0)$ is the angular rotation rate. R_* , R_c , i , and θ are the stellar radius, radius of the cloud, axial inclination and stellar latitude respectively. If we assume that the radial velocity of a cloud changes linearly with time as it transits the stellar disc is made, then for two successive spectra, $\Delta \sin \omega(t - t_0) \simeq \omega \Delta t$. The distance, $\varpi = R_c \cos \theta$ of the cloud from the stellar rotation axis is given by

$$\frac{\varpi}{R_*} = \frac{d\lambda}{d(\phi/2\pi)} \cdot \frac{c}{\lambda_0} \cdot \frac{1}{2\pi v_c \sin i}. \quad (7.4)$$

Direct measurement of the dark prominence features (Figures 7.2, 7.6, 7.9 and 7.4) can be made by measurement of the straight line gradient. By shifting the phased H α time series images in phase and subtracting (effectively giving the time derivative of the absorption at each wavelength), it is possible through measurement of the straight line gradient $d\lambda/d(\phi/2\pi)$ from the resulting ridge-line of each absorption feature, to obtain an estimate of ϖ/R_* . This latter method makes measurement easier, but with the relatively low S:N ratio at the wavelength of H α direct measurement of the straight line gradient is necessary.

7.3 Results & Discussion

7.3.1 α Persei G dwarfs

The mean H α profiles are shown in Figure 7.1. The stellar spectra have been smoothed with a gaussian filter of width 5 pixels. The H α region of the spectral standard used for Doppler imaging (HD 42807) was convolved with the mean stellar rotation profile to obtain a broadened spectral standard as a comparison. Both He 520 and He 699 clearly

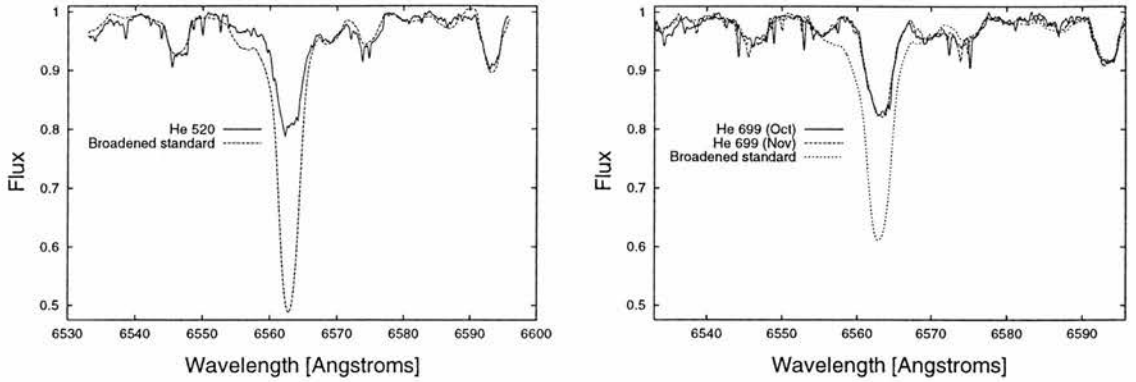


Figure 7.1: He 520 and He 699 mean (gaussian filtered with a FWHM of 5 pixels) $H\alpha$ profiles, plotted with broadened spectral standard (see text for details). Convolution of the standard with the mean least squares profile preserves EW, hence the different apparent depth between the plots (The equivalent width of the mean deconvolved He 699 line is also 3.5 per cent greater than that of the mean deconvolved He 520 line).

show a large degree of chromospheric infilling as may be expected on young active stars. There is very little variability in the mean profile shape of the He 699 $H\alpha$ line over the one month gap between observations. The fact that little variation in the $H\alpha$ EW is seen combined with the similarity of the two photospheric Doppler images suggests that He 699 is in a fairly steady state on this timescale.

Prominences are found to be present on He 520 (Figure 7.2). He 699 however exhibits features that seem to be located at a relatively low distance, ϖ from the rotation axis. Since the time resolution is only ~ 1000 s (i.e. 900 s exposures plus CCD readout time), the use of back projection techniques as used by Collier Cameron & Robinson (1989a) to obtain prominence position estimates is not valid. In the case of He 520, the absorption features seen crossing the profile must be at some relatively large axial distance by estimate of the rate at which they cross the stellar profile. More spectra are needed if back projection is to be used, as the distance probability image becomes fragmented at $\sim 3R_*$ in this case. Although He 699 appears to exhibit absorption features in $H\alpha$, as can be seen from Figure 7.2, they cross the profile at a much slower rate, and appear much closer to the surface.

The results are shown in Table 7.1 and demonstrate that in the case of He 520, the prominences appear to be located at or near the co-rotation radius if the structure were at

Table 7.1: He 520 and He 699 prominence positions and stellar parameters. $\varpi \equiv R_p \cos \theta$, the distance from the rotation axis.

		He 520	He 699
P	[d]	0.6079	0.4908
$v \sin i$	[km s ⁻¹]	91 ± 1	96 ± 1
$(B - V)_0$	-	0.69	0.61
R_c	[R_\odot]	3.0	2.6
R_c	[R_*]	2.5 (R_*) = 1.18 R_\odot	2.4 (R_*) = 1.1 R_\odot
ϖ , 1996 October	[R_*]		1.6 ± 0.3
ϖ , 1996 November	[R_*]	2.6 & 2.8 ± 0.2	1.7 ± 0.3

the equator. In the case of He 699 the location of the prominences, taking into account the error in measurement is much closer to the stellar surface, and may indeed be located only just above the photosphere. As a result, we cannot exclude that they are active regions seen crossing the surface, although it is difficult to find any link with the spotted regions seen in either the deconvolved time series or the image reconstructions.

We have also examined the H α profiles of AP 149 and AP 193 for transients. We find no obvious variability in H α for the phases at which AP 193 is observed. There is a considerable degree of filling in of the absorption line (Figure 7.3) however. AP 149 on the other hand shows H α in emission. A double peaked profile is evident at most phases, with the H α time series showing s-wave modulations of the double peak. Donati et al. (1999b) recently discovered a similar situation on the low inclination ($i = 30^\circ$) post T Tauri star RX J1508.6-4423. Given the repeat in the pattern from one rotation cycle to the next, it was inferred that most of the H α emission was locked in co-rotation with the stellar surface.

The maximum entropy tomographic code of Marsh & Horne (1988) was used (D.H Steeghs, private communication) to derive velocity space Doppler maps from the H α emission line. The intrinsic profile for the H α emission was assumed to be a gaussian with instrumental profile width. The assumption that the broadened H α line profile is not distorted due to downflows of cool material (e.g. Eibe et al. 1999) has been made. The

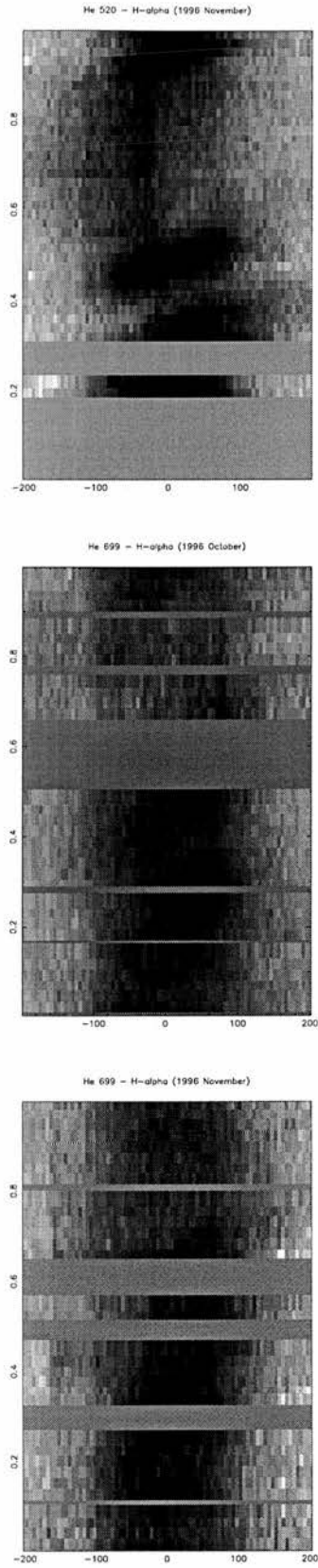


Figure 7.2: Time series spectra of He 520 and He 699 H α lines, Top: He 520, Middle: He 699 (Oct), Bottom: He 699 (Nov)

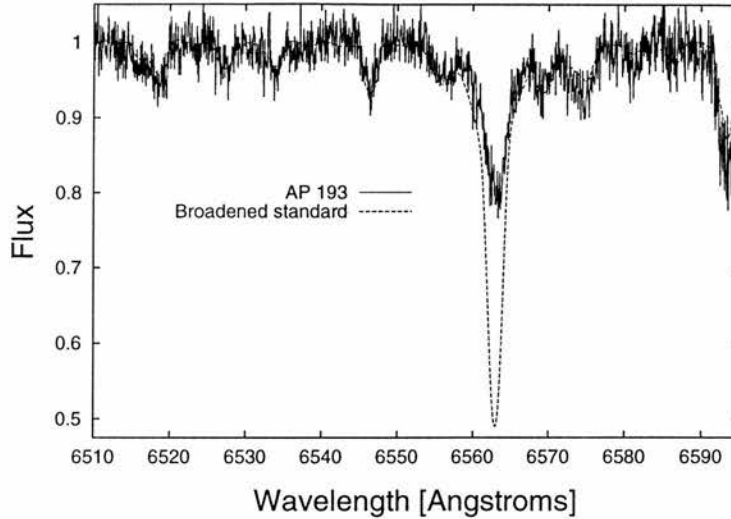


Figure 7.3: $H\alpha$ mean profile for AP 193. Broadened standard is HD 101501 (G8V)

results are shown in Figure 7.4 and quite clearly show (bottom left) regions of strong emission located close to or beyond the co-rotation radius, $R_c = 1.5 R_*$. Subtraction of the azimuthal average of the emission distribution reveals four emitting regions more clearly. The white region is weak relative to the mean symmetrical image and does not represent $H\alpha$ absorption as such (see caption for details). Table 7.2 shows the location and extent of the emitting clouds. It is not possible to make any definite assumptions about the stellar latitude of these prominences. However the feature located at phase 0.91 which covers the greatest radial extent stretches to within the stellar surface. Given the low inclination, this suggests at least that the prominence is situated at high latitude, and partially in front of the stellar disc.

We believe that an analogous situation to that on RX J1508.6-4423 exists on AP 149. Unlike other stars observed at higher inclination such as AB Dor, PZ Tel, Speedy Mic, and α Persei G dwarfs, the prominences are not seen transiting the stellar disc. Both RX J1508.6-4423 and AP 149 on the other hand are fast rotators at low axial inclination, and hence the co-rotation radius is closer to the equator. In both cases, the tomograms confirm that emission originates near and above the co-rotation radius. The low inclination makes $H\alpha$ absorption transits unlikely. It is otherwise unclear why $H\alpha$ should be seen in emission in some stars and not others. The K dwarf BD+22 4409 also shows chromospheric $H\alpha$ emission (Jeffries et al. 1994) but there are no satellite emission features which can be attributed to prominence activity at the time of observations.

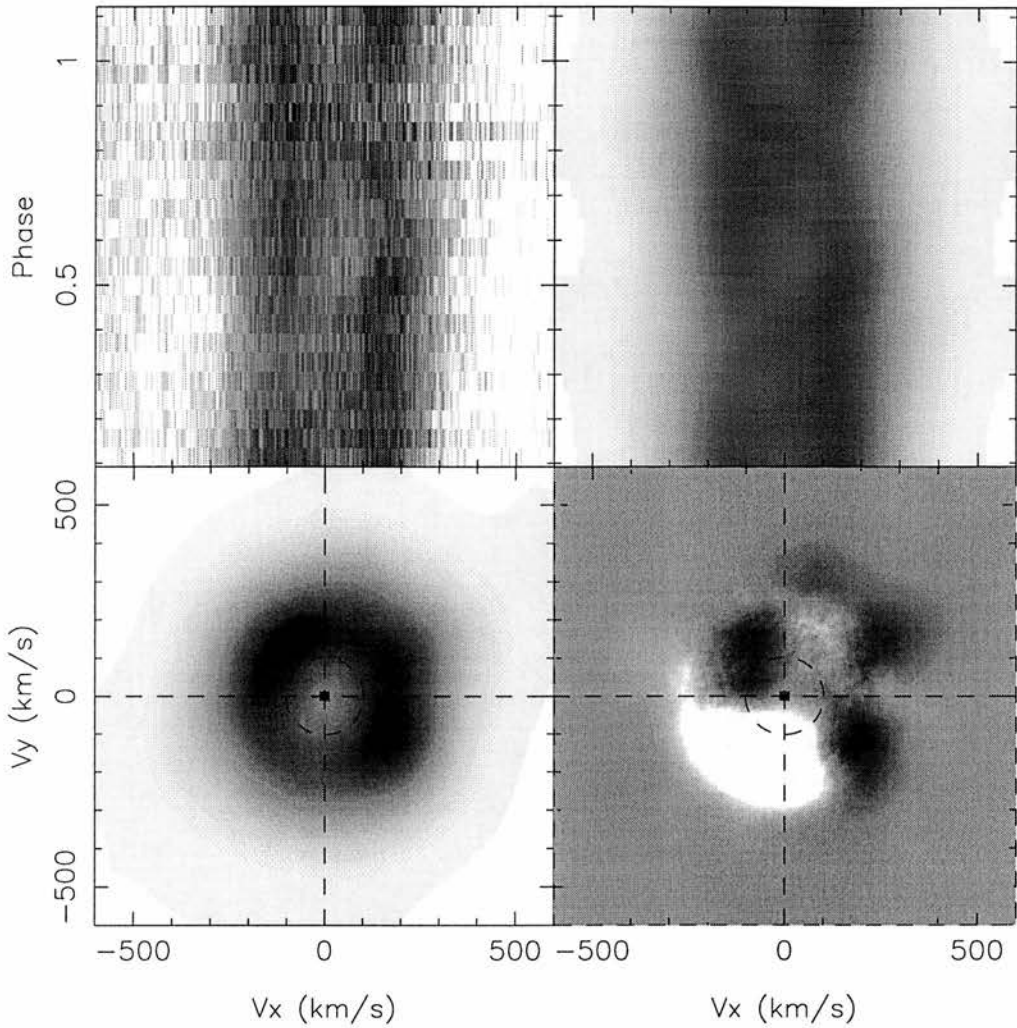


Figure 7.4: Time series and Doppler maps of H α emission on AP 149. Top left: Time series. Emission features are shown in black. Bottom left: Maximum entropy Doppler map. Top right: predicted data from Maximum entropy Doppler map. The greyscale is the same as the H α *data* showing the complete range of pixel values (white to black) Bottom right: The mean pixel value is calculated in a given annulus to give a mean azimuthal emission map, which is then subtracted from the Doppler image. The whole range of values varies from -0.2 to 0.15 (greyscale shows white = -0.05, black = 0.15). There are clearly four relative condensations or clouds seen in emission. The white region is negative relative to the mean symmetrical image and doesn't necessarily indicate absorption. Zero phase is at 12 o'clock and increases clockwise. The dashed circle represents the stellar surface at $v \sin i = 102 \text{ km s}^{-1}$. The Co-rotation radius is at $R_c = 1.51 R_*$ or $v \sin i = 120 \text{ km s}^{-1}$.

Table 7.2: AP 149 Prominence details. Column 4 gives distance from rotation axis in units of the stellar radius along with mean radial spatial extent. Co-rotation radius is at $R_c = 1.5 R_*$.

Phase	V_x [km s ⁻¹]	V_x [km s ⁻¹]	Distance ϖ/R_*
0.04	86 ± 12	318 ± 12	3.23 ± 0.74
0.17	266 ± 13	154 ± 13	3.01 ± 0.80
0.33	202 ± 12	-188 ± 8	2.29 ± 0.88
0.91	-90 ± 14	134 ± 7	1.58 ± 0.96

In many stars, the H α profile is filled (often almost to the continuum level) by chromospheric emission (Collier 1982, Innis et al. 1988). The background illuminating source can therefore be treated as a flat continuum in H α (Collier Cameron et al. 1990). A cloud passing between the stellar disc and the observer then scatters photons arising in the chromosphere out of the line of sight, resulting in relative absorption. Most of the clouds at the time of observations reported by these authors on AB Dor were located at approximately 3 R_* from the rotation axis. At such a distance, it was inferred that the emission component of the source function arising from recombination and collisional excitation was negligible. The cloud source function at this distance was expected to be at most 3 per cent of the intensity of the chromospheric background in H α . In fact weak emission from off disc clouds was detected with at most 1 to 2 per cent of the stellar background H α .

This is clearly not the scenario on AP 149 which shows satellite H α features in emission at all phases. The reason for emission may be a combination of higher photospheric temperature and greater cloud opacity. Prominences are found at over 3 stellar radii from the rotation axis, and we also see that they have projected areas of similar size to that of AP 149. If the clouds are larger and more dense, collisions between chromospheric H α photons and prominence material are much more likely. In such a case, the source function becomes dominated by recombination and collisional excitation. Since the stellar flux intercepted by the prominence system follows an inverse square law, the proximity of the cloud to the stellar surface is a sensitive factor in determining whether H α will appear in emission. Most of the emitting material appears at or above the co-rotation

radius in a torus, with little emission occurring inside the co-rotation radius. Indeed, if there were actually emission inside co-rotation, one would expect it to be even stronger as the stellar flux density would be greater. This is clearly not evident in the $H\alpha$ profile and adds support to the toroidal morphology of the emitting region.

Unfortunately the single epoch of observations does not allow an evolution timescale of the prominence system to be estimated. Both Collier Cameron & Robinson (1989b) and Donati et al. (1999b) determined timescales of ~ 4 days for evolution of prominences, which could then be taken as the time taken for the total prominence system to regenerate. Further studies are required in order to estimate this timescale. This may be useful in determining the spin down time due to the loss of angular momentum through the expulsion of material in this way. Collier Cameron & Robinson (1989b) gave estimates of 100 Myr for the spindown time of AB Dor based on the assumption of this mechanism alone. Donati et al. (1999b) also provided an estimate for RX J1508.6-4423 of 100 Myr, which is in good agreement with the spindown times inferred from rapidly rotating G dwarfs in young clusters at an age of ~ 15 Myr (Bouvier, Forestini & Allain 1997).

7.3.2 PZ Tel

The excess $H\alpha$ emission from PZ Tel (Figure 7.5) has been measured using an inactive-standard star subtraction technique following Soderblom et al. (1998). They convert the $H\alpha$ EW (minus the photospheric contribution) to a flux relative to the bolometric flux. A comparison with similar measurements in the Pleiades unsurprisingly shows that PZ Tel has extremely strong $H\alpha$ emission, and lies near to the peak of the Pleiades distribution at the B-V colour of PZ Tel (Soderblom et al. 1993a). An $H\alpha$ EW of 430 mÅ is found, which is lower than the 630 mÅ EW reported by Soderblom et al. (1998). This demonstrates the highly variable nature of this object hinted at by Innis et al. (1988) who found the profile to be completely filled in at times.

Figure 7.6 (AAT, 10/07/98) appears to reveal two regions at different distances from the rotation axis. The feature centred near phase 0.8 is obviously much closer to the stellar surface than that at phase 0.45. Comparison with the second time-series at the AAT also reveals that these structures evolve on short timescales, with a new feature centred at phase 0.7. It is possible to make an estimate of the distance of these transients from the plotted time-series.

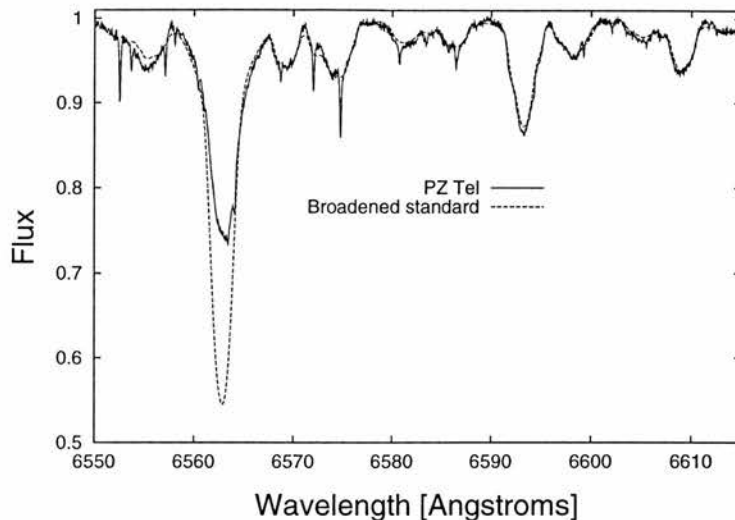


Figure 7.5: $H\alpha$ mean profile for PZ Tel. Broadened standard is Gl 472 (K1V)

Table 7.3: Distance of prominences on PZ Tel above rotation axis. Errors are estimated from measured uncertainties in $d\lambda/d(\phi/2\pi)$.

Time	series	Phase	ϖ/R_*
AAT	10/07/98	0.45	2.3 ± 1.5
		0.60	4.9 ± 1.9
AAT	12/07/98	0.70	1.5 ± 0.6
SAAO	12/07/98	0.00	2.0 ± 1.1

One possible site for the location of prominences in magnetic loops is at the co-rotation radius ($4.18 R_\odot$ for PZ Tel) where the gravitational force is balanced by the outward centrifugal force. Prominences are found to lie both within, and above the co-rotation radius of PZ Tel. Given that the inclination of PZ Tel is probably $60^\circ - 70^\circ$, this implies that the prominences at higher distances from the rotation axis must be at similar stellar co-latitudes (latitudes $20^\circ - 30^\circ$) rather than at equatorial latitudes. The location of prominences outside the co-rotation radius and above the equatorial plane indicates that the field is both closed and complex at large axial distances. A dipolar field would result in the formation of slingshot prominences in the equatorial plane only, with magnetic foot-points in both hemispheres. This is clearly not the case for the prominences we observe on PZ Tel which suggests that the foot-points of magnetic loops are in one hemisphere. This does not rule out the possibility of prominences at equatorial latitudes which we are not able to observe.

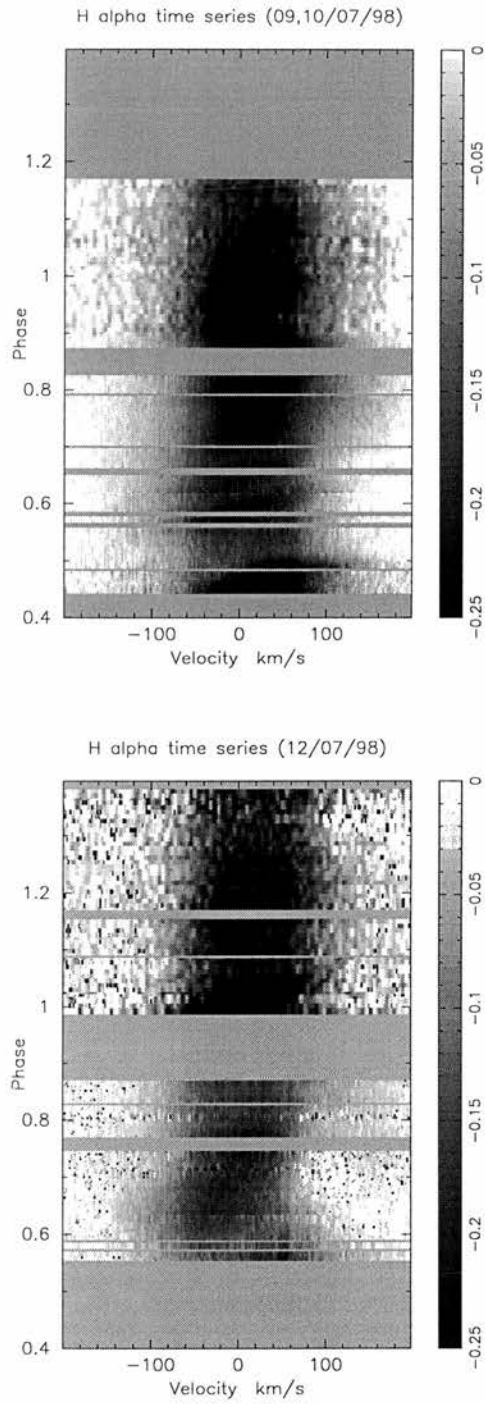


Figure 7.6: Time series spectra for H α profiles of PZ Tel for Left: 09,10/07/98. Right: 12/07/98. Absorption features appear black in the plots.

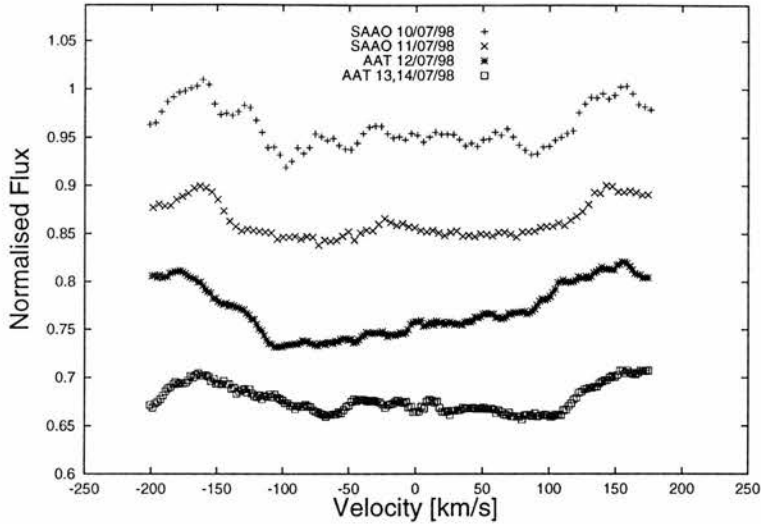


Figure 7.7: $H\alpha$ average profiles of Speedy Mic demonstrating the high degree of chromospheric filling. The profiles have been smoothed with a gaussian filter of width 5 pixels, and are displaced for display purposes. The asymmetry in the averaged AAT profiles is most certainly due to incomplete phase coverage.

7.3.3 Speedy Mic

At the time of observations, the $H\alpha$ profile is filled in almost to the continuum level as shown in Figures 7.7 and 7.8. Despite this, the $H\alpha$ time series shown in Figure 7.9 clearly show a number of transients at the time of observations. This confirms the presence of prominences as reported by Jeffries (1993a). Although the S:N ratio in the SAAO data is not high, prominence features which appear on July 10 are also visible on July 11. The feature at phase ~ 0.75 in the SAAO July 11 data is perhaps also seen in the July 10 data. Also there is tentative evidence that the feature seen in the short AAT July 12 time series is visible in the SAAO July 11 data. Unfortunately, the lack of prolonged blocks of phase coverage at the AAT on July 13 and 14 makes identification difficult. The inclination of Speedy Mic at 55° , implies the prominences at higher distances from the rotation axis must be at similar stellar co-latitudes (i.e. 35°) rather than at equatorial latitudes.

Speedy Mic was observed by Jeffries (1993a) who noted that in addition to the $H\alpha$ absorption transients, a preceding emission feature was seen. It was suggested that this may be the result of flaring activity triggered by the prominence moving outward from the stellar surface. The foot points of the magnetic loop involved in the flare then become

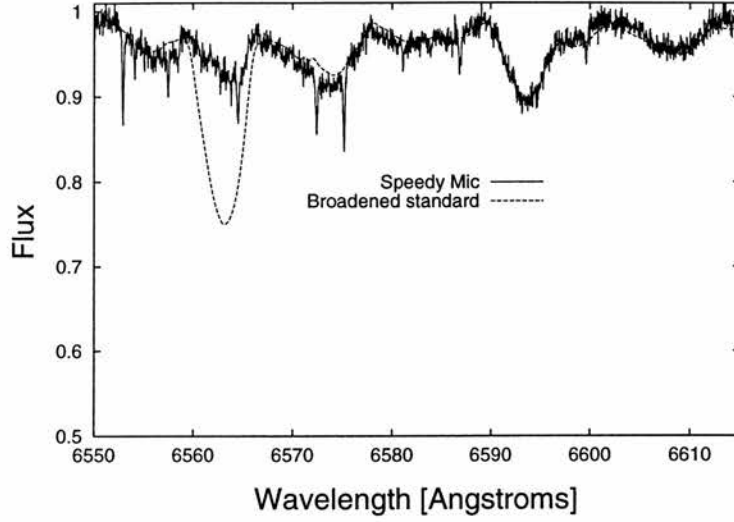


Figure 7.8: Speedy Mic mean H α profile for 14/07/98. Broadened standard is HD 16160

Table 7.4: Distance of prominences from rotation axis of Speedy Mic. Errors are estimated from measured uncertainties in $d\lambda/d(\phi/2\pi)$.

Time	series	Phase	ϖ/R_*
SAAO	10/07/98	0.15	1.3 ± 0.9
		0.45	3.2 ± 1.3
SAAO	11/07/98	0.65	2.4 ± 0.9
AAT	12/07/98	0.95	3.8 ± 1.3

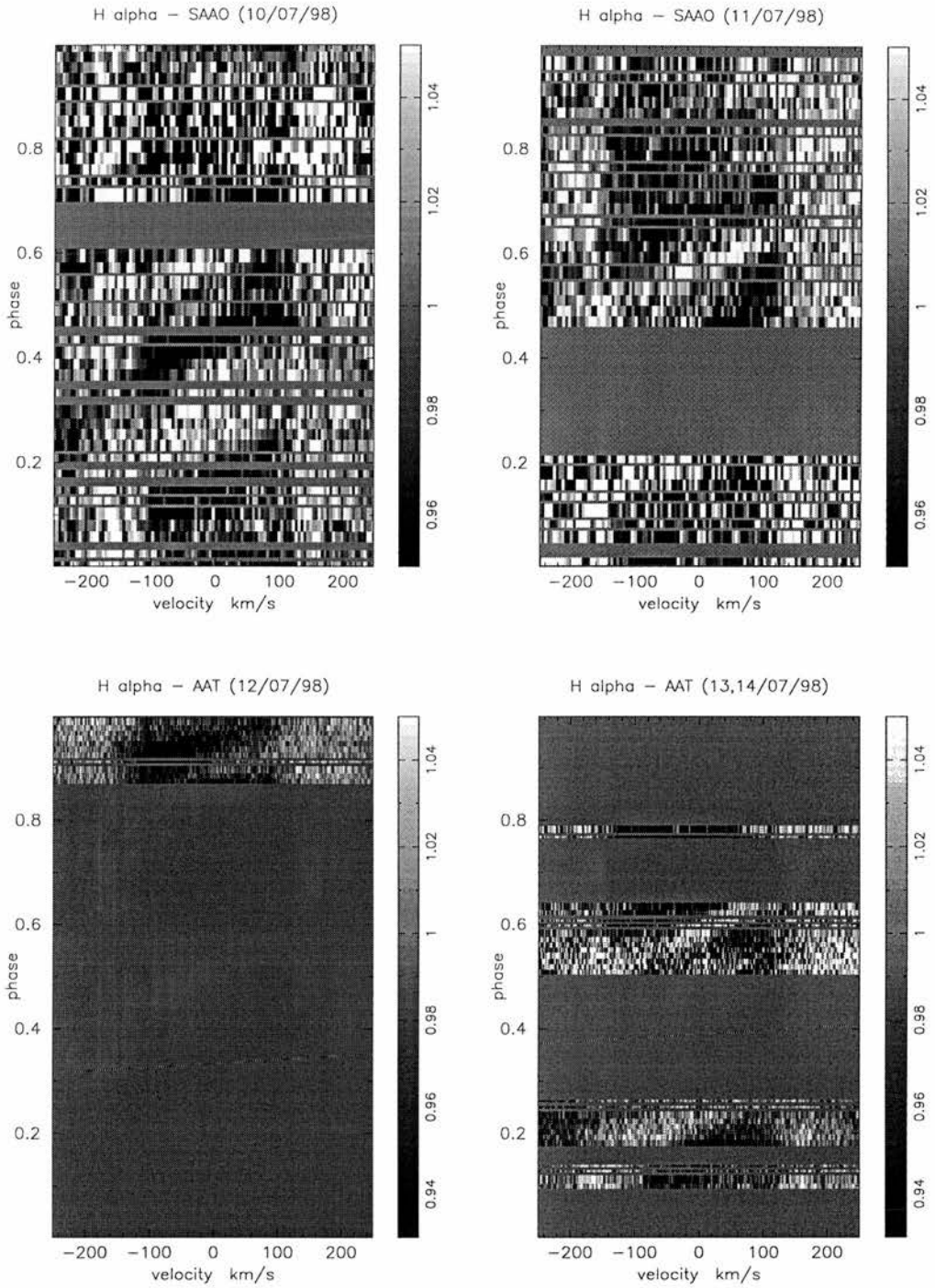


Figure 7.9: Time series spectra for H α profiles (The H α line was not available with the UCLES E79 grating). Absorption features appear black in the H α plots. Several features are identifiable, with the same features appearing in the 1998 July 10 & 11 SAAO data sets, indicating stable prominences over two rotation cycles apart.

the sites of H α emission. The quality of the present data make detection of similar features difficult. There is no apparent evidence for flaring activity at the time of observations in any case.

7.4 Summary and Discussion

All the stars studied here show a strong degree of chromospheric filling in the H α line, whereas most of the stars show variable H α , revealing the presence of circum-stellar sling-shot prominences. Because the spectra were taken primarily for Doppler imaging of least squares deconvolved profiles, the exposure lengths are relatively short and the S:N ratios are not high. Combined with incomplete phase coverage, this has precluded the use of back projection techniques (Collier Cameron & Robinson 1989a) to determine prominence positions. Most spectra do however allow detection of H α transients, which are most easily shown in the form of greyscale time series. Interestingly, of the stars which show H α in emission, none appear to be as active AB Dor, which typically reveals 6-10 prominences in a given rotation cycle. This may in part be due to the lower S:N of the spectra, but may also be related to the degree of activity the star in question is undergoing at the epoch of observation. Speedy Mic and PZ Tel were observed at close epochs, and whereas some transients are seen only once, others appear to be longer lived. Unfortunately lack of phase coverage makes measurements at separate epochs difficult.

It is becoming clear that axial inclination and location of the co-rotation radius are important factors which determine whether H α absorption transients can be observed. Because of the balance of gravitational and centrifugal forces, prominences appear to cluster around the co-rotation radius. Table 7.5 lists the axial inclination and co-rotation radius for each object studied (and BD +22^o4409). Column 4 gives information of the state of H α (i.e. e=emission, a=absorption) and whether prominences are seen. The highest inclination stars, He 520 and PZ Tel both exhibit H α absorption transients as discussed, because prominences transit the stellar disc.

Of greater interest are the intermediate and low inclination objects. Of these objects, it appears that only the shorter period stars exhibit variable H α . AP 149 shows H α in emission, and being the shortest period object is the star with co-rotation radius closest to the rotation axis. The close proximity of the prominence clouds and low inclination are

probably the cause, as discussed. He 699 shows transients, but they appear to be slowly moving. The relatively large co-rotation radius combined with intermediate inclination mean that prominences at large distances from the rotation axis cannot be seen. As noted, the features are very close to the stellar surface, and may in fact be active regions. Speedy Mic however, at only slightly higher inclination clearly reveals several prominences. This can be explained by the lower co-rotation radius which increases the chance of seeing prominences crossing the stellar disc. The relatively large co-rotation radius combined with the inclination of 50° , reduce the chance of seeing $H\alpha$ absorption transients on BD +22^o4409 which are attributable to prominences. It is hard to explain why $H\alpha$ is seen in emission given the high co-rotation radius however. Finally AP 193 exhibits the least degree of variability in $H\alpha$. This is easily explained by the large co-rotation radius and intermediate axial inclination.

Apart from a low co-rotation radius, there may be an additional factor which determines whether $H\alpha$ is seen in *emission* as in the case of Ap 149 and RX J1508.6-4423. If the circumstellar $H\alpha$ emitting region is imagined to be a torus, as shown by the Doppler tomogram of AP 149, the axial inclination determines the projected area we see. The projected ratio of the cross-section of the torus when viewed at an axial inclination of $i = 0^\circ$ to that for an axial inclination of $i = 90^\circ$ is π . In other words, the projected emitting area is π times larger, which may be enough to push $H\alpha$ into emission if most stars possess a high latitude circumstellar toroidal condensation. Hence, we are much more likely to see $H\alpha$ emission on low inclination rapid rotators and more likely to find $H\alpha$ in absorption on high inclination rapid rotators. In this scenario, despite the relatively large co-rotation radius of BD +22^o440, the intermediate inclination of $i = 50 \pm 10^\circ$ (Jeffries et al. 1994) may be sufficient to push $H\alpha$ into emission. This explanation may be a dangerous generalisation because it is known that whether $H\alpha$ appears in emission is a function of both spectral type and age. For example, Prosser, Stauffer & Kraft (1991) showed that $H\alpha$ is nearly always in emission for late-K and M dwarfs in the Pleiades, while field stars mostly show $H\alpha$ in absorption (Herbst & Miller 1989). By the age of the Pleiades, no stars display $H\alpha$ in overt emission, but the core of the line *is* filled relative to field stars of the same colour.

The fact that features appear to be short lived, as also evinced by other authors suggests that structures in the corona evolve much faster than those in the photosphere. As noted by Hussain (1999), this may indicate that surface differential rotation plays only

Table 7.5: Axial inclination and co-rotation radii for all stars. In column 4, ‘e/a’ indicates H α is in emission/absorption whereas y=yes/n=no indicates whether the star has a prominence system

Object	axial inclination [degs]	Co-rotation radius $R_c [R_\star]$	Details
AP 149	30	1.5	e,y
BD +22 ^o 4409	50	2.8	e,n
He 699	52.5	2.4	a,n?
AP 193	55	3.0	a,n
Speedy Mic	55	1.7	a,y
PZ Tel	60	2.6	a,y
He 520	65	2.5	a,y

a small part in the evolution of prominences since these stars rotate almost as solid bodies. On the other hand, rapid evolution in the corona may be a result from small changes due to differential rotation at the photospheric level.

CHAPTER 8

Summary and Conclusions

With the purpose of increasing our understanding of late or solar type stars, high resolution time series spectra of a number of rapid rotators have been obtained. Least squares deconvolution was applied to all spectra in order to obtain a single high S:N ratio absorption profile from the large number of absorption lines in a typical échelle spectrum. High resolution surface images were obtained through maximum-entropy regularised fits to the spectra.

8.1 Least squares deconvolution

The least squares routine, in providing deconvolved profiles of S:N ratios typically > 1000 , results in Doppler images which are well constrained by the data. This in turn allows much better latitude discrimination and higher surface resolution of cool temperature inhomogeneities when compared with single or even multiple line techniques.

Use of least squares deconvolution requires careful consideration of the properties of the deconvolved profile. Factors such as the mean wavelength, limb-darkening and output S:N ratio must be correctly determined. A means of accurately determining these parameters and values is presented. Consideration of the deconvolved profile shape with the intrinsic shape of a single line shows good agreement for a range of $v \sin i$ values. Even spectra with high $v \sin i$ rotation profiles which suffer from larger amounts of rotational blending of the absorption lines allow a reliable deconvolved profile to be recovered. With this reliability confirmed, we are able to apply the technique of least squares deconvolution to a number of real data sets. Figure 8.1 shows the multiplex gain (defined as the SPDECON output S:N divided by the *mean* S:N of the input spectrum) plotted against the square

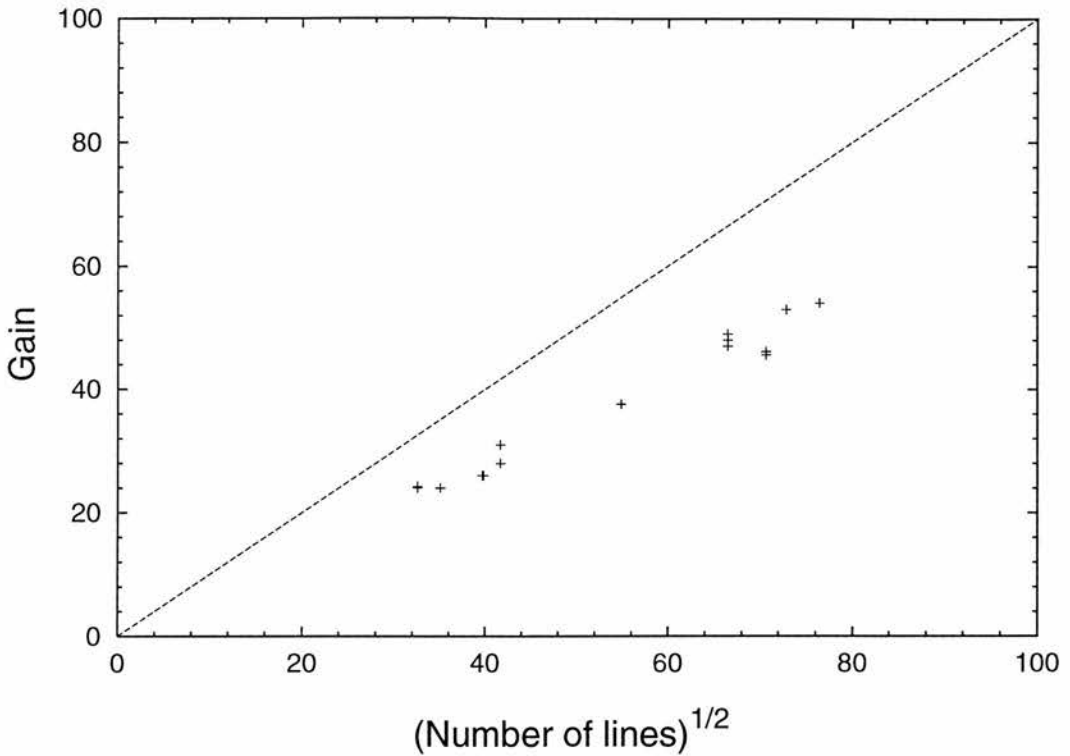


Figure 8.1: Multiplex gain vs $(\text{Number of lines})^{1/2}$.

root of the number of lines used for each separate data set used throughout this work. The straight line is the theoretical upper limit of the gain. The observed gain approximately obeys a square root relationship, but with a slope less than the upper gain limit. This indicates that the deconvolution process is more efficient for lower input S:N ratio values in agreement with the findings of Donati et al. (1997).

8.2 Surface distribution of starspots

The images of the six young rapidly rotating G and K dwarfs presented in Chapters 4 to 6 reveal similarities and differences when compared with other images of single rapid rotators, both relative to each other, and when compared with the other images available in the literature. Some of the main similarities and differences are listed below

Similarities

- 1) All stars exhibit starspot activity at low to intermediate latitudes
- 2) All stars exhibit high latitude or (circum-) polar starspot activity

3) Most stars have a lack of features at intermediate latitudes. This indicates that it is the spots at low latitudes which cause the broadband light variations which are used to determine the axial rotation periods.

Differences

1) The total resolved spot coverage differs from star to star at both the lower latitudes and higher latitudes. The stars imaged here do not always exhibit true polar caps.

2) The images of PZ Tel more than any other star show spots at *all* latitudes (The images of Speedy Mic are difficult to compare with other images because of the poor range of phase coverage and S:N ratio used in the various image reconstructions). Since most stars exhibit a paucity of spots at intermediate latitudes, it may be that they only appear at these latitudes on relatively short timescales, perhaps determined in some way by an activity cycle.

It seems pertinent to compare the results with other Doppler images of single stars. The global latitudinal extent of starspots are given in Table 8.1. It is immediately apparent that the precise position and extent of the low latitude band varies from star to star. While most stars exhibit a polar spot, some stars show only a decentred polar spot feature, while others shown no spot at all.

8.3 Comparison of theory and observations

The fact that a number of Doppler imaging groups find low latitude features, and polar spots for either a number of different stars, or the same star (e.g. LQ Hya) suggests that the reconstructed features are real and not artifacts due to incorrect treatment in the image inversion process. As can be seen, most stars do indeed show a low latitude band centred at different latitudes and covering different ranges. Of particular concern is the fact that all images show low latitude structure. This is incompatible with the convective overshoot dynamo models which predict the emergence of magnetic field at intermediate to high latitudes.

Recent Zeeman Doppler Images (Donati & Collier Cameron 1997) of AB Dor have revealed the structure of the radial and azimuthal magnetic field. The main radial field features detected at intermediate latitude are spatially associated with equally intense

Table 8.1: Spot distributions for a number of single rapid rotators. References are (1) This work, (2) Donati & Cameron, 1999 (3) Donati et al. 1999 (4) Lister et al. 1999 (5) Rice & Strassmeier, 1998, (6) Donati, 1999b (7) Strassmeier & Rice, 1998

Object	Polar spot	Low latitude	reference(s)
AP 149	y, decentred	$35^{\circ} \pm 15^{\circ}$	1
AP 193	no	$20^{\circ} \pm 15^{\circ}$	1
He 520	y, decentred	$0^{\circ} \pm 20^{\circ}$	1
He 699	y	$10^{\circ} \pm 20^{\circ}$	1
PZ Tel	y	$0^{\circ} \pm 30^{\circ}$	1
Speedy Mic	n	$10^{\circ} \pm 20/30^{\circ}$	1
AB Dor	y	$20^{\circ} \pm 20^{\circ}$	2,3
LO Peg	y	$25^{\circ} \pm 10^{\circ}$	4
LQ Hya	y	-10° to 40°	5,6
EK Dra	y	all / 40° preferred	7

azimuthal field regions. This implies that the corresponding field lines are significantly tilted, by as much as 45° with respect to the local normal to the stellar surface. Donati & Collier Cameron speculated that the local toroidal field structure is not confined to the overshoot layer at the base of the convection zone, since buoyancy would turn it into a purely radial structure at the photospheric level. Rather, the toroidal field appears to be distributed at least partially throughout the whole convective envelope. Although only the azimuthal field structure which is formed from the poloidal field via differential rotation (the Ω -effect) is detected, Donati & Collier Cameron suggested that in order to produce a strong azimuthal field that preserves such a high global coherency, the poloidal field must be several orders of magnitude greater than the solar value. The existence of a large scale poloidal field component would then also explain the origin of the cool polar cap on stars such as AB Dor. This could be taken as a clue that the dynamo mechanism on AB Dor is not purely solar-like, but also includes a significant distributed component.

It is not clear how the magnetic field varies on a long term basis. Kürster, Schmitt & Cutispoto (1994) derived images of AB Dor in February 1989 when the activity of AB Dor was at a minimum. This is reflected in the plot of long-term brightness variation (Figure 1.6) which shows a *minimum* around 1988 to 1989. Image reconstructions revealed *no* polar

spot at this time. If the α Persei G dwarfs also undergo long-term activity variations, it may be that He 520 and He 699 are at different stages in their long term activity cycles. The de-centred spot on He 520 and arguably AP 149 may be a manifestation of change in the field structure as a consequence of the activity cycle. It is apparent that further observations are needed to test this idea. The stars which exhibit no polar cap at all, AP 193 and Speedy Mic, may be in a still different stage of a magnetic cycle. Interestingly the α Persei stars also reveal low-latitude bands at 10° (He 520) and 20° (He 699), along with higher ($\sim 55^\circ$) features and and polar or de-centred polar caps. Again, the different latitudes exhibited may be due to these stars being at different points in their magnetic activity cycles, effectively offering snapshots of stellar butterfly diagrams. Given that both the later type stars, PZ Tel and Speedy Mic show spot patterns which are not largely different from their α Persei G dwarf cousins suggests that the dynamo mechanism is only weakly dependent upon spectral type.

From updated stellar structure models, Granzer et al. (2000) have carried out new simulations for flux emergence on stars at a number of rotation rates, masses and ages. These models essentially agree with the Schüssler et al. (1996) models while being more detailed. While starspots are seen at the predicted (maximum likelihood 50° to 55°) latitudes, the images of PZ Tel clearly also show starspots above and below the range of possible latitudes. The simulations of Granzer et al. (2000) do not include the actual flux emergence at the surface where the thin flux tube approximation breaks down. It is therefore unclear exactly what happens to the buoyant flux tubes between the simulation limit and the stellar surface. Since the low latitude features are weaker, it may be that they are carried from higher latitudes by meridional flows. As mentioned by Donati & Collier Cameron (1997), the similarity in field strength of the azimuthal and radial components on AB Dor suggests a dynamo distributed throughout the convection zone. If the dynamo is located at the bottom of the stellar convection zone, one would expect predominantly radial magnetic flux at the stellar surface. One of the main conclusions of Granzer et al. (2000) is that the $m = 0$ axisymmetric instability is only present at very high latitudes or in the very young (primarily T Tauri) models. This instability results in the eruption of the whole flux tube at the stellar surface, which could contribute to the large amounts of azimuthal flux seen on AB Dor. Given that PZ Tel and AB Dor are both approaching the main sequence, this scenario is perhaps unlikely, unless the radiative core is somewhat smaller than expected. The poleward slip instability (Spruit

& Van Ballegoijen 1982 and Moreno-Insertis, Schüssler & Ferriz-Mas 1992) may account for the polar spot and high latitude eruption of magnetic flux (Schüssler et al. 1996). The slip of flux in the overshoot layer (which can be thought of as a rubber-band on a smooth sphere) is driven by magnetic tension and hence high magnetic field strengths.

Further work on LQ Hya and the RS CVn binary, HR 1099 (Donati 1999) has found similar results. A detailed discussion in favour of the distributed dynamo has been presented for this reason, and the fact that the starspots appear at latitudes below those allowed by the Schüssler et al. (1996) and DeLuca, Fan & Saar (1997) overshoot models.

The overshoot-layer type dynamo has been favoured because of the interpretation of helioseismological observations which show that the radial gradient in angular velocity is almost zero throughout the convection zone. Because the overshoot layer is the only region where radial shear takes place, it has been suggested that this is the only region in which the poloidal fields can be converted into toroidal fields through rotational shear (i.e. the Ω -effect). It has been suggested that the small scale solar magnetic fields such as the intra-network fields which are generated in the convection zone contribute significantly to the solar dynamo (Lites et al. 1996).

The hydrodynamical models (e.g. Kitchatinov & Rüdiger 1995 and Rüdiger et al. 1998) of stellar convective zones show that stars which rotate faster than the Sun are quite different from the solar case. The models suggest that differential rotation as a function of radius is not constant as in the solar case, so that the shear layer is not confined to the base of the convection zone. This adds support to the idea of distributed dynamo action presented here, and first put forward by Donati & Collier Cameron (1997), Donati et al. (1999a) & Donati (1999) as discussed above.

8.4 Differential rotation

There have been attempts to indirectly measure the differential rotation rate in a number of late type stars. Donahue, Saar & Baliunas (1996) have measured the modulation of Ca II H & K fluxes in a number of late-type dwarfs. Several observations per week over a 10 year period have yielded a range of periods for some objects. If the active regions causing the Ca II H & K emission occur at different stellar latitudes throughout the stellar magnetic cycle, the corresponding change in the period, is due to differential

rotation. The range of the observed period, ΔP thus represents a lower limit to the surface differential rotation. Donahue, Saar & Baliunas (1996) find that the mass independent relation $\Delta P \propto \langle P \rangle^{1.3 \pm 0.1}$ holds, where $\langle P \rangle$ is the mean seasonal rotation period of the star.

The work presented in Chapter 5 shows that the K0 dwarf PZ Tel, the K0 dwarf AB Dor, and the Sun rotate nearly as solid bodies with approximately the same degree of absolute differential rotation. The time it takes the equator to lap the polar regions in these stars is the same, at 100-120 d, and approximately independent of rotation period and spectral type in agreement with the theoretical predictions of Kitchatinov & Rüdiger (1999).

In terms of the angular velocity,

$$\Delta\Omega \propto \Omega^n, \tag{8.1}$$

which can be written as

$$\frac{\Delta\Omega}{\Omega} \propto \Omega^{n-1}, \tag{8.2}$$

which in terms of rotation period is

$$\Delta P \propto P^{2-n}. \tag{8.3}$$

The results of Donahue, Saar & Baliunas (1996) yield $n = 0.7 \pm 0.1$, whereas the differential rotation measurements from Doppler images and directly from the Sun with $n \approx 0$ are reasonably consistent with those of Hall (1991) where $n = 0.15$ for RS CVn binaries. The power index, n , in equation 8.2 is not in fact constant as shown by the models of Kitchatinov & Rüdiger (1999). For a G dwarf, it is found to vary from a value of -0.56 at the solar rotation rate to a value of 0 at a rotation period of 1 d, with a mean value of $n = -0.15$. Similarly for a K5 Kitchatinov & Rüdiger (1999) find values of $n = -0.21$ (solar rotation rate), 0.05 ($P = 1$ d) and -0.04 (mean) respectively. The difference of the mean power law for the observed data of Donahue, Saar & Baliunas (1996) may be due to the fact that in the sample, the slowest rotators are represented by K dwarfs whereas the fastest rotators are mainly G and F dwarfs.

8.5 Future Work

There is still a need for further Doppler images, many of which will have to be cluster dwarfs. This work is only becoming possible with the advent of 8m class telescopes and techniques such as least squares deconvolution. The whole of parameter space available to Doppler imaging has barely been touched upon. For instance, to date there are no Doppler images of late-K dwarfs and M dwarfs. These stars are of interest because they have the deepest convective zones. If the latitude distributions are at all similar to those found on the existing early-G to mid-K dwarfs, a distributed dynamo seems all the more likely. If convective overshoot models are to have any credence, it is in these stars that low latitude structure should not be found.

REFERENCES

- Adams N. R., Walter F. M., Wolk S. J., 1998, *AJ*, 116, 237
- Allain S., 1998, *A&A*, 333, 629
- Anders G. J., Coates D. W., Jeffries R. D., Kellett B. J., 1993, *MNRAS*, 265, 941
- Andretta V., Doyle J. G., Byrne P. B., 1997, *A&A*, 322, 266
- Attridge J. M., Herbst W., 1992, *ApJ*, 398, L61
- Baliunas S. et al., 1995, *ApJ*, 438, 269
- Balona L. A., 1987, *South African Astronomical Observatory Circular*, 11, 1
- Barnes T. G., Evans D. S., Moffett T. J., 1978, *MNRAS*, 183, 285
- Barnes J., Collier Cameron A., Unruh Y., Donati J.-F., Hussain G., 1998, *MNRAS*, 299, 904
- Barnes J., Collier Cameron A., James D., Donati J.-F., 2000, *MNRAS*, In Press
- Bell S., Hilditch R., Edwin R., 1993, *MNRAS*, 260, 478
- Bessell M., 1990, *PASP*, 102, 1181
- Bouvier J., Forestini M., Allain S., 1997, *A&A*, 326, 1023
- Bouvier J., Bertout C., Benz W., Mayor M., 1986, *A&A*, 165, 110
- Bouvier J., Cabrit S., Fernandez M., Martin E. L., Matthews J. M., 1993, *A&AS*, 101(3), 485
- Bromage G. E., Kellett B. J., Jeffries R. D., Innis J. L., Matthews L., Anders G. J.,
Coates D. W., 1992, *ASP Conf. Ser. 26: Seventh Cambridge Workshop on Cool Stars, Stellar
Systems, and the Sun*, 7, 80
- Bruls J. H. M. J., Solanki S. K., Schüssler M., 1998, *A&A*, 336, 231
- Byrne P. B., 1996, in *IAU Symposia*. p. 299
- Cameron A. C., Campbell C. G., 1993, *A&A*, 274, 309
- Cameron A. C., Foing B. H., 1997, *The Observatory*, 117, 218
- Cameron A. C., Campbell C. G., Quaintrell H., 1995, *A&A*, 298, 133
- Carlsson M., Rutten R. J., Bruls J. H. M. J., Shchukina N. G., 1994, *A&A*, 288, 860
- CDS-Catalogue, 1999, Release 3.0. Centre de Données astronomiques de Strasbourg,
<http://cdsweb.u-strasbg.fr/>
- Charbonnel C., Vauclair S., Zahn J.-P., 1992, *A&A*, 255, 191
- Choi P. I., Herbst W., 1996, *AJ*, 111, 283
- Collier Cameron A., Robinson R. D., 1989a, *MNRAS*, 236, 57
- Collier Cameron A., Robinson R. D., 1989b, *MNRAS*, 238, 657
- Collier Cameron A., Unruh Y. C., 1994, *MNRAS*, 269, 814
- Collier Cameron A., Woods J. A., 1992, *MNRAS*, 258, 360
- Collier Cameron A., Jeffery C. S., Unruh Y. C., 1992, in Jeffery C. S., Griffin R. E. M., eds,
Stellar Chromospheres, Coronae and Winds. Institute of Astronomy, Cambridge, p. 81
- Collier Cameron A., Duncan D. K., Ehrenfreund P., Foing B. H., Kuntz K. D., Penston M. V.,
Robinson R. D., Soderblom D. R., 1990, *MNRAS*, 247, 415

- Collier Cameron A., 1992, in Byrne P. B., Mullan D. J., eds, Surface Inhomogeneities on Late-type Stars. Springer-Verlag, Berlin, p. 33
- Collier Cameron A., 1998, in IAU Colloquium 170, Precise stellar radial velocities, Victoria BC Canada, eds J.B.Hearnshaw and C.D.Scarfe, ASP Conference Series (1999) in press. p. E12
- Collier A. C., 1982, MNRAS, 200, 489
- Cutispoto G., Kurster M., Pagano I., Rodono M., 1997, Informational Bulletin on Variable Stars, 4419, 1
- Cutispoto G., 1997, A&AS, 121, 369
- Cutispoto G., 1998, A&AS, 127, 207
- D'Antona F. Mazzitelli I., 1994, ApJS, 90, 467
- DeLuca E., Fan Y., Saar S., 1997, ApJ, 481, 369
- Donahue R. A., Saar S. H., Baliunas S. L., 1996, ApJ, 466, 384
- Donati J.-F., Collier Cameron A., 1997, MNRAS, 291, 1
- Donati J.-F., Brown S. F., Semel M., Rees D. E., Dempsey R. C., Matthews J. M., Henry G. W., HALL D. S., 1992, A&A, 265, 682
- Donati J.-F., Semel M., Carter B., Rees D. E., Collier Cameron A., 1997, MNRAS, 291, 658
- Donati J.-F., Collier Cameron A., Hussain G., Semel M., 1999a, MNRAS, 302, 437
- Donati J., Mengel M., Carter B., Marsden S., Collier Cameron A., Wichmann R., 1999b, MNRAS, Submitted
- Donati J.-F., 1999, MNRAS, 302, 457
- Doyle J. G., Byrne P. B., van den Oord G. H. J., 1989, A&A, 223, 219
- Doyle J. G., 1996, A&A, 307, 162
- Duncan D. K., 1993, ApJ, 406, 172
- Edwards S. et al., 1993, AJ, 106, 372
- Eggen O. J., 1975, PASP, 87, 37
- Eggen O. J., 1983a, MNRAS, 204, 377
- Eggen O. J., 1983b, MNRAS, 204, 391
- Eggen O. J., 1989, AJ, 98, 1842
- Eggen O. J., 1998, AJ, 115, 2397
- Eibe M. T., Byrne P. B., Jeffries R. D., Gunn A. G., 1999, A&A, 341, 527
- Eibe M. T., 1998, A&A, 337, 757
- Favata F., Micela G., Sciortino S., D'Antona F., 1998, A&A, 335, 218
- Fleming T. A., Giampapa M. S., Schmitt J. H. M. M., Bookbinder J. A., 1993, ApJ, 410, 387
- Flower P., 1996, ApJ, 469, 355
- Forestini M., 1994, A&A, 285, 473
- Granzer T., Caligari P., Schüssler M., Strassmeier K., 2000, AA, Submitted
- Gray D. F., 1992, The observation and analysis of stellar photospheres. CUP, University of Cambridge

- Grevesse N., Anders E., 1989, American Institute of Physics Conference Series, 183, 1
- Haisch B. M., Linsky J. L., Bornmann P. L., Stencel R. E., Antiochos S. A., Golub L.,
Vaiana G. S., 1983, ApJ, 267, 280
- Hale G. E., 1908, ApJ, 28, 315
- Hall D. S., 1991, in IAU Colloq. 130: The Sun and Cool Stars. Activity, Magnetism, Dynamos.
p. 353
- Hartmann L., Hewett R., Stahler S., Mathieu R., 1986, ApJ, 309, 275
- Hatzes A. P., Kürster M., 1999, A&A, 346, 432
- Hatzes A. P., Vogt S. S., 1992, MNRAS, 258, 387
- Hatzes A. P., Vogt S., Ramseyer T., Misch A., 1996, A&A, 469, 808
- Hatzes A. P., 1990, MNRAS, 245, 56
- Hatzes A. P., 1995, ApJ, 451, 784
- Hendry M. A., O'Dell M. A., Collier Cameron A., 1993, MNRAS, 265, 983
- Henry G. W., Eaton J. A., Hamer J., Hall D. S., 1995, ApJS, 97, 513
- Herbst W., Miller J. R., 1989, AJ, 97, 891
- Herbst W., 1989, AJ, 98, 2268
- Horne K. D., 1986, PASP, 98, 609
- Houk N., 1978, Michigan Catalogue of Two Dimensional Spectral Types for the HD Stars. Vol.2,
Ann Arbor, University of Michigan
- Hussain G. A. J., Unruh Y. C., Collier Cameron A., 1997, MNRAS, 288, 343
- Hussain G., 1999, PhD thesis, University of St Andrews, St Andrews, Scotland
- Innis J. L., Thompson K., Coates D. W., Lloyd Evans T., 1988, MNRAS, 233, 887
- Innis J. L., Coates D. W., Thompson K., Lloyd Evans T., 1990, MNRAS, 242, 306
- Jardine M., Unruh Y. C., 1999, A&A, 346, 883
- Jeffries R. D., James D. J., 1999, ApJ, 511, 218
- Jeffries R. D., Byrne P. B., Doyle J. G., Anders G. J., James D. J., Lanzafame A. C., 1994,
MNRAS, 270, 153
- Jeffries R. D., 1993, MNRAS, 262, 369
- Jeffries R. D., 1993b, MNRAS, 262, 369
- Jeffries R. D., 1995, MNRAS, 273, 559
- Jensen K. A., Swank J. H., Petre R., Guinan E. F., Sion E. M., Shipman H. L., 1986, ApJ, 309,
L27
- Johns-Krull C. M., Hatzes A. P., 1997, ApJ, 487, 896
- Johns-Krull C. M., 1996, A&A, 306, 803
- Johnson D. R. H., Soderblom D. R., 1987, AJ, 93, 864
- Joncour I., Bertout C., Bouvier J., 1994, A&A, 291, L19
- Joncour I., Bertout C., Menard F., 1994, A&A, 285, L25
- Jones B. F., Fischer D., Shetrone M., Soderblom D. R., 1997, AJ, 114, 352

- Kawaler S. D., 1988, *ApJ*, 333, 236
- Kearns K. E., Herbst W., 1998, *AJ*, 116, 261
- Kearns K. E., Eaton N. L., Herbst W., Mazzurco C. J., 1997, *AJ*, 114, 1098
- Keppens R., Macgregor K. B., Charbonneau P., 1995, *A&A*, 294, 469
- Kitchatinov L., Rüdiger G., 1995, *A&A*, 299, 446
- Kitchatinov L. L., Rüdiger G., 1999, *A&A*, 344, 911
- Krishnamurthi A., Pinsonneault M. H., Barnes S., Sofia S., 1997, *ApJ*, 480, 303
- Kuerster M., Schmitt J., Cutispoto G., Dennerl K., 1997, *A&A*, 320, 831
- Küker M., Rüdiger G., 1997, *A&A*, 328, 253
- Kürster M., Schmitt J., Cutispoto G., 1994, *A&A*, 289, 899
- Kurucz R. L., 1993, CDROM # 13 (ATLAS9 atmospheric models) and # 18 (ATLAS9 and SYNTHE routines, spectral line database), Cambridge, MA
- Kuschnig R., Ryabchikova T. A., Piskunov N. E., Weiss W. W., Gelbmann M. J., 1999, *A&A*, 348, 924
- Lang K. R., 1992, *Astrophysical Data I. Planets and Stars*. Springer-Verlag Berlin Heidelberg New York
- Leighton R., 1959, *ApJ*, 130, 366
- Li J., Collier Cameron A., 1993, *MNRAS*, 261, 766
- Lister T., Collier Cameron A., Bartus J., 1999, *MNRAS*, In press
- Lites B. W., Leka K. D., Skumanich A., Martinez Pillet V., Shimizu T., 1996, *ApJ*, 460, 1019
- Macgregor K. B., Brenner M., 1991, *ApJ*, 376, 204
- Maeder A., Meynet G., 1989, *A&A*, 210, 155
- Manrique W. T., Lizhi L., Perdomo R., Podesta R. C., Zezhi W., 1999, *A&AS*, 136, 7
- Marsh T. R., Horne K., 1988, *MNRAS*, 235, 269
- Matthews L. et al., 1994, *MNRAS*, 266, 757
- Mills D., 1994, Starlink User Note 152, Rutherford Appleton Laboratory
- Montes D., Saar S. H., Collier Cameron A., Unruh Y. C., 1999, *MNRAS*, 305, 45
- Moreno-Insertis F., Schüssler M., Ferriz-Mas A., 1992, *A&A*, 264, 686
- O'Dell M. A., Collier Cameron A., 1993, *MNRAS*, 262, 521
- O'Dell M. A., Hendry M. A., Collier Cameron A., 1994, *MNRAS*, 268, 181
- O'Dell M. A., Panagi P. M., Hendry M. A., Collier Cameron A., 1995, *A&A*, 294, 715
- O'Dell M. A., Hilditch R. W., Collier Cameron A., Bell S. A., 1997, *MNRAS*, 284, 874
- O'Neal D. Neff J., Saar S., 1998, *ApJ*, 507, 919
- Parker E. N., 1955, *ApJ*, 122, 293
- Parker E. N., 1979, *Cosmical magnetic fields: Their origin and their activity*. Oxford, Clarendon Press; New York, Oxford University Press, 1979, 858 p.
- Patenaude M., 1978, *ApJ*, 66, 225
- Press W. H., Flannery B. P., Teukolsky S. A., Vetterling W. T., 1986, *Numerical Recipes: The*

- Art of Scientific Computing. Cambridge University Press, Cambridge
- Priest E. R., 1984, *Solar Magnetohydrodynamics*. D. Reidel, Dordrecht
- Prosser C. F. et al., 1993, *PASP*, 105, 1407
- Prosser C. F., Randich S., Stauffer J. R., Schmitt J., Simon T., 1996, *AJ*, 112, 1570
- Prosser C. F., Stauffer J., Kraft R. P., 1991, *AJ*, 101, 1361
- Prosser C., 1991, PhD thesis, University of California, Santa Cruz
- Prosser C. F., 1992, *AJ*, 103, 488
- Radick R. R., Thompson D. T., Lockwood G. W., Duncan D. K., Baggett W. E., 1987, *ApJ*, 321, 459
- Radick R. R., Lockwood G. W., Skiff B. A., Baliunas S. L., 1998, *ApJS*, 118, 239
- Ramseyer T. F., Hatzes A. P., Jablonski F., 1995, *AJ*, 110, 1364
- Randich S., Gratton R., Pallavicini R., 1993, *A&A*, 273, 194
- Randich S., Schmitt J. H. M. M., Prosser C. F., Stauffer J. R., 1996, *A&A*, 305, 785
- Randich S., 1998, in *ASP Conf. Ser. 154: Tenth Cambridge Workshop on Cool Stars, Stellar Systems, and the Sun*. p. 501
- Rice J. B., Strassmeier K. G., 1996, *A&A*, 316, 164
- Rice J. B., Strassmeier K. G., 1998, *A&A*, 336, 972
- Robinson R. D., Collier Cameron A., 1986, *Proc. Astron. Soc. Aust.*, 6, 308
- Rüdiger G., Von Rekowski B., Donahue R. A., Baliunas S. L., 1998, *ApJ*, 494, 691
- Saar S. H., 1996, in *IAU Symposia*. p. 237+
- Schatzman E., 1962, *Ann. Astrophys.*, 25, 1
- Schüssler M., Solanki S. K., 1992, *A&A*, 264, L13
- Schüssler M., Caligari P., Ferriz-Mas A., Solanki S. K., Stix M., 1996, *A&A*, 314, 503
- Simkin S., 1974, *A&A*, 31, 129
- Skilling J., Bryan R. K., 1984, *MNRAS*, 211, 111
- Skumanich A., 1972, *ApJ*, 171, 565
- Smith M. D., 1994, *A&A*, 287, 523
- Soderblom D., King J., Henry T., 1998, *ApJ*, 116, 396
- Soderblom D. R., Oey M. S., Johnson D. R. H., Stone R. P. S., 1990, *AJ*, 99, 595
- Soderblom D. R., Jones B. F., Balachandran S., Stauffer J. R., Duncan D. K., Fedele S. B., Hudon J. D., 1993a, *AJ*, 106, 1059
- Soderblom D. R., Stauffer J. R., Hudon J. D., Jones B. F., 1993b, *ApJS*, 85, 315
- Soderblom D. R., Stauffer J. R., MacGregor K. B., Jones B. F., 1993, *ApJ*, 409, 624
- Spiegel E. A., Weiss N. O., 1980, *Nat*, 287, 616
- Spruit H. C., Van Ballegoijen A. A., 1982, *A&A*, 106, 58
- Spruit H. C., 1982, *A&A*, 108, 348
- Stassun K. G., Mathieu R. D., Mazeh T., Vrba F. J., 1999, *AJ*, 117, 2941
- Stauffer J. R., Hartmann L. W., 1987, *ApJ*, 318, 337

- Stauffer J. R., Hartmann L., Latham D., 1987, ApJ, 320, L51
- Stauffer J. R., Hartmann L., Soderblom D. R., Burnham N., 1984, ApJ, 280, 202
- Stauffer J. R., Hartmann L. W., Burnham N., Jones B. F., 1985, ApJ, 289, 247
- Stauffer J. R., Caillault J. P., Gagne M., Prosser C. F., Hartmann L. W., 1994, ApJS, 91, 625
- Stauffer J. R. et al., 1999, ApJ, 527, 219
- Stauffer J., 1999, in *Stellar Clusters and Associations: Convection, Rotation and Dynamos*. ASP Conference Series, p. x, In preparation
- Stout-Batalha N. M., Vogt S. S., 1999, ApJS, 123, 251
- Strassmeier K. G., Rice J. B., 1998, A&A, 330, 685
- Strassmeier K. G., Rice J. B., Wehlau W. H., Hill G. M., Matthews J. M., 1993, A&A, 268, 671
- Strassmeier K. G., Bartus J., Kovari Z., Weber M., Washuettl A., 1998, A&A, 336, 587
- Strassmeier K. G., Welty A. D., Rice J. B., 1994, A&A, 285, L17
- Strassmeier K. G., 1994, A&A, 281, 395
- Strassmeier K. G., 1996a, in *IAU Symposia*. p. 289
- Strassmeier K. G., 1996, A&A, 314, 558
- Stuik R., Bruls J., Rutten R., 1997, AA, 322, 911
- Tikhonov A. N., 1963, *Soviet Math. Dokl.*, 4, 1624
- Tonry J., Davis M., 1979, AJ, 84, 1511
- Unruh Y. C., Collier Cameron A., 1997, MNRAS, 290, L37
- Unruh Y. C., Collier Cameron A., Cutispoto G., 1995, MNRAS, 277, 1145
- Unruh Y. C., Collier Cameron A., Guenther E., 1997, MNRAS, Submitted
- Unruh Y. C., 1996, in *Stellar Surface Structure*. IAU symposium No. 176, Dordrecht, Boston and London, p. 35
- Vilhu O., 1984, A&A, 133, 117
- VizieR-service, 1997, CDS, Release 2.0. Centre de Données astronomiques de Strasbourg,
<http://vizier.u-strasbg.fr/cgi-bin/VizieR>
- Vogel S. N., Kuhl L. V., 1981, ApJ, 245, 960
- Vogt S. S., Hatzes A. P., 1991, in *IAU Colloq. 130: The Sun and Cool Stars. Activity, Magnetism, Dynamos*. p. 297
- Vogt S. S., Penrod G. D., 1983, PASP, 95, 565
- Vogt S. S., Penrod G. D., Hatzes A. P., 1987, ApJ, 321, 496
- Vogt S. S., Hatzes A. P., Misch A. A., Kürster M., 1999, ApJS, 121, 547
- Weber E. J., Davis L., 1967, ApJ, 148, 217
- Weber M., Strassmeier K. G., 1998, A&A, 330, 1029
- Wilson O. C., 1963, ApJ, 138, 832
- Wilson O. C., 1978, ApJ, 225, 396
- Zirin H., 1988, *Astrophysics of the sun*. Cambridge and New York, Cambridge University Press, 1988, 440 p.

APPENDIX A

Spdecon Guide

A.1 Introduction

SPDECON is the implementation of least squares deconvolution used in this work. I give a brief description of the internal workings of the program followed by a description of each input parameter.

A.2 Program subroutines

SPDECON is written as a FIGARO routine and takes 2D-NDF and ASCII input files. The fortran source code is well commented, however, I give a description of the workings of each major subroutine.

A.2.1 `acc_decon`

The wavelength data is converted to velocity space using $c \cdot \ln(\lambda)$, where c is the speed of light in km s^{-1} , and λ the wavelength. A simple cosmic ray fixing routine searches for pixels which are deviant by more than the user defined σ from the median. A sharpness test divides the number of deviant pixels by the deviant value of the mid pixel to determine whether the feature is a cosmic. The sharpness value is user defined. All the necessary arrays are set up and the continuum normalisation described in Equations 2.10 & 2.11 is carried out. All subsequent sub-routines are called from `acc_decon`.

A.2.2 acc_decon1

This subroutine calculates the design matrix in the manner described in Chapter 2. Since the matrix contains mostly zeros which would result in many unnecessary calculations, an indexed system is used. Arrays of the same dimension as the input data which contain the value of the limb-darkening coefficients for the photospheric and spot temperatures at each wavelength point are also calculated.

A.2.3 acc_decon2

The centroidal wavelength, mean weighted limb-darkening coefficients and mean weighted profile depth are calculated and output to the screen. The square symmetrical auto-correlation matrix $\alpha^T \cdot \mathbf{V} \cdot \alpha$ and cross-correlation vector arrays ($\alpha^T \cdot \mathbf{V} \cdot \mathbf{R}$) are calculated from the indexed arrays.

A.2.4 choldc and cholsl

The Cholesky Decomposition used to invert the matrix (Press et al. 1986) and the solution containing the least squares profile are calculated using these routines given by Press et al. (1986).

A.2.5 acc_decon3

Calculates the convolution of the design matrix and the least squares profile to produce a synthetic spectrum as given in Equation 2.1.

A.3 Input Parameters

Extracted échellogram: <SPECTRUM> The extracted echellogram in STARLINK NDF format. The echellogram should be a 2D image with dispersion running along the x-axis, the y-axis representing the cross-dispersion direction or order number

échellogram continuum fit: <CONTFIT> A continuum fit to the input echellogram defined by <SPECTRUM>.

Standard continuum fit: <STDTFIT> A standard continuum fit. As described in Chapter 2, a standard continuum is used to ensure approximately constant weighting across each order for different spectra. The standard spectrum is scaled according to Equation 2.10 & 2.11 thereby accounting for changes in continuum tilt due to starspots and atmospheric extinction.

Wavelength file: <WAVES> The arc-calibrated wavelength file

Line list file: <TABLE> SPDECON requires a synthetic line list giving the wavelength position and line depth of unbroadened lines for a star of the same approximate spectral type as the star being deconvolved. The format of the line list is such that the first line contains the number of lines in the file. Subsequent lines consist of 6 columns of which only columns 1 and 3 are used (The columns are wavelength (nm), atomic number, line depth, Lande factor, excitation potential, 1)

e.g.

2832

426.9874 26.00 0.940 3.397 2.060 1

etc.

Limb darkening coefficients: <LDVAL> Table containing the limb-darkening coefficients in Cousins UBVRI. The first line gives the number of lines which should normally be 5 corresponding to each passband.

e.g.

5

0.737 0.947

0.681 0.822

0.618 0.684

0.556 0.566

0.420 0.464

Number of pixels in deconvolved profile: <PLENGTH> The number of pixels to be deconvolved. This will vary depending upon the size of each pixel, the $v \sin i$ of the object being deconvolved, and the amount of binning (defined by <DVEL>).

Velocity at centre of first pixel: <VSTART> The start velocity for each profile.

Velocity increment per pixel in output profile: <DVEL> The size of each de-

convolved pixel element. This should normally be set to the average pixel increment (in velocity space). The pixel increment in velocity space varies slightly across the chip.

Reject lines near order edges: <EREJVAL> The user can choose to reject line close to the edges of orders. The effects of rejection/no rejection are discussed in Chapter 2.

Rejection threshold: <REJTHR> Rejection threshold for cosmics which were not removed at the extraction stage.

Sharpness test for cosmics: <EREJVAL> Simple sharpness test for cosmic rays. The width divided by the deviation from the median value of the order of the central pixel in the cosmic.

Deconvolved profile name: <PROFIL> Name for the NDF file to hold the deconvolved profile.

Synthetic spectrum: <OUTPUT> The deconvolved profile is multiplied by the corresponding line-mask to create a synthetic échellogram (Equation 2.1).